

Functionalized epitaxial graphene as  
versatile platform for air quality sensors

Dissertation  
zur Erlangung des Grades  
des Doktors der Ingenieurwissenschaften  
der Naturwissenschaftlich-Technischen Fakultät  
der Universität des Saarlandes

von  
Marius Rodner

Saarbrücken  
2021

Tag des Kolloquiums: 28.05.2021  
Dekan: Prof. Dr. Jörn Walter  
Berichterstatter: Prof. Dr. Andreas Schütze  
Dr. Jens Eriksson  
Dr. Anton Köck  
Vorsitz: Prof. Dr. Uwe Hartmann  
Akad. Mitarbeiter: Dr. Flavio Soldera  
Dr. Karin Enander

2021 Linköping Studies in Science and Technology  
Dissertation Thesis No. 2134

# **Functionalized epitaxial graphene as versatile platform for air quality sensors**

Marius Rodner



Applied Sensor Science Unit  
Sensors and Actuators Division  
Department of Physics, Chemistry and Biology  
Linköping University  
SE-581 83 Linköping  
Sweden

Linköping 2021

ISBN: 978-91-7929-675-9  
ISSN: 0345-7524

# ABSTRACT

The work presented in this thesis focuses on epitaxial graphene on SiC as a platform for air quality sensors. Several approaches have been tested and evaluated to increase the sensitivity, selectivity, speed of response and stability of the sensors. The graphene surfaces have been functionalized, for example, with different metal oxide nanoparticles and nanolayers using hollow-cathode sputtering and pulsed laser deposition. The modified surfaces were investigated towards topography, integrity and chemical composition with characterization methods such as atomic force microscopy and Raman spectroscopy. Interaction energies between several analytes and nanoparticle-graphene-combinations were calculated by density functional theory to find the optimal material for specific target gases, and to verify the usefulness of this approach. The impact of environmental influences such as operating temperature, relative humidity and UV irradiation on sensing properties was investigated as well. To further enhance sensor performances, the first-order time-derivative of the sensor's resistance was introduced to speed up sensor response and a temperature cycled operation mode was investigated towards selectivity.

Applying these methods in laboratory conditions, sensors with a quantitative readout of single ppb benzene and formaldehyde were developed. These results show promise to fill the existing gap of low-cost but highly sensitive and fast gas sensors for air quality monitoring.



# ZUSAMMENFASSUNG

Der Fokus dieser Thesis liegt auf der Erforschung von epitaxialem Graphen auf SiC als Plattform für Luftgütesensoren. Diverse Ansätze wurden untersucht, um die Sensitivität, Selektivität, Reaktionsgeschwindigkeit und Stabilität der Sensoren zu verbessern. Die Graphenoberfläche wurde unter anderem mit Metalloxid-Nanopartikeln oder nanometerdünnen Schichten funktionalisiert. Die funktionalisierten Sensorschichten wurden hinsichtlich ihrer Oberflächenbeschaffenheit, Unversehrtheit und chemischen Zusammensetzung mittels Rasterkraftmikroskopie und Raman Spektroskopie untersucht. Die Reaktionsenergien zwischen verschiedenen Analyten und Nanopartikel-Graphen-Kombinationen wurden mit Dichtefunktionaltheorie berechnet, um das optimale Material für spezifische Gase zu finden und um die Brauchbarkeit dieser Funktionalisierungsmethode zu verifizieren. Der Einfluss von äußeren Parametern wie Sensortemperatur, Luftfeuchte und UV-Einstrahlung auf die Sensoreigenschaften wurde ebenfalls untersucht. Um die Sensorleistung zu verbessern, wurde die erste zeitliche Ableitung des Sensorwiderstands als zusätzliches Signal eingeführt und ein temperaturzyklischer Betriebsmodus hinsichtlich seiner Eignung erforscht.

Durch die Anwendung dieser Methoden ist es möglich, einzelne ppbs Benzol und Formaldehyd unter Laborbedingungen zu detektieren. Diese Ergebnisse sind vielversprechend, um die bestehende Lücke der günstigen, aber sehr sensitiven Sensoren für Luftqualitätsüberwachung zu schließen.



# SAMMANFATTNING

Arbetet som presenteras i denna avhandling fokuserar på epitaxiell grafen på SiC som en plattform för luftkvalitetssensorer. Flera tillvägagångssätt har testats och utvärderats för att öka känsligheten, selektiviteten, responstiden, och stabiliteten hos sensorerna. Grafenytorna har modifierats till exempel med olika metalloxid-nanopartiklar och nanolager med användning av hålkatodsputtring och PLD. De modifierade ytorna undersöktes mot topografi, strukturell integritet och kemisk sammansättning med karakteriseringsmetoder som atomkraftsmikroskopi och Ramanspektroskopi. Interaktionsenergies mellan flera analyter och nanopartiklar-grafen-materialkombinationer beräknades med täthetsfunktionalteori för att hitta de optimala materialkombinationerna för specifika målgaser och för att verifiera användbarheten av ytmodifieringarna. Effekten av externa faktorer som arbetstemperatur, relativ fuktighet och UV-bestrålning på avkänningssegenskaper undersöktes också. För att ytterligare förbättra sensorprestanda introducerades första ordningens tidsderivat av sensorns resistans för att snabbare utvärdera sensorns respons, och ett temperaturcyklat driftläge i kombination med multivariat dataanalys undersöktes mot selektivitet.

Genom att använda dessa metoder under laboratorieförhållanden utvecklades sensorer med en kvantitativ avläsning av enstaka ppb bensen och formaldehyd. Dessa resultat visar på en möjlig lösning för att fylla det hålrum som finns i dagens sensorteknologier för luftkvalitetsövervakning, där flera relevanta gaser i dagsläget inte kan mätas med kostnadseffektiva men mycket känsliga och snabba gassensorer.



# POPULÄRVETENSKAPLIG

## SAMMANFATTNING

Förorenad luft är globalt den största enskilda orsaken till förtida dödsfall. Problemet är så allvarligt att världshälsoorganisationen, WHO, beskriver det som ”den nya tobaken”. Luftföroreningar medför enorma samhällskostnader. De tros bära ansvar för cirka åtta miljoner förtida dödsfall per år, och världsbanken har uppskattat att dålig utomhusluft årligen kostar det globala samhället mer än 5000 miljarder dollar i välfärdsbelastning.

Att övervaka hur giftiga luftföroreningar sprider sig lokalt i bebodda områden, framförallt storstäder där föroreningar är högre, är avgörande för att förmildra deras samhällspåverkan. Tyvärr kan inte dagens sensorteknologier mäta vissa föroreningar som är giftiga redan vid extremt låga koncentrationer med den noggrannhet som krävs för att garantera en säker levnadsmiljö.

Linköpings universitet har utvecklat sensorer i speciella sensor-material som ligger i teknisk framkant vad gäller prestanda för de aktuella föroreningarna baserat på tester i labbmiljö. Sensorerna baseras på högkvalitativt grafen på kiselkarbid vars yta modifierats till exempel med nanostrukturer av metall eller metalloxid för att skraddarsyensoregenskaperna. De modifierade ytorna undersöktes mot dess topografi, integritet och kemiska sammansättning med olika karakteriseringsmetoder. Flera sensorer testades för reaktion mot gasformiga föroreningar vid koncentrationer som är relevanta för övervakning av luftkvaliteten. Förutom välkända gaser som CO, NO<sub>2</sub> och NH<sub>3</sub>, har också giftigare gaser som bensen och formaldehyd (VOCs) undersökts. Dessutom applicerades olika nivåer av relativ fuktighet i omgivningen, sensortemperatur och ytterligare UV-bestrålning för att undersöka dessa effekter på sensorsvaret.

Som förväntat beror sensorernas prestanda på material/gas-kombination. Alla sensorer reagerade på NO<sub>2</sub> and NH<sub>3</sub>, men endast ett fåtal visade respons för VOCs, vars svar ytterligare försvårades med fuktighet i omgivningen. Sensorsvarets magnitud varierar beroende på sensorernas ystruktur och vilken gas de exponeras mot, men överlag erhålls störst reaktion gentemot NO<sub>2</sub> och NH<sub>3</sub>. Trots detta är dessa sensorer lovande även för detektion av VOCs, då de sensorer som reagerade mot VOCs uppvisade svar för koncentrationer ner till låga miljarddelar, som är precis vad som

behövs för luftkvalitetsövervakning. Detektion av så pass låga koncentrationer är möjlig tack vare den höga graden av uniformitet och låga mängden defekter i grafen på kiselkarbid, vilket i sin tur resulterar i ett material som karakteriseras av lågt brus och hög känslighet.

I nuläget kan vi inte detektera och samtidigt särskilja mellan alla gaser med bara en sensor. Vi tror att detta kommer bli möjligt i framtiden genom att använda flera sensorer samtidigt och/eller cyklade driftlägen, i kombination med smart analys av flerdimensionella data, ett koncept som ofta kallas elektronisk näsa.

# PREFACE

The present dissertation thesis is the result of my binational doctoral studies carried out between November 2016 and May 2021. The work was supervised by Dr. Jens Eriksson at the Sensors and Actuators Division at the Department of Physics, Chemistry and Biology (IFM), Linköping University, Sweden and Prof. Andreas Schütze at the Lab for Measurement Technology, Saarland University, Germany. It was performed in close collaboration with other divisions at IFM and the Department of Microtechnology and Nanoscience at Chalmers University of Technology, Sweden. Part of the contents of these chapters have been previously published in my Licentiate Thesis (No. 1851, Linköping Studies in Science and Technology, ISBN 978-91-7519-010-5). My research was financially supported by the Swedish Foundation for Strategic Research (SSF) through the grants GMT14-0077 and RMA15-024. During the course of research underlying this thesis, I was enrolled in Agora Materiae, a multidisciplinary doctoral program at Linköping University, Sweden. Research results are summarized, brought into context and then presented in the appended papers, preceded by an introduction to the scientific field and used research methods. For a better overview of my work, the latest unpublished results are included as well. However, to comply with regulations from both universities, only papers that have at least been accepted can be part of the formal evaluation.

Marius Rodner  
Linköping, March 2021



# APPENDED PAPERS

- Paper 1** M. Rodner, J. Bahonjic, M. Mathisen, R. Gunnarsson, S. Ekeroth, U. Helmersson, I. G. Ivanov, R. Yakimova, J. Eriksson, Performance tuning of gas sensors based on epitaxial graphene on silicon carbide, *Materials and Design* (2018)
- Paper 2** M. Rodner, D. Puglisi, S. Ekeroth, U. Helmersson, I. Shteplyuk, R. Yakimova, A. Skallberg, K. Uvdal, A. Schütze, J. Eriksson, Graphene Decorated with Iron Oxide Nanoparticles for Highly Sensitive Interaction with Volatile Organic Compounds, *Sensors* (2019)
- Paper 3** M. Rodner and J. Eriksson, First-order time-derivative readout of epitaxial graphene-based gas sensors for fast analyte determination, *Sensors and Actuators Reports* (2020)
- Paper 4** M. Rodner, A. Icardi, M. Kodu, R. Jaaniso, A. Schütze, J. Eriksson, Metal Oxide Nanolayer-Decorated Epitaxial Graphene: A Gas Sensor Study, *Nanomaterials* (2020)

## Author's contribution to appended papers

- Paper 1** I evaluated and interpreted all measurement data and wrote the manuscript.
- Paper 2** I designed and performed all gas and AFM measurements, evaluated and interpreted the data and wrote the main part of the manuscript.
- Paper 3** I designed and performed all measurements, evaluated and interpreted the data and wrote the manuscript.
- Paper 4** I designed and performed most of the measurements, evaluated and interpreted the data and wrote the main part of the manuscript.

Published articles have been reprinted with the permission of the copyright holders.

## OTHER RELATED PUBLICATIONS

- Paper A** M. Rodner, D. Puglisi, R. Yakimova, J. Eriksson, A Platform for Extremely Sensitive Gas Sensing: 2D Materials on Silicon Carbide, *TechConnect Briefs* (2018)
- Paper B** M. Rodner, D. Puglisi, S. Ekeröth, U. Helmersson, I. G. Ivanov, R. Yakimova, K. Uvdal, A. Schütze, J. Eriksson, Iron Oxide Nanoparticle Decorated Graphene for Ultra-Sensitive Detection of Volatile Organic Compounds, *Proceedings* (2018)
- Paper C** P. Darshni Kaushik, M. Rodner, G. B. V. S. Lakshmi, I. G. Ivanov, G. Greczynski, J. Palisaitis, J. Eriksson, P. Solanki, A. Aziz, A. M. Siddiqui, R. Yakimova, M. Syväjärvi, G. R. Yazdi, Surface functionalization of epitaxial graphene using ion implantation for sensing and optical applications, *Carbon* (2019)
- Paper D** K. H. Kim, H. He, M. Rodner, R. Yakimova, K. Larsson, M. Piantek, D. Serrate, A. Zakharov, S. Kubatkin, J. Eriksson, S. Lara-Avila, Chemical Sensing with Atomically Thin Platinum Templated by a 2D Insulator, *Advanced Materials Interfaces* (2020)
- Paper E** M. Rodner, A. Icardi, M. Kodu, R. Jaaniso, J. Eriksson, Metal Oxide Nanolayer Decorated Epitaxial Graphene Gas Sensors for Air Quality Monitoring, *SMSI 2020 Conference – Sensor and Measurement Science International* (2020)
- Paper F** G. Domènech-Gil, M. Rodner, J. Eriksson, D. Puglisi, Temperature Cycled Operation and Multivariate Statistics for Electronic-Nose Applications Using Field Effect Transistors, *Proceedings* (2020)

# ACKNOWLEDGEMENTS

First of all, I want to thank my supervisor Jens Eriksson for accepting me into his group and guiding me through this scientific journey on the search for the ultimate graphene gas sensor. I am grateful for your support with so many scientific questions and your patience, especially, when I come knocking again asking supposedly silly questions. Research is not all about science and, therefore, thank you for being a good friend also outside of work.

Moreover, I would like to thank all the former and current members of our small research group, Anette Andersson, Anita Lloyd Spetz, Donatella Puglisi, Maria Francesca Santangelo, Guillem Domènech Gil, Jasna Bahunjic, Lida Khajavizadeh, Manuel Bastuck, Mike Andersson, Peter Möller and Yuki Hasegawa. Even the most interesting project would not be any fun without a good work environment. So thank you all for all the Fikas, country dinners, work and non-work related trips around the world, group activities and of course a lot of scientific and non-scientific discussions. A special thanks to Donatella, who took care of me when I was new to this group and to Sweden. And also to Mike for his company in and outside of IFM and without whom our laboratory would not function at all. Moreover, I want to thank our current and former master students Adam Icardi, Alberto Zilli, Cecilia Gullström, Isac Cederquist and Marcus Mathisen for their contributions to this work.

For the opportunity to continue a collaboration with my old group at Saarland University, I want to thank especially Andreas Schütze for joining my doctorate as my supervisor on the German side. In general, I want to thank Andreas and the members of his Laboratory for Measurement Technology group for the hospitality throughout the years and the traditional “Fleischkäse-Freitage”. A very special thanks to Manuel Bastuck, who was also a part time member of our group here in Linköping, when he was not pursuing his PhD in Germany. Thank you for taking care of me and my measurement needs when I came for visits to the old lab and all the help and discussions about our courses, papers, ongoing work, theses and life in general. A similar important thanks also to Caroline Schultealbert, Henrik Lensch and Tobias Baur, who helped me during and between my visits in Germany, making sure that everything from data acquisition over data handling and analysis to just having a good time went well.

## Acknowledgements

Furthermore, I want to thank my co-supervisor Kajsa Uvdal and my mentors Fredrik Karlsson and Jianwu Sun for all the fruitful discussions and helpful suggestions.

In general, I would also like to thank all the people I have collaborated with during this project and who supported me from sample preparations, over characterizations to evaluations and discussions. Thanks to Andreas Skallberg, Ivan G. Ivanov, Ivan Shtepliuk, Rickard Gunnarsson, Rositsa Yakimova, Sebastian Ekeröth and Ulf Helmersson from IFM at Linköping University, Hans He, Kyung Ho Kim, Samuel Lara-Avila, Sergey Kubatkin and Tomas Löfwander from the MC2 Lab at Chalmers University of Technology and Margus Kodu and Raivo Jaaniso from the Institute of Physics at University of Tartu.

Many thanks to my friends and colleagues from the Agora Materiae graduate school, the Agora Student Council of which I was a member of for longer than expected, and the former and current heads of Agora, Per-Olof Holz, Fredrik Karlsson and Caroline Brommesson, for all the nice study trips, seminars, summer conferences and discussions.

I had also a very nice time being a member of the PhD Reference Group (now Doctoral Student Council – DoStuC) at IFM, thus getting involved in many interesting projects and boards throughout the whole university. It was a pleasure to work with you guys.

I would like to acknowledge the financial support from the Swedish Foundation for Strategic Research (SSF) through the grants GMT14-0077 and RMA15-024, and from the Centre in Nano science and technology (CeNano) through the “Graphene-nanoparticle hybrid gas sensor” projects. The research visits in Germany were financially supported by travel grants from the Hans Werthén Foundation and the Swedish Chapter of International Society of Indoor Air Quality and Climate (SWESIAQ).

A PhD student life which is just about the PhD studies would be rather annoying and so I am glad to have made many new friends from all over the world during my time here. Thanks for the nice lunch group, my climbing buddies, tennis opponents, hiking comrades, techno-totem ravers, travel fellows and more. It was seldom boring (except during COVID-19 restrictions) and someone was always up for Fika, beers, dinners, concerts, parties, games, BBQs and so on. So thanks to Alex, Andreas, Arnaud, Claudia & Mattias, Clio, Davide, Fredrik & Matilda, Hassan & Anna-Giulia, Judit & Kevin, Johan & Julia, Karina, Laurent, Nikos, Pernilla, Robin & Paula, Serge, Tim and Victor. In case I have forgotten anyone, I apologize. It was not on purpose, so thank you as well.

Of course, I also want to thank my 'old' friends from Germany for their support and a special thanks to those who have even managed to visit me during my time here in Sweden.

Last and most important, I want to thank my family and my girlfriend Lisa. Thank you very much for so much support and motivation both from Germany and on site here in Linköping. This whole expedition would not have been possible without you.



# Table of contents

<b>Preface</b> .....	<b>ix</b>
<b>1 Motivation</b> .....	<b>1</b>
<b>2 Theory and concepts</b> .....	<b>5</b>
<b>2.1 Chemical gas sensors</b> .....	<b>5</b>
<b>2.2 Graphene</b> .....	<b>6</b>
2.2.1 Electronic properties .....	8
2.2.2 Epitaxial graphene on SiC .....	10
<b>2.3 Graphene as sensor platform</b> .....	<b>11</b>
2.3.1 Optimizing EG gas sensors .....	12
2.3.2 Sensing mechanism .....	14
<b>2.4 Multivariate data analysis</b> .....	<b>16</b>
<b>3 Experimental methods</b> .....	<b>19</b>
<b>3.1 Deposition techniques</b> .....	<b>19</b>
3.1.1 Sputter deposition .....	19
3.1.2 Pulsed laser deposition.....	24
<b>3.2 Characterization methods</b> .....	<b>26</b>
3.2.1 Atomic force microscopy .....	26
3.2.2 Raman spectroscopy .....	27
3.2.3 Density functional theory .....	28
<b>3.3 Sensor fabrication</b> .....	<b>29</b>
3.3.1 Graphene growth .....	29
3.3.2 Sensor mounting.....	31
<b>3.4 Data handling</b> .....	<b>33</b>
3.4.1 Data acquisition.....	33
3.4.2 Data analysis .....	34
<b>3.5 Gas mixing apparatus</b> .....	<b>37</b>
3.5.1 Target analytes.....	39
<b>4 Results and discussion</b> .....	<b>45</b>
<b>4.1 Layer characterization</b> .....	<b>45</b>

## Table of contents

4.1.1	Topography .....	45
4.1.2	Structural integrity .....	48
4.1.3	Theoretical considerations .....	50
<b>4.2</b>	<b>Gas measurements .....</b>	<b>51</b>
4.2.1	Influence of temperature .....	51
4.2.2	Influence of humidity .....	53
4.2.3	Influence of UV irradiation.....	56
4.2.4	Influence of defects.....	58
4.2.5	Target analyte detection .....	60
<b>4.3</b>	<b>Advanced data evaluation.....</b>	<b>68</b>
4.3.1	First-order time-derivative signal .....	68
4.3.2	Multivariate analysis .....	74
<b>4.4</b>	<b>Inter-lab studies.....</b>	<b>80</b>
<b>4.5</b>	<b>More EG sensor applications.....</b>	<b>82</b>
<b>5</b>	<b>Conclusions and outlook .....</b>	<b>85</b>
	<b>References .....</b>	<b>87</b>
	<b>Abbreviations .....</b>	<b>103</b>

# 1 Motivation

According to the World Health Organization (WHO), several toxic air pollutants exceed the recommended exposure levels in more than 91 % of the monitored urban areas [1, 2]. It is estimated that poor air quality is currently accountable for more than 8 million premature deaths per year with indoor air quality being the single largest environmental health risk factor worldwide [3]. With people in North America and Europe spending about 90 % of their time indoors, a single short time exposure to most air pollutants is not dangerous, but reoccurring exposures over long periods of time can cause severe health risks and diseases referred to as “sick building syndrome” [4]. Poor air quality is also inflicting a yearly financial burden of about 5 trillion US dollars [5], with emissions from fossil fuels alone costing about 3.3 % of global GDP, which is about 8 billion US dollars per day [6]. Therefore, a proper way of assessing air quality needs to be established.

The key is to be able to detect even trace amounts of hazardous gases. When it comes to the detection of carcinogenic volatile organic compounds (VOCs) like benzene ( $C_6H_6$ ) and formaldehyde ( $CH_2O$ ) at relevant levels, there are analytical instruments available which are, however, large, complex, and expensive. Small low-cost sensor systems, on the other hand, suffer from limited sensitivity, selectivity and stability [7, 8]. A portable low-cost sensor capable of rapid quantification of relevant VOCs at single digit parts per billion (ppb<sup>1</sup>) or even lower would thus be a breakthrough in the field of air quality monitoring (AQM). Moreover, a current report from IDTechEx expects that the total market for environmental sensors will be over 3.8 billion US dollars by 2030 [9].

Two-dimensional materials like graphene exhibit several outstanding properties which enable the fabrication of sensor devices that can be used for quantification of very small gas concentrations as even a small change in the number of charge carriers results in a large change in the electronic state, which then can easily be measured as a change in resistance of the sensor surface [10, 11]. In this work, epitaxial graphene on silicon carbide, which has been demonstrated to outperform standard CVD graphene if used as gas sensor [12], was studied as transducer or sensor material for AQM applications.

---

<sup>1</sup> ppb refers here to the ratio in volume. Also known as ppb<sub>v</sub>.

## 1 Motivation

One way to strongly increase the sensitivity and, potentially, selectivity of a gas sensor is the combination of different materials or the decoration of a sensitive transducer with a reaction-selective material, like metal oxides, combining their individual advantages [13]. For example, the combination of sensitive and more selective nanostructured metal oxides with very sensitive and low noise graphene leads to promising sensor hybrids. There, the gas reaction mainly takes place on the metal oxide nanostructure, and the graphene is used as a highly sensitive transducer [14, 15] leading to an increased sensitivity and selectivity to gases like nitrogen dioxide (NO<sub>2</sub>), benzene and formaldehyde [16].

High sensitivity alone though is not sufficient to produce a useful gas sensor. Other properties such as stability, selectivity and fast time constants are also necessary. Especially for AQM, a sensor needs to be sensitive, selective, stable and it must have a high enough sampling rate to allow near-real-time monitoring with high time and concentration resolution [17, 18]. To speed up the sensor response, usually the sensor is irradiated with a light source during the gas measurement [19] or operated at elevated temperatures [20]. A different method is the use of the sensor signal's first-order time-derivative which was shown to drastically decrease the detection time [21]. Improved stability, selectivity and sometimes even sensitivity can also be gained through a temperature cycled operation mode and multivariate data analysis [20, 22].

Here, epitaxial graphene on SiC-based gas sensors have been investigated regarding their capability of quickly detecting VOCs at concentrations of interest for AQM by combining several of the mentioned approaches. Evaluations performed at two independent laboratories verify the reliability of the obtained results.

This thesis summarizes and elaborates upon the work published in Papers 1-4. Additionally, unpublished content from latest research is included for a better overview.

Paper 1 discusses ways to improve the performance of gas sensors based on epitaxially grown graphene on silicon carbide with metal oxide nanoparticle decoration, UV irradiation and a smart sensor readout utilizing the first-order time-derivative of the sensor's resistance to evaluate them for AQM applications.

Paper 2 focuses on the surface decoration with iron oxide nanoparticles, and the implications for sensing properties to C<sub>6</sub>H<sub>6</sub> and CH<sub>2</sub>O in the concentration range from parts per million down to single-digit parts per billion to create ultra-sensitive gas sensors for hazardous VOCs.

Paper 3 investigates the utilization of the first-order time-derivative of the sensor's resistance as an additional sensor signal, its impact for time constants and its stability to external influences to enhance speed and stability of the sensor response to pulsed gas exposures.

Paper 4 studies the sensor properties of epitaxial graphene sensors decorated with several different metal oxide nanolayers, their response to various gases, the impact of environmental influences and an inter-lab comparison with measurements performed both at Linköping University and Saarland University.



# 2 Theory and concepts

This chapter discusses the general properties of graphene and its peculiarities if grown on silicon carbide (SiC). It also gives a short introduction to chemical gas sensors and graphene sensors in general with a focus on possible surface modifications to tailor them for optimal gas detection.

## 2.1 Chemical gas sensors

In the context of this thesis, a chemical sensor is a sensor able to detect a chemical analyte, i.e., the presence of a specific gas. The sensing mechanism itself can be of physical, chemical or biological nature [23]. Focusing on gas sensors that rely on the analyte to adsorb to the sensor surface, the weakest possible interaction would be physisorption, where the analyte only binds through van der Waals forces. A chemisorption, usually in the form of ionic binding, is much stronger and can occur after the physisorption. Moreover, gas molecules can also dissociate and then react with reactive oxygen ions that are normally adsorbed on the sensor surface.

There are many different types of chemical gas sensors, but here, the focus is on resistive-type sensors, where a gas exposure leads to a change in the sensor's resistivity (or conductivity). The sensing layer is normally based on grainy, metal oxide semiconducting (MOS) materials such as tin dioxide ( $\text{SnO}_2$ ), tungsten trioxide ( $\text{WO}_3$ ) or zirconium dioxide ( $\text{ZrO}_2$ ) [24–26]. Two neighboring grains of the sensing material form an energy barrier, which each electron contributing to the electric current has to overcome. The energy barrier depends on the depletion layer, which in turn depends on the surface states of each grain [27]. Oxygen adsorption on the sensor surface in the form of  $\text{O}^{2-}$  or  $2\text{O}^-$  can bind formerly free electrons, thus forming a depletion layer. Therefore, the energy barrier between two grains will increase and the conductivity will decrease [27]. Equation (2.1) describes the dependence of the conductivity  $\kappa$  for an n-type sensor material:

$$\kappa = \kappa_B \cdot \exp\left(-\frac{E_B}{k_B T}\right) \quad (2.1)$$

where  $\kappa_B$  is the conductivity of the bulk material,  $k_B$  the Boltzmann constant,  $T$  the temperature, and  $E_B$  the energy barrier. The energy barrier is

## 2 Theory and concepts

dependent on the surface charge density  $Q_s$  and the density of donors  $N_D$  according to the Schottky approximation as follows [27]:

$$E_B \sim \frac{Q_s^2}{N_D} \quad (2.2)$$

A reducing gas will bind and remove oxygen from the surface, decreasing the energy barrier between two grains and decreasing the resistivity. A more in-depth study on metal oxide semiconductor gas sensors can be found in [28].

## 2.2 Graphene

The existence of graphene was predicted already in 1947, but it took until 2004 to produce a free-standing, monoatomic layer of graphene that could be studied with regards to its special properties [29]. Since then, extensive research was conducted and graphene became the most studied two-dimensional material until now. Its two-dimensional structure consists of an arrangement of hexagonal covalently bound carbon atoms forming a honeycomb structure. The planar structure is due to  $sp^2$  hybridization of orbitals between carbon atoms. Three out of four valence electrons are involved in strong covalent  $\sigma$ -bonds (binding energy of  $\sim 5.9$  eV) with adjacent carbon atoms. These bonds are responsible for the flat structure of graphene and the exceptional structural strength. The solitary p-orbital, i.e., the fourth valence electron, forms an aromatic  $\pi$ -bond with the adjacent carbon atoms [30]. These delocalized electrons construct the valence and conduction bands in graphene and give rise to the materials conductivity. A schematic depiction of the honeycomb lattice structure of graphene and its corresponding reciprocal counterpart is shown in Figure 2.1. The lattice vectors of the real space unit cell are described as

$$a_1 = \frac{3a}{2} \hat{x} + \frac{\sqrt{3}a}{2} \hat{y} \quad ; \quad a_2 = \frac{3a}{2} \hat{x} - \frac{\sqrt{3}a}{2} \hat{y} \quad (2.3)$$

where  $a$  is the distance between adjacent carbon atoms ( $1.42 \text{ \AA}$ ). The hexagonal lattice of graphene can be described as a combination of two triangular sublattices, A and B. The primitive cell contains two atoms in total, one from each sublattice.

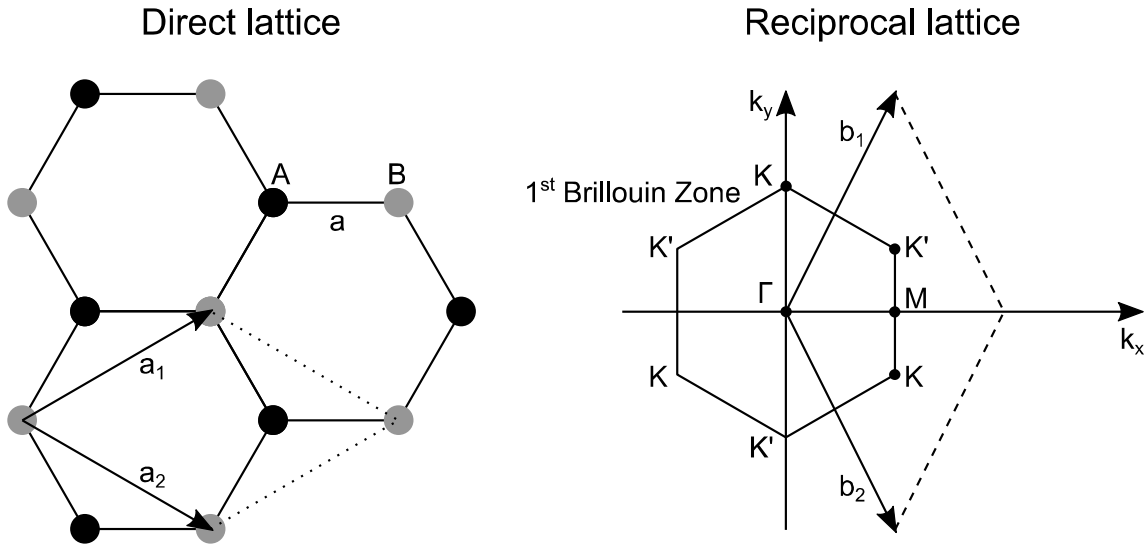


**Figure 2.1:** Left: Real space honeycomb lattice of graphene, consisting of two overlapping triangular sublattices A (black atoms) and B (grey atoms). The lattice vectors  $\mathbf{a}_1$  and  $\mathbf{a}_2$  form the primitive cell together with the dotted lines. Right: Reciprocal lattice with the first Brillouin zone. Adapted from [31].

The first Brillouin zone (BZ) is represented in the reciprocal lattice, which is defined by the reciprocal lattice vectors  $b_1$  and  $b_2$ . The corners of the hexagonal first BZ are marked by six points, with only two non-equivalent points  $K$  and  $K'$ , due to the two sublattices A and B. These six points are called Dirac points. The reciprocal vectors and the Dirac points can be calculated using

$$b_i a_j = 2\pi \delta_{ij} \quad (2.4)$$

where  $\delta_{ij}$  is the Kronecker delta, leading to

$$b_1 = \frac{2\pi}{3a} \hat{x} + \frac{2\pi}{\sqrt{3}a} \hat{y} \quad ; \quad b_2 = \frac{2\pi}{3a} \hat{x} - \frac{2\pi}{\sqrt{3}a} \hat{y} \quad (2.5)$$

$$K = \frac{2\pi}{3a} \hat{x} + \frac{2\pi}{\sqrt{3} \cdot 3a} \hat{y} \quad ; \quad K' = \frac{2\pi}{3a} \hat{x} - \frac{2\pi}{\sqrt{3} \cdot 3a} \hat{y} \quad (2.6)$$

A monolayer graphene can also be the starting point for other interesting carbon allotropes (see Figure 2.2). It can be wrapped into 0D fullerenes (also referred to as ‘Buckyballs’), rolled into 1D nanotubes (also referred to as ‘CNTs’) or stacked into 3D graphite (also referred to as ‘multilayer graphene’ if containing only a low number of layers). Each structure, with its specific properties, is used in different fields of research and applications.

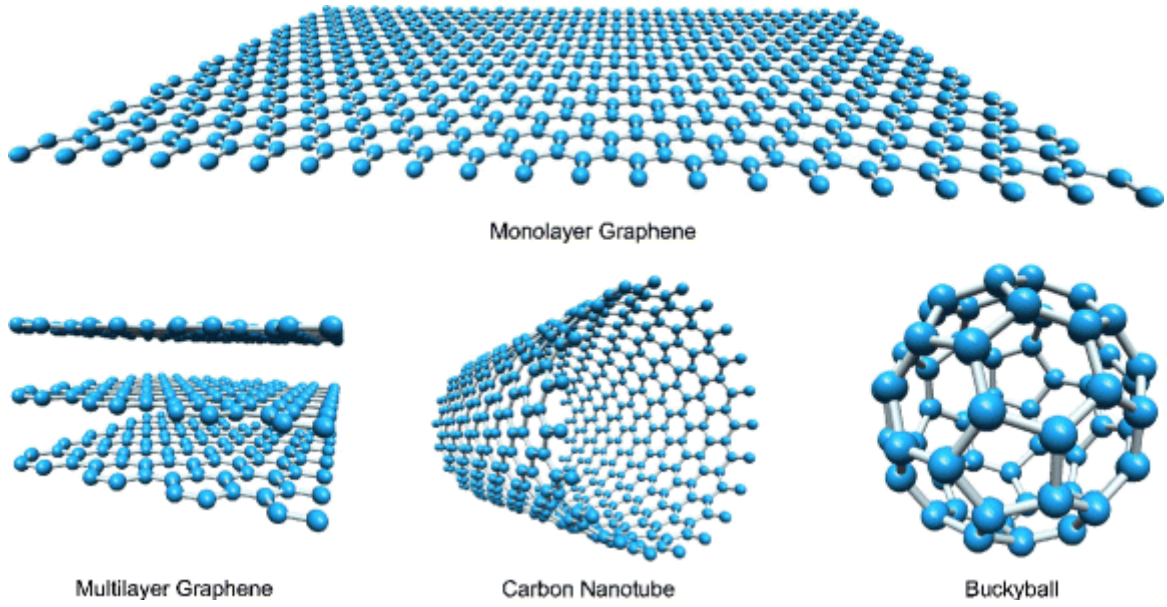


**Figure 2.2:** Different structures formed out of graphene. Reprinted with permission from Springer Nature, Journal of Infrared, Millimeter and Terahertz Waves: A Review of the Terahertz Conductivity of Bulk and Nano-Materials by James Lloyd-Hughes et al. (2012) [32].

## 2.2.1 Electronic properties

Graphene has some outstanding properties like high electrical conductivity ( $\sim 10^8 \text{ S m}^{-1}$ ), a high melting point (4510 K), high thermal conductivity (up to  $5000 \text{ W m}^{-1} \text{ K}^{-1}$ ), a high maximum current density ( $\sim 1.6 \cdot 10^9 \text{ A cm}^{-2}$ ) and a high electron mobility ( $2 \cdot 10^5 \text{ cm}^2 \text{ V}^{-1} \text{ s}^{-1}$  at an electron density of  $\sim 2 \cdot 10^{11} \text{ cm}^{-2}$ ) [33]. Figure 2.3 shows the low energy band structure of graphene with the six Dirac points. At the Dirac points, valence and conduction band meet in the reciprocal space. Since the energy dispersion is linear close to the Dirac points at low energies  $|E| < 3 \text{ eV}$  and the effective mass is equal to the second derivative of the energy versus momentum relations, charge carriers in graphene behave as ultra-relativistic particles with zero rest mass, hence like photons. Therefore, the Schrödinger equation reduces to the 2D Dirac equation which is used to describe the behavior of massless Dirac fermions. This is also the reason why the  $K$  and  $K'$  points are called Dirac points. The linear dispersion creates a conical shape in reciprocal space, the so-called Dirac cone. The density of states DOS can then be calculated as

$$\text{DOS}(E) = \frac{2|E|}{\pi(\hbar v_F)^2} \quad (2.7)$$

where  $\hbar$  is the so-called reduced Planck constant and  $v_F$  is the Fermi velocity. Electron hopping is the dominating charge transfer mechanism in graphene and therefore the charge carriers move at the Fermi velocity ( $\sim 10^6$  m/s) [31]. The DOS is linear with energy and vanishes at the Dirac points. In theory this means that, at absolute zero, graphene is electrically insulating with infinite resistance at the Dirac points. Since there is no band gap, graphene is often referred to as a zero-bandgap semi-metal. In practice, there are other factors such as spatial charge disorder which complicate this relation though. Experiments show a very high, instead of infinite, resistance at the Dirac points, with the maximum resistance of graphene being controversial with different theories predicting varying values [34].

It is important to note that multilayer graphene can grow in the AB (Bernal) or the AA stacked form depending on the substrate. In the AA stacked form, all layers are perfectly aligned, whereas in the AB stacked form, half of the atoms lie directly over the center of a hexagon in the lower graphene sheet, and half of the atoms lie over an atom. The stacking mode is very important for the electrical properties of the resulting graphene sheets [31]. The binding energy between AB stacked layers is higher compared to AA stacked layers, leading to a more stable structure [35].

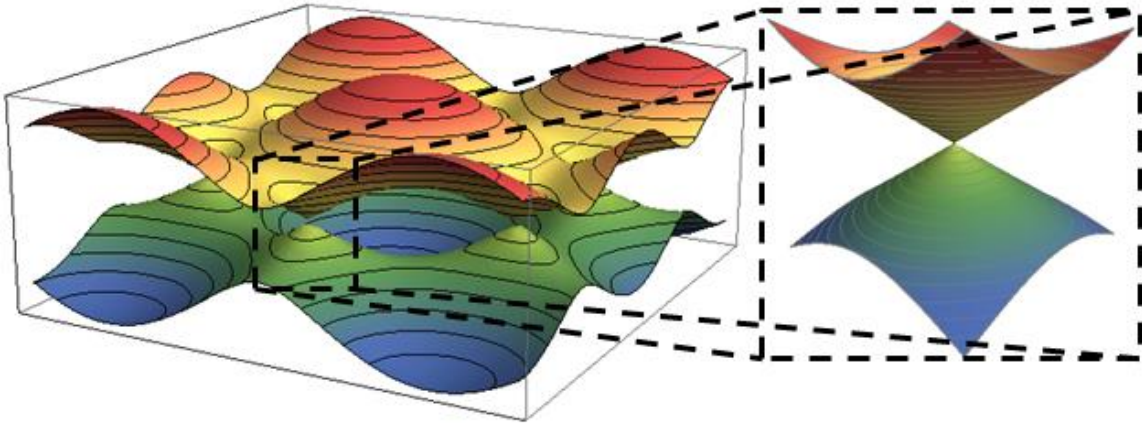


**Figure 2.3:** Dirac points in graphene with the electronic dispersion of the honeycomb lattice in terms of (zoomed in) the energy spectrum of finite values. Reprinted under the CC BY-SA 3.0 license, Yomach (2014) [36].

## 2.2.2 Epitaxial graphene on SiC

SiC is a binary crystal comprising Si and C atoms in a 1:1 distribution. SiC can crystallize in about 250 different configurations that are chemically identical but have different electronic properties. The crystal structure, called polytype, is determined by the stacking sequence of the SiC tetrahedron during growth. The most commonly used polytypes of SiC for graphene growth are 4H-SiC and 6H-SiC. In theory 3C-SiC is better as it has a uniform step decomposition velocity, thus no step-bunching [37], and also no spontaneous polarization, which therefore should result in less charge transfer to graphene compared to 4H- and 6H-SiC. However, the latter two are the only stable hexagonal polytypes [38], and since they are of high interest in the field of power semiconductor devices to replace Si in high-end power electronics applications to reduce device-related energy losses, their growth has been optimized to the point where 4H- and 6H SiC wafers of very high quality are available at costs that would have seemed impossible a decade ago. The letter H indicates the hexagonal crystal structure and the numbers 6 and 4 define the number of Si-C pairs stacked per unit cell. SiC wafers cut along the c-axis (0001) have two different surface terminations: Si-face (Si atoms) or C-face (C atoms). For the growth of monolayer graphene, the Si-terminated surface (0001) is normally used, as it exhibits a slower and more controlled Bernal stack growth process [39]. C-terminated SiC ( $000\bar{1}$ ) leads to a multi-layered and more inhomogeneous growth instead [40]. Therefore, the Si-face is used for applications where high quality graphene is needed, such as Quantum Hall Effect (QHE) devices [41, 42] or gas sensors [43].

If SiC is heated to sufficiently high temperatures, Si-atoms sublime and leave a carbon-rich layer beneath, which eventually forms graphene. The growth is explained in more detail in section 3.3.1. The very first layer of graphene forms the so-called buffer layer, which is a  $(6\sqrt{3} \times 6\sqrt{3})R30^\circ$  reconstruction of the SiC surface [40]. In the buffer layer, about 30 % of the carbon atoms are covalently bound to the SiC bulk, turning it into an insulating layer. It is often also referred to as zero-layer graphene. The second layer then forms the conducting monolayer of graphene. Figure 2.4 represents a schematic of the grown graphene lattice on top of SiC with the buffer layer in between.

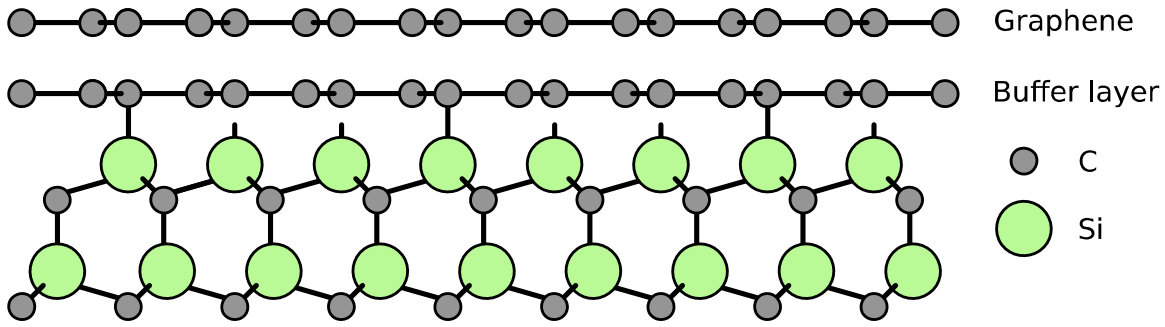


**Figure 2.4:** Schematic of epitaxial graphene on SiC.

The graphene layer is influenced electrically by the buffer layer and the SiC bulk. The buffer layer has a distance of  $\sim 3.24 \text{ \AA}$  to the graphene layer [44] and acts as a mediator for charge transfer between the SiC bulk and the graphene leading to intrinsic n-doping in the order of  $10^{13} \text{ cm}^{-2}$  [45]. As a result, the graphene lattice has a high density of states. The SiC bulk also affects the doping of graphene in the same direction as the buffer layer [46]. The buffer layer reduces the mobility in epitaxial graphene (EG) compared to exfoliated graphene due to the introduction of charges and scattering centers [47]. To eliminate the influence of the buffer layer, the covalent bonds between buffer and SiC can be removed through the intercalation of, for example, hydrogen which will decouple the buffer layer into a freestanding graphene layer [46]. To produce monolayer graphene in this manner it is necessary to perform the intercalation step on SiC that has been processed to have just the buffer layer with no graphene on top.

## 2.3 Graphene as sensor platform

Besides the already mentioned properties, graphene's exceptionally low electronic noise makes it very promising for a large variety of sensing applications. Only few crystal defects occur leading to low Johnson [48] and thermal switching noise [49], which in turn lead to a high signal-to-noise-ratio (SNR). Graphene sensors are currently being studied by the scientific community to investigate among others mechanical, electro-magnetic or bio-/chemical properties with, e.g., strain, Hall or gas sensors, respectively [33, 42, 50]. Fluctuations due to thermal motion of charges and defects lead to intrinsic noise, limiting the detection resolution of gas sensors. Due to the low density of states near the Dirac point even a minimal charge transfer yields a significant change in the electronic state, leading to a high

sensor response even to low analyte concentrations. Schedin et al. demonstrated already in 2007 that graphene can be used to detect single atoms/molecules [51], albeit under optimized laboratory and rather unrealistic ambient conditions. Adsorbates can attach to a graphene surface, alter the local carrier concentration and, thus, change the resistivity accordingly. Since then, a lot of research has been conducted to utilize graphene as ‘the ultimate gas sensor’. It was found that when using graphene as a sensitive layer, the number of layers greatly affects the sensor performance [10]. This is especially true for EG on SiC, as the sensitivity depends on the band structure which in turn depends on the number of layers, as SiC exhibits Bernal stacking of graphene layers. Furthermore, graphene has been found to be very sensitive to some gases like ammonia ( $\text{NH}_3$ ) or  $\text{NO}_2$ , but needs functionalization to fully exploit its potential [52]. Due to its high sensitivity to many gases, graphene suffers from poor selectivity. At the same time, graphene exhibits poor interaction with several gases of interests in AQM such as VOCs and also slow adsorption and desorption processes, leading to long response and recovery times. Moreover, its low number of dangling bonds on the surface limits the chemisorption of target gases, thus limiting the sensitivity [53].

### 2.3.1 Optimizing EG gas sensors

There are many different ways to overcome the limitations of pristine graphene gas sensors. Graphene can be functionalized via additional doping or defects, decoration or intercalation with other functional materials, combined into a compound material or controlling the sensing environment.

The most common and extensively studied approach is to work with graphene itself and turn it into a hybrid structure together with metal oxides [14, 15]. Metal oxides are very well studied in the gas sensor community and are dominating in industrial applications due to their advantages like low cost and controlled production [13]. Having the optimal metal oxide and target gas combination already leads to a very good sensor performance. The sensitivity to most analytes can drastically be increased by increasing the surface-to-volume ratio of the sensing layer as a larger detection area per unit volume results in a higher adsorption of gas molecules per volume, thus leading to more material/gas interaction. Therefore, nano-sized structures are often used in combination with highly sensitive materials [13]. Combining the advantages of sensitive metal oxides with

low-noise graphene can lead to very promising new sensor hybrids where the surface chemistry is controlled by the metal oxide nanostructure and the graphene acts as a highly sensitive transducer [14, 15]. Moreover, graphene can be turned into graphene oxide or wrapped into CNTs, which are then again used as a transducer and functionalized with different sensitive materials. In this work, graphene was decorated with different metal oxide nanoparticles (NPs) and nanolayers (NLs).

The intercalation of atomic species into the graphene lattice is another method of changing the surface properties. This is especially interesting when doing so with epitaxial graphene on SiC where the buffer layer can be turned into the topmost quasi-free-standing epitaxial graphene (QFSEG) layer or the existing monolayer graphene into a bilayer graphene sample. This intercalation has been done with several different species ranging from salts over metals to gases [54]. Here, only hydrogen intercalated sensors were investigated as it is the most common intercalation method.

The controlled introduction of defects, vacancies or doping impurities into the graphene lattice can also lead to an increased sensitivity [55, 56]. However, this procedure normally entails a higher noise level, due to local disruptions of the  $sp^2$  hybridization, which could be detrimental for the detection limit. In this work, defects were introduced into graphene with  $Ag^+$  ion irradiation [Paper C].

A rather drastic idea is to use the known substrates on which graphene can be grown and substitute the graphene lattice with another material like two-dimensional platinum and use it as sensor or transducer instead [Paper D].

The enhancement of sensitivity and decrease of time constants using additional UV irradiation during the gas exposure was shown for many different material/gas combinations [19]. The irradiation with light allows energized photons to interact with the target gas or sensing material. This interaction highly depends on the possibility to adsorb photons at the given photon energy. Thus, the photon energy level has to be compatible both with the sensing material and the target analyte. This in turn means that the interaction depends on the wavelength of the irradiation source and might be enhanced for a specific wavelength but has no effect for longer wavelengths. The photon interaction can help to split up gas molecules into detectable atoms or it can help to clean the sensor surface from the adsorbed gas and activate adsorption sites. For example, it was reported that UV irradiation can be attributed to cleaning of the graphene surface,

## 2 Theory and concepts

thus freeing active sites for target gas adsorption [57]. Unfortunately, this method does not work for all material/gas combinations, making it a useful, but not very versatile add-on.

One option where no actual functionalization is needed is the use of transient or secondary data, generated during the measurement. A common approach, usually applied for MOS or field effect transistor (FET) devices, is the operating mode called temperature cycled operation (TCO) [22, 58]. In general, a relatively high operation temperature is often desirable, as it accelerates reactions on the sensor like ad- and desorption, influences speed and repeatability, and can change the catalytic activity of the sensor surface. Even more information can be gained by quickly cycling between different temperatures to create non-equilibrium states that can be used to enhance sensitivity and selectivity [59]. If the sensor does not support high temperatures or the system should exhibit a low power consumption, other methods like cycling the gate bias [60] or utilizing a pulsed UV irradiation [61] are possible alternatives. To substantially decrease the sensor's time constants at a constant temperature, the first-order time-derivative of the signal can be calculated and used as well [21]. This approach focuses on the change in signal during ad- and desorption phases and can be extracted from almost any pulsed sensor signal.

### 2.3.2 Sensing mechanism

A change in the sensor's resistivity follows from a change in charge carrier concentration or mobility. The resistivity  $\rho$  is inversely proportional to the product of the charge carrier concentration and the mobility [62].

$$\rho = \frac{1}{ne\mu_e + pe\mu_h} \quad (2.8)$$

$e$  is the elementary charge,  $n$  and  $p$  are the electron and hole concentrations, and  $\mu_e$  and  $\mu_h$  are their respective mobilities.

Adsorption of molecules on the graphene lattice can result in a charge transfer between the surface and the adsorbed molecule, thus changing the measured resistance. The adsorbent acts as chemical dopant, changing the Fermi level  $E_F$  [63]. If electron-accepting molecules adsorb, i.e., an oxidizing gas, extra holes are introduced, resulting in p-type doping, shifting the Fermi level down and increasing the resistivity for n-doped graphene, such as EG on SiC [10]. Adsorption of electron-donating molecules, i.e., a reducing gas, on the other hand, results in extra electrons, leading to

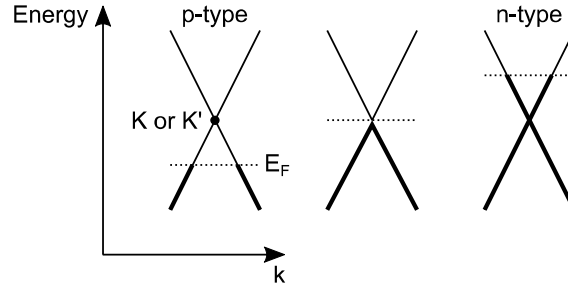


**Figure 2.5:** Schematic of Fermi level ( $E_F$ ) dependence on doping in graphene.

n-type doping, shifting the Fermi level up and decreasing the resistivity. For the Fermi level and thus the sensor resistance to change, a physisorption can already be enough. The effects of doping on the Fermi level are displayed in Figure 2.5.

In free-standing graphene, the Fermi level is located at the charge neutrality point, the Dirac point. In as-grown epitaxial graphene, the Fermi level is shifted to approximately 0.4 eV above the Dirac point, due to the n-type doping from the buffer layer and the SiC substrate [64].

The sensing mechanism of graphene decorated with metal oxide NPs or NLs can be modeled by a receptor and a transducer process. Physisorption and chemisorption occur mainly at the metal oxide surface, forming the receptor process. The transport of electrons between metal oxide and graphene as well as establishing the electrical signal belongs to the transducer process [15]. It is believed that the change in resistivity is due to trapping of electrons by adsorbed molecules and additional scattering points induced by such. For example, adsorbed oxygen ( $O_2$ ) on the sensing material withdraws electrons from the metal oxide NPs as shown in Equation (2.9).



Note that this simplification is only true up to about 150 °C as above this temperature ionic oxygen species dominate [65]. The negatively charged, adsorbed oxygen molecules cause a depletion area at the interface between the metal oxide and the graphene lattice, lowering the resistivity of the graphene lattice [15]. Reactions with oxidizing molecules will further increase the depletion region, whereas reactions with reducing molecules result in the trapped electrons being returned to the metal oxide, thus increasing the resistivity of the graphene lattice again [66]. The mentioned mechanisms are described disregarding the dissociation of more complex

molecules. This can, of course, happen as well, depending on the active sensing sites and might lead to a more complex sensing mechanism.

## 2.4 Multivariate data analysis

A raw sensor signal, e.g., resistance, is usually not the desired output of a sensor device, especially if the user expects an easily interpretable reading. To convert this signal into the property of interest, e.g., gas concentration in ppb, models are normally used instead. As mentioned in section 2.3.1, models can also help to improve the sensing performance if done properly. To fully exploit a sensor's potential, more information than just the raw signal can be created by looking also at other or alternating properties, e.g., cycled operating temperature, which is then evaluated with multivariate data analysis methods [58]. Therefore, sensor devices usually contain sensor arrays. These are either physical arrays, i.e., sensors with, for example, different sensing materials, or one sensor that is operated in a way resulting in a virtual array, e.g., cycled operating temperature or bias. The resulting signal patterns often contain more information than a single sensor, hence enabling the classification or quantification of individual gases even in rather complex gas mixtures. However, since chemical reactions strongly depend on the material/gas combination, each sensor device needs to be calibrated with individual models for the desired application. Good overviews together with more in-depth discussions about multivariate data analysis can be found in [67, 68].

Before a model is created, the recorded set of data usually undergoes a so-called preprocessing or data cleaning step to remove obvious imperfections, noise or sensor drift. For example, baseline drift of MOS sensors in TCO mode can be compensated by dividing each measurement cycle by its own mean value [69].

The next steps are feature selection and dimensionality reduction. Features refer to a specific data value over all observations, e.g., last point of the temperature plateau in TCO, or the method of how the value is extracted, e.g., the mean value of the temperature plateau in TCO. Target values contain the predefined label of each observation, such as gas type or concentration and are sometimes also referred to as target, target classes or groups, while one observation could for example be one TCO cycle. Each feature can be seen as an additional dimension, which might contain useful information. Too many features, however, lead to negative effects

with the model not performing as well as it could [70]. Therefore, and to make the calculations manageable, the dimensionality of the given dataset needs to be reduced as much as possible while not losing too much information. There are several different methods on how this reduction can be obtained like feature extraction, feature selection or multivariate statistics [68]. Features can be extracted based on the shape of the signal, e.g., mean value or slope of the sensor signal, mathematically, e.g., with Fourier analysis or wavelet transform, or as a combination. The most common approaches based on multivariate statistical methods are linear discriminant analysis (LDA)<sup>2</sup> and principal component analysis (PCA). Both project the data into a new subspace with the aim of retaining as much information as possible while reducing the dimensionality down to usually 1-3 for easier visual representation [71]. The original LDA algorithm, was described already in 1936 [72] for two-dimensional data, but is today also used for multi-dimensional problems. LDA is a so-called supervised method. This means that the target values are known and used for model-building, projecting the data into separated clusters corresponding to the target values. LDA searches for a set of axes that maximize the variance between points, minimizing the distance within a group of points corresponding to a particular gas, and maximize the distance between different groups or gases. PCA, on the other hand, is unsupervised, which means that the target values are not known while the model tries to project the data into a new, orthogonal space, where the first axis points along the direction of highest variance and the last axis to the direction with the lowest variance.

Classification or quantification of unknown observations is the ultimate goal of any model. A classification assigns a predefined target to each observation, e.g., if the exposed gas is reducing or oxidizing. Examples for common classification models are knn (k nearest neighbors) or again LDA. To determine, for example, gas concentrations, a regression model would be the better option with PLSR (partial least squares regression) being the most common one for chemical gas sensors [70].

After the model has been built, which is often called training of the model, it has to be validated and tested. During training, the model parameters are determined as, e.g., linear combinations of the features. The

---

<sup>2</sup> LDA is often also referred to as canonical discriminant analysis (CDA) if used for dimensionality reduction.

## 2 Theory and concepts

validation step then determines the model's hyperparameters, i.e., dimensions, and finally, the performance of the model is tested with new data, thus giving feedback on how close predicted values are compared to the known real values of the dataset. To obtain the optimal model, the validation and testing should be done with a new, independent dataset. However, parts of the same dataset can also be used for training, validation and testing of the model. For this, the most common method is k-fold, which randomly divides the dataset into k parts, using k-1 parts to train the model and the remaining part for validation or testing. This is performed k times until each part had been left out once. The final outcome is then the average of all validation or testing folds.

# 3 Experimental methods

The research and development from idea to realization of a novel sensing material involves several different fabrication and characterization techniques and systems. This chapter gives an overview of what is needed to end up with a functioning and functionalized EG gas sensor. It starts with the different deposition techniques and material characterization methods. Thereafter, the process of sensor fabrication itself and handling of the obtained data is addressed and, finally, the gas mixing systems with the utilized test gases are described.

## 3.1 Deposition techniques

Depending on the application in mind, several different deposition techniques may be used to grow a thin film on an already existing substrate. One distinguishes usually between physical vapor deposition (PVD) and chemical vapor deposition (CVD) techniques. In the case of CVD, a liquid or gaseous precursor undergoes a chemical change at a solid surface, resulting in the growth of a new solid film on top. PVD, on the other hand, uses thermal, mechanical or electromechanical processes to produce a thin solid film on top of a substrate. All techniques applied in this work belong to the family of PVD and are described in the following sections. Sputter deposition was used to deposit contact pads on the sensor surface or decorate it with nanoparticles. Continuous nanolayers were deposited utilizing pulsed laser deposition.

### 3.1.1 Sputter deposition

Sputter deposition techniques are usually divided into non-reactive and reactive sputtering. For non-reactive sputtering, the background ambient consists only of an inert gas like argon (Ar), whereas for the reactive sputtering a more reactive gas like oxygen is present as well, which then reacts with the ejected target atoms to form oxides. The main principle though is similar for both techniques: A sputter gas, normally argon, is ionized with a high energy source and directed to the so-called sputter target where it bombards the surface and ejects target atoms from the bulk [73]. Depending on the atomic weight of the sputter atom, the ejection mechanisms

### 3 Experimental methods

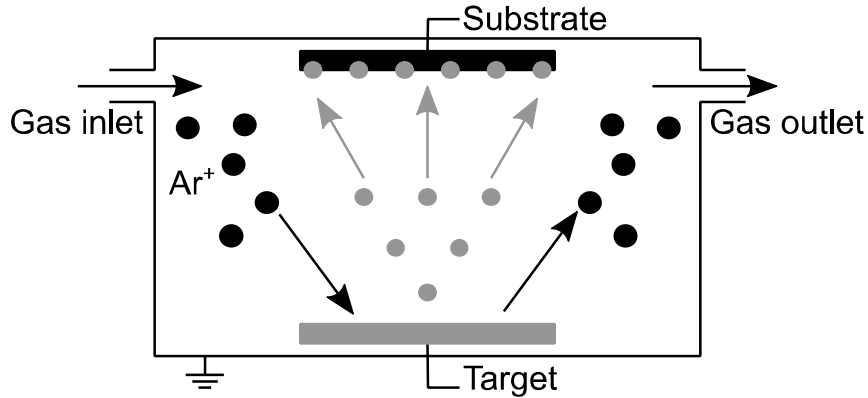


**Figure 3.1:** Schematic of sputter process.

differ. If heavy sputter atoms hit the surface, they transfer their energy into the surface, which generates a cascade of collisions and eventually ejects atoms out of the surface. If a rather light atom hits the surface, it does not produce a cascade of collisions. Instead, those ions are reflected inside the surface layer and eject surface atoms by hitting them from the bulk side. For argon with its intermediate mass, both mechanisms contribute to the sputter yield [74]. The sputter yield, defined as the ratio between ejected target atoms and incoming ions, is highly dependent on the angle, mass and kinetic energy of the incoming ion as well as the target material. The ejected atoms move to the opposing substrate and grow into a film on it. Figure 3.1 presents a schematic of the general sputter process. Besides the ejection of target atoms, also secondary electrons are ejected. Accelerating these free electrons close to the target surface will further increase the rate of ionization, eventually leading to the formation of a plasma with its origin on the target surface. In this work, only “soft” deposition techniques were used with a rather low kinetic energy of the incoming target atoms to maintain the integrity of the graphene lattice and to not induce structural damage to it.

#### 3.1.1.1 Magnetron sputtering

As the name suggests, in a magnetron sputter system a magnet is utilized to confine the sputter electrons close to the target. The magnetic field bends the electrons’ trajectory back to the target surface. This locally increases the plasma density through ionizing collisions with neutral atoms [75]. Figure 3.2 (a) shows an image of the deposition process with the plasma occurring in the top left and particles depositing over the whole

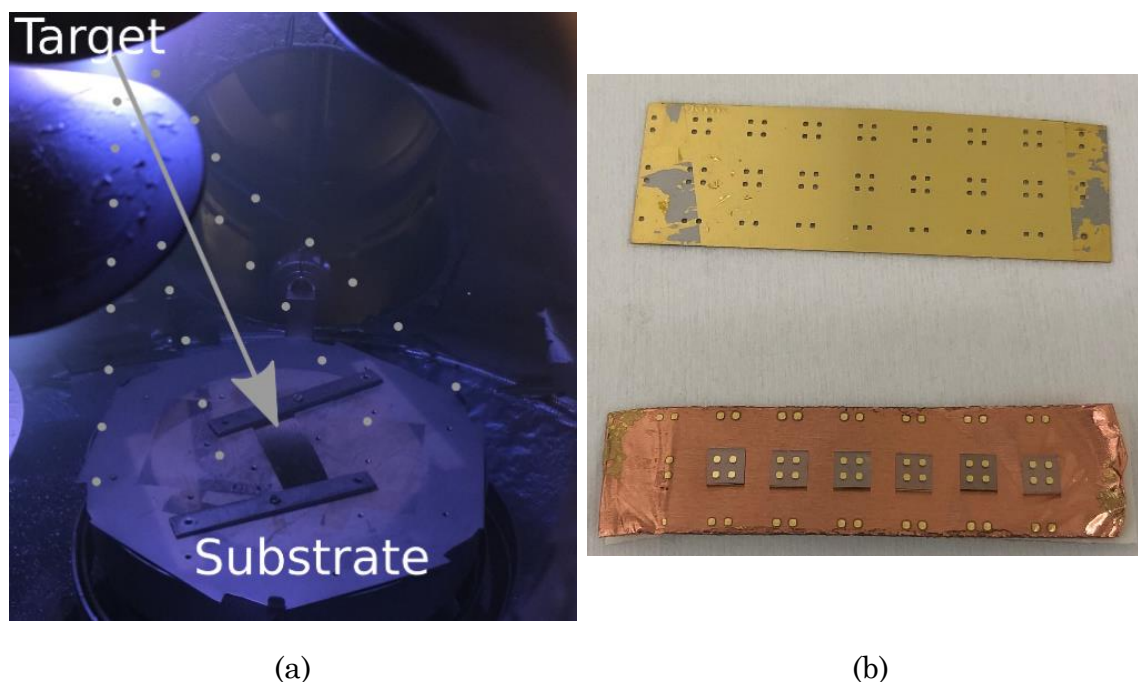


**Figure 3.2:** (a) Overlay of schematic with real image of the magnetron sputter process with the occurring plasma plume within the vacuum chamber and (b) sensor chips with deposited contacts.

chamber including the substrate on the substrate holder as the target shutter is open.

A custom-built magnetron sputter system was used to deposit contacts (Ti/Au or Cr/Au with 2/200 nm) on top of the sensor chips. Titanium and chromium have been used, depending on availability of the target material, as a binding layer between the graphene surface and the gold layer. For titanium, the base pressure was 1.5 mTorr with a voltage of 350 V and a current of 300 mA, for chromium the base pressure was 1.7 mTorr with 300 V and 360 mA, and for gold the values were 1.9 mTorr, 400 V and 200 mA, respectively. Depositions were performed with an argon flow of 25 ml/min for all materials. Sensor chips with deposited contacts can be seen in Figure 3.2 (b) together with the used mask. The chips are fixated on copper tape for better stability during the deposition. Note that a few early sensors had contacts deposited via thermal evaporation, but since sputter deposition did not damage the graphene lattice, produces better quality layers and was more easily available, sputter deposition was used for almost all sensors.

#### 3.1.1.2 Pulsed plasma hollow cathode sputtering

A hollow cathode sputter system traps the electrons inside the cathode cylinder where they are accelerated and repelled by the opposing cathode sheaths. This leads to an oscillation of electrons inside the cathode and collisions of gas atoms with these highly energized electrons form a plasma with a high degree of ionization. High power pulses are applied similar to high power impulse magnetron sputtering, to substantially enhance the ionization of the sputtered species as compared to direct current magnetron sputtering. A schematic view of the experimental arrangement is given in Figure 3.3. In this work, the technique has been leveraged for fabrication and deposition of metal oxide NPs on graphene substrates.

One of the main advantages of hollow cathode sputtering is the control of size, shape and dispersion of the deposited nanoparticles, as well as minimizing agglomeration on the substrate surface by alternating pulse amplitude, length and frequency [76, 77]. The NPs are formed in the gas phase of the sputter vapor and their growth undergoes three main stages: In the first stage, a dimer is formed by nucleation during a three-body collision. This dimer then grows into a small cluster through the addition of more individual metal atoms/ions. If the cluster is large enough, it gets negatively charged in the second stage as the electron mobility becomes higher as the mobility of positive ions. This leads to coagulation. When the coagulated cluster reaches sizes of  $> 10$  nm, the built-up negative charge prevents it from further coagulation. In the third stage, the particle grows only due to slow addition of metal atoms/ions [76].

Here, titanium dioxide ( $\text{TiO}_2$ ), magnetite ( $\text{Fe}_3\text{O}_4$ ) and platinum (Pt) NPs were deposited on top of graphene using this technique. The substrates were placed outside the dense plasma region, preventing energetic species from reaching and damaging the graphene lattice. The discharge parameters for the  $\text{Fe}_3\text{O}_4$  NPs were: a pulse frequency of 1200 Hz, a pulse width of 80  $\mu\text{s}$  and an average power of 90 W. A substrate bias can be used to attract the particles to the substrate surface. For the  $\text{Fe}_3\text{O}_4$  particles no bias was applied, referred to as floating<sup>3</sup>, and the substrates were exposed to NP deposition ranging from 0.5 to 4 minutes. Pt NPs were deposited with similar parameters, only the average power was lower (30 W) and the deposition time was 3 min. For the  $\text{TiO}_2$  NPs the deposition time was 15 s

---

<sup>3</sup> Floating means that the samples were not connected to the electrical circuit, which, therefore, is different from 0 V.

and the bias was +10 V. Other process parameters are given in reference [77]. Important deposition parameters are summarized in Table 1. The main results are only based on  $\text{Fe}_3\text{O}_4$  NP decorated sensors, in particular the ones with deposition times of 2 and 4 minutes, respectively, as they show comparable surface coverage (compare Table 5) and sensor response (compare section 4.2.5).  $\text{TiO}_2$  NP decorated sensors were mainly investigated prior to and at the very beginning of this project. Investigations regarding Pt NP decorated sensors are still ongoing and are not published yet.

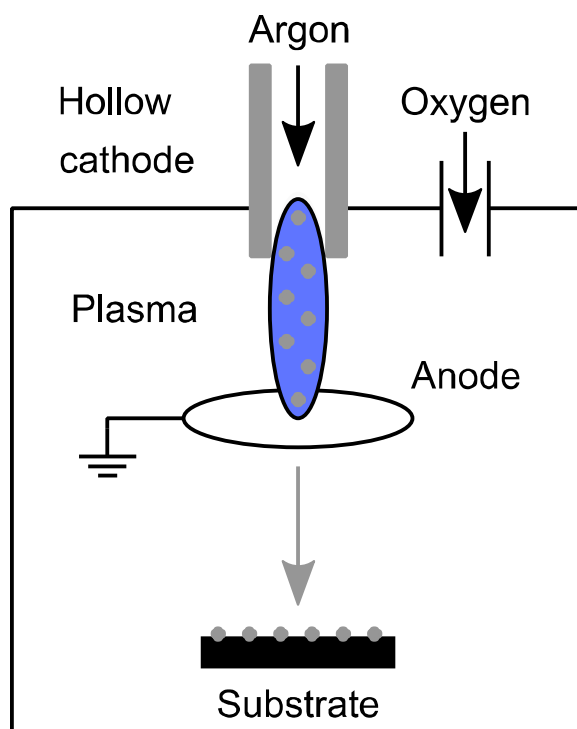


**Figure 3.3:** Schematic of hollow cathode sputter process based on [77].

### 3 Experimental methods

**Table 1:** Hollow cathode targets and their deposition parameters.

Sputter material	Deposition time (min)	Substrate bias (V)
Fe <sub>3</sub> O <sub>4</sub>	0.50	floating
Fe <sub>3</sub> O <sub>4</sub>	1.00	floating
Fe <sub>3</sub> O <sub>4</sub>	2.00	floating
Fe <sub>3</sub> O <sub>4</sub>	4.00	floating
Pt	3.00	floating
TiO <sub>2</sub>	0.25	+10

#### 3.1.2 Pulsed laser deposition

Pulsed laser deposition (PLD) uses a coupling of photonic energy to a bulk target material through electronic processes for growing a layer on a substrate opposite of the target. Both target and substrate are positioned within a vacuum chamber with an optical quartz glass window and usually with several in- and outlets for gases. A high energy laser pulse is focused onto the rotating target and is partially absorbed near its surface. Exceeding the ablation threshold of the target, a plasma plume occurs with particles moving perpendicular to the target. The material within the plasma plume can collide and react with background or inlet gases or ion sources. Eventually, it will recondense on the substrate and grow into a layer. A schematic of the general principle is presented in Figure 3.4.

The detailed PLD process used here is described in [12]. Different target materials were ablated using a krypton fluoride (KrF) excimer laser at a wavelength of 248 nm. The oxygen partial pressure was kept at either 0.1 or 0.05 mbar. The laser pulses were adjusted to keep a layer thickness of  $\sim 0.5 - 1$  nm. The sensor substrates were kept at room temperature during deposition. Copper oxide (CuO), magnetite (Fe<sub>3</sub>O<sub>4</sub>), vanadium pentoxide (V<sub>2</sub>O<sub>5</sub>) and zirconium dioxide (ZrO<sub>2</sub>) have been used as target materials. Their process properties are summarized in Table 2. Unfortunately, the ZrO<sub>2</sub> sample processed at 0.05 mbar was not available for measurements and the V<sub>2</sub>O<sub>5</sub> (0.1 mbar) sample physically broke during the project.

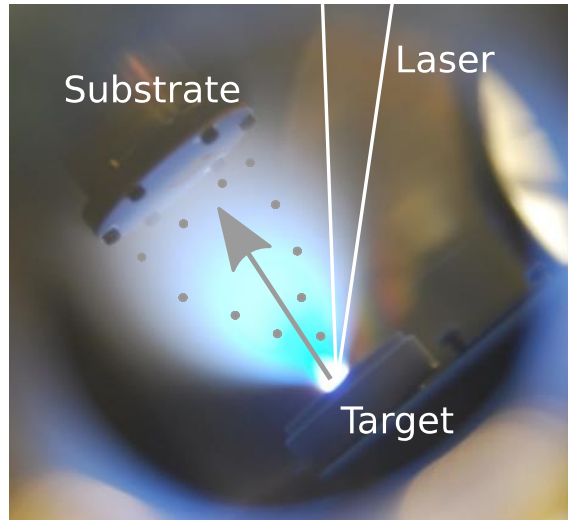


**Figure 3.4:** Overlay of schematic with real image of the PLD process and the occurring plasma plume within the vacuum chamber. Adapted from [78].

As the sensors with the same deposition material showed very similar sensor responses, only one of each is discussed here for the sake of readability. Included are CuO (0.1 mbar), Fe<sub>3</sub>O<sub>4</sub> (0.1 mbar), V<sub>2</sub>O<sub>5</sub> (0.05 mbar) and ZrO<sub>2</sub> (0.1 mbar) NL DEG sensors, which are also the ones [Paper 4] is based on.

**Table 2:** PLD targets and their deposition parameters.

PLD material	O <sub>2</sub> pressure (mbar)	Laser fluence (J/cm <sup>2</sup> )	Number of laser pulses
CuO	0.05	5	120
CuO	0.10	5	180
Fe <sub>3</sub> O <sub>4</sub>	0.05	7	150
Fe <sub>3</sub> O <sub>4</sub>	0.10	7	200
V <sub>2</sub> O <sub>5</sub>	0.05	5	120
V <sub>2</sub> O <sub>5</sub>	0.10	3	200
ZrO <sub>2</sub>	0.10	3	220

## 3.2 Characterization methods

To gain information about the purity, thickness uniformity and integrity of the used graphene samples, they were analyzed using atomic force microscopy (AFM) and Raman spectroscopy before and after the applied surface modifications. AFM gives information about the topography, while Raman spectroscopy is used to acquire information about structural properties of the graphene lattice. Density functional theory (DFT) calculations were used to theoretically investigate the binding energies between the sensor surface and a specific analyte, thus possibly predicting the sensor response.

### 3.2.1 Atomic force microscopy

Using a very sharp needle attached to a micro-cantilever, the AFM scans the surface of a specimen. Different scanning modes are possible: contact mode, non-contact mode and tapping mode. Here, only the tapping mode was used, where the cantilever oscillates close to its resonance frequency in z-direction while scanning the whole surface in an x-y raster scan. Depending on the topography, van der Waals forces change the oscillation amplitude of the cantilever, which is detected by reflecting a laser beam of the back of the cantilever and onto a position-sensitive photodiode. Resolutions down to an atomic level can be achieved in height, which provides an opportunity to gain topographical information of very flat samples such as graphene. In addition to the amplitude, also the phase difference between the excitation signal of the cantilever and its actual oscillation is recorded. The phase provides an insight into mechanical properties and the viscoelasticity of the studied sample as it responds to energy loss. For example, for EG on SiC it can reveal whether the surface consists of different graphene domains as different graphene thicknesses, i.e., monolayer, bilayer or multilayer, exhibit different Young's moduli. Besides topographical measurements, AFM measurements can also be adapted to measure, e.g., the work function (Kelvin Probe Microscopy) or conductivity using a conductive tip.

In this work, a Dimension 3100 (Veeco Instruments Inc., New York, USA), with a Nanoscope IVa controller was used with silicon tips (PPP-NCHR-50 from Nanosensors, Neuchatel, Switzerland) with a tip radius of curvature below 7 nm exclusively in tapping mode.

The overall roughness is calculated as the deviation of the root mean square  $R_q$ :

$$R_q = \sqrt{\frac{\sum_{i=1}^N (Z_i - Z_{\text{average}})^2}{N}} \quad (3.1)$$

where  $N$  is the total number of measurement points,  $Z_i$  is the height at measurement point  $i$  and  $Z_{\text{average}}$  is the average height. Note that the roughness in height is calculated for an arbitrary area within the AFM measurement and should only be utilized to compare similar samples with each other.

### 3.2.2 Raman spectroscopy

With Raman spectroscopy, incoming monochromatic light gets scattered inelastically on the sample surface due to interactions with molecular vibrations or excitations. This inelastic scattering leads to a characteristic energy shift of the outgoing laser light, the so-called Raman effect. Raman scattering can be separated into Stokes scattering and Anti-Stokes scattering. The incident radiation has a higher frequency than the scattered radiation for Stokes scattering and vice versa for Anti-Stokes scattering [79]. Narrow optical filters shield the detector from reflected, non-scattered light coming from the laser.

The quality and especially the integrity of graphene surfaces can easily be verified using Raman spectroscopy. A typical Raman spectrum of EG on SiC is shown in Figure 3.5. The important modes are D at  $1350 \text{ cm}^{-1}$ , G at  $1582 \text{ cm}^{-1}$ , D' at  $1620 \text{ cm}^{-1}$  (not present here) and 2D (also referred to as G') at  $2700 \text{ cm}^{-1}$  [80]. The G and 2D peaks, specifically their intensity ratio and the full width at half maximum of the 2D peak, can be used to determine the quality of the graphene while the D peak arises only when disorder or lattice defects are present. Furthermore, the whole sample surface can be mapped giving information about spatial distribution of graphene features, such as peak ratios and FWHM (full width at half maximum) values [81, 82].

A micro-Raman setup was used to perform Raman spectroscopy and reflectance measurements. A CCD (charge-coupled device) camera coupled to a monochromator (HR460) was utilized along with a  $100\times$  magnification objective. The samples were excited using a  $532 \text{ nm}$  diode-pumped solid-state laser, with a power of  $17 \text{ mW}$  for pristine EG (PEG) and  $< 1 \text{ mW}$  for

### 3 Experimental methods

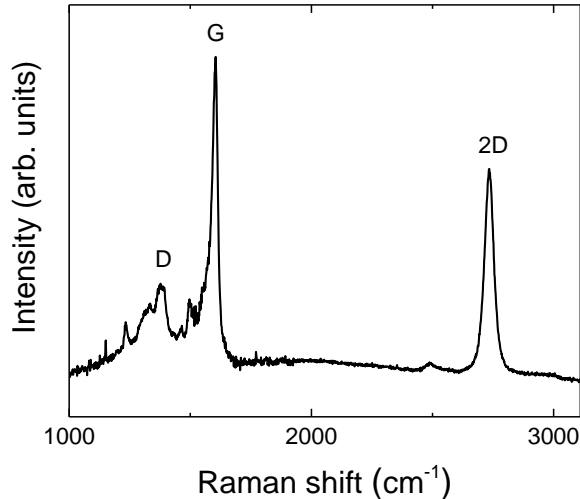


**Figure 3.5:** Typical Raman spectra of EG on SiC with important modes. Adapted from [Paper 1].

surface decorated EG (DEG) samples, respectively. The lower laser powers were used as a safety procedure, to make sure that the decorated metal oxide nanostructures do not burn. The focused spot size had a diameter of  $\sim 0.9 \mu\text{m}$  on the sample and a system spectral resolution of approximately  $5 \text{ cm}^{-1}$  could be achieved. The Raman spectra of Si-face graphene were obtained by subtracting a reference spectrum of 4H-SiC (0001). A more detailed description of this setup can be found in [81].

#### 3.2.3 Density functional theory

DFT is used to calculate and predict material behavior. It is based on quantum mechanical models which in turn are based on the Hohenberg-Kohn theorems [83]. DFT is often put to use in material science to investigate the electronic structure of many-body systems. Here, the adsorption of gas molecules on PEG and metal oxide NP DEG was investigated. The calculations are based on hybrid gas-phase DFT and executed with the Gaussian 16 Rev. B.01 program package [84]. PEG has been modeled as one  $4 \times 5$  graphene layer on top of a  $4 \times 5$  buffer layer, which is covalently bound to the  $4 \times 4$  Si-face surface of hexagonal 4H-SiC. DEG was simulated by full geometrical optimization of  $\text{Fe}_3\text{O}_4$  and  $\text{TiO}_2$  located on PEG, where all dangling bonds are passivated by hydrogen atoms. M06-2X level theory with consideration of a split basis set was used for all calculations [85]. The dispersion-corrected DFT functional M06-2X implicitly includes modified parameters associated with the Hartree-Fock exchange interaction, allowing the prediction of weak van der Waals interactions [86]. A LANL2DZ

(Los Alamos National Laboratory 2 Double-Zeta) basis set was applied for iron (Fe) and titanium (Ti) atoms, and a 6-31G basis set for carbon, silicon, oxygen and hydrogen species [87]. All atoms were allowed to fully relax during geometrical optimization and no symmetry restrictions have been applied. The adsorption energy of gas molecules ( $E_{ads}$ ) was calculated as

$$E_{ads} = \left( E_{tot}^{PEG/DEG} + E_{tot}^{gas} \right) - E_{tot}^{gas@PEG/DEG} \quad (3.2)$$

where  $E_{tot}^{PEG/DEG}$  and  $E_{tot}^{gas}$  are the total energies of isolated PEG or DEG templates and gas molecules, respectively. The total energy of PEG or DEG after the reaction with gas molecules is defined as  $E_{tot}^{gas@PEG/DEG}$ . A compensating correction for basis set superposition error (BSSE) was applied for a more accurate prediction of the adsorption energies [88].

## 3.3 Sensor fabrication

In this section, all processes involved in the fabrication of the studied sensors are discussed. It starts with the growth of graphene on SiC and then elaborates on how this chip is mounted to become a stand-alone sensor unit.

### 3.3.1 Graphene growth

Since it was first experimentally produced in 2004, scientific advances and technology development in graphene have virtually exploded. As such, also the definition of graphene has been expanded to include materials that are not strictly only monoatomic carbon, but also chemically reduced graphene oxide, composite materials comprising of micrometer-sized graphene flakes, and multilayer graphene. Clearly, these different types of graphene will have different mechanical, optical, and electrical properties, where the choice of material should depend on the intended application. The type of graphene depends on how it is synthesized, and there are many well-established methods for graphene growth [89]. The most common method for production of large area monolayer graphene relies on chemical vapor deposition, where a carbon-rich precursor gas is used to grow graphene on a metallic catalyst substrate [90]. This approach is highly scalable and can produce high quality graphene [91]. However, the necessary transfer of the graphene to an insulating substrate – for electronic devices – adds an addi-

### 3 Experimental methods

tional step which can lead to a degradation or contamination of the graphene surface [89]. Another, rather hands-on method is mechanical exfoliation. This method produces the highest quality graphene and is mainly used in fundamental research, but the process is very slow and not scalable [89]. The method employed to grow graphene in this work was epitaxial growth of graphene through thermal decomposition of a SiC substrate. Figure 3.6 demonstrates a simplified growth process of EG on SiC.

At elevated temperatures sublimation of silicon occurs at a much faster rate compared to carbon atoms due to its higher vapor pressure[92]. The underlying Si-terminated SiC substrate reconstructs in a supercell of the gained buffer layer, on which the graphene is grown, which matches quite well with the graphene lattice. Usually, an overpressure of argon is applied to enhance the uniformity of the EG layer. Monocrystalline graphene can be grown over an entire wafer with very high quality on insulating or semiconducting SiC, thus allowing the direct fabrication of electronic devices [89].

In this work, growth was performed on  $7\times 7$  mm hexagonal polytype 4H-SiC (0001) on-axis Si-terminated substrates. 4H-SiC is, with a bandgap of 3.26 eV, a wide bandgap semiconductor that is either semiconducting or semi-insulating depending on the doping. Here, only semi-insulating SiC was used. EG was prepared by sublimation of SiC and subsequent graphene formation at 2000 °C in argon at a pressure of 1 atm [93]. The graphene layer forms on top of a monoatomic carbon buffer layer, which is still partially covalently bound to the SiC substrate [40]. As a result, and sensor basis, EG with a monolayer ratio of about 98 % (2 % bilayer) was achieved. Depending on the wanted outcome, the growth can also be stopped after the buffer layer has formed. In this case, argon is introduced to the chamber at 1400 °C and the buffer growth is completed already at 1700 °C. A high-quality buffer layer is especially important for the H<sub>2</sub>-intercalation (here referred to as intercalated EG or IEG) and graphene-substitution samples. The exact growth processes for those two latter samples are explained in [94] and [Paper D], respectively. Note that results obtained with the IEG sensor are not published yet.

Due to better accessibility, EG was also acquired as a 4" wafer from Graphensic AB, Stockholm, Sweden, and diced into the desired geometries at a later stage of the PhD work (includes Pt NP DEG and several PEG sensors). The graphene was grown on a SiC wafer with similar settings in a comparable reactor.

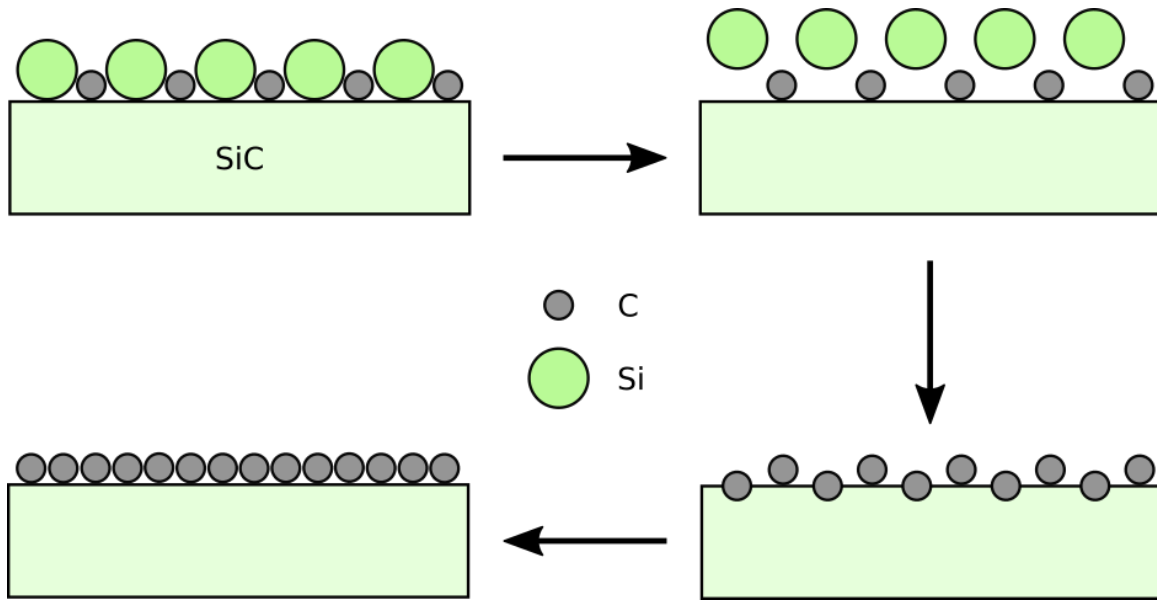


**Figure 3.6:** Schematic of EG growth on SiC.

### 3.3.2 Sensor mounting

To dice the chips, a 30  $\mu\text{m}$  thin diamond blade is used with an automatic dicing saw (DAD321 from DISCO, Tokyo, Japan) and deionized water cooling during the cutting process. The resulting cut has a width of about 50  $\mu\text{m}$ . To ensure no contamination is added to the graphene surface, a protective layer of positive photoresist (SU1818) was applied beforehand. The photoresist was applied via spin coating for 30 s at 4000 rpm with an acceleration speed of 2000 rpm/s. The sample was then baked for 20 min at 100  $^{\circ}\text{C}$  in an oven in ambient air for curing. The backside of each fully transparent chip was marked with a diamond pen to prevent using the wrong side. To remove the photoresist after cutting, the chip was put into pure acetone, then into pure ethanol, blow-dried using a handheld nitrogen gun and finally baked at 100  $^{\circ}\text{C}$  for 10 min. After successful growth and dicing of the chips, the high quality of the graphene surface was verified for each applied functionalization method via AFM and Raman spectroscopy (compare section 4.1).

As a first step of transforming the EG on SiC chip into a graphene gas sensor, electrodes were deposited on top. The contacts were deposited mainly through sputter deposition<sup>4</sup> of titanium (2 nm) or chromium (2 nm) and gold (200 nm) sequentially. The arrangement of electrodes varies,

<sup>4</sup> Some early samples had contacts deposited via thermal evaporation (compare section 3.1.1).

### 3 Experimental methods

thus influencing the baseline resistance measured between two electrodes. In this work, all tested gas sensors had several, i.e., at least two, square contacts with either 0.5 mm width (PEG and NP DEG sensors) or 2 mm width (NL DEG and IEG sensors) with a 1 mm gap in between. To enable a closed-loop temperature control, each sensor chip was glued on top of a ceramic heater substrate (Heraeus GmbH, Hanau, Germany) with an additional Pt-100 temperature sensor (Heraeus GmbH, Hanau, Germany) using Ceramabond 571 (Aremco, Valley Cottage, New York, USA). This whole device was mounted on top of a TO8-socket and connected to its pins using gold-wire bonding and silver glue (Epotek E3081 from Epoxy Technology, Inc., Billerica, Massachusetts, USA). The silver glue is necessary as the deposited gold contacts have only a weak adhesion to the graphene lattice and would be destroyed or even lift off with conventional ball- or wedge-bonding techniques. This setup limits the working temperature to 300 °C, wherefore measurements were only performed up to 200 °C as a safety measure. Figure 3.7 shows a mounted sensor with all necessary parts.

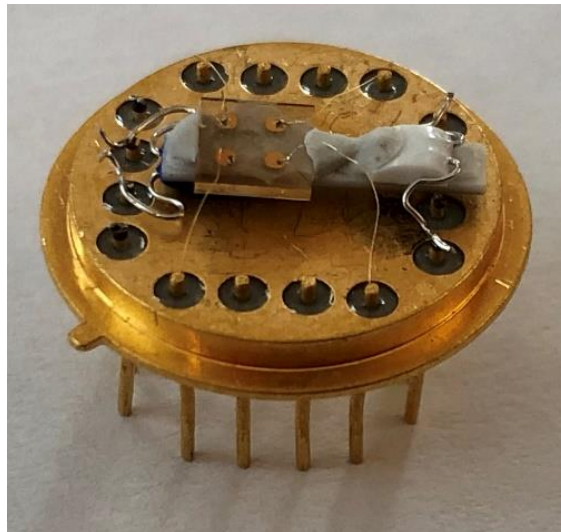


**Figure 3.7:** Photograph of mounted sensor device. Here Pt NP DEG.

## 3.4 Data handling

As the sensor signal, the resistance is recorded over time and then evaluated. How this was performed is described in detail in the following sections.

### 3.4.1 Data acquisition

The resistance of the graphene layer between the deposited contacts, i.e., two-point resistance, was measured over time and used as the sensor signal. As mentioned in section 2.3.2, the charge carrier density will change due to gas interaction, thus altering the sensor's resistance. A schematic of this is demonstrated in Figure 3.8. The resistance was measured with a Sourcemeter (Keithley 2601 from Tektronix Inc., Solon, Ohio, USA) and transferred to a custom-made computer program with a sampling rate of 1 or 5 Hz. The resistance was calculated from the current measured at 1 or 3 V. For sensors with lower baseline resistance values, the measurement voltage was decreased to stay approximately below 1 mA of measured current. This small variation, i.e., 1-3 V, is not expected to have a notable impact on the sensor performance and the only sensors measured at 1 V are Pt NP DEG and IEG. Some measurements were performed using a specialized board from 3S GmbH (Saarbrücken, Germany) instead. The measurement voltage, however, was kept the same. More information about this system can be found in [95]. Either a custom-made temperature controller or a 3S-board was used to monitor and adjust the sensor operating temperature. The controller can be programmed to keep the sensor at a given temperature or change it over time to create ramps or plateaus. The ceramic heater heats the sensor and the Pt-100 reads back the actual temperature.

### 3 Experimental methods

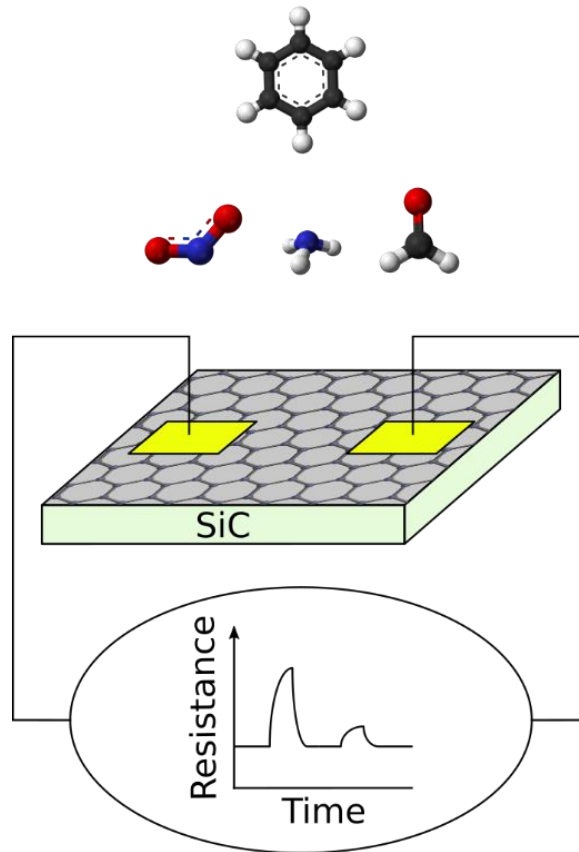


**Figure 3.8:** Schematic of graphene sensor readout.

#### 3.4.2 Data analysis

To facilitate a better understanding of the presented results, the most common sensor properties are defined here. An exemplary response is presented in Figure 3.9, where a  $\text{Fe}_3\text{O}_4$  NP DEG sensor was exposed to 30 min pulses of  $\text{CH}_2\text{O}$  at concentrations between 5 and 0.1 ppm at 150 °C at 0 % relative humidity (RH). If applicable, the sensor properties were calculated for this example and are stated alongside their definition.

**Response:** The (relative) response  $r$  is calculated as the maximum difference in resistance, i.e., with and without gas exposure, in relation to its baseline.

$$r = \frac{R - R_0}{R_0} \cdot 100 \% \quad (3.3)$$

$R$  is either the equilibrated resistance signal or the absolute maximum value of resistance before the gas exposure is switched back to background gas and  $R_0$  corresponds to the baseline resistance before the gas exposure.

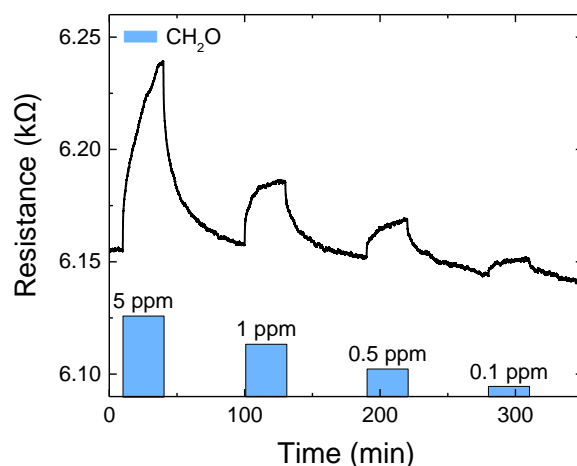


**Figure 3.9:** Resistance over time of Fe<sub>3</sub>O<sub>4</sub> NP DEG for CH<sub>2</sub>O exposures at 150 °C at 0 %RH. Adapted from [Paper 2].

In this example (compare Figure 3.9), the relative response is 0.45 % for 1 ppm CH<sub>2</sub>O.

**Sensitivity:** The sensitivity is defined as the derivative in output signal (response) by the input variation (gas concentration) and has therefore the unit %/ppb.

**Cross-sensitivity:** In case the sensor reacts to several analytes in a gas mixture or additional influences, the sensor is cross-sensitive and the sensor response depends on more than just one gas reaction.

**Selectivity:** Selectivity is the ability to respond to only the target analyte or to be able to distinguish between the responses to several analytes or influences.

**Stability:** If the sensor exhibits a non-changing baseline (resistance) over a certain period of time at the same operating conditions, it can be called stable. If there is a clear trend of a baseline shift instead, this change is called drift.

**Repeatability:** If the sensor exhibits the same response to the same measurement at different points in time, the measured response is repeatable.

**Reproducibility:** Reproducibility is the ability to generate the same relative sensor response with different sensors of the exact same kind.

**Speed of response:** The speed of response of a sensor is usually expressed by the time constant and is calculated either as  $\tau_{90}$  as  $\tau_{63}$ . Here, only  $\tau_{63}$  values, defined as when 63 % of the change has happened, are stated and simply referred to as  $\tau$ . An exponential fit is applied to the gas response as

### 3 Experimental methods

$$y = A_1 e^{-x/\tau} + y_0 \quad (3.4)$$

where  $A_1$ ,  $\tau$  and  $y_0$  are the optimized fitting parameters, whereof  $\tau$  corresponds to  $\tau_{63}$ . In this example (compare Figure 3.9),  $\tau$  is about 300 s for 1 ppm CH<sub>2</sub>O.

**Signal-to-noise-ratio:** The signal-to-noise-ratio (SNR) in decibel (dB) is a good value to compare sensor properties and is calculated as

$$\text{SNR}_{\text{dB}} = 20 \log_{10} \left( \frac{A_{\text{signal}}}{A_{\text{noise}}} \right) \quad (3.5)$$

where  $A_{\text{signal}}$  is the maximum absolute response, i.e., difference between  $R$  and  $R_0$ , at a given concentration and  $A_{\text{noise}}$  is calculated as three times the standard deviation of the baseline noise (also referred to as  $3\sigma$ <sup>5</sup>). For the absolute response to 1 ppm CH<sub>2</sub>O (28  $\Omega$ ) shown in Figure 3.9, the standard deviation is 0.32  $\Omega$  and the SNR is 29 dB.

**Detection limit:** The detection limit (or limit of detection, LOD) is the smallest concentration possible to detect reliably, i.e., a response smaller than  $A_{\text{noise}}$  cannot be counted as it could be a noise artifact. Here, it is calculated assuming a linear correlation of response over concentration, which results in the worst case LOD scenario, and a detectable response larger than  $3\sigma$ .

If multivariate data analysis was performed, it was either carried out using DAV<sup>3</sup>E [96], which is a MATLAB toolbox developed by the Lab for Measurement Technology at Saarland University, or a custom-made MATLAB script (compare results in section 4.3.2). LDA and PCA were evaluated for classification, and PLSR for quantification. For baseline and/or sensor drift correction, the measured cycles were either normalized or standardized, respectively [95]. For normalization, each cycle was divided by its own mean and for standardization, the mean of each cycle was subtracted from the cycle itself and then divided by the standard deviation of all cycles.

---

<sup>5</sup>  $3\sigma$  is the standard confidence interval used in analytical chemistry [162].

## 3.5 Gas mixing apparatus

To perform gas measurements with well-defined gas flows and concentrations over the sensor, a gas mixing apparatus (GMA) was used. The GMA can provide different gases whose flows are regulated by mass flow controllers (MFCs). Known gas mixtures, usually from a gas cylinder, are connected to MFCs. Each mass flow controller has a fixed maximum flow of which a range between 5 and 100 % can be set reliably. Zero air out of a zero air generator or pure nitrogen ( $N_2$ ) was used as the background or carrier gas with the possibility of varying humidity and oxygen partial pressure. A humid gas flow is produced by splitting the dry<sup>6</sup> carrier gas into two streams, one of which goes through a water bottle, the so-called “bubbler”, which can be assumed having 100 %RH. After this, both streams are unified, hence the humidity can be adjusted by varying the split ratio. If not especially mentioned, a total flow of either 100 or 200 ml/min was applied for all experiments. Test gases are provided via a gas bottle or via a permeation oven. The sensors were inserted in a flow chamber with a volume of 3 ml. Using specially designed flow chambers, either one sensor, two sensors, or one sensor with a UV-LED (light emitting diode) on the opposite side of the sensor can be used during a measurement. Figure 3.10 gives a simplified overview of how such a gas mixing system can look like.

For the system at Linköping University (LiU), the background and purging gas was applied through two MFCs giving a mixture of 80 % nitrogen and 20 % oxygen. The test gas was added through an additional MFC into the same line. In total, up to six different test gases can be applied during a single measurement session. The whole gas flow enters a four-way valve which can direct the flow either through the sensor chamber or directly to waste. To maintain a constant flow and background, a second branch with only nitrogen and oxygen MFCs is connected to the four-way valve. When the valve switches, one gas flow goes to the waste line and the other is automatically led through the sensor chamber. This system enables sharp switching steps and time for a new gas mixture to settle. The MFCs had maximum flow rates of 20, 50 or 100 ml/min. Nitrogen MFCs had a maximum flow of 100 ml/min whereas all other MFCs

---

<sup>6</sup> 0% RH: <5 ppm  $H_2O$  for gas from gas cylinders with purity 6.0 and <63.2 ppm for gas from the zero air generator.

### 3 Experimental methods

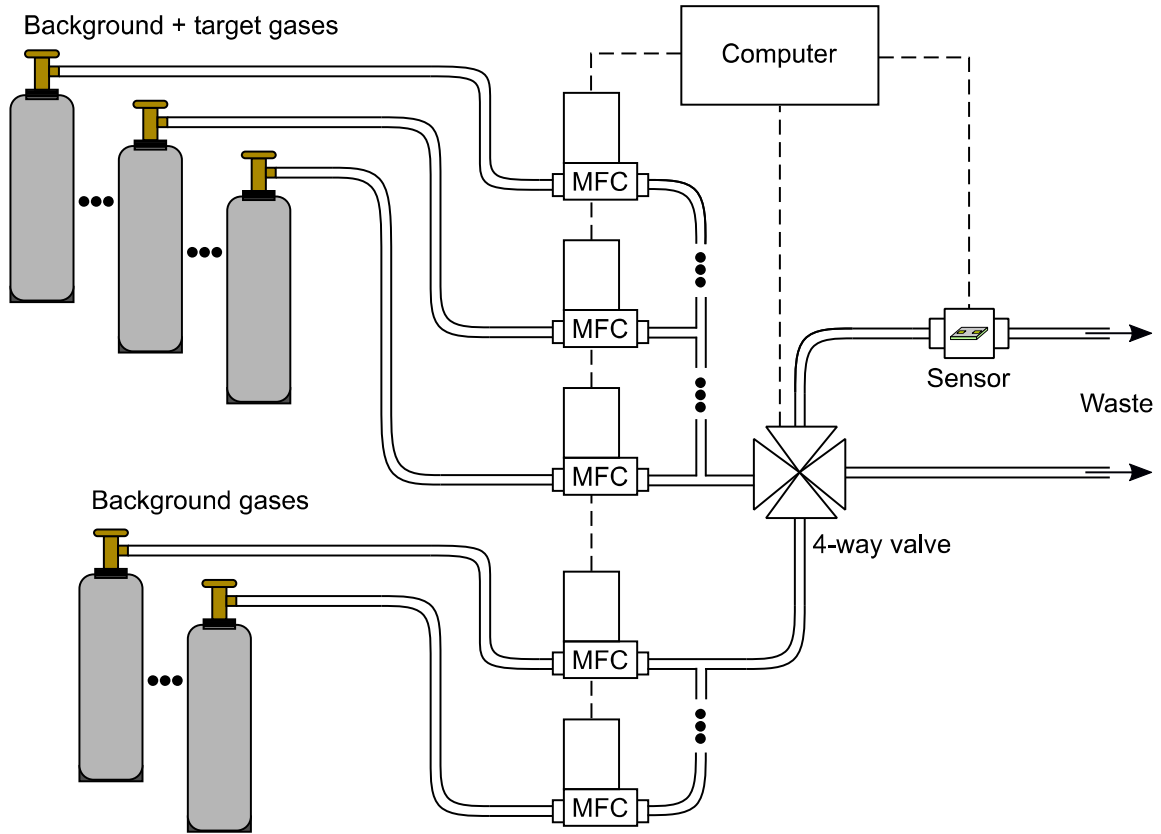


**Figure 3.10:** Simplified schematic of a gas mixing apparatus similar to what is used at LiU.

had 50 ml/min except for the  $\text{NH}_3$  MFC (20 ml/min). To ensure that no humidity could leak into the system when performing measurements under dry conditions, the bubbler line was disconnected in this case. A more detailed description of the system can be found in [97].

Measurements performed at Saarland University (UdS) used zero air generated by a GT Plus ultra-zero air generator (VICI AG International, Schenkon, Switzerland) as background gas instead with an approximate mixture of 79 %  $\text{N}_2$  and 21 %  $\text{O}_2$ . To enable measurements with lower concentrations than what is possible with the standard procedure of injecting the test gas with one MFC, an additional flow line can be connected to predilute the test gas. In this case, two additional MFCs (500 ml/min for carrier gas and 10 or 20 ml/min for test gas) are added to predilute the test gas before the gas mixture is injected into the main gas stream. With this procedure, a dynamic dilution over more than four orders of magnitude can be achieved [98]. This allows the dilution of 100 ppm gas bottles down to one-digit ppb concentrations over the sensor. Another option to prepare rather low concentrations in the gas flow is the use of a permeation oven.

Here, a permeation tube is placed in a heated and sealed oven chamber. The permeation tube contains the pure test substance which slowly diffuses through the tube walls made of perfluoroalkoxy alkane (PFA). The rate of diffusion is highly dependent on the oven temperature which therefore needs to be kept constant. The outflow is connected to the main gas flow via an MFC so that the permeation oven is conceptually similar to a gas bottle with a variable test gas concentration. Permeation tubes do not only enable low concentrations but can also be used for gases with very high vapor pressure, which cannot be kept in gaseous form in pressurized gas bottles. More details about the system can be found in [68, 99].

If UV irradiation of the sensor is desired during a measurement, a special sensor chamber was used where the UV-LED was placed opposite of the sensor. Two different LEDs with wavelengths of 265 nm (s-T39B-F1-265-01-1-050 from Sensor Electronic Technology Inc., Columbia, South Carolina, USA) and 355 nm (XSL-355-3E-R6 from Roithner Lasertechnik GmbH, Vienna, Austria) have been used.

### 3.5.1 Target analytes

In this section, all test gases are briefly defined and characterized through their chemical composition, appearance and pollutant guidelines. The World Health Organization [100] as well as the European Parliament [101] have guidelines for pollutant acceptance levels for indoor-air quality and these references are used if not specified otherwise.

Ammonia ( $\text{NH}_3$ ) is only toxic to humans at comparably high concentrations and has a 8-hour exposure limit of 20 ppm [102]. Nevertheless, it is one of the most produced inorganic chemicals with a wide use in the production of pharmaceuticals, explosives, cleaning products and as a precursor for fertilizers, with the latter alone being responsible for 80 % of the total  $\text{NH}_3$  production [103]. Furthermore,  $\text{NH}_3$  can be related to the formation of secondary particulate matter by reacting with acidic species, like  $\text{NO}_x$  or sulfur dioxide ( $\text{SO}_2$ ), to form ammonium-containing aerosols, which constitute the major fraction of  $\text{PM}_{2.5}$  aerosols in the atmosphere [104].

Carbon monoxide (CO) is toxic under exposure of high concentrations and listed with an acceptance level of 8.7 ppm for 8 hours of exposure. It is mainly produced in combustion processes, whenever there is not enough oxygen to oxidize the carbon fully to carbon dioxide and through breathing and photochemical reactions in the troposphere.

### 3 Experimental methods

Hydrogen was tested as well but not due to its toxicity, but rather as it is a very common gas in the ambient and can be used as a marker for human presence [105]. Moreover, many known sensor principles show a cross-sensitivity to changes in hydrogen concentration [106]. Hydrogen can also become explosive if more than 4 vol% are present in air and should therefore not exceed this threshold.

Nitrogen dioxide ( $\text{NO}_2$ ) can cause respiratory symptoms and has an acceptance level of 21 ppb annual average. It is mostly produced in internal combustion engines, accountable for around 40.5% of  $\text{NO}_x$  emissions in Europe, followed by energy production (22.5%) [107].

Volatile organic compounds (VOCs) have, unfortunately, no universal definition. They are defined via boiling points [108], vapor pressures [109], or their participation in atmospheric photochemical reactions [110]. Although some of them are hazardous to humans even at very low concentrations, they are widely put to use in industry and everyday products as solvents. For example, VOCs are still a big problem for the air quality of nail salons, as the main product is based on such solvents [111]. Additionally to the safety levels, also the chronic reference exposure levels (REL) for an 8-hour exposure are given [112]. In this work, benzene and formaldehyde are used as model VOCs:

Benzene ( $\text{C}_6\text{H}_6$ ) is a genotoxic aromatic compound, especially associated with leukemia, and has therefore very low acceptance levels and a REL value of 9.4 ppb. At the time of writing, France has the lowest acceptance level with 0.6 ppb [113]. According to the latest published WHO recommendations and a directive of the European Parliament, however, there is no safe level for benzene. It is mostly produced as a byproduct of traffic and is, additionally, often used as a component of solvents in cleaning agents or paint [114].

Formaldehyde ( $\text{CH}_2\text{O}$ ) has an acceptance level of 80 ppb, a REL value of 7.3 ppb and is genotoxic. France limits short-term exposures towards  $\text{CH}_2\text{O}$  to 24 ppb over a 2 h period [113]. In low concentrations,  $\text{CH}_2\text{O}$  usually does not pass beyond the respiratory system which limits direct cause to portal-of-entry effects like nasal cancer and sensory irritation. It is produced in combustion processes and is often used in its aqueous solution as disinfectant or conservative in everyday products as well as in the production of plastics [115].

All gases come with a purity level of at least 5.0. Nitrogen, generated from a liquid source has a purity of 6.0 in gaseous form. 5.0 and 6.0 purity level means that either 99.999 % or 99.9999 % of the gas volume belong to

the desired species with 10 ppm or 1 ppm of unknown molecules, respectively. All test gases used at LiU had nitrogen as their carrier gas within the gas bottle, whereas all test gas bottles used at UdS had zero air as carrier. Only CH<sub>2</sub>O had also nitrogen as carrier gas at UdS<sup>7</sup>, hence an addition of CH<sub>2</sub>O to the gas stream slightly changed the oxygen concentration as well. The maximum change in oxygen concentration is 0.4 % for 1 ppm of CH<sub>2</sub>O and only 0.003 % for 1 ppb. Exemplarily, the Fe<sub>3</sub>O<sub>4</sub> NP DEG sensor was exposed to a varying oxygen concentration and the response towards a change from 20 to 15 % O<sub>2</sub> was 0.08 %. Comparing this to the maximum occurring difference of 0.4 % change in O<sub>2</sub> level, the relative response should be approximately one order of magnitude lower and is then no longer of interest when comparing the gas responses.

Table 3 gives an overview of the gases and their specifications for measurements performed at LiU and UdS, respectively. Each gas and other environmental sensor influence has its own color code used throughout the whole thesis. They are summarized in Table 4<sup>8</sup>.

---

<sup>7</sup> Formaldehyde tends to polymerize in air over time and is more stable in an inert ambient like N<sub>2</sub>.

<sup>8</sup> The colors were chosen from a color palette for color blind people.

### 3 Experimental methods

**Table 3:** Test gases and their system properties.

Test gas	LiU	UdS
	Bottle concentration (ppm)	Bottle concentration (ppm)
Zero air <sup>9</sup>	/	100 %
Nitrogen	100 % <sup>10</sup>	100 %
Oxygen	100 %	/
Ammonia	2, 500	2900
Benzene	0.5	0.1 <sup>11</sup> , 100
Carbon monoxide	/	1000, 4000
Formaldehyde	4, 6	48, 50, 57
Hydrogen	/	100
Nitrogen dioxide	1, 5	10

---

<sup>9</sup> Zero air is generated using a GT Plus ultra-zero air generator (VICI AG International, Schenkon, Switzerland) and is not retrieved from a gas cylinder.

<sup>10</sup> Nitrogen is generated from a liquid source and is not retrieved from a gas cylinder.

<sup>11</sup> 0.1 ppm source concentration from permeation tube at 80 °C.

**Table 4:** Color codes of used gases and environmental influences.

Test gas/ influence	Color	RGB values
Ammonia		000 146 146
Benzene		209 109 000
Carbon monoxide		000 000 000
Formaldehyde		109 182 255
Hydrogen		000 073 073
Nitrogen dioxide		255 109 182
Oxygen		036 255 036
dR/dt		146 073 000
Humidity		000 109 219
Temperature		146 000 000
UV (265 nm)		182 109 255
UV (355 nm)		073 000 146



# 4 Results and discussion

This chapter presents and discusses the experimental results of the work. The first section describes integrity studies performed on the graphene samples before and after functionalization. Then the gas measurements of the different sensors with different gases and environmental influences are discussed. The last section deals with advanced data treatment to further improve the sensing properties.

## 4.1 Layer characterization

Before using a pristine or functionalized graphene layer for the production of a sensor device, its topography and structural integrity was analyzed.

### 4.1.1 Topography

To make sure that graphene formed a continuous layer over the SiC substrate and was free from contaminations, the topography was measured using AFM. A typical topography of the grown pristine graphene layer is shown in Figure 4.1 (a). The steps from the SiC step bunching that occurs during the high temperature growth have a height of typically 0.5-1.5 nm and form terraces [92]. The low height difference can be seen in the inset of Figure 4.1 (a), which presents the horizontal height profile for a 2  $\mu\text{m}$  line scan across the surface. The surface roughness  $R_q$  within such a terrace is very small ( $\sim 0.25$  nm). The corresponding phase image (Figure 4.1 (b)) exhibits a very continuous reading with the only exceptions being the step edges and a bi- or multilayer graphene patch in the lower left corner. This is an additional indicator for a high-quality monolayer graphene lattice. Figure 4.1 (c) shows the C-terminated backside surface of such a chip. It is still very flat but exhibits a completely different crystalline structure pattern with presumably several layers of graphene grown on it.

The samples were analyzed again after surface decorations. Figure 4.2 (a) represents an AFM image of the  $\text{Fe}_3\text{O}_4$  NL DEG sample. The surface does not differ much from PEG, as a very thin ( $\sim 0.5$ -1 nm), continuous layer is deposited onto the graphene surface. The dominating features are still the step edges formed by the SiC chip. After the decoration with  $\text{Fe}_3\text{O}_4$

## 4 Results and discussion

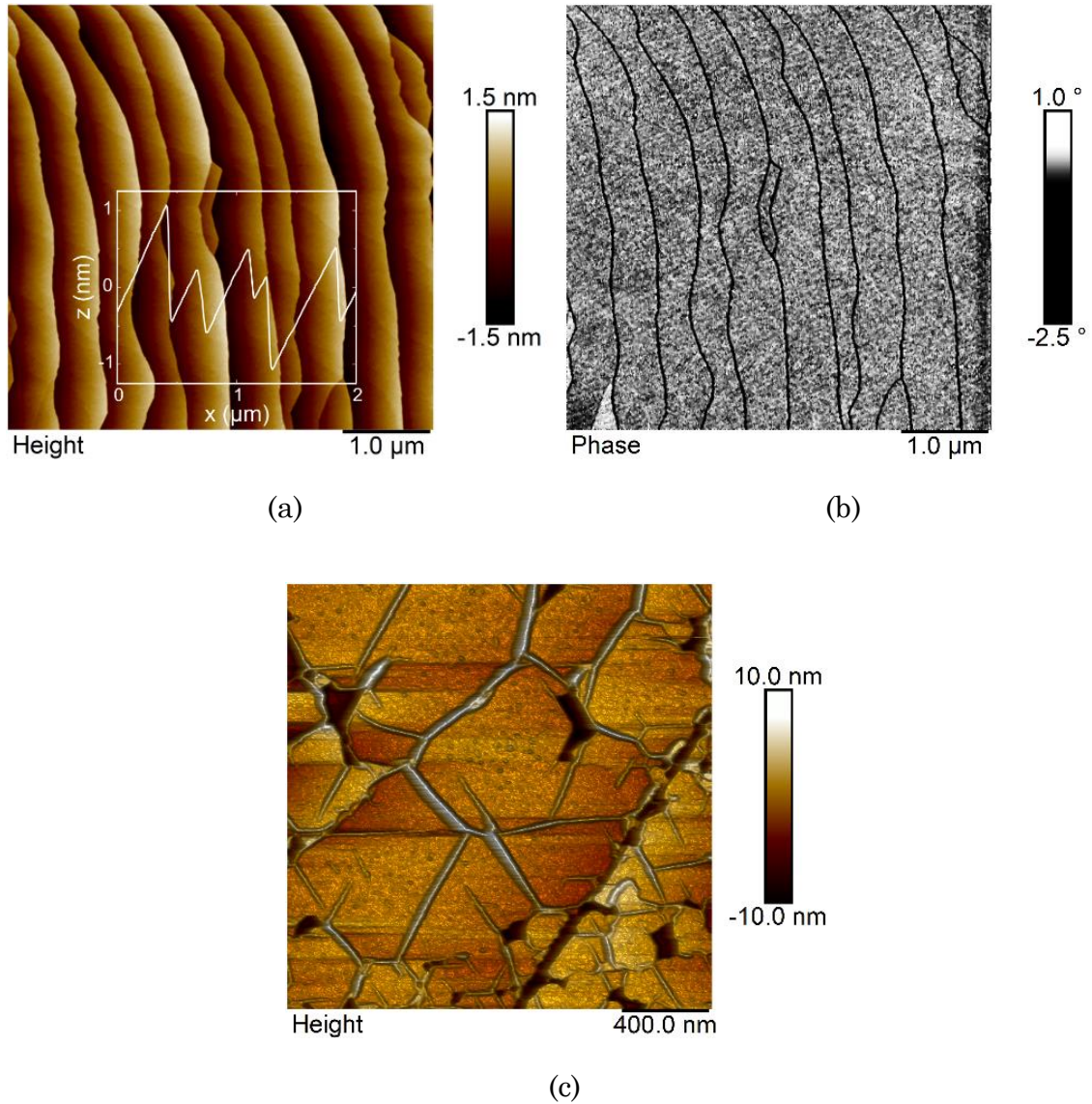


**Figure 4.1:** AFM images of (a) pristine graphene on Si-terminated 4H-SiC with height profile as inset, (b) its corresponding phase image and (c) backside (C-face) of a SiC chip.

NPs, the graphene surface looks completely different (Figure 4.2 (b), here 0.5 min deposition time). The NPs are now dominating the surface roughness and the step-like plateaus with their small differences in height can hardly be resolved with the set z-scale. The particle coverages and average particle diameters of the NP DEG samples investigated in this work are summarized in Table 5. The particle size was calculated after evaluating at least 100 single particles and agglomerates per sample. For the  $\text{Fe}_3\text{O}_4$  samples with different deposition times, the single particle size should stay approximately constant, as no other deposition parameters have been

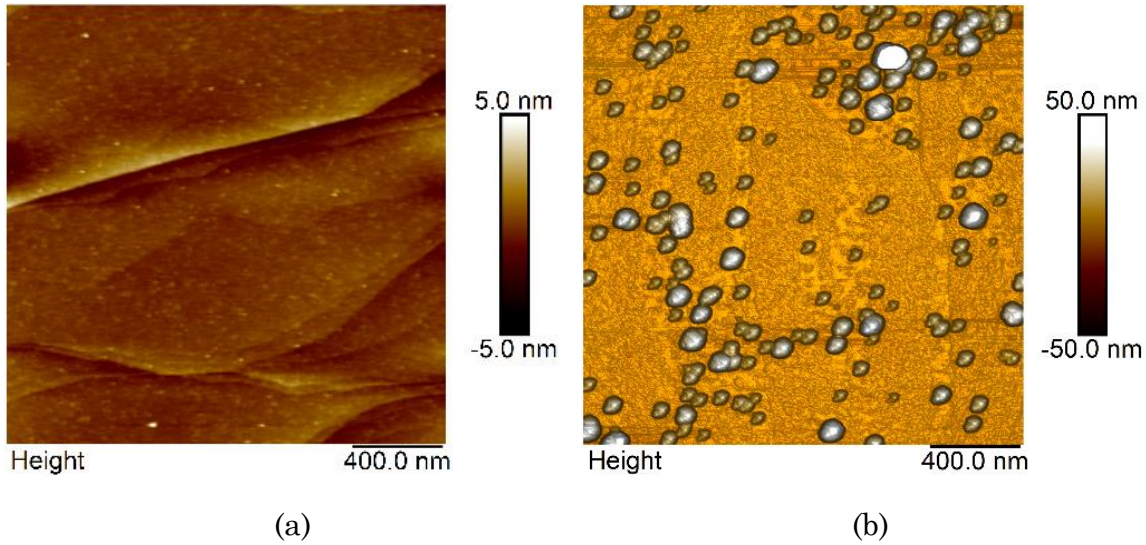


**Figure 4.2:** AFM image of (a)  $\text{Fe}_3\text{O}_4$  NL and (b) NP DEG.

modified. This is true to a large extent for single particles, but with a longer deposition time, more agglomerates are formed. An exemplary histogram of the particle size distribution is discussed in [Paper 2]. The Pt NPs are the smallest of all with a diameter of only approximately 25 nm. The particle size itself can have an impact on the sensor's sensitivity and selectivity and thus is another parameter that can be optimized for sensor performance tuning [16]. This was, however, not investigated in this work. With an increase in deposition time, the coverage should increase. This can be seen for most of the  $\text{Fe}_3\text{O}_4$  NP DEG surfaces. Only the sample deposited for 2 min resulted in a slightly higher coverage than the one deposited for 4 min. However, the coverage percentages are within the margin of error, so they could have roughly the same coverage, which still would not be desired, but leads to comparable sensors in this case. Regarding AFM images, all graphene samples are very clean, except for the deposited functionalization material. This also demonstrates that the addition and eventual removal of the used photoresist does not leave residues, which could be a problem otherwise [116, 117].

AFM images regarding IEG samples and the 2D Pt sensors are not shown here, but their quality was evaluated in other publications [47, 118].

**Table 5:** Resulting coverages and particle sizes after the decoration with NPs.

Sputter material	Deposition time (min)	Avg. particle size (nm)	Coverage (%)
Fe <sub>3</sub> O <sub>4</sub>	0.50	80 ±10	15 ±5
Fe <sub>3</sub> O <sub>4</sub>	1.00	80 ±10	25 ±5
Fe <sub>3</sub> O <sub>4</sub>	2.00	80 ±10	55 ±5
Fe <sub>3</sub> O <sub>4</sub>	4.00	80 ±10	45 ±5
Pt	3.00	25 ±10	20 ±5
TiO <sub>2</sub>	0.25	90 ±10	15 ±5

### 4.1.2 Structural integrity

Raman measurements were performed by Ivan G. Ivanov at Linköping University to verify that the integrity of the graphene layer was maintained after the decoration with NPs or NLs. The comparison between PEG, Fe<sub>3</sub>O<sub>4</sub> NP DEG and Fe<sub>3</sub>O<sub>4</sub> NL DEG is shown in Figure 4.3. For a better comparison, all spectra were normalized to the G peak. The lower line belongs to the PEG reference which has distinct G and 2D peaks, typical for sp<sup>2</sup>-hybridized carbon, around 1600 cm<sup>-1</sup> and 2737 cm<sup>-1</sup>, respectively [119]. The rather small FWHM value of 35 cm<sup>-1</sup> at the 2D peak is indicative of uniform monolayer graphene within the irradiated spot [120]. The features above 1280 cm<sup>-1</sup> and extending into the G peak are related to the interfacial buffer layer between the graphene and the SiC substrate [119]. Although they overlap with the position of the D peak at 1350 cm<sup>-1</sup>, they are not related to defects. If damage is induced into the graphene lattice, the D peak would rise. It can be clearly seen that the spectra after decoration are almost the same as the reference, indicating that no damage was introduced. The position of the 2D peak is the same for all samples, but the G peak varies slightly (±10 cm<sup>-1</sup>). This is most likely due to different levels of strain in the graphene lattices [121] or possibly a result of different doping in the graphene due to charge transfer between graphene and decoration material. Moreover, the 2D peak broadens for the NL DEG sample which could be related to the inclusion of bi- or multilayer

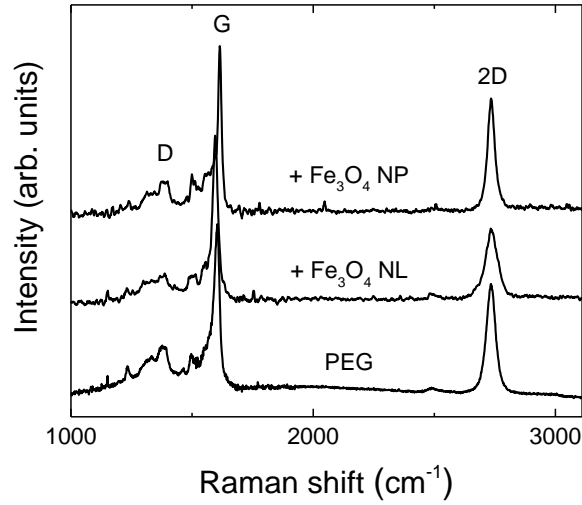


**Figure 4.3:** Raman spectra of PEG,  $\text{Fe}_3\text{O}_4$  NL and NP DEG. Adapted from [Paper 1, 4].

graphene in the measured spot. The lower G/2D peak ratio is another indication for this [81].

Figure 4.4 shows the Raman spectra of damaged graphene surfaces, i.e., hydrogen intercalated graphene and  $\text{Ag}^+$  ion irradiated graphene, along with PEG as reference. The peaks corresponding to the graphene lattice are still distinct and if the graphene framework would be disrupted completely, the Raman features would change drastically (compare [Paper C]). However, the rising D peak is a clear indication of significant amounts of defects in the graphene lattice. For example, the ratio between the intensity of the D and G peak is approximately 1.8 for the  $5 \times 10^{12}$  ions/ $\text{cm}^2$  irradiated sample which hints to a dominance of vacancy defects compared to the dominating  $\text{sp}^3$  defects for IEG with a ratio below 1, i.e., 0.6 [122]. The occurring red shift of the 2D peak, i.e., moving to lower values, of the defective graphene layers compared to PEG can be associated with relaxation of the compressive strain by defect creation [123]. Furthermore, the FWHM of the 2D peak increases for both treated samples to 48 and 56  $\text{cm}^{-1}$  for IEG and ion irradiated EG, respectively, which is another indication for a defective graphene layer. The peaks  $\text{D}'$  and  $\text{D}+\text{D}'$  arising around 1200 and 2960  $\text{cm}^{-1}$  also indicate rising defect levels. The  $\text{D}'$  peak can only be properly seen for the IEG sample whereas for the ion irradiated EG, it becomes part of the broader G peak.

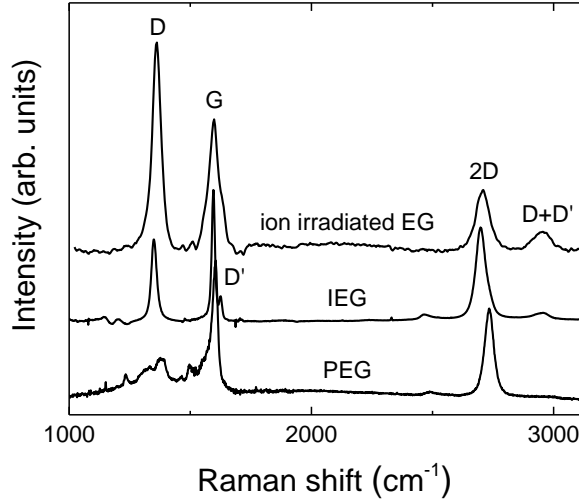


**Figure 4.4:** Raman spectra of PEG, IEG and  $5 \times 10^{12}$  ions/cm<sup>2</sup> irradiated EG. Adapted from [Paper 1, C].

### 4.1.3 Theoretical considerations

DFT calculations have been performed by Ivan Shtepliuk at Linköping University to investigate the different adsorption energies between C<sub>6</sub>H<sub>6</sub> and CH<sub>2</sub>O, and PEG and NP DEG, i.e., Fe<sub>3</sub>O<sub>4</sub> and TiO<sub>2</sub>, respectively, to theoretically verify that the NP decoration increases the gas sensitivity. The adsorption energy for C<sub>6</sub>H<sub>6</sub> on Fe<sub>3</sub>O<sub>4</sub> NP DEG is  $E_{\text{ads}} = 1.795$  eV, whereas the adsorption energy on PEG is significantly lower with  $E_{\text{ads}} = 0.284$  eV. For TiO<sub>2</sub> NP DEG, the adsorption energy is also higher compared to PEG, but about 0.4 eV lower compared to Fe<sub>3</sub>O<sub>4</sub> NP DEG. Therefore, further optimizations and gas measurements have not been performed with the TiO<sub>2</sub> NP DEG sample. Figure 4.5 shows the energetically favored adsorption configurations of the gas molecules on PEG and Fe<sub>3</sub>O<sub>4</sub> NP DEG. In the absence of the Fe<sub>3</sub>O<sub>4</sub> NPs, the C<sub>6</sub>H<sub>6</sub> molecule adsorbs parallel to the surface in a flat geometry. In this case, the center of the C<sub>6</sub>H<sub>6</sub> ring lays on top of a carbon atom belonging to the graphene. With Fe<sub>3</sub>O<sub>4</sub> NPs being present, the formation of a strong chemical bond between the C<sub>6</sub>H<sub>6</sub> ring and one of the Fe atoms is facilitated, leading to a tilted C<sub>6</sub>H<sub>6</sub> adsorption.

The CH<sub>2</sub>O molecule behaves similarly with adsorption energies of 0.149 eV and 1.870 eV for the adsorption on PEG and Fe<sub>3</sub>O<sub>4</sub> NP DEG, respectively (compare [Paper 2]). In conclusion, weak physisorption of C<sub>6</sub>H<sub>6</sub> and CH<sub>2</sub>O on PEG can be altered to strong chemisorption with the presence of NPs. Therefore, Fe<sub>3</sub>O<sub>4</sub> DEG graphene should exhibit an enhanced

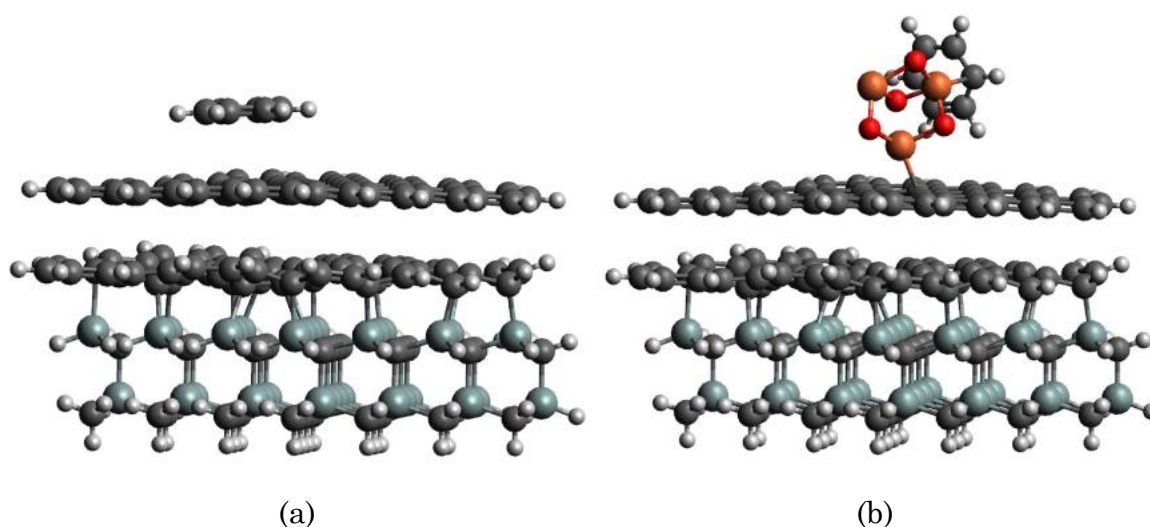


**Figure 4.5:** Optimized adsorption configurations of  $C_6H_6$  on (a) PEG and (b)  $Fe_3O_4$  NP DEG [Paper 2].

sensor reaction to the exposure of  $C_6H_6$  and  $CH_2O$  compared to  $TiO_2$  NP DEG and PEG, with a slightly higher estimated interaction with  $CH_2O$ .

## 4.2 Gas measurements

To evaluate the performance of the prepared EG-based gas sensors and their applicability in AQM, measurements with several test gases under varying operating conditions have been performed and their results are discussed in the following subsections.

### 4.2.1 Influence of temperature

The sensor temperature plays an important role for the performance of gas sensors. To ensure adsorption and reaction of gases at the sensor surface and thus a sensor response, a specific activation energy has to be overcome [27]. This leads to different reaction times caused by different rate constants for specific gases [20]. As already mentioned, the current sensor setup limits the operating temperature to about 300 °C and no measurements above 200 °C were performed as a precaution. To be able to work at higher temperatures, sensors are usually annealed at an even higher temperature, which was not done here.

The influence of the operating temperature is shown exemplarily in Figure 4.6. Figure 4.6 (a) represents a measurement with the  $V_2O_5$  NL DEG sensor over a temperature range from 50 to 125 °C and 30 min  $NH_3$

## 4 Results and discussion

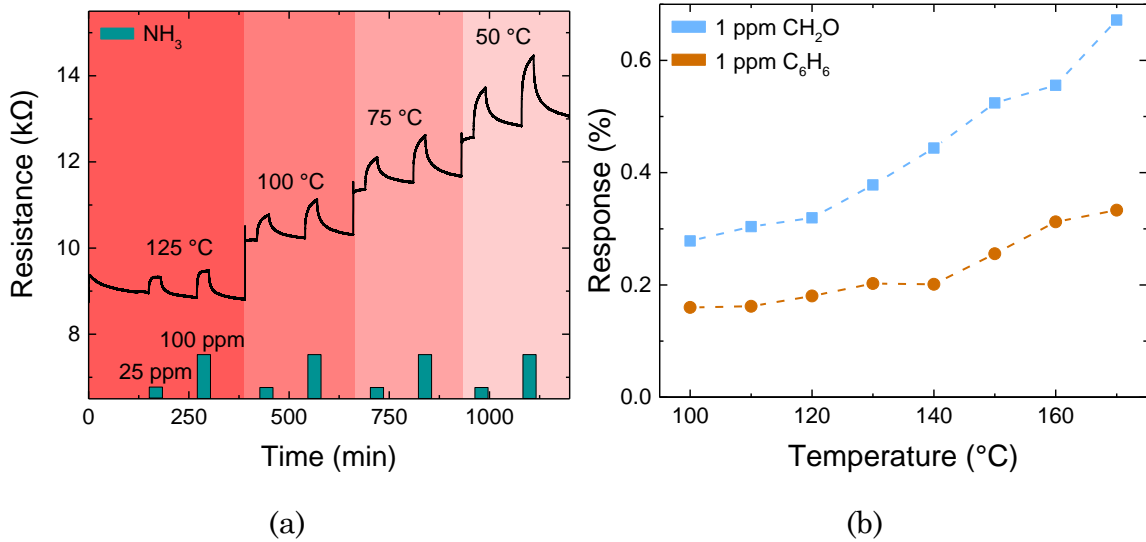


**Figure 4.6:** (a) Resistance over time of V<sub>2</sub>O<sub>5</sub> NL DEG for NH<sub>3</sub> exposures at different temperatures at 50 %RH based on [Paper 4] and (b) response of Fe<sub>3</sub>O<sub>4</sub> NP DEG for CH<sub>2</sub>O and C<sub>6</sub>H<sub>6</sub> exposures at different temperatures at 0 %RH.

exposures at 50 %RH. The measurement clearly shows that the baseline resistance decreases with increasing temperature. A higher operating temperature results in a faster equilibration of the resistance, but does not automatically lead to a larger absolute response.  $\tau$  decreases from approximately 550 s at 50 °C down to 150 s at 125 °C. Moreover, at lower temperatures, the sensor is not always able to relax back to its baseline after 90 min. More results with all four NL DEG sensors are discussed in [Paper 4]. Figure 4.6 (b) shows the response of a Fe<sub>3</sub>O<sub>4</sub> NP DEG sensor for 30 min of 1 ppm CH<sub>2</sub>O and C<sub>6</sub>H<sub>6</sub> exposures at temperatures ranging from 100 °C up to 170 °C in steps of 10 °C at 0 %RH. In this case, a higher operating temperature leads to a higher sensor response, e.g., the response to 1 ppm CH<sub>2</sub>O increases from 0.28 % at 100 °C to 0.67 % at 170 °C.

A compromise between level of response, speed of response and stability of the baseline has to be established. Therefore, and for better comparability between the different sensors, most measurements presented in this work have been performed at 150 °C. To make the most use of the different performances at varying temperatures, the operating temperature can also be cycled within a gas measurement. This so-called TCO approach will be discussed in section 4.3.2.

## 4.2.2 Influence of humidity

Perhaps even more critical for the sensor response than the operating temperature is the influence of relative humidity in the ambient. Many metal oxides have been found to exhibit a cross-sensitivity to RH and for most materials, a higher level of RH means a lower sensitivity to other gases as they must compete with water for available adsorption sites [26, 28]. Adsorption of water molecules on graphene can provide additional Coulomb and impurity scattering centers decreasing the free charge carrier mobility, thus decreasing the possible sensor response [124].

Not only the sensitivity, but also the baseline resistance of a sensor can strongly be affected by a humid ambient as additional water molecules act as p-dopants. Most measurements were performed in a dry environment for optimal sensitivity. Nevertheless, the effect of RH was explored separately with different samples, gases and operating temperatures.

Figure 4.7 (a) shows the response of PEG as the difference between the baseline resistances at two different humidity levels  $x$  and  $y$ , written as  $x-y$  %RH. The humidity was varied from 0 %RH up to 40 %RH while the sensor was kept at 150 °C in a constant flow of zero air. The resistance decreases with an increase in RH, thus exhibiting typical p-type behavior as additional H<sub>2</sub>O molecules act as p-dopants [124]. However, the used PEG is an n-type material and, therefore, the change in resistance should occur in the opposite direction. As the sensor is operated at 150 °C, hence no water film should form on the sensor surface, and ionic oxygen species are already present, p-doping by water is not the sole answer for the change in resistance. Water vapor forms hydroxyl groups which can react with surface oxygen forming rooted hydroxyl groups acting as electron donors and also a dissociated neutral hydrogen atom can react with surface oxygen, resulting in an oxygen vacancy, which is also an electron donor, thus reversing the expected p-type doping from the water molecule alone [125]. It can be clearly seen that for a change from any level of relative humidity to one that is not zero, the change in baseline resistance is rather small while a change from or to 0 %RH has a rather large impact on the baseline resistance. The observed logarithmically decreasing sensor response is typical for exposures towards decreasing gas concentrations, which also would suggest that the relative humidity rather acts as a target gas and not as a surface poisoning substance forming a passivating water film on the sensor surface. This would fit the observation that the sensors react to changes in relative humidity even if operated well above 100 °C.

## 4 Results and discussion

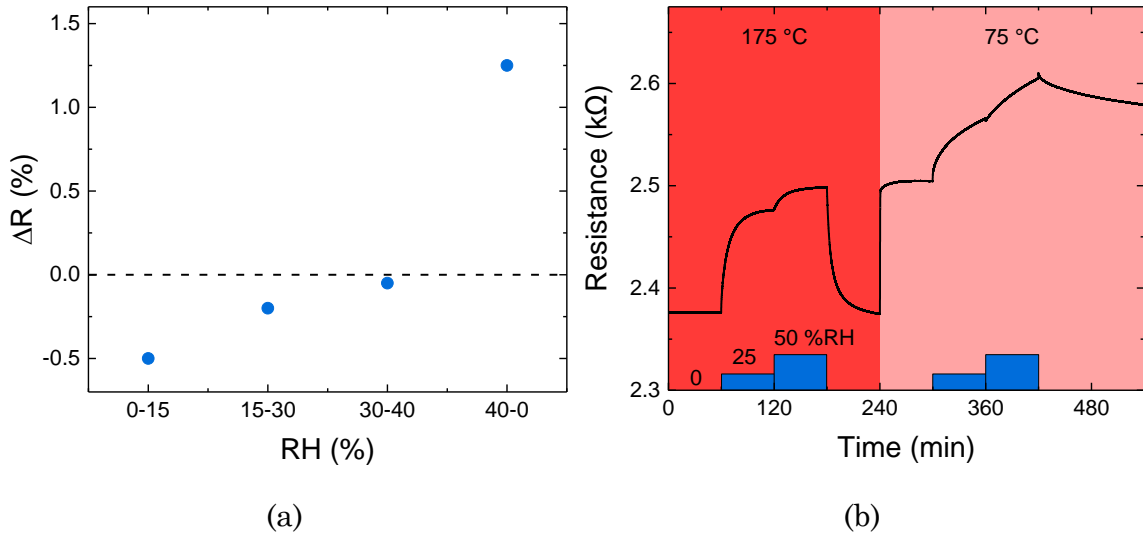


**Figure 4.7:** (a) Changes of baseline resistance of PEG at 150 °C at different RH and (b) resistance over time of IEG for RH variations at 175 and 75 °C, respectively.

To support this, the change in RH was investigated for several different temperatures. This is exemplarily shown for the IEG sensor in Figure 4.7 (b), which shows the response to changes in relative humidity first at 175 °C and then at 75 °C operating temperature. Note that the resistance increases with increasing relative humidity, which is opposite the reaction of PEG, but expected as the IEG sensor reacts as a p-type sensor instead. It can be clearly seen that the change in resistance is completely reversible to an zero air exposure with and without RH at 175 °C and occurs rather fast, whereas the sensor resistance changes very slowly at 75 °C when 25 %RH are introduced the first time. Furthermore, when changing back from 50 to 0 %RH at 75 °C, the baseline does not fully recover, which hints at the formation of a water film on the sensor surface, not possible at elevated temperatures. Moreover, when comparing the relative responses to changes in RH, it decreased slightly with increasing temperature for temperatures between 125 and 175 °C. For example from -3.4 to -2.8 % for PEG and from 5.7 to 5.2 % for IEG, respectively.

Figure 4.8 (a) shows the response of Fe<sub>3</sub>O<sub>4</sub> NP DEG to 1.6 and 0.8 ppm of CH<sub>2</sub>O, and 100 and 200 ppb of C<sub>6</sub>H<sub>6</sub> for 30 min at 150 °C for 50, 25 and 0 %RH. No response is observed for humidity levels above zero for both gases. Similarly, NL DEG sensors only respond to C<sub>6</sub>H<sub>6</sub>, CH<sub>2</sub>O and CO in a dry ambient (compare [Paper 4]). This means that the complete sensor system for AQM would need to run in a dry environment, which is a draw-

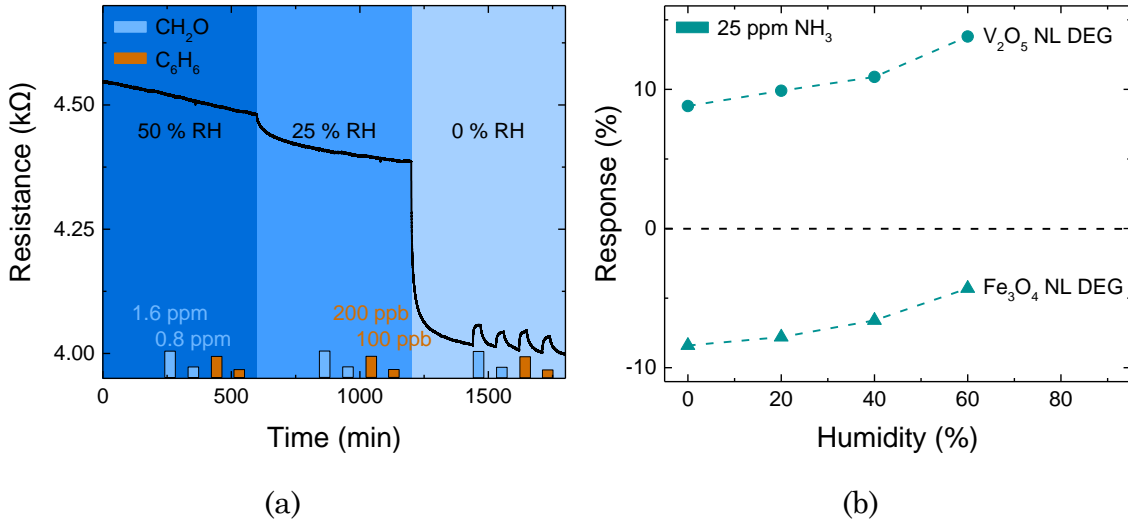


**Figure 4.8:** (a) Resistance over time of Fe<sub>3</sub>O<sub>4</sub> NP DEG for CH<sub>2</sub>O and C<sub>6</sub>H<sub>6</sub> exposures at 150 °C at different RH and (b) responses of Fe<sub>3</sub>O<sub>4</sub> and V<sub>2</sub>O<sub>5</sub> NL DEG sensors for 25 ppm NH<sub>3</sub> exposures at 75 °C at different RH. (b) is based on [Paper 4].

back, but technologically possible. However, other sensors, i.e., IEG and Pt NP DEG, are still able to detect both VOCs with humidity present, which would make the overall AQM system much simpler (compare section 4.2.5).

For other material/gas combinations, a humid ambient can boost the sensor response compared to the corresponding performance in a dry ambient. This is exemplarily demonstrated in Figure 4.8 (b), where the response of Fe<sub>3</sub>O<sub>4</sub> and V<sub>2</sub>O<sub>5</sub> NL DEG to 30 min of 25 ppm NH<sub>3</sub> exposure at 75 °C and various RH is shown. While the response of the Fe<sub>3</sub>O<sub>4</sub> NL DEG sensor decreases with increasing RH, the response of the V<sub>2</sub>O<sub>5</sub> NL DEG sensors increases from initially 8.8 % up to 13.8 % at 0 and 60 %RH, respectively. It is interesting that an increase in humidity increases the response, even exceeding the response at zero humidity. Especially when measuring NH<sub>3</sub>, this increase could be due to the reaction with OH<sup>-</sup> groups or of products of reactions from OH groups and NH<sub>3</sub> instead. This phenomenon was found to occur for metal oxide gas sensors when operating them at relatively low temperatures in a humid environment [65, 126]. Similarly, also V<sub>2</sub>O<sub>5</sub> NL DEG, Pt NP DEG and the IEG sensors exhibit an increase in response to NO<sub>2</sub> with increasing RH in the ambient even when measured at 150 °C (compare for example [Paper 4]). One possible explanation for the IEG sensor could be that NO<sub>2</sub> mostly changes, i.e., enhances, the mobility but not the carrier density. In such a case, graphene with low

doping introduced to  $\text{NO}_2$  would show only a small change in resistance, because there are only a few charge carriers with their mobility being enhanced. When graphene is strongly doped (e.g., by ambient humidity),  $\text{NO}_2$  gas enhances the mobility of the charge carriers, resulting in a stronger change in resistance [127].

### 4.2.3 Influence of UV irradiation

As mentioned before, the sensor performance can be enhanced by additional UV irradiation. It is known that if the band gap is below the wavelength energy (4.48 eV for 265 nm and 3.49 eV for 355 nm), there will be charge excitation changing the charge density in the exposed surface material, i.e., the decorated nanostructures and/or the graphene lattice. This could increase or counteract the effect of the gas response depending on the material/gas combination and should be more pronounced for thicker layers, where the net charge excitation is higher.

Figure 4.9 shows the response of a  $\text{TiO}_2$  NP DEG sensor to varying oxygen percentages without and with UV irradiation. The UV LED has a wavelength of 265 nm and an optical output power of 0.8 mW. The operating temperature was 100 °C and oxygen was varied from a baseline of 20 % to values ranging between 16 and 1 %. It can be clearly seen that the measurement without UV irradiation shows changes in resistance when varying the oxygen concentration, but they are not distinct and cannot be related to the specific concentrations. Introducing the UV irradiation, the baseline resistance drops by about 270  $\Omega$ . Moreover, the changes in oxygen concentration can now be distinctively observed as the resistance exhibits the typical shape of a gas sensor response. Unfortunately, the exposure time of 10 min was not enough to arrive at an equilibrated response level. The desorption process is enhanced under the irradiation as well, decreasing the time needed for the sensor to return to its baseline after the gas exposure, making it faster and more efficient [19]. The low response without UV is likely due to an oxygen saturated surface in the background of 20 %  $\text{O}_2$ . UV irradiation promotes oxygen desorption, leading to an increased dynamic range for oxygen detection [57].

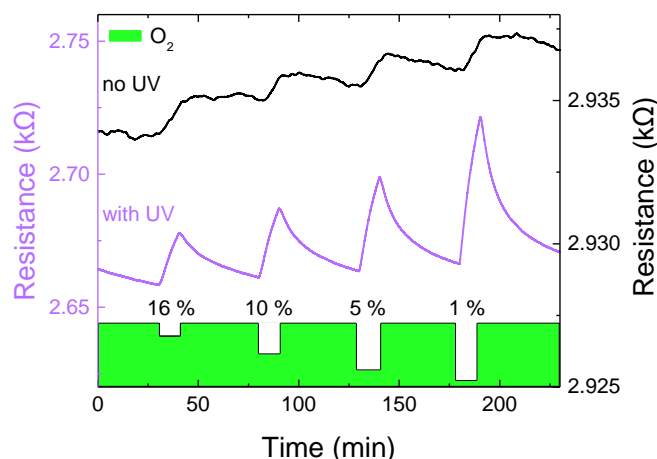


**Figure 4.9:** Resistance over time of TiO<sub>2</sub> NP DEG to a variation of oxygen changing from a background of 20 % without and with UV irradiation at 100 °C at 0 %RH. Adapted from [Paper 1].

Depending on the material/gas combination, additional UV irradiation can have no or only a rather small impact on the sensor properties. This is exemplarily shown in Figure 4.10. V<sub>2</sub>O<sub>5</sub> and ZrO<sub>2</sub> NL DEG sensors were exposed to 30 min of 25 ppm NH<sub>3</sub> with and without additional UV irradiation. Both UV wavelengths increase the sensor response for V<sub>2</sub>O<sub>5</sub>, while the response for ZrO<sub>2</sub> is almost constant for all measurements. This is expected as ZrO<sub>2</sub> has a comparably large bandgap (>5 eV), while V<sub>2</sub>O<sub>5</sub> with ~2.4 eV has a bandgap smaller than the used photon energies (e.g., 3.49 eV for 355 nm). UV irradiation can also have a positive effect on the time constants. For example,  $\tau$  decreases for V<sub>2</sub>O<sub>5</sub> from approximately 500 s without irradiation down to 400 s at 265 nm UV irradiation. An irradiation with 355 nm does decrease  $\tau$  as well, but not as much as 265 nm UV irradiation. This could be due to the higher energy at shorter wavelength. The same trend could be expected for the response as well, i.e., higher energy due to the shorter wavelength would lead to an increased response, but for all three NL DEG, where the response increased with UV, the maximum was reached with 355 nm irradiation. This could be due to the fact that energetically higher irradiation does not only facilitate stronger surface reactions, but also better molecule desorption, thus two competing mechanisms occur at the same time as mentioned in [57].

In general, additional UV irradiation is often used for graphene when NH<sub>3</sub> or NO<sub>x</sub> should be detected (see also [Paper 4, C] and [128]) and can even be used in pulsed mode to generate transient data [61].

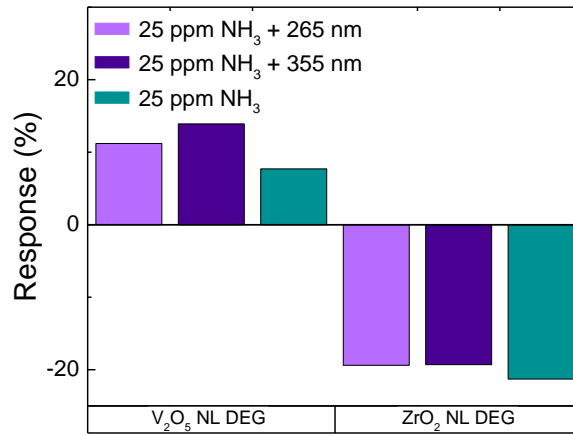


**Figure 4.10:** Responses of V<sub>2</sub>O<sub>5</sub> and ZrO<sub>2</sub> NL DEG for 25 ppm NH<sub>3</sub> exposures at 75 °C and 125 °C, respectively at 50% RH without and with UV irradiation. Adapted from [Paper 4].

#### 4.2.4 Influence of defects

Another way to tailor the sensing properties of graphene is by introducing structural defects or impurities. Assuming that the gas sensing takes place at graphene's  $\pi$ -electrons, which are directly exposed to adsorbed molecules, more available  $\pi$ -electrons would lead to an increase in sensor response. Thus, it was reported that dopants and defects can increase the sensing capabilities of graphene [56]. In general, carbon atoms on a defective graphene surface hold higher dipole moments compared to PEG, which can result in a stronger bond formation with foreign molecules. Here, defects were introduced using low energy ion beam implantation (30 keV) with Ag<sup>+</sup> ions.

Figure 4.11 summarizes the responses for PEG and ion irradiated EG sensors to 50 ppb NO<sub>2</sub> and NH<sub>3</sub> exposures at 150 °C at 0 %RH. Without any ion treatment, the PEG sensor exhibits typical n-type behavior with a positive response to NO<sub>2</sub> and a negative response to NH<sub>3</sub>. With increasing ion irradiation fluence, the sensor response first increases in magnitude before it inverts its behavior just below a fluence of  $5 \times 10^{13}$  ions/cm<sup>2</sup>, with a decrease in response and a change in response direction for both gases. This means that there is not only an optimal defect density achieving the absolute highest sensor response, but also that doping by defect introduction can change the sensing behavior from initial n-type EG to p-type EG on SiC. Moreover, the corresponding response and recovery time constants are inversely correlated with the ion irradiation, i.e., first decreasing with ion irradiation fluence and then increasing again (compare [Paper C]).

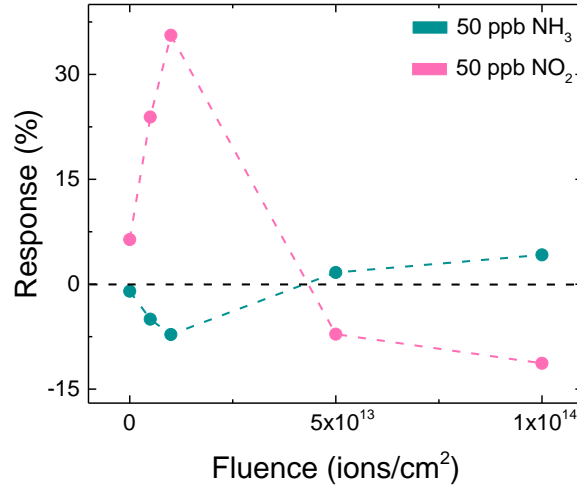


**Figure 4.11:** Response of EG for 50 ppb NH<sub>3</sub> and NO<sub>2</sub> exposures at 150 °C at 0 %RH over increase in Ag<sup>+</sup> ion irradiation. Based on [Paper C].

The initial increase in sensor response observed for low fluences could be explained with an increased interaction between NO<sub>2</sub> molecules and defective graphene compared to PEG [56] (compare section 4.1.2). Furthermore, additional adsorption sites are available on defective graphene compared to PEG and defects increase the charge transfer between graphene and NO<sub>2</sub> molecules, both leading to an increased sensor response [129]. The higher the irradiation fluence, the more carbon vacancies and dangling bonds are produced. These dangling bonds correlate with sp<sup>3</sup> defects, which also represent C-OH and C-O-C bonds. These carbon bonds are electron acceptors, i.e., p-type dopants, which could explain the change from n- to p-type behavior. Similar explanations can be given for the observed differences in sensor response for increasing defect density when exposed to NH<sub>3</sub> as well [130]. An in-depth study of the defect generation can be found in [Paper C].

This change in response behavior, i.e., from n- to p-type, can also be achieved with a sufficiently high concentration of a strongly oxidizing gas. This is shown in Figure 4.12, where a PEG and an ion irradiated sensor (5x10<sup>12</sup> ions/cm<sup>2</sup> fluence) were exposed to NO<sub>2</sub> at 150 °C at 0 %RH. While the PEG sensor exhibited an n-type behavior for the whole tested concentration range, i.e., from 50 ppb to 50 ppm, the irradiated sensor inverts its response direction when ppm concentrations were provided. This is most probably due to a doping effect corresponding to the gas species, which increases with an increase in concentration. This doping changes the

## 4 Results and discussion

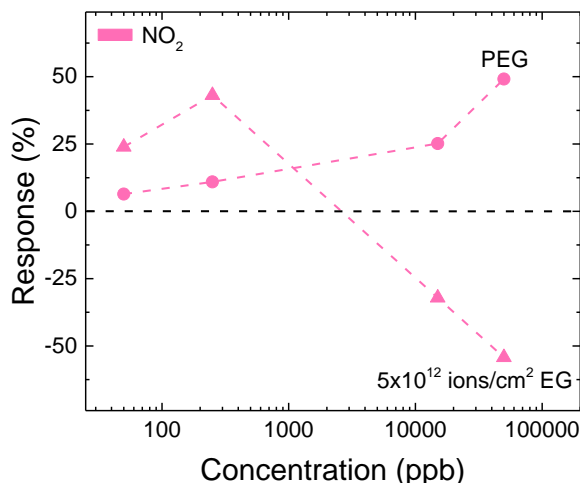


**Figure 4.12:** Responses of PEG and  $5 \times 10^{12}$  ions/cm<sup>2</sup> irradiated EG for NO<sub>2</sub> exposures at 150 °C at 0 %RH. Based on [Paper C].

position of the Fermi level, which can change the response direction if the Dirac point is passed from below to above or vice versa (compare section 2.3.2).

### 4.2.5 Target analyte detection

One of the main findings of this work is the ability to detect concentrations of hazardous VOC, i.e., C<sub>6</sub>H<sub>6</sub> and CH<sub>2</sub>O, quantitatively down to single ppb and also over a large dynamic range of three orders of magnitude under lab conditions (compare Figure 4.13). This was first presented in [Paper 2] with the Fe<sub>3</sub>O<sub>4</sub> NP DEG sensors. This measurement was repeated twice in the same environment and once more approximately one year later with the same sensor. The measured responses show some small deviations between the measurements but without a clear trend of decreasing response over time. This shows the long-term stability of the sensor. What decreases though is the SNR. More noise can be seen for a sensor if operated over a longer time compared to a ‘fresh’ one. Fe<sub>3</sub>O<sub>4</sub> (4min) NP DEG was also tested to C<sub>6</sub>H<sub>6</sub> in the lower ppb range at 150 °C at 0 %RH, resulting in very similar response values as Fe<sub>3</sub>O<sub>4</sub> (2min) NP DEG, e.g., 0.049 % and 0.052 % for 10 ppb for Fe<sub>3</sub>O<sub>4</sub> (2min) and (4min) NP DEG, respectively. This fits the observation that the NP coverage is similar for both samples, indicating a reproducible sensor performance. A systematic study of the influence of particle coverage on the sensor response was not done here, but it was already found that it can have a significant impact [131]. However, as

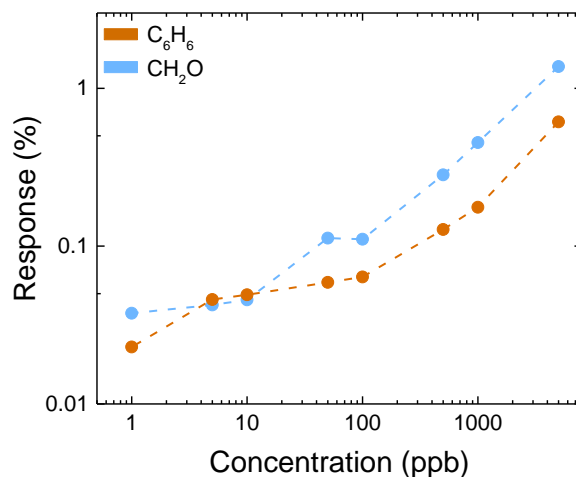


**Figure 4.13:** Response of Fe<sub>3</sub>O<sub>4</sub> NP DEG for C<sub>6</sub>H<sub>6</sub> and CH<sub>2</sub>O exposures at 150 °C at 0 %RH. Adapted from [Paper 2].

mentioned in section 4.2.2, the sensors were able to detect both gases only in a dry environment.

Latest results show that it is possible to detect these VOCs at low concentrations in a humid environment as well. In Figure 4.14, the responses for Pt NP DEG and IEG sensors to C<sub>6</sub>H<sub>6</sub> exposures at 150 °C are summarized. It can clearly be seen that the sensors react even with relative humidity present in the ambient. The response at 50 %RH is, however, smaller compared to the one in dry ambient, resulting in approximately half of the response compared to 0 %RH. The response of the Pt NP DEG sensor is the highest of all observed responses (compare also Figure 4.15), but it is also approximately one order of magnitude higher than the only other sensor, i.e., IEG, able to detect C<sub>6</sub>H<sub>6</sub> and CH<sub>2</sub>O at

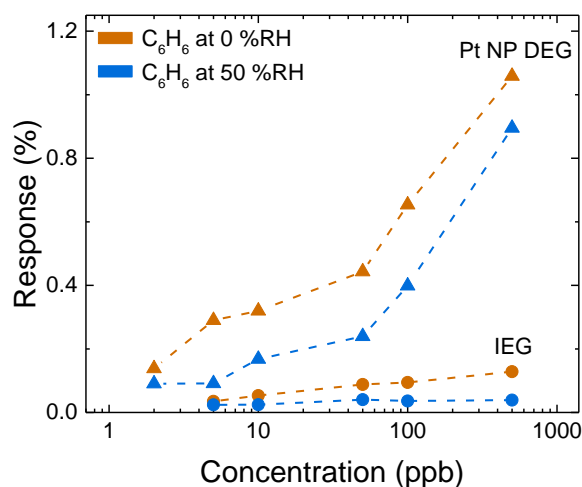


**Figure 4.14:** Responses of Pt NP DEG and IEG for C<sub>6</sub>H<sub>6</sub> exposures at 150 °C.

## 4 Results and discussion

50 %RH. This results in LODs of 0.05 and 0.09 ppb for  $C_6H_6$  at 0 and 50 %RH and 0.07 and 0.17 ppb for  $CH_2O$ , respectively. It was already found in other studies that Pt doped sensors showed superior gas response to relative humidity compared to their undoped counterparts [132, 133]. However, also there, an increase in RH leads to a decrease in response.

The appearance of sensitivity for IEG compared to PEG is most probably due to the known increased defect density for IEG (compare [134] and section 4.2.4). Another possible explanation could be the difference in carrier density between the sensors [134]. The response of the IEG sensor is comparably small (see also Figure 4.15), but still has estimated LODs of 0.68 and 1.40 ppb for  $C_6H_6$  at 0 and 50 %RH. Exposures to formaldehyde result in very similar responses, e.g., 0.04 % vs 0.05 % for 10 ppb  $CH_2O$  and  $C_6H_6$  at 0 %RH, respectively. This leads to similar LODs for  $CH_2O$  exposures of 0.97 and 1.74 ppb at 0 and 50 %RH, respectively. The promising outcome with this sensor surface is that it could additionally be decorated with other nanostructures, thus further enhancing its sensor properties.

For a better comparability, all sensors were exposed to 500 ppb  $C_6H_6$  and  $CH_2O$ , respectively, at 150 °C and 0 %RH. The results are shown in Figure 4.15. As expected from theoretical calculations (see section 4.1.3), the PEG sensor did not exhibit any response for both gases and also  $ZrO_2$  NL DEG did not react discernibly. Both  $Fe_3O_4$  DEG sensors have similar responses with a small increase with the NL compared to the NP DEG sensor to  $C_6H_6$  but vice versa for  $CH_2O$ . This would support the claim that the reaction mainly takes place at the  $Fe_3O_4$  sites as the NL DEG sensor is completely covered with an ultra-thin layer, whereby no direct graphene-gas interaction can occur. Both  $CuO$  and  $V_2O_5$  NL DEG sensors outperform the  $Fe_3O_4$  DEG in regards to their responses. The highest response of all sensors was exhibited by the Pt NP DEG sensor, which was more than twice as high as the second highest response observed with the  $CuO$  NL DEG sensor. The IEG sensor showed a comparably low response, but as it is without any additional metal oxide decoration and also operable in a humid environment (compare also Figure 4.14), this is especially interesting as both techniques, i.e., hydrogen intercalation and metal oxide decoration, could be combined in the future to obtain even better sensors.

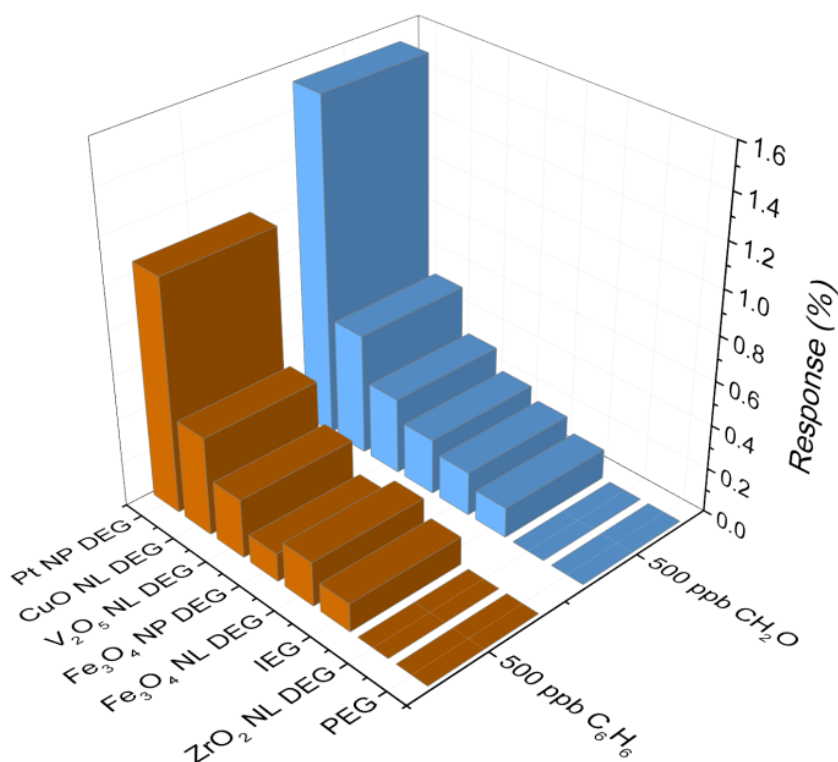


**Figure 4.15:** Responses of all sensors for 500 ppb C<sub>6</sub>H<sub>6</sub> and CH<sub>2</sub>O exposures at 150 °C at 0 %RH. Partly based on [Paper 2, 4].

Furthermore, the responses towards CH<sub>2</sub>O compared to C<sub>6</sub>H<sub>6</sub> were higher for all sensors except for the Fe<sub>3</sub>O<sub>4</sub> NL DEG one, where the response was approximately the same (compare also section 4.1.3). An overview about LOD and SNR values is given at the end of this section.

As already mentioned, the main focus was the detection of VOCs down to as low concentrations as possible. Nevertheless, experiments with other gases can highly contribute to the understanding of sensor properties, especially when it comes to selectivity or even cross-sensitivity. For example, NH<sub>3</sub> was used as either a common interference gas or common reducing agent. All tested sensors in this work have exhibited a response to NH<sub>3</sub>. In general, PEG showed the smallest response compared to all modified sensors. Some more in-depth results regarding ammonia detection are included in [Paper 4, C]. NH<sub>3</sub> is an interesting gas also at low concentration for example as analyte in breath analysis applications. Hibbard and Killard state that there is a need of simple, non-invasive detection methods that can detect ammonia with a limit of detection of at least 50 ppb at high levels of relative humidity [135]. This was not evaluated in this work, but could be investigated with some of the sensors in the future due to their promising detection behaviors.

## 4 Results and discussion

Other very common gases in the ambient are CO and NO<sub>2</sub>. The responses are summarized in Table 6 for 30 min exposures to 500 ppb of CO and NO<sub>2</sub>, respectively, at 150 °C at 0 %RH. For all tested sensors, the response to CO was smallest. Interestingly, the IEG sensor has an almost 10-times larger response compared to most other sensors. The only sensors not reacting to CO at all were the Pt NP and ZrO<sub>2</sub> NL DEG sensor. The Fe<sub>3</sub>O<sub>4</sub> NP DEG sensor was not tested with CO. To NO<sub>2</sub>, the Fe<sub>3</sub>O<sub>4</sub> NL DEG sensor exhibited the highest and the untreated PEG sensor the second highest response. The strong gas response towards NO<sub>2</sub> with PEG could be due to the fact that NO<sub>2</sub> sensing is highly dependent on the substrate and has a known high binding energy with EG [136]. The Fe<sub>3</sub>O<sub>4</sub> NP DEG sensor (not shown in Table 6) exhibited one of the lowest responses of all sensors, which can partly be explained with the lower exposure time (see section 4.3.1 for influence of exposure time on response magnitude). But a high SNR (64 dB) at 400 ppb hints to a much lower detection limit of approximately 0.15 ppb. However, the time constant  $\tau$  is rather long with approximately 500 s for a 100 ppb exposure.

In summary, the investigated EG sensors react with many different gases and not only the desired VOC targets. A method to obtain faster time constants and proper selectivity nevertheless is discussed in section 4.3.

**Table 6:** Summary of responses for 500 ppb CO and NO<sub>2</sub> exposures at 150 °C at 0 %RH partly based on [Paper 4]. Fe<sub>3</sub>O<sub>4</sub> NP DEG is not shown here due to different experimental conditions.

		Response (%)						
		PEG	Pt NP DEG	CuO NL DEG	Fe <sub>3</sub> O <sub>4</sub> NL DEG	V <sub>2</sub> O <sub>5</sub> NL DEG	ZrO <sub>2</sub> NL DEG	IEG
CO	500 ppb	-0.06	0	0.12	0.09	0.14	0	0.98
NO <sub>2</sub>	500 ppb	42.50	-8.65	14.60	65.82	-8.93	-17.10	-5.42

Table 7 gives an overview of SNR and LOD values for all different sensors and various gases. The SNR values are based on 500 ppb exposures at 150 °C at 0 %RH similar to Figure 4.15 and Table 6, and LOD values are based on 10 ppb for C<sub>6</sub>H<sub>6</sub> and CH<sub>2</sub>O, and 100 ppb for CO and NO<sub>2</sub>, respectively. NH<sub>3</sub> is not included as not all sensors were exposed to ppb level concentrations, thus limiting the comparability with the other gases. It can be seen that the highest SNR and lowest LOD values occur for NO<sub>2</sub> exposures, which is expected as also the relative responses towards NO<sub>2</sub> are highest compared to other gases. In general, the SNR values are rather high indicating that 500 ppb exposures are easily detectable with all sensors for all gases. The LOD values however range from about 0.01 up to 16 ppb spanning approximately three orders of magnitude. This demonstrates that the 21 ppb NO<sub>2</sub> exposure limit for AQM could easily be detected and could even outperform state of the art commercial sensors, such as NO<sub>2</sub>-A1 from Alphasense (Essex, United Kingdom [137]) with a resolution of 20 ppb. Moreover, the detection of NO<sub>2</sub> at these very low concentrations is of interest as a marker for the production of ultra-fine particles [138]. Buckley et al. give a comprehensive overview about the sensor performances of graphene based chemiresistors and, depending on the functionalization, LODs ranging from single ppt up to tens of ppm are observed for NO<sub>2</sub> [139].

For both VOCs, the detection limit is always below 4 ppb and theoretically reaches even down to 0.05 ppb for the Pt NP DEG sensor. However, the SNR and LOD highly depend on the amount of baseline noise, which increases over time. This is most probably due to a slow degradation of the contacts. For example, the Fe<sub>3</sub>O<sub>4</sub> NP DEG sensor has today, i.e., after 4 years of repeated operation, values of 16 dB and 3.97 ppb but it had 58 dB and 0.03 ppb when the sensor was new. Knowing that the Pt NP DEG sensor is relatively new, this might lead to a decreased detection limit of approximately 100 times more, i.e., 5 ppb for C<sub>6</sub>H<sub>6</sub>, if operated for 4 years. Nevertheless, assuming an increase in baseline noise, thus a decrease in SNR and an increase in LOD, detection of hazardous VOCs would still be possible down to ~10 ppb with all sensors<sup>12</sup>. Furthermore, the SNR highly depends on the used readout electronics (compare section 4.4). Since measurements could be performed with the same sensor over a period of several

---

<sup>12</sup> Fe<sub>3</sub>O<sub>4</sub> NP DEG sensors were operated for more than a period of 4 years, NL DEG sensors for over 3 years, and PEG, Pt NP DEG and IEG only for about 1 year.

## 4 Results and discussion

years including two different laboratories (compare section 4.4), the long-time stability is still promising.

One of the main drawbacks are the slow ad- and desorption times. Comparing the investigated epitaxial graphene sensors in this thesis with commercially available sensors on the market, they nevertheless perform rather well. According to Spinelle et al. [8], the VOC sensors with the lowest detection limit and best accuracy are still chromatographic instruments. In a slightly more user-friendly portable system, these gas chromatographs reach LODs between 0.01-10 ppb with time constants between 30-900 s, but are neither handheld nor cheap. Sensors with LODs comparable to the investigated EG sensors are based on photo-ionization detectors (PID). Their LODs are in the range between 1 ppb (Honeywell ppbRAE 3000+ from Geotech Environmental Equipment Inc., Denver, Colorado, USA [140]) and 10 ppb (X-am 8000 from Dräger, Lübeck, Germany [141]). Their big advantage is the fast sampling time of only a few seconds and good selectivity. However, such handheld devices are still not small and cheap enough for a versatile device integration. Commercially available VOC sensors based on metal oxides are usually not selective to one gas and give a TVOC (total VOC) level as output, which would also be a valid option for the EG sensors investigated here (compare section 4.3.2). However, the operation range of available sensors is in the 0.1-100 ppm range with best detection limits of around 50-100 ppb (AS-MLV-P2 from Sciosense, former AMS, Eindhoven, the Netherlands [142], SGPC3 from Sensirion, Zürich, Switzerland [143], VOC/CO<sub>2</sub> Sensor from UST, Geschwenda, Germany [144] and MiCS-VZ-89TE from SGX Sensortech, Corcelles-Cormondreche, Switzerland [145]). Note that it is not easy to define reliable detection limits as the sensor response highly depends on the operation environment and specific applications. Nevertheless, these sensors are comparably fast with time constants of about 10 s and are all very small, cheap and ready for device integration.

**Table 7:** Comparison of the LOD and SNR values for different EG sensors and test gases at 150 °C at 0 %RH. The SNR was calculated based on 500 ppb exposures for all gases and the LOD was calculated based on 10 ppb for C<sub>6</sub>H<sub>6</sub> and CH<sub>2</sub>O, and 100 ppb for CO and NO<sub>2</sub>, respectively.

	SNR (dB)			
	LOD (ppb)			
	C <sub>6</sub> H <sub>6</sub>	CH <sub>2</sub> O	CO	NO <sub>2</sub>
PEG	0 0	0 0	32 3.80	88 0.01
Fe <sub>3</sub> O <sub>4</sub> NP DEG	16 3.97	22 2.71	/ /	64 <sup>13</sup> 0.15
Pt NP DEG	56 0.05	58 0.07	0 0	74 0.04
CuO NL DEG	31 0.86	33 0.90	20 14.34	61 0.23
Fe <sub>3</sub> O <sub>4</sub> NL DEG	26 1.54	26 1.42	19 12.29	77 0.03
V <sub>2</sub> O <sub>5</sub> NL DEG	25 3.90	27 2.73	19 16.73	56 0.46
ZrO <sub>2</sub> NL DEG	0 0	0 0	0 0	78 0.02
IEG	31 0.68	31 0.97	50 1.58 <sup>14</sup>	63 0.16

<sup>13</sup> Based on 15 min and 400 ppb exposure instead of 30 min and 500 ppb.

<sup>14</sup> Based on 500 ppb exposure instead of 10 ppb.

## 4.3 Advanced data evaluation

As mentioned earlier, a sensor with only good sensitivity is not sufficient and properties like stability, selectivity and speed of response need to be addressed as well. In this section, different methods are discussed on how to improve these parameters with smart sensor operation modes and enhanced data treatment.

### 4.3.1 First-order time-derivative signal

One method to achieve faster time constants is the use of the sensor signal's first-order time-derivative [21, 146]. In this section, the sensor response is evaluated based on the first-order time-derivative to introduce an alternative sensor signal. The response is calculated as

$$r_{dt} = R_{dt} - R_{0,dt} \quad (4.1)$$

where  $R_{dt}$  is the highest absolute derivative signal during a gas pulse and  $R_{0,dt}$  is the derivative baseline value before gas exposure. For most sensors, smoothening is necessary to eliminate the rapid fluctuations in the resistance value due to background noise. Here, a moving average filter with 10 points smoothening was used if not specified otherwise<sup>15</sup>.

Figure 4.16 shows the resistance over time of a Fe<sub>3</sub>O<sub>4</sub> NP DEG sensor (upper black line) when exposed for 15 min to different NO<sub>2</sub> concentrations similar to what is presented in [Paper 3]. It can be clearly seen that 15 min of exposure is not enough for the sensor to reach an equilibrated response. During the recovery time of 60 min, it was also not possible for the sensor to fully relax back to its initial baseline. This is a common problem for rather slow reacting sensors. If the signal is far from reaching an equilibrated response level during the exposure, it is not very reliable to calculate the real maximum response and the common time constants, such as  $\tau_{63}$  or  $\tau_{90}$ . Therefore, a direct comparison with sensor performances reported in literature and product specification sheets is not possible. To overcome these issues without adding more exposure or relaxation time, the first-order time-derivative of the sensor resistance is introduced as an additional sensor signal (see lower brown line in Figure 4.16).

---

<sup>15</sup> For more considerations regarding signal smoothening, confer the supplementary material of [Paper 3].

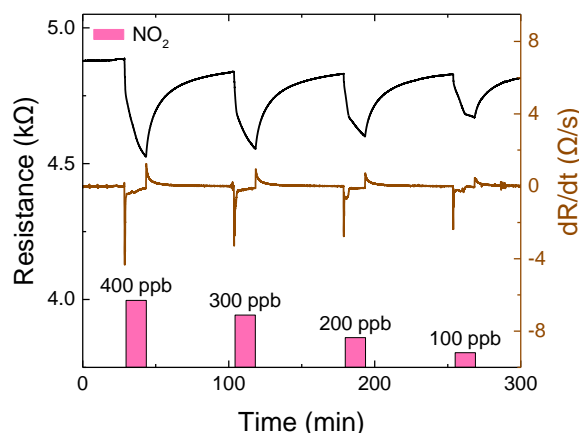


**Figure 4.16:** Resistance over time of  $\text{Fe}_3\text{O}_4$  NP DEG (black, upper) with its corresponding time-derivative (brown, lower) for  $\text{NO}_2$  exposures at  $150\text{ }^\circ\text{C}$  at  $0\text{ \%RH}$ . Adapted from [Paper 3].

The peaks of the first-order time-derivative signal arise much faster and are also concentration-dependent, which is in good agreement with Wu et al., stating that  $r_{dt}$  is directly proportional to the applied gas concentration [21]. This behavior is here exemplarily shown with the  $\text{Fe}_3\text{O}_4$  NP DEG sensor, but was also observed, for example, with the NL DEG or 2D Pt sensors. The desorption peak is concentration-dependent as well. However, the desorption response is normally not utilized as a standard indicator as it occurs after the adsorption, but it might be useful as a feature in multivariate statistics for selectivity enhancement [67, 147].

Because the peak of  $dR/dt$  is reached much faster, it is also more robust against not sufficiently long exposure or relaxation times. If the exposure time is not long enough for the sensor to reach an equilibrated response, the maximum response increases with increasing exposure time, potentially leading to a misquantification. As the first-order time-derivative of the resistance signal is the slope of the change, it should be independent of the exposure time (if the exposure time is long enough for  $dR/dt$  to reach its peak). Exactly this phenomenon can be seen in Figure 4.17 (a). The sensor response to  $50\text{ ppb}$   $\text{NO}_2$  increases from  $-1.2\text{ \%}$  after  $5\text{ min}$  to  $-2.8\text{ \%}$  after  $20\text{ min}$ . On the other hand,  $r_{dt}$  remains at approximately  $2.5\text{ }\Omega/\text{s}$ , with a slight increase after the third exposure, regardless of the exposure time. The constant time-derivative response is due to  $r_{dt}$  being determined by the initial adsorption/desorption phase during which the change in resistance is the highest. After this, further adsorption/desorption proceeds at a slower speed. Figure 4.17 (b) shows the sensor behavior with

## 4 Results and discussion

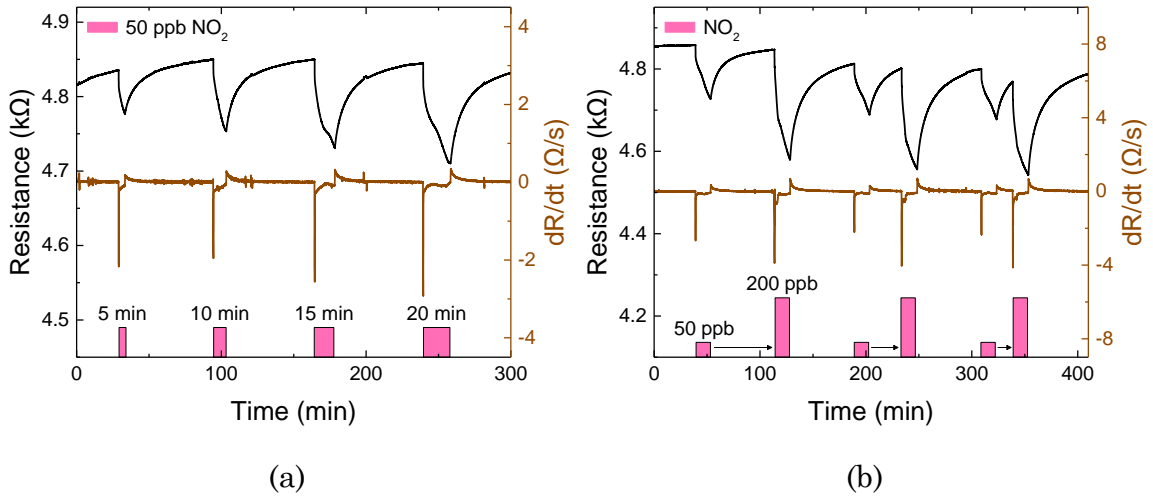


**Figure 4.17:** Resistance over time of Fe<sub>3</sub>O<sub>4</sub> NP DEG (black, upper) with its corresponding time-derivative (brown, lower) for NO<sub>2</sub> exposures at 150 °C at 0 %RH with different (a) exposure and (b) relaxation times. Adapted from [Paper 3].

decreasing relaxation times in between two gas exposures. Here, the sensor was repeatedly exposed for 15 min to 50 and 200 ppb NO<sub>2</sub> while altering the relaxation time from initially 60 down to 15 min after the 50 ppb exposure. If the sensor is not able to fully relax to its initial baseline between gas exposures, a drift is induced which could lead to a possible misquantification of the measured gas concentration. Using the standard sensor signal, the sensor is still able to distinguish between 50 and 200 ppb of NO<sub>2</sub> for all relaxation times. However, while the response to 50 ppb stays approximately constant (-2.6 %), the response to 200 ppb decreases from -5.5 to -4.7 % for 60 and 15 min relaxation time, respectively. This reduction in response is mainly due to the fact that the resistance does not return back to its initial baseline level with decreasing relaxation time. Therefore, the ratio between the responses at 200 and 50 ppb continuously decreases with a decrease in relaxation time. This is a clear sign that the sensor surface is not fully recovered, and, thus, not the same amount of adsorption sites is available for a reaction with NO<sub>2</sub> molecules at the second exposure. For the time-derivative signal, the ratio between the responses at 200 and 50 ppb stays approximately the same. This could be due to the baseline of the derivative signal relaxing much faster after the initial adsorption/desorption phase, while the change in the raw sensor signal occurs very slowly. Furthermore, the standard deviation of the responses to a given concentration changes drastically for the relative sensor responses. For the relative response to 50 ppb exposures it is only

about  $-2.6 \pm 0.08$  %, but it is with  $-5.1 \pm 0.38$  % almost five times higher for 200 ppb. For the time-derivative signal, the response changes for  $-2.4 \pm 0.20$   $\Omega/s$  and  $-4.0 \pm 0.13$   $\Omega/s$  for 50 and 200 ppb, respectively. This is a slightly larger relative fluctuation for the time-derivative signal, but without a large difference between the two concentrations. Therefore, it can be assumed that the time-derivative readout has a slightly worse uncertainty in general, but at least it is not negatively affected by sensor relaxation times.

It is known that not only the sensor response but also the speed of response heavily depends on the sensor temperature [20]. Also the first-order time-derivative signal was found to vary with a change in temperature. Moreover, it was found that the time-derivative response follows the same pattern as the standard response when adding UV irradiation or varying the amount of relative humidity between gas measurements. More interesting is the time needed to reach  $r_{dt}$ . For changes in operating temperature or additional UV irradiation  $\tau_{dt}$  stayed approximately constant but as shown in Figure 4.18,  $\tau_{dt}$  increases if more humidity is introduced (compare also [Paper 3]). This could be due to water molecules occupying possible reaction sites, i.e., a competition between  $H_2O$  and  $NH_3$  over available sites, or reactions between the two molecules to form ammonium and hydroxyl groups on the sensor surface, thus increasing the reaction time [65].

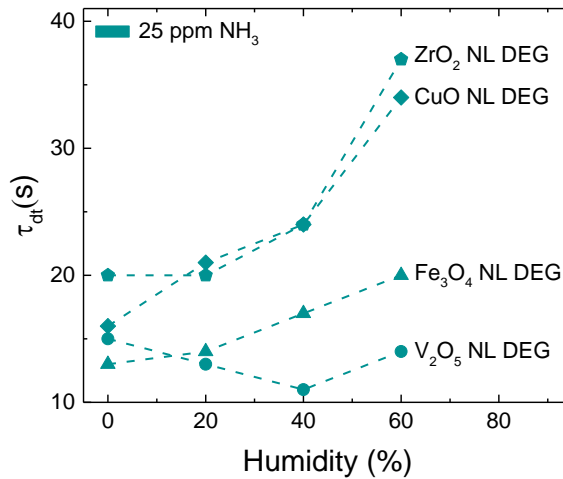


**Figure 4.18:**  $\tau_{dt}$  of first-order time-derivative responses of NL DEG sensors for 25 ppm  $NH_3$  exposures at 75 °C (except  $ZrO_2$  at 125 °C) at different RH based on [Paper 3].<sup>16</sup>

<sup>16</sup> Here,  $Fe_3O_4$  (0.05) is used as the measurement with  $Fe_3O_4$  (0.1) was flawed.

## 4 Results and discussion

Especially for indoor air quality monitoring, the sampling period should be rather fast, but at least within the range of a few minutes to allow real-time monitoring [17]. As already mentioned above, the peaks of the derivative signal reach their highest points already after a short period of time. Similar to Table 7, Table 8 gives an overview of the regular ( $\tau$ ) and derivative ( $\tau_{dt}$ ) time constants for different EG sensors and test gases at 150 °C at 0 %RH calculated from 500 ppb exposures. In case a sensor did not exhibit a response towards a specific gas, this is specified as n.a. (not applicable).  $\text{NH}_3$  is not included as not all sensors were exposed to ppb level concentrations, thus limiting the comparability with the other gases. In general,  $\tau_{dt}$  did not vary much between the different sensors and gases but stayed between 5 and  $10 \pm 5$  s. This, and the fact that it also did not vary for changes in operating temperature or UV irradiation, but only for variations in RH, is rather unexpected. It would fit the assumption that the initial material/gas-reaction takes place within the first 10 seconds of exposure and that the time-resolution, especially after signal smoothening, is not good enough to reveal occurring differences. Looking at the regular  $\tau$ , this does not apply and the different sensors have very different time constants, thus reaction behaviors, for specific gases. For example, all NL DEG sensors exhibit a faster response towards  $\text{C}_6\text{H}_6$  and  $\text{CH}_2\text{O}$  compared to  $\text{CO}$  and  $\text{NO}_2$ , with  $\text{NO}_2$  exhibiting the largest  $\tau$ , but PEG has a higher  $\tau$  for  $\text{CO}$  compared to  $\text{NO}_2$ . Comparing the differences between  $\tau$  and  $\tau_{dt}$ , for example, the  $\text{Fe}_3\text{O}_4$  NP DEG sensor to a  $\text{NO}_2$  exposure has a  $\tau_{dt}$  of about 10 s (Figure 4.16) which is 25 times faster compared to  $\tau$ . Other measurements suggest a decrease of time constants from approximately 350 s down to 10 s for measurements with the same sensor to  $\text{C}_6\text{H}_6$  and  $\text{CH}_2\text{O}$  [Paper 2]<sup>17</sup>. For a  $\text{TiO}_2$  NP DEG sample (not shown in Table 8), the time constants with oxygen measurements could be decreased from 1500 s down to 25 s [Paper 1]<sup>18</sup>. This is an improvement by a factor of 60 in response time compared to the standard resistance signal. In general, even the smallest observed improvement is already 15 times lower/faster.

---

<sup>17</sup> In [Paper 2],  $\tau_{dt}$  is specified with 50 s and smoothening was performed with 500 points. This was necessary, as the baseline signal exhibited strong noise.

<sup>18</sup> In [Paper 1],  $\tau_{dt}$  is specified with 60 s as smoothening was performed with 100 points.

**Table 8:** Comparison of the regular ( $\tau$ ) and derivative ( $\tau_{dt}$ ) time constants for different EG sensors and test gases at 150 °C at 0 %RH calculated from 500 ppb exposures. In case a sensor did not exhibit a response towards a specific gas, this is denoted as n.a. (not applicable).

	$\tau$ (s) $\pm$ 60			
	$\tau_{dt}$ (s) $\pm$ 5			
	C <sub>6</sub> H <sub>6</sub>	CH <sub>2</sub> O	CO	NO <sub>2</sub>
PEG	n.a.	n.a.	1500 10	425 5
Fe <sub>3</sub> O <sub>4</sub> NP DEG	350 10	350 10	n.a.	400 10 <sup>19</sup>
Pt NP DEG	425 5	475 5	n.a.	750 10
CuO NL DEG	150 10	175 5	250 5	300 5
Fe <sub>3</sub> O <sub>4</sub> NL DEG	175 10	175 5	200 5	375 5
V <sub>2</sub> O <sub>5</sub> NL DEG	425 10	375 5	700 10	800 10
ZrO <sub>2</sub> NL DEG	n.a.	n.a.	n.a.	650 10
IEG	475 5	200 5	475 20	475 5

<sup>19</sup> Based on 15 min and 400 ppb exposure instead of 30 min and 500 ppb.

## 4 Results and discussion

It should be noted that in practical applications of gas sensors, the change in the gas concentration in the environment is usually a slow-changing process and does not occur by leaps and bounds. Therefore, the first-order time-derivative signal might not give useful information for processes where the concentration change to be measured occurs slowly over time. To still apply this method, an option could be a sensor setup where an abrupt change in concentration is actively induced. This could, for example, be realized by changing between a reference and test gas flow. In stand-alone systems, this would require extra costs and space, as a defined reference flow would need to be established, for example through a reference gas reservoir and a pump. Nonetheless, there are still applications where this approach might be used even if an abrupt switch needs to be implemented either passively, e.g., for leak testing or battery system fault detection [148], or actively, e.g., with a valve switch between two existing gas streams. Another example would be the use of pre-concentrators, where the test gas is not continuously measured, but rather collected first and only released under defined conditions, e.g., degassing through heating [149]. Other possible applications where abrupt changes are monitored are, for example, measuring the gaseous by-product of biological processes or breath-analysis [150]. Furthermore, this method could also be used as an additional signal to create more transient data for multivariate statistical analysis [67, 147].

### 4.3.2 Multivariate analysis

As explained in section 3.4.2, one sensor alone is usually not able to distinguish between different gases very effectively, a sensor array can lead to a better classification [151]. However, when sensor arrays, physical or virtual, are used, more complex analysis methods are necessary to obtain useful results.

A very rudimentary example of an evaluation of a non-cyclic sensor response using LDA is shown in Figure 4.19. The evaluation was performed with the help of Tobias Baur at Saarland University. There, a sensor array of the four different NL DEG sensors was used at a constant temperature. Therefore, each measurement point is used as a feature as this is how it would be in a real setup, where the resistance over time is measured and gas exposures need to be determined. It is easily possible to distinguish between a strong-reacting gas and a weak-reacting one,  $\text{NO}_2$  and VOCs in

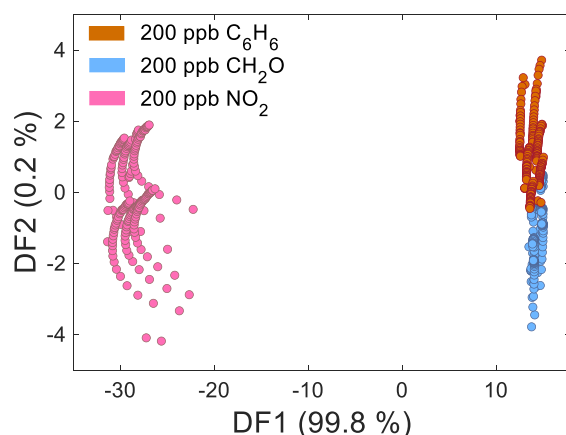


**Figure 4.19:** LDA based on all four NL DEG sensors for 200 ppb  $C_6H_6$ ,  $CH_2O$  and  $NO_2$  exposures at 150 °C at 0 %RH. Adapted from [Paper 4].

this case. But a similar response could still be achieved with different concentrations of different gases, leading to a not very meaningful sensor system. More details are discussed in [Paper 4].

One way to obtain additional transient data from a single sensor for evaluation is the application of cycled methods such as TCO [59, 151]. To study if the IEG sensor in TCO mode is able to distinguish between different, but similarly reacting gases and different RH levels, the sensor was exposed to 1000 and 500 ppb of  $C_6H_6$ ,  $CH_2O$ , CO and  $H_2$  at 0, 15, 30 and 40 %RH. The temperature was changed in plateaus from 30 s at 175 °C to 30 s at 150 °C to 40 s at 125 °C. The central temperature of the cycle was 150 °C because this was the main operating temperature of comparable measurements in this thesis. 175 °C was included to have a slightly higher temperature with expected stronger gas interaction, which was also observed to be operational without stability issues (compare section 3.3.2). To maximize the temperature interval 125 °C was chosen as the lowest temperature as temperatures below or around 100 °C with RH lead to additional slow sensor drift (compare section 4.2.2). Figure 4.20 (a) and (b) show the normalized and standardized temperature cycles, respectively, for all four gases and RH levels. The data treatment and evaluation was performed with the help of Guillem Domenèch Gil at Linköping University. As one can see, the normalized cycles exhibit differences for different gas exposures and RH levels (compare inset in Figure 4.20 (a)). The top three cycles of the 125 °C plateau correspond to air at the three non-zero RH levels studied, i.e., 15, 30 and 40 %RH, the lowest to dry air and the four in the middle to the four gases. For the four different gases, both VOCs

## 4 Results and discussion

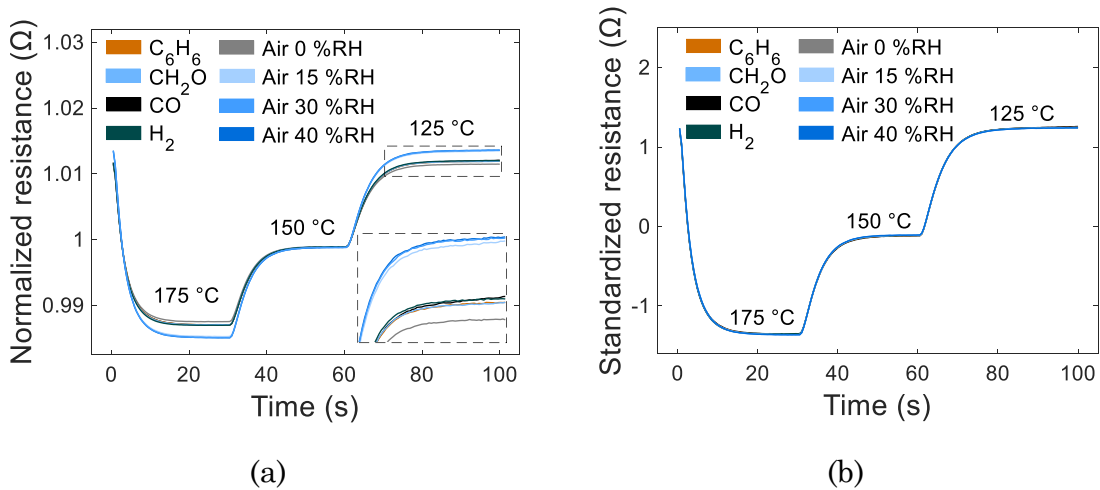


**Figure 4.20:** (a) Normalized and (b) standardized temperature cycles of IEG for C<sub>6</sub>H<sub>6</sub>, CH<sub>2</sub>O, CO and H<sub>2</sub> exposures and RH levels with temperature plateaus of 175, 150 and 125 °C. The inset in the lower right corner in (a) shows the enlarged normalized resistances of the 125 °C temperature plateau.

have almost exactly the same cycle shape, i.e., resistance value for the given temperature, whereas CO and H<sub>2</sub> have both distinguishably higher and lower resistances at the 125 and 175 °C temperature plateaus, respectively. If the cycles are standardized (Figure 4.20 (b)), only small differences can be appreciated between cycles, which only become visible if zooming in enough. The reason for this difference between normalization and standardization is because normalization divides the whole cycle by its own mean, thus centering all middle temperature plateaus at 1 and opening up the differences between the different cycles at the ends, i.e. lower and higher temperature plateaus. The standardization, however, centers the middle temperature plateau at 0 and, therefore, each plateau exhibits differences between the cycles but they are all comparably small. For further evaluation with LDA or PCA, this does not matter much as the used features will also be standardized, hence both preprocessing steps can lead to the same result. Here, only LDA and PCA results based on normalized cycles are shown. Similar measurements have been performed with PEG, but since it did not exhibit any response to both VOCs, the results are not discussed here.

To start with, it is worth looking at the different quasistatic plots. A quasistatic plot is obtained by plotting all points of all cycles at one given position in the temperature cycle. Here, one position was chosen at each

temperature plateau. Figure 4.21 (a), (b) and (c) show the untreated quasistatic plots, the normalized quasistatic plots and a zoom-in of the exposures at 0 %RH for the untreated quasistatic plots, respectively. The untreated quasistatic plots show changes in resistance, that correspond to the applied gas exposures and changes of RH. This could give valuable information about which temperature should be included in the cycle in general, in case strong difference would be observed. Here, since the temperatures are very close to each other, no strong differences between the three quasistatic plots can be seen. After normalization (Figure 4.21 (b)), the highest change observed is due to the increase of humidity, from 0 to 15 %RH, while an additional increase in RH and the gas exposures induce smaller changes. A similar distinct change can be seen at the end of the

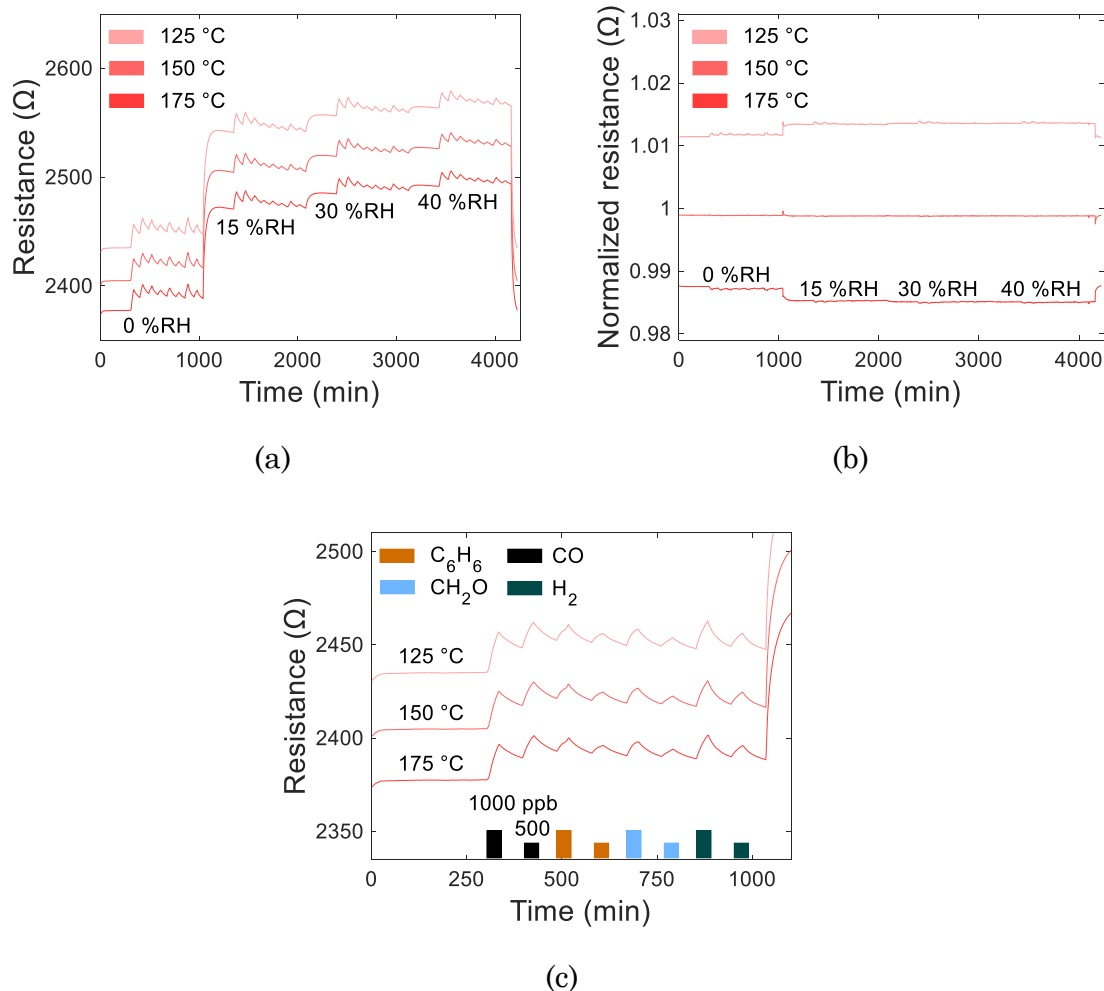


**Figure 4.21:** (a) Quasistatic and (b) normalized quasistatic plots of IEG for C<sub>6</sub>H<sub>6</sub>, CH<sub>2</sub>O, CO and H<sub>2</sub> exposures at 0, 15, 30 and 40 %RH at 175, 150 and 125 °C with (c) as zoom-in of the quasistatic plots for gas exposures at 0 %RH.

## 4 Results and discussion

measurement, when the RH level is changed back from 40 to 0 %RH. This is in agreement with the findings in section 4.2.2. In case that the standardized quasistatic plot would only be a flat line without any distinct features, then the TCO mode would not give additional information compared to the operation at a constant temperature.

After the first measurement evaluations through quasistatic plots, further multivariate statistic algorithms, i.e., LDA and PCA, were implemented to differentiate between the different gases. For the gases, the points corresponding to 500 ppb exposures at 0% RH were used. As features, part of the slopes between the three temperature plateaus and the lifting, i.e., absolute difference in resistance between the 125 and 175 °C plateaus, were utilized (compare Figure 4.22).

Figure 4.23 shows the results of LDA and PCA evaluations. Both methods can cluster the four gases, with LDA reaching a better cluster separation. However, both VOC clusters are very close to each other and not always distinguishable. Therefore, a TVOC indicator, i.e., the total amount of VOCs present, instead of single gas determinations, might be a more feasible application. Furthermore, since a steady state in the sensor response was never reached during the gas exposure, it is expected that the points corresponding to the same gas do not group very closely, forming widespread clusters. These results are a first approximation, as a proof-of-concept, similar to Figure 4.19, showing that this kind of EG sensors could potentially discriminate among different gases with further optimization.

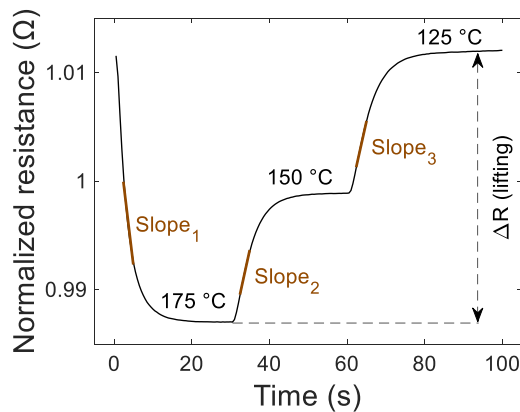


**Figure 4.22:** Exemplary normalized temperature cycle for CO exposure together with the used features.

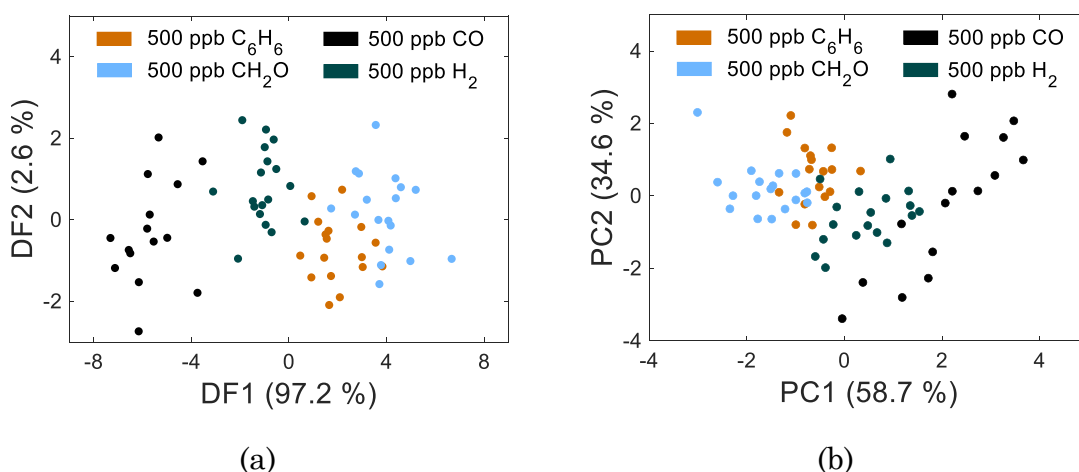


**Figure 4.23:** (a) LDA and (b) PCA of IEG to 500 ppb  $C_6H_6$ ,  $CH_2O$ , CO and  $H_2$  exposures at 0 %RH.

Besides classification, i.e., determination of the specific gas, quantification of the gas concentration was studied. Therefore, a PLSR was performed with the IEG sensor data for  $C_6H_6$  and  $CH_2O$  exposures with concentrations ranging from 2 (1 for  $CH_2O$ ) to 1000 ppb at 0 %RH. However, since the sensor response is rather slow and, consequently, does not reach a steady state even after 30 min exposure, the cycled operation mode does not help as only the last cycle of each exposure could be used for a concentration calibration. Another reason is very likely the chosen narrow temperature range as the physical and/or chemical surface reactions with the specific gases do not differ strongly at the different temperatures. Therefore, PLSR did not conclude in a meaningful evaluation, thus not giving an advantage compared to a static measurement (compare for example Figure 4.14).

In summary, applying TCO mode and multivariate statistics analysis methods lead to a differentiation between different gases. To fully exploit these methods, a broader operating temperature range would possibly improve the results, and also speed up the sensor response at higher temperatures to some extent.

## 4.4 Inter-lab studies

It is very important to conduct inter-lab studies to independently verify sensor performances as a specific setup itself can have a strong influence on the sensor behavior and, therefore, the obtained results may only be valid under given circumstances. In-depth studies have shown that even for measurements performed in certified labs, unexpected deviations can occur, which opens the possibility for more insight into sensor behavior in general [152, 153]. Unfortunately, round-robin testing, which is the standard in analytical chemistry to ensure that experimental procedures are correct, is still not applied in the field of chemical sensor research [154, 155].

To verify that the observed results are valid regardless of the lab-setting in this work, some measurements were first performed in the gas sensing lab at Linköping University (LiU) and then repeated in another lab at Saarland University (UdS) or vice versa. All measurements were performed at 150 °C operating temperature, but the tested gas concentrations and levels of relative humidity were not always exactly the same due to some restrictions of the respective systems. A summary of several different gas measurements with the NL DEG sensors at both laboratories is discussed in detail in [Paper 4].

In general, it was found that exposures to  $C_6H_6$  and  $CH_2O$  resulted in a systematically lower response if measured at UdS except for  $V_2O_5$ . Exposures to  $NO_2$  also showed the same trend in response for three of the four sensors, i.e., an increase with increased gas concentration and a decrease with the introduction of relative humidity, indicating that the sensors have very similar performances at both laboratories. Only the CuO NL DEG resulted in a rather peculiar change in response direction if exposed to 200 ppb  $NO_2$  at 25% RH at LiU, compared to the exposure at 0% RH. This change could be due to the competing effects of  $NO_2$  and RH on the sensor surface.

In a different investigation, the  $Fe_3O_4$  NP DEG sensor was evaluated first with one setup at UdS and then one year later with another setup in the same laboratory<sup>20</sup>. At both times, the sensor was exposed for 30 min to 5 ppb of  $C_6H_6$  at 150 °C and 0 %RH (compare section 4.2.4 and [Paper 2]). The response varied between 0.05 % and 0.08 %. This might seem like a

---

<sup>20</sup> Note that this measurement was rather an intra-lab than an inter-lab study.

large difference, but taking into account that the sensor was not calibrated for one system and was operated over a long time, the repeatability is rather good.

Additional differences in sensor response could arise from the uncertainties in concentration of the gas bottles. Even with a purity of 6.0, each gas bottle has an approximate error range in concentration of up to  $\pm 10\%$ . Moreover, the background gas (purity of 6.0) used for mixing of test gases also still contains approximately 1 ppm of contaminants. Therefore, a higher target analyte concentration in a gas cylinder results in a lower relative error as a smaller concentration if both are diluted in the gas mixing system to reach the same concentration. This uncertainty in gas concentrations is believed to be the main impact on the observed responses here. Different background gases could also lead to differences between both labs. The background gas at LiU is mixed from 80 %  $\text{N}_2$  (liquid source) and 20 %  $\text{O}_2$ , while the background gas at UdS comes from a zero air generator (79 %  $\text{N}_2$  and 21 %  $\text{O}_2$ ), but these differences are not believed to have a major impact here (compare section 3.5.1). A difference in response due to a different background gas flow, i.e., 100 ml/min at LiU and 200 ml/min at UdS, is not expected. However, the systems could be contaminated by prior gas exposures [156]<sup>21</sup>. Another problem could come from the applied flows from the MFCs, although this is rather unlikely as only calibrated MFCs were used and frequently reassessed. A variation due to the very small difference in background humidity is also not expected (compare section 3.5). Another very important aspect is the electric noise of the laboratory environment and the resolution of the readout hardware. In early measurements at UdS the resistance-readout was done with the 3S-board, while the measurements at LiU were always carried out with a Sourcemeter. The SNR for a 5 ppb  $\text{C}_6\text{H}_6$  exposure varied for the  $\text{Fe}_3\text{O}_4$  NP DEG from 1.6 dB to 35 dB, depending on the setup, with the Sourcemeter hardware being the superior solution. Looking only at the single standard deviation of the baseline resistance as indicator of noise when a Sourcemeter is used in both laboratories, there was no distinct difference in noise level anymore and it stayed below 0.1  $\Omega$  for all four NL DEG sensors for example, which corresponds to a worst-case relative noise level of approximately 0.007% in terms of sensor response.

---

<sup>21</sup> The gas mixing system at LiU was entirely cleaned and calibrated before low concentration measurements with VOCs have been performed as a contamination of the system was previously determined.

## 4.5 More EG sensor applications

Even if the main focus of this work was to investigate EG on SiC as versatile gas sensing platform, sensing with this material is not limited to gaseous analytes. In this section, a short outlook to other sensing fields is given that were investigated with EG on SiC.

In its pristine form, EG is rather inert, but it does not need to chemically bind to an analyte to be able to detect its presence. When an ion, e.g., a dissolved heavy metal ion, is in physical contact with the graphene lattice, the local doping changes and thus a change in resistance can be measured. For example, when pumping a solution with diluted heavy metal ions through a lab-on-chip device over the graphene lattice, the resistance of graphene changes as soon as the dissolved ions come in contact with the exposed graphene surface in the detection chamber, resembling a reaction to specific heavy metal ions [157]. With this approach, heavy metals like lead can be detected at very low concentration, i.e., 95 nM for  $\text{Pb}^{2+}$  ions, and, as the response is geometry dependent, a larger relative EG exposure area is expected to further increase the sensitivity, thus further decreasing the detection limit [158]. Note that the required recommended limit for lead ions in drinking water by the WHO is 180 nM [159], so about twice as high as the achieved LOD here.

Another advancement is the use of epitaxial graphene in bio-inspired applications, such as the detection of certain proteins. It was demonstrated that when exposed to HSA (human serum albumin) diluted in PBS (Phosphate-buffered saline) buffer, the sensor reacts rather fast to the analyte exposure with a stable baseline and the response is repeatable [160]. The idea is to eventually substitute HSA with other proteins that are important for medical applications where the exact determination of analytes reflects the health status. A similar approach is used for a rather new study, where EG is used to detect toxic dioxins in a buffer solution, but instead of a simple dilution process, electrophoresis is used additionally to separate molecules and isolate the target analyte.

As already mentioned, EG can also be used as the transducer and not the primary sensing material. Another side-project investigated the possible detection of bark beetle pheromones, in the perspective of a sensor for early detection of bark beetle infestation in spruce forests. Fresh bark beetle antennas should detect the pheromones and transfer this detection via an ionic gel onto the graphene surface. There, the change in resistance

between two contacts should then resemble the difference between ambient air and ambient air with pheromones present. More can be found in [161].

All these projects are examples of what might be possible when detecting low concentrations of specific analytes with EG on SiC as the transducer or even sensing material. There will be a paper giving an overview about all these different EG sensors, but it was not published by the time of printing of this thesis.



## 5 Conclusions and outlook

In summary, the work presented in this thesis focused on how to utilize epitaxially grown graphene on SiC as an ultra-sensitive gas sensor platform for gases of interest for air quality monitoring. Three main approaches have been tested and evaluated to their impacts on sensitivity, selectivity, speed of response and stability of the graphene based sensors.

First, the graphene surface was modified with several different methods. It was decorated with different metal oxide nanoparticles and nanolayers, intercalated with hydrogen, or defects have been introduced with Ag<sup>+</sup> ion bombardment. With most of the decorated sensors, it was easily possible to detect and quantitatively measure concentrations down to single ppb of benzene and formaldehyde and their limits of detection can be even in the ppt range. VOC detection was possible with relative humidity in the ambient only after platinum decoration or hydrogen intercalation though, making these materials very promising for air quality monitoring applications. The integrity of the graphene lattice was maintained after surface decoration, which was verified for each sample using characterization methods like atomic force microscopy and Raman spectroscopy.

The second approach is the optimization of the sensing environment. Here, the influence of operating temperature, relative humidity and additional UV irradiation during the measurement was evaluated. All three parameters are well known to have a strong impact on the sensor sensitivity and speed of response for some material/gas combinations.

As a last step, generation of richer data and extended data evaluation led to a better sensor performance. The first-order time-derivative was investigated as an additional sensor signal. With this approach, the time constants could be drastically reduced as the peak of slope reaches its maximum much faster compared to the resistance value, which opens an opportunity for rather slow gas sensors in areas where a fast sensor readout is compulsory. Moreover, reduced time constants can save lab testing time, thus saving time, resources and money during research activities. This peak is concentration dependent and almost independent of exposure and relaxation times. If operated in temperature cycled operation mode, it was possible to distinguish between different gases, thus increasing selectivity.

Furthermore, some sensors have been evaluated at two independent laboratories to ensure the reliability of the obtained results.

## 5 Conclusions and outlook

All three investigated methods show very promising results to improve sensing performance and a combination of them opens new fields of possible applications. To fully exploit the potential of these epitaxial graphene based sensors, more work in terms of production optimization, method combination and application-specific testing would need to be done. For example, to stay within the idea of AQM, measurements with normal air, i.e., air with various contaminants, as background and not zero air should be investigated, higher temperature ranges for cycled operation established and sensors processed with a glue-less contact mechanism.

# References

- [1] World Health Organisation, *Ambient air pollution: A global assessment of exposure and burden of disease*. Geneva, 2016.
- [2] World Health Organisation, “Ambient air pollution - a major threat to health and climate,” 2020. <https://www.who.int/airpollution/ambient/en/> (accessed Mar. 28, 2021).
- [3] World Health Organisation, “WHO Social media toolkit for Air pollution and Child Health: Prescribing Clean Air Launch,” Geneva, 2018. [Online]. Available: <https://www.who.int/ceh/publications/air-pollution-child-health/en/>.
- [4] P. S. Burge, “Sick building syndrome,” *Occup. Environ. Med.*, vol. 61, no. 2, 2004, doi: 10.1136/oem.2003.008813.
- [5] The World Bank, “The Cost of Air Pollution: Strengthening the Economic Case for Action,” Washington, 2016.
- [6] A. Farrow, K. A. Miller, and L. Myllyvirta, “Toxic air: The price of fossil fuels,” Seoul, 2020.
- [7] B. Szulczyński and J. Gębicki, “Currently Commercially Available Chemical Sensors Employed for Detection of Volatile Organic Compounds in Outdoor and Indoor Air,” *Environments*, vol. 4, no. 1, p. 21, 2017, doi: 10.3390/environments4010021.
- [8] L. Spinelle, M. Gerboles, G. Kok, S. Persijn, and T. Sauerwald, “Review of portable and low-cost sensors for the ambient air monitoring of benzene and other volatile organic compounds,” *Sensors (Switzerland)*, vol. 17, no. 7. 2017, doi: 10.3390/s17071520.
- [9] L. Jiang, “Environmental Gas Sensors 2020-2030: Technologies, manufacturers, forecasts,” 2020.
- [10] R. Pearce, J. Eriksson, T. Iakimov, L. Hultman, A. Lloyd Spetz, and R. Yakimova, “On the differing sensitivity to chemical gating of single and double layer epitaxial graphene explored using scanning kelvin probe microscopy,” *ACS Nano*, vol. 7, no. 5, pp. 4647–4656, 2013, doi: 10.1021/nn3052633.
- [11] C. Anichini, W. Czepa, D. Pakulski, A. Aliprandi, A. Ciesielski, and P. Samorì, “Chemical sensing with 2D materials,” *Chem. Soc. Rev.*, vol. 47, no. 13, pp. 4860–4908, 2018, doi: 10.1039/c8cs00417j.
- [12] M. Kodu, A. Berholts, T. Kahro, J. Eriksson, R. Yakimova, T. Avarmaa, I. Renge, H. Alles, and R. Jaaniso, “Graphene-Based Ammonia Sensors Functionalised with Sub-Monolayer V<sub>2</sub>O<sub>5</sub>: A Comparative Study of Chemical Vapour Deposited and Epitaxial Graphene,” *Sensors*, vol. 19, no. 4, pp. 1–17, 2019, doi: 10.3390/s19040951.

## References

- [13] R. Malik, V. K. Tomer, Y. K. Mishra, and L. Lin, “Functional gas sensing nanomaterials: A panoramic view,” *Appl. Phys. Rev.*, vol. 7, no. 2, 2020, doi: 10.1063/1.5123479.
- [14] F. L. Meng, Z. Guo, and X. J. Huang, “Graphene-based hybrids for chemiresistive gas sensors,” *TrAC - Trends Anal. Chem.*, vol. 68, pp. 37–47, 2015, doi: 10.1016/j.trac.2015.02.008.
- [15] S. Gupta Chatterjee, S. Chatterjee, A. K. Ray, and A. K. Chakraborty, “Graphene-metal oxide nanohybrids for toxic gas sensor: A review,” *Sensors Actuators, B Chem.*, vol. 221, no. 2, pp. 1170–1181, 2015, doi: 10.1016/j.snb.2015.07.070.
- [16] J. Eriksson, D. Puglisi, C. Strandqvist, R. Gunnarsson, S. Ekeröth, I. G. Ivanov, U. Helmersson, K. Uvdal, R. Yakimova, and A. Lloyd Spetz, “Modified epitaxial graphene on SiC for extremely sensitive and selective gas sensors,” *Mater. Sci. Forum*, vol. 858, pp. 1145–1148, 2016, doi: 10.4028/www.scientific.net/MSF.858.1145.
- [17] B. Timmer, W. Olthuis, and A. Van Den Berg, “Ammonia sensors and their applications - A review,” *Sensors Actuators, B Chem.*, vol. 107, no. 2, pp. 666–677, 2005, doi: 10.1016/j.snb.2004.11.054.
- [18] S. Batterman, S. Chambliss, and V. Isakov, “Spatial resolution requirements for traffic-related air pollutant exposure evaluations,” *Atmos. Environ.*, vol. 94, pp. 518–528, 2014, doi: 10.1016/j.atmosenv.2014.05.065.
- [19] E. Espid and F. Taghipour, “UV-LED Photo-activated Chemical Gas Sensors: A Review,” *Crit. Rev. Solid State Mater. Sci.*, vol. 42, no. 5, pp. 416–432, 2017, doi: 10.1080/10408436.2016.1226161.
- [20] C. Schultealbert, T. Baur, A. Schütze, S. Böttcher, and T. Sauerwald, “A novel approach towards calibrated measurement of trace gases using metal oxide semiconductor sensors,” *Sensors Actuators B Chem.*, vol. 239, pp. 390–396, 2017, doi: <http://dx.doi.org/10.1016/j.snb.2016.08.002>.
- [21] C. H. Wu, G. J. Jiang, C. C. Chiu, P. Chong, C. C. Jeng, R. J. Wu, and J. H. Chen, “Fast gas concentration sensing by analyzing the rate of resistance change,” *Sensors Actuators, B Chem.*, vol. 209, pp. 906–910, 2015, doi: 10.1016/j.snb.2014.12.066.
- [22] A. P. Lee and B. J. Reedy, “Temperature modulation in semiconductor gas sensing,” *Sensors Actuators, B Chem.*, vol. 60, no. 1, pp. 35–42, 1999, doi: 10.1016/S0925-4005(99)00241-5.
- [23] A. D’Amico, C. Di Natale, and P. M. Sarro, “Ingredients for sensors science,” *Sensors Actuators, B Chem.*, vol. 207, no. PB, pp. 1060–1068, 2015, doi: 10.1016/j.snb.2014.07.065.
- [24] P. T. Mosely and B. C. Tofield, “Semiconductor gas sensors,” *Sensors and Actuators*, vol. 1, no. July, pp. 505–509, 1985, doi: 10.1016/0250-6874(81)80054-6.

- [25] A. Dey, “Semiconductor metal oxide gas sensors: A review,” *Mater. Sci. Eng. B Solid-State Mater. Adv. Technol.*, vol. 229, no. November 2017, pp. 206–217, 2018, doi: 10.1016/j.mseb.2017.12.036.
- [26] C. Wang, L. Yin, L. Zhang, D. Xiang, and R. Gao, “Metal oxide gas sensors: Sensitivity and influencing factors,” *Sensors*, vol. 10, no. 3, pp. 2088–2106, 2010, doi: 10.3390/s100302088.
- [27] M. J. Madou and S. R. Morrison, *Chemical Sensing with Solid State Devices*. San Diego: Academic Press, 1989.
- [28] N. Barsan, D. Koziej, and U. Weimar, “Metal oxide-based gas sensor research: How to?,” *Sensors Actuators, B Chem.*, vol. 121, no. 1, pp. 18–35, 2007, doi: 10.1016/j.snb.2006.09.047.
- [29] K. S. Novoselov, A. K. Geim, S. V. Morozov, D. Jiang, Y. Zhang, S. V. Dubonos, I. V. Grigorieva, and A. A. Firsov, “Electric Field Effect in Atomically Thin Carbon Films,” *Science (80-. )*, vol. 306, pp. 666–669, 2004, doi: 10.1126/science.1102896.
- [30] F. Bonaccorso, Z. Sun, T. Hasan, and A. C. Ferrari, “Graphene photonics and optoelectronics,” *Nat. Photonics*, vol. 4, no. 9, pp. 611–622, 2010, doi: 10.1038/nphoton.2010.186.
- [31] A. H. Castro Neto, F. Guinea, N. M. R. Peres, K. S. Novoselov, and A. K. Geim, “The electronic properties of graphene,” *Rev. Mod. Phys.*, vol. 81, no. 1, pp. 109–162, 2009, doi: 10.1103/RevModPhys.81.109.
- [32] J. Lloyd-Hughes and T. I. Jeon, “A review of the terahertz conductivity of bulk and nano-materials,” *J. Infrared, Millimeter, Terahertz Waves*, vol. 33, no. 9, pp. 871–925, 2012, doi: 10.1007/s10762-012-9905-y.
- [33] A. Nag, A. Mitra, and S. C. Mukhopadhyay, “Graphene and its sensor-based applications: A review,” *Sensors Actuators, A Phys.*, vol. 270, pp. 177–194, 2018, doi: 10.1016/j.sna.2017.12.028.
- [34] J. Huang, J. A. Alexander-Webber, A. M. R. Baker, T. J. B. M. Janssen, A. Tzalenchuk, V. Antonov, T. Yager, S. Lara-Avila, S. Kubatkin, R. Yakimova, and R. J. Nicholas, “Disorder induced Dirac-point physics in epitaxial graphene from temperature-dependent magneto-transport measurements,” *Phys. Rev. B - Condens. Matter Mater. Phys.*, vol. 92, no. 7, pp. 1–6, 2015, doi: 10.1103/PhysRevB.92.075407.
- [35] E. Mostaani, N. D. Drummond, and V. I. Fal’ko, “Quantum Monte Carlo Calculation of the Binding Energy of Bilayer Graphene,” *Phys. Rev. Lett.*, vol. 115, no. 11, pp. 1–5, 2015, doi: 10.1103/PhysRevLett.115.115501.
- [36] Yomach, “Graphene Brillouin Zone & Linear Dispersion,” 2014. [https://commons.wikimedia.org/wiki/File:Graphene\\_Brillouin\\_Zone\\_%26\\_Linear\\_Dispersion.PNG](https://commons.wikimedia.org/wiki/File:Graphene_Brillouin_Zone_%26_Linear_Dispersion.PNG) (accessed Mar. 28, 2021).

## References

- [37] G. R. Yazdi, R. Vasiliauskas, T. Iakimov, A. Zakharov, M. Syväjärvi, and R. Yakimova, “Growth of large area monolayer graphene on 3C-SiC and a comparison with other SiC polytypes,” *Carbon N. Y.*, vol. 57, pp. 477–484, 2013, doi: 10.1016/j.carbon.2013.02.022.
- [38] W. F. Knippenberg, “Growth Phenomena in Silicon Carbide,” *Philips Res. Reports*, vol. 18, no. R480, pp. 161–274, 1963.
- [39] C. Virojanadara, M. Syväjärvi, R. Yakimova, L. I. Johansson, A. A. Zakharov, and T. Balasubramanian, “Homogeneous large-area graphene layer growth on 6H-SiC(0001),” *Phys. Rev. B - Condens. Matter Mater. Phys.*, vol. 78, no. 24, pp. 1–6, 2008, doi: 10.1103/PhysRevB.78.245403.
- [40] U. Starke and C. Riedl, “Epitaxial graphene on SiC(0001) and SiC(000-1): from surface reconstructions to carbon electronics,” *J. Phys. Condens. Matter*, vol. 21, no. 13, 2009, doi: 10.1088/0953-8984/21/13/134016.
- [41] K. von Klitzing, “The quantized Hall effect,” *Rev. Mod. Phys.*, vol. 58, no. 3, pp. 519–531, 1986, doi: 10.1103/RevModPhys.58.519.
- [42] A. Tzalenchuk, S. Lara-Avila, A. Kalaboukhov, S. Paolillo, M. Syväjärvi, R. Yakimova, O. Kazakova, T. J. B. M. Janssen, V. Fal’ko, and S. Kubatkin, “Towards a quantum resistance standard based on epitaxial graphene,” *Nat. Nanotechnol.*, vol. 5, no. 3, pp. 186–189, 2010, doi: 10.1038/nnano.2009.474.
- [43] M. Beshkova, L. Hultman, and R. Yakimova, “Device applications of epitaxial graphene on silicon carbide,” *Vacuum*, vol. 128, pp. 186–197, 2016, doi: 10.1016/j.vacuum.2016.03.027.
- [44] I. Razado-Colambo, J. Avila, D. Vignaud, S. Godey, X. Wallart, D. P. Woodruff, and M. C. Asensio, “Structural determination of bilayer graphene on SiC(0001) using synchrotron radiation photoelectron diffraction,” *Sci. Rep.*, vol. 8, no. 1, pp. 1–10, 2018, doi: 10.1038/s41598-018-28402-0.
- [45] S. V. Kopylov, A. Tzalenchuk, S. Kubatkin, and V. I. Fal’ko, “Charge transfer between epitaxial graphene and silicon carbide,” *Appl. Phys. Lett.*, vol. 97, no. 11, pp. 11–14, 2010, doi: 10.1063/1.3487782.
- [46] C. Riedl, C. Coletti, T. Iwasaki, A. A. Zakharov, and U. Starke, “Quasi-free-standing epitaxial graphene on SiC obtained by hydrogen intercalation,” *Phys. Rev. Lett.*, vol. 103, no. 24, pp. 1–4, 2009, doi: 10.1103/PhysRevLett.103.246804.
- [47] I. Shtepliuk, I. G. Ivanov, T. Iakimov, R. Yakimova, A. Kakanakova-Georgieva, P. Fiorenza, and F. Giannazzo, “Raman probing of hydrogen-intercalated graphene on Si-face 4H-SiC,” *Mater. Sci. Semicond. Process.*, vol. 96, pp. 145–152, 2019, doi: 10.1016/j.mssp.2019.02.039.

- [48] K. S. Novoselov, A. K. Geim, S. V. Morozov, D. Jiang, M. I. Katsnelson, I. V. Grigorieva, S. V. Dubonos, and A. A. Firsov, "Two-dimensional gas of massless Dirac fermions in graphene," *Nature*, vol. 438, no. 7065, pp. 197–200, 2005, doi: 10.1038/nature04233.
- [49] G. Liu, W. Stillman, S. Rumyantsev, Q. Shao, M. Shur, and A. A. Balandin, "Low-frequency electronic noise in the double-gate single-layer graphene transistors," *Appl. Phys. Lett.*, vol. 95, no. 3, pp. 1–4, 2009, doi: 10.1063/1.3180707.
- [50] M. Pumera, A. Ambrosi, A. Bonanni, E. L. K. Chng, and H. L. Poh, "Graphene for electrochemical sensing and biosensing," *TrAC - Trends Anal. Chem.*, vol. 29, no. 9, pp. 954–965, 2010, doi: 10.1016/j.trac.2010.05.011.
- [51] F. Schedin, A. K. Geim, S. V. Morozov, E. W. Hill, P. Blake, M. I. Katsnelson, and K. S. Novoselov, "Detection of individual gas molecules adsorbed on graphene," *Nat. Mater.*, vol. 6, no. 9, pp. 652–655, 2007, doi: 10.1038/nmat1967.
- [52] F. Yavari, E. Castillo, H. Gullapalli, P. M. Ajayan, and N. Koratkar, "High sensitivity detection of NO<sub>2</sub> and NH<sub>3</sub> in air using chemical vapor deposition grown graphene," *Appl. Phys. Lett.*, vol. 100, no. 20, 2012, doi: 10.1063/1.4720074.
- [53] S. S. Varghese, S. Lonkar, K. K. Singh, S. Swaminathan, and A. Abdala, "Recent advances in graphene based gas sensors," *Sensors Actuators, B Chem.*, vol. 218, pp. 160–183, 2015, doi: 10.1016/j.snb.2015.04.062.
- [54] N. Briggs, Z. M. Gebeyehu, A. Vera, T. Zhao, K. Wang, A. De La Fuente Duran, B. Bersch, T. Bowen, K. L. Knappenberger, and J. A. Robinson, "Epitaxial graphene/silicon carbide intercalation: A minireview on graphene modulation and unique 2D materials," *Nanoscale*, vol. 11, no. 33, pp. 15440–15447, 2019, doi: 10.1039/c9nr03721g.
- [55] Y. You, J. Deng, X. Tan, N. Gorjizadeh, M. Yoshimura, S. C. Smith, V. Sahajwalla, and R. K. Joshi, "On the mechanism of gas adsorption for pristine, defective and functionalized graphene," *Phys. Chem. Chem. Phys.*, vol. 19, no. 8, pp. 6051–6056, 2017, doi: 10.1039/c6cp07654h.
- [56] Y. H. Zhang, Y. Bin Chen, K. G. Zhou, C. H. Liu, J. Zeng, H. L. Zhang, and Y. Peng, "Improving gas sensing properties of graphene by introducing dopants and defects: A first-principles study," *Nanotechnology*, vol. 20, no. 18, 2009, doi: 10.1088/0957-4484/20/18/185504.
- [57] A. Berholts, T. Kahro, A. Floren, H. Alles, and R. Jaaniso, "Photo-activated oxygen sensitivity of graphene at room temperature," *Appl. Phys. Lett.*, vol. 105, no. 16, 2014, doi: 10.1063/1.4899276.

## References

- [58] C. Bur, “Selectivity Enhancement of Gas Sensitive Field Effect Transistors by Dynamic Operation,” Saarland University, Saarbrücken, 2015.
- [59] C. Bur, M. Bastuck, D. Puglisi, A. Schütze, A. Lloyd Spetz, and M. Andersson, “Discrimination and quantification of volatile organic compounds in the ppb-range with gas sensitive SiC-FETs using multivariate statistics,” in *Sensors and Actuators, B: Chemical*, 2015, vol. 214, pp. 225–233, doi: 10.1016/j.snb.2015.03.016.
- [60] M. Rodner, M. Bastuck, A. Schütze, M. Andersson, J. Huotari, J. Puustinen, J. Lappalainen, and T. Sauerwald, “Enabling a new method of dynamic field-effect gas sensor operation through lithium-doped tungsten oxide,” *J. Sensors Sens. Syst.*, vol. 8, no. 2, pp. 261–267, 2019, doi: 10.5194/jsss-8-261-2019.
- [61] E. Gonzalez, E. Llobet, A. Romero, and X. Vilanova, “A New Approach to NO<sub>2</sub> Gas Sensing Based on Pulsed UV Light and FFT Analysis Using MOX Sensors,” *IEEE Sens. J.*, vol. 20, no. 1, pp. 397–404, 2020, doi: 10.1109/JSEN.2019.2942490.
- [62] F. Yavari and N. Koratkar, “Graphene-based chemical sensors,” *J. Phys. Chem. Lett.*, vol. 3, no. 13, pp. 1746–1753, 2012, doi: 10.1021/jz300358t.
- [63] A. Di Bartolomeo, “Graphene Schottky diodes: An experimental review of the rectifying graphene/semiconductor heterojunction,” *Phys. Rep.*, vol. 606, pp. 1–58, 2016, doi: 10.1016/j.physrep.2015.10.003.
- [64] S. Y. Zhou, G. H. Gweon, A. V. Fedorov, P. N. First, W. A. De Heer, D. H. Lee, F. Guinea, A. H. Castro Neto, and A. Lanzara, “Substrate-induced bandgap opening in epitaxial graphene,” *Nat. Mater.*, vol. 6, no. 10, pp. 770–775, 2007, doi: 10.1038/nmat2003.
- [65] N. Barsan and U. Weimar, “Conduction model of metal oxide gas sensors,” *J. Electroceramics*, vol. 7, pp. 143–167, 2001, doi: 10.1023/A:1014405811371.
- [66] Y. F. Sun, S. B. Liu, F. L. Meng, J. Y. Liu, Z. Jin, L. T. Kong, and J. H. Liu, “Metal oxide nanostructures and their gas sensing properties: A review,” *Sensors*, vol. 12, no. 3, pp. 2610–2631, 2012, doi: 10.3390/s120302610.
- [67] S. Marco and A. Gutierrez-Galvez, “Signal and data processing for machine olfaction and chemical sensing: A review,” *IEEE Sens. J.*, vol. 12, no. 11, pp. 3189–3214, 2012, doi: 10.1109/JSEN.2012.2192920.
- [68] M. Bastuck, “Improving the Performance of Gas Sensor Systems with Advanced Data Evaluation, Operation, and Calibration Methods,” Linköping University, 2019.

- [69] A. Gramm and A. Schütze, “High performance solvent vapor identification with a two sensor array using temperature cycling and pattern classification,” *Sensors Actuators B Chem.*, vol. 95, no. 1–3, pp. 58–65, 2003, doi: 10.1016/S0925-4005(03)00404-0.
- [70] R. Gutierrez-Osuna, “Pattern analysis for machine olfaction: A review,” *IEEE Sens. J.*, vol. 2, no. 3, pp. 189–202, 2002, doi: 10.1109/JSEN.2002.800688.
- [71] R. Duda, P. Hart, and D. Stork, *Pattern Classification*. John Wiley & Sons, 2001.
- [72] R. A. Fisher, “The Use of Multiple Measurements in Taxonomic Problems,” *Ann. Eugen.*, vol. 7, no. 2, pp. 179–188, 1936, doi: 10.1111/j.1469-1809.1936.tb02137.x.
- [73] D. Depla, S. Mahieu, and J. E. Greene, “Sputter Deposition Processes,” in *Handbook of Deposition Technologies for Films and Coatings*, Third., P. M. Martin, Ed. Elsevier, 2010, pp. 253–296.
- [74] Y. Yamamura and H. Tawara, “Energy dependence of ion-induced sputtering yields from monatomic solids at normal incidence,” *At. Data Nucl. Data Tables*, vol. 62, no. 2, pp. 149–253, 1996, doi: 10.1006/adnd.1996.0005.
- [75] M. Ohring, *Materials Science of Thin Films*. Academic Press, 1992.
- [76] I. Pilch, D. Söderström, N. Brenning, and U. Helmersson, “Size-controlled growth of nanoparticles in a highly ionized pulsed plasma,” *Appl. Phys. Lett.*, vol. 102, no. 3, 2013, doi: 10.1063/1.4788739.
- [77] R. Gunnarsson, U. Helmersson, and I. Pilch, “Synthesis of titanium-oxide nanoparticles with size and stoichiometry control,” *J. Nanoparticle Res.*, vol. 17, no. 9, pp. 1–11, 2015, doi: 10.1007/s11051-015-3158-3.
- [78] M. Rodner, “Lithium doped tungsten oxide films for gas sensor applications,” Saarland University, 2016.
- [79] G. S. Bumbrah and R. M. Sharma, “Raman spectroscopy – Basic principle, instrumentation and selected applications for the characterization of drugs of abuse,” *Egypt. J. Forensic Sci.*, vol. 6, no. 3, pp. 209–215, 2016, doi: 10.1016/j.ejfs.2015.06.001.
- [80] L. M. Malard, M. A. Pimenta, G. Dresselhaus, and M. S. Dresselhaus, “Raman spectroscopy in graphene,” *Phys. Rep.*, vol. 473, no. 5–6, pp. 51–87, 2009, doi: 10.1016/j.physrep.2009.02.003.
- [81] I. G. Ivanov, J. U. Hassan, T. Iakimov, A. A. Zakharov, R. Yakimova, and E. Janzén, “Layer-number determination in graphene on SiC by reflectance mapping,” *Carbon N. Y.*, vol. 77, pp. 492–500, 2014, doi: 10.1016/j.carbon.2014.05.054.

## References

- [82] I. Shtepliuk, I. G. Ivanov, N. Pliatsikas, T. Iakimov, A. Jamnig, K. Sarakinos, and R. Yakimova, “Probing the uniformity of silver-doped epitaxial graphene by micro-Raman mapping,” *Phys. B Condens. Matter*, p. 411751, 2019, doi: 10.1016/j.physb.2019.411751.
- [83] P. Hohenberg and W. Kohn, “Inhomogeneous Electron Gas,” *Phys. Rev.*, vol. 136, no. 3B, pp. 864–871, 1964, doi: 10.1007/BF01198136.
- [84] M. J. Frisch, G. W. Trucks, H. E. Schlegel, G. E. Scuseria, M. A. Robb, J. R. Cheeseman, G. Scalmani, V. Barone, G. A. Petersson, F. O., J. B. Foresman, and J. D. Fox, “Gaussian 16,” *Gaussian, Inc., Wallingford CT*,. Gaussian Inc, Wallingford CT, 2016.
- [85] Y. Zhao and D. G. Truhlar, “A new local density functional for main-group thermochemistry, transition metal bonding, thermochemical kinetics, and noncovalent interactions,” *J. Chem. Phys.*, vol. 125, no. 19, 2006, doi: 10.1063/1.2370993.
- [86] Y. Zhao and D. G. Truhlar, “The M06 suite of density functionals for main group thermochemistry, thermochemical kinetics, noncovalent interactions, excited states, and transition elements: Two new functionals and systematic testing of four M06-class functionals and 12 other function,” *Theor. Chem. Acc.*, vol. 120, no. 1–3, pp. 215–241, 2008, doi: 10.1007/s00214-007-0310-x.
- [87] P. J. Hay and W. R. Wadt, “Ab initio effective core potentials for molecular calculations. Potentials for K to Au including the outermost core orbitals,” *J. Chem. Phys.*, vol. 82, no. 1, pp. 299–310, 1985, doi: 10.1063/1.448975.
- [88] S. F. Boys and F. Bernardi, “The calculation of small molecular interactions by the differences of separate total energies. Some procedures with reduced errors,” *Mol. Phys.*, vol. 19, no. 4, pp. 553–566, 1970, doi: 10.1080/00268977000101561.
- [89] A. C. Ferrari *et al.*, “Science and technology roadmap for graphene, related two-dimensional crystals, and hybrid systems,” *Nanoscale*, vol. 7, no. 11, pp. 4598–4810, 2015, doi: 10.1039/c4nr01600a.
- [90] B. Deng, Z. Liu, and H. Peng, “Toward Mass Production of CVD Graphene Films,” *Adv. Mater.*, vol. 31, no. 9, pp. 1–25, 2019, doi: 10.1002/adma.201800996.
- [91] L. Lin, H. Peng, and Z. Liu, “Synthesis challenges for graphene industry,” *Nat. Mater.*, vol. 18, no. 6, pp. 520–524, 2019, doi: 10.1038/s41563-019-0341-4.
- [92] G. R. Yazdi, T. Iakimov, and R. Yakimova, “Epitaxial graphene on SiC: A review of growth and characterization,” *Crystals*, vol. 6, no. 5, 2016, doi: 10.3390/cryst6050053.

- [93] R. Yakimova, C. Virojanadara, D. Gogova, M. Syväjärvi, D. Siche, K. Larsson, and L. I. Johansson, “Analysis of the formation conditions for large area epitaxial graphene on SiC substrates,” *Mater. Sci. Forum*, vol. 645–648, pp. 565–568, 2010, doi: 10.4028/www.scientific.net/MSF.645-648.565.
- [94] F. Giannazzo, I. Shtepliuk, I. G. Ivanov, T. Iakimov, A. Kakanakova-Georgieva, E. Schiliro, P. Fiorenza, and R. Yakimova, “Probing the uniformity of hydrogen intercalation in quasi-free-standing epitaxial graphene on SiC by micro-Raman mapping and conductive atomic force microscopy,” *Nanotechnology*, vol. 30, no. 28, 2019, doi: 10.1088/1361-6528/ab134e.
- [95] C. Bur, “New method for selectivity enhancement of SiC field effect gas sensors for quantification of NO<sub>x</sub>,” Saarland University, 2012.
- [96] M. Bastuck, T. Baur, and A. Schütze, “DAV<sup>3</sup>E – a MATLAB toolbox for multivariate sensor data evaluation,” *Sensors*, pp. 489–506, 2018.
- [97] A. Lloyd Spetz and M. Andersson, “Technology and Application Opportunities for SiC-FET Gas Sensors,” in *Solid State Gas Sensors - Industrial Application*, M. Fleischer and M. Lehmann, Eds. Berlin: Springer, 2011, pp. 189–214.
- [98] M. Leidinger, C. Schultealbert, J. Neu, A. Schütze, and T. Sauerwald, “Characterization and calibration of gas sensor systems at ppb level - A versatile test gas generation system,” *Meas. Sci. Technol.*, vol. 29, no. 1, 2018, doi: 10.1088/1361-6501/aa91da.
- [99] N. Helwig, M. Schüler, C. Bur, A. Schütze, and T. Sauerwald, “Gas mixing apparatus for automated gas sensor characterization,” *Meas. Sci. Technol.*, vol. 25, no. 5, p. 055903, 2014, doi: 10.1088/0957-0233/25/5/055903.
- [100] World Health Organisation, “Guidelines for Indoor Air Quality: Selected Pollutants,” *WHO Guidel.*, vol. 9, p. 454, 2010.
- [101] The European Parliament and the Council of the European Union, “DIRECTIVE 2008/50/EC OF THE EUROPEAN PARLIAMENT AND OF THE COUNCIL of 21 May 2008 on ambient air quality and cleaner air for Europe,” *Off. J. Eur. Communities*, pp. 1–43, 2008, doi: <http://eur-lex.europa.eu/LexUriServ/LexUriServ.do?uri=OJ:L:2008:152:0001:0044:EN:PDF>.
- [102] The Commission of the European Communities, “EU exposure limit chemical agents at work, Commission Directive 2000/39/EC,” *Off. J. Eur. Communities*, vol. L142, no. 47, 2001, [Online]. Available: <https://eur-lex.europa.eu/legal-content/en/ALL/?uri=CELEX%3A32000L0039>.

## References

- [103] H. Jasuja, G. W. Peterson, J. B. Decoste, M. A. Browe, and K. S. Walton, "Evaluation of MOFs for air purification and air quality control applications: Ammonia removal from air," *Chem. Eng. Sci.*, vol. 124, pp. 118–124, 2015, doi: 10.1016/j.ces.2014.08.050.
- [104] S. N. Behera and M. Sharma, "Investigating the potential role of ammonia in ion chemistry of fine particulate matter formation for an urban environment," *Sci. Total Environ.*, vol. 408, no. 17, pp. 3569–3575, 2010, doi: 10.1016/j.scitotenv.2010.04.017.
- [105] D. Ruffer, F. Hoehne, and J. Bühler, "New digital metal-oxide (MOx) sensor platform," *Sensors (Switzerland)*, vol. 18, no. 4, 2018, doi: 10.3390/s18041052.
- [106] V. Palmisano, L. Boon-Brett, C. Bonato, F. Harskamp, W. J. Buttner, M. B. Post, R. Burgess, and C. Rivkin, "Evaluation of selectivity of commercial hydrogen sensors," *Int. J. Hydrogen Energy*, vol. 39, no. 35, pp. 20491–20496, 2014, doi: 10.1016/j.ijhydene.2014.03.251.
- [107] European Environment Agency, "Nitrogen oxides (NOx) emissions," Copenhagen, 2014.
- [108] The European Parliament and the Council of the European Union, "Directive 2004/42/CE on the limitation of emissions of volatile organic compounds due to the use of organic solvents in certain paints and varnishes and vehicle refinishing products and amending Directive 1999/13/EC," *Off. J. Eur. Union*, vol. L143, no. 47, pp. 87–96, 2004, [Online]. Available: <https://eur-lex.europa.eu/legal-content/EN/TXT/PDF/?uri=CELEX:32004L0042&from=EN>.
- [109] The Council of the European Union, "Council Directive 1999/13/EC of 11 March 1999 on the limitation of emissions of volatile organic compounds due to the use of organic solvents in certain activities and installations," *Off. J. Eur. Communities*, vol. L85, no. 42, pp. 1–22, 1999, doi: <http://eur-lex.europa.eu/LexUriServ/LexUriServ.do?uri=OJ:L:1999:085:0001:0022:EN:PDF>.
- [110] US Environmental Protection Agency, "40 CFR Part 51, Subpart F - Procedural Requirements," 2018. [Online]. Available: <https://www.govinfo.gov/content/pkg/CFR-2018-title40-vol2/xml/CFR-2018-title40-vol2-part51.xml#seqnum51.100>.
- [111] L. Zhong, S. Batterman, and C. W. Milando, "VOC sources and exposures in nail salons: a pilot study in Michigan, USA," *Int. Arch. Occup. Environ. Health*, vol. 92, no. 1, pp. 141–153, 2019, doi: 10.1007/s00420-018-1353-0.

- [112] OEHHA California Office of Environmental Health Hazard Assessment, “OEHHA Acute, 8-hour and Chronic Reference Exposure Level (REL) Summary,” 2020. <https://oehha.ca.gov/air/general-info/oehha-acute-8-hour-and-chronic-reference-exposure-level-rel-summary> (accessed Mar. 28, 2021).
- [113] Ministère de l’Ecologie du Développement Durable des Transports et du Logement, “Décret no 2011-1727 du 2 décembre 2011 relatif aux valeurs-guides pour l’air intérieur pour le formaldéhyde et le benzène,” 2011. [Online]. Available: <https://www.legifrance.gouv.fr/affichTexte.do?cidTexte=JORFTEXT000024909119&categorieLien=id>.
- [114] M. Schiavon, M. Redivo, G. Antonacci, E. C. Rada, M. Ragazzi, D. Zardi, and L. Giovannini, “Assessing the air quality impact of nitrogen oxides and benzene from road traffic and domestic heating and the associated cancer risk in an urban area of Verona (Italy),” *Atmos. Environ.*, vol. 120, pp. 234–243, 2015, doi: 10.1016/j.atmosenv.2015.08.054.
- [115] G. D. Nielsen, S. T. Larsen, and P. Wolkoff, “Re-evaluation of the WHO (2010) formaldehyde indoor air quality guideline for cancer risk assessment,” *Arch. Toxicol.*, vol. 91, no. 1, pp. 35–61, 2017, doi: 10.1007/s00204-016-1733-8.
- [116] T. Yager, “Epitaxial Graphene Technology for Quantum Metrology,” Chalmers University of Technology, 2015.
- [117] Y. C. Lin, C. C. Lu, C. H. Yeh, C. Jin, K. Suenaga, and P. W. Chiu, “Graphene annealing: How clean can it be?,” *Nano Lett.*, vol. 12, no. 1, pp. 414–419, 2012, doi: 10.1021/nl203733r.
- [118] K. H. Kim, H. He, M. Rodner, R. Yakimova, K. Larsson, M. Piantek, D. Serrate, A. Zakharov, S. Kubatkin, J. Eriksson, and S. Lara-Avila, “Chemical sensing with atomically-thin metals templated by a two-dimensional insulator,” *Adv. Mater. Interfaces*, vol. 1902104, pp. 1–7, 2020, doi: 10.1002/admi.201902104.
- [119] D. S. Lee, C. Riedl, B. Krauss, K. Von Klitzing, U. Starke, and J. H. Smet, “Raman spectra of epitaxial graphene on SiC and of epitaxial graphene transferred to SiO<sub>2</sub>,” *Nano Lett.*, vol. 8, no. 12, pp. 4320–4325, 2008, doi: 10.1021/nl802156w.
- [120] A. C. Ferrari, “Raman spectroscopy of graphene and graphite: Disorder, electron-phonon coupling, doping and nonadiabatic effects,” *Solid State Commun.*, vol. 143, no. 1–2, pp. 47–57, 2007, doi: 10.1016/j.ssc.2007.03.052.

## References

- [121] C. Bouhafs, A. A. Zakharov, I. G. Ivanov, F. Giannazzo, J. Eriksson, V. Stanishev, P. Kühne, T. Iakimov, T. Hofmann, M. Schubert, F. Roccaforte, R. Yakimova, and V. Darakchieva, “Multi-scale investigation of interface properties, stacking order and decoupling of few layer graphene on C-face 4H-SiC,” *Carbon N. Y.*, vol. 116, pp. 722–732, 2017, doi: 10.1016/j.carbon.2017.02.026.
- [122] A. Zandiatashbar, G. H. Lee, S. J. An, S. Lee, N. Mathew, M. Terrones, T. Hayashi, C. R. Picu, J. Hone, and N. Koratkar, “Effect of defects on the intrinsic strength and stiffness of graphene,” *Nat. Commun.*, vol. 5, pp. 1–9, 2014, doi: 10.1038/ncomms4186.
- [123] E. Del Corro, M. Taravillo, and V. G. Baonza, “Nonlinear strain effects in double-resonance Raman bands of graphite, graphene, and related materials,” *Phys. Rev. B - Condens. Matter Mater. Phys.*, vol. 85, no. 3, pp. 1–5, 2012, doi: 10.1103/PhysRevB.85.033407.
- [124] C. Melios, C. E. Giusca, V. Panchal, and O. Kazakova, “Water on graphene: Review of recent progress,” *2D Mater.*, vol. 5, no. 2, 2018, doi: 10.1088/2053-1583/aa9ea9.
- [125] N. Barsan and U. Weimar, “Understanding the fundamental principles of metal oxide based gas sensors; the example of CO sensing with SnO<sub>2</sub> sensors in the presence of humidity,” *J. Phys. Condens. Matter*, vol. 15, no. 20, 2003, doi: 10.1088/0953-8984/15/20/201.
- [126] E. C. Dickey, O. K. Varghese, K. G. Ong, D. Gong, M. Paulose, and C. A. Grimes, “Room Temperature Ammonia and Humidity Sensing Using Highly Ordered Nanoporous Alumina Films,” *Sensors*, vol. 2, pp. 91–110, 2002, doi: 10.3390/s20300091.
- [127] E. H. Hwang, S. Adam, and S. Das Sarma, “Transport in chemically doped graphene in the presence of adsorbed molecules,” *Phys. Rev. B - Condens. Matter Mater. Phys.*, vol. 76, no. 19, pp. 1–6, 2007, doi: 10.1103/PhysRevB.76.195421.
- [128] G. Chen, T. M. Paronyan, and A. R. Harutyunyan, “Sub-ppt gas detection with pristine graphene,” *Appl. Phys. Lett.*, vol. 101, no. 5, 2012, doi: 10.1063/1.4742327.
- [129] A. Cagliani, D. M. A. Mackenzie, L. K. Tschammer, F. Pizzocchero, K. Almdal, and P. Bøggild, “Large-area nanopatterned graphene for ultrasensitive gas sensing,” *Nano Res.*, vol. 7, no. 5, pp. 743–754, 2014, doi: 10.1007/s12274-014-0435-x.
- [130] G. Lee, G. Yang, A. Cho, J. W. Han, and J. Kim, “Defect-engineered graphene chemical sensors with ultrahigh sensitivity,” *Phys. Chem. Chem. Phys.*, vol. 18, no. 21, pp. 14198–14204, 2016, doi: 10.1039/c5cp04422g.

- [131] J. H. Lee, A. Mirzaei, J. Y. Kim, J. H. Kim, H. W. Kim, and S. S. Kim, "Optimization of the surface coverage of metal nanoparticles on nanowires gas sensors to achieve the optimal sensing performance," *Sensors Actuators, B Chem.*, vol. 302, no. September 2019, p. 127196, 2020, doi: 10.1016/j.snb.2019.127196.
- [132] K. Großmann, S. Wicker, U. Weimar, and N. Barsan, "Impact of Pt additives on the surface reactions between SnO<sub>2</sub>, water vapour, CO and H<sub>2</sub>; An operando investigation," *Phys. Chem. Chem. Phys.*, vol. 15, no. 44, pp. 19151–19158, 2013, doi: 10.1039/c3cp52782d.
- [133] S. Steinhauer, E. Lackner, F. Sosada-Ludwikowska, V. Singh, J. Krainer, R. Wimmer-Teubenbacher, P. Grammatikopoulos, A. Köck, and M. Sowwan, "Atomic-scale structure and chemical sensing application of ultrasmall size-selected Pt nanoparticles supported on SnO<sub>2</sub>," *Mater. Adv.*, vol. 1, no. 9, pp. 3200–3207, 2020, doi: 10.1039/d0ma00244e.
- [134] N. Armakavicius, P. Kühne, J. Eriksson, C. Bouhafs, V. Stanishev, I. G. Ivanov, R. Yakimova, A. A. Zakharov, A. Al-Temimy, C. Coletti, M. Schubert, and V. Darakchieva, "Resolving mobility anisotropy in quasi-free-standing epitaxial graphene by terahertz optical Hall effect," *Carbon N. Y.*, vol. 172, pp. 248–259, 2021, doi: 10.1016/j.carbon.2020.09.035.
- [135] T. Hibbard and A. J. Killard, "Breath ammonia analysis: Clinical application and measurement," *Crit. Rev. Anal. Chem.*, vol. 41, no. 1, pp. 21–35, 2011, doi: 10.1080/10408347.2011.521729.
- [136] N. M. Caffrey, R. Armiento, R. Yakimova, and I. A. Abrikosov, "Changes in work function due to NO<sub>2</sub> adsorption on monolayer and bilayer epitaxial graphene on SiC(0001)," *Phys. Rev. B*, vol. 94, no. 20, pp. 1–7, 2016, doi: 10.1103/PhysRevB.94.205411.
- [137] Alphasense, "NO<sub>2</sub>-A1 Nitrogen Dioxide Sensor Data Sheet," Essex, 2015. [Online]. Available: <http://www.alphasense.com/WEB1213/wp-content/uploads/2015/09/NO2-A1.pdf>.
- [138] K. Wolf, J. Cyrus, T. Harciníková, J. Gu, T. Kusch, R. Hampel, A. Schneider, and A. Peters, "Land use regression modeling of ultrafine particles, ozone, nitrogen oxides and markers of particulate matter pollution in Augsburg, Germany," *Sci. Total Environ.*, vol. 579, pp. 1531–1540, 2017, doi: 10.1016/j.scitotenv.2016.11.160.
- [139] D. J. Buckley, N. C. G. Black, E. G. Castanon, C. Melios, M. Hardman, and O. Kazakova, "Frontiers of graphene and 2D material-based gas sensors for environmental monitoring," *2D Mater.*, vol. 7, no. 3, 2020, doi: 10.1088/2053-1583/ab7bc5.

## References

- [140] Geotech Environmental Equipment Inc., “Honeywell ppbRAE 3000+ Data Sheet,” Denver, Colorado, 2019. [Online]. Available: [http://www.geotechenv.com/pdf/air\\_quality/minirae\\_ppbrae\\_3000.pdf](http://www.geotechenv.com/pdf/air_quality/minirae_ppbrae_3000.pdf).
- [141] Dräger, “X-am 8000 Multi-Gas Detector Data Sheet,” Lübeck, 2020. [Online]. Available: <https://www.draeger.com/Products/Content/x-am-8000-pi-9104484-en-master.pdf>.
- [142] AMS, “AS-MLV-P2 Air Quality Sensor Data Sheet,” Eindhoven, 2015. [Online]. Available: <https://www.sciosense.com/wp-content/uploads/documents/AS-MLV-P2-Datasheet.pdf>.
- [143] Sensirion, “SGPC3 Data Sheet,” Zürich, 2020. [Online]. Available: [https://www.sensirion.com/fileadmin/user\\_upload/customers/sensirion/Dokumente/9\\_Gas\\_Sensors/Datasheets/Sensirion\\_Gas\\_Sensors\\_Datasheet\\_SGPC3.pdf](https://www.sensirion.com/fileadmin/user_upload/customers/sensirion/Dokumente/9_Gas_Sensors/Datasheets/Sensirion_Gas_Sensors_Datasheet_SGPC3.pdf).
- [144] UST, “VOC/CO2 Sensor Data Sheet,” Geschwenda, 2017. [Online]. Available: [https://www.umweltsensortechnik.de/fileadmin/assets/downloads/gassensoren/module/Datasheet\\_VOC-CO2-Sensor\\_Rev1700.pdf](https://www.umweltsensortechnik.de/fileadmin/assets/downloads/gassensoren/module/Datasheet_VOC-CO2-Sensor_Rev1700.pdf).
- [145] SGX Sensortech, “MiCS-VZ-89TE Data sheet,” Corcelles-Cormondreche. [Online]. Available: <https://www.sgxsensortech.com/content/uploads/2016/07/MiCS-VZ-89TE-V1.0.pdf>.
- [146] R. Muller and E. Lange, “Multidimensional Sensor for Gas Analysis,” *Sensors and Actuators*, vol. 9, pp. 39–48, 1986.
- [147] T. Eklöv, P. Mårtensson, and I. Lundström, “Enhanced selectivity of MOSFET gas sensors by systematical analysis of transient parameters,” *Anal. Chim. Acta*, vol. 353, no. 2–3, pp. 291–300, 1997, doi: 10.1016/S0003-2670(97)87788-4.
- [148] M. Wenger, R. Waller, V. R. H. Lorentz, M. Marz, and M. Herold, “Investigation of gas sensing in large lithium-ion battery systems for early fault detection and safety improvement,” *IECON Proc. (Industrial Electron. Conf.)*, pp. 5654–5659, 2014, doi: 10.1109/IECON.2014.7049366.
- [149] M. Leidinger, M. Rieger, T. Sauerwald, C. Alépée, and A. Schütze, “Integrated pre-concentrator gas sensor microsystem for ppb level benzene detection,” *Sensors Actuators, B Chem.*, vol. 236, pp. 988–996, 2016, doi: 10.1016/j.snb.2016.04.064.
- [150] N. A. Rakow and K. S. Suslick, “A colorimetric sensor array for odour visualization,” *Nature*, vol. 406, no. 6797, pp. 710–713, 2000, doi: 10.1038/35021028.
- [151] P. Reimann and A. Schütze, “Sensor Arrays, Virtual Multisensors, Data Fusion, and Gas Sensor Data Evaluation,” in *Springer Series on Chemical Sensors and Biosensors, Volume 15 2014*, Springer Berlin Heidelberg, 2014, pp. 67–107.

- [152] M. Bastuck, T. Baur, M. Richter, B. Mull, A. Schütze, and T. Sauerwald, “Comparison of ppb-level gas measurements with a metal-oxide semiconductor gas sensor in two independent laboratories,” *Sensors Actuators, B Chem.*, vol. 273, no. March, pp. 1037–1046, 2018, doi: 10.1016/j.snb.2018.06.097.
- [153] T. Sauerwald, T. Baur, M. Leidinger, W. Reimringer, L. Spinelle, M. Gerboles, G. Kok, and A. Schütze, “Highly sensitive benzene detection with metal oxide semiconductor gas sensors - an inter-laboratory comparison,” *J. Sensors Sens. Syst.*, vol. 7, no. 1, pp. 235–243, 2018, doi: 10.5194/jsss-7-235-2018.
- [154] W. Buttner, R. Burgess, C. Rivkin, M. Post, L. Boon-Brett, G. Black, F. Harskamp, and P. Moretto, “Round Robin Testing of Commercial Hydrogen Sensor Performance - Observations and Results: Preprint,” 2010, [Online]. Available: <http://www.osti.gov/bridge>.
- [155] A. Moritz and D. Breuer, “Production of test gases in the ppb range for round-robin tests and quality assurance measures during the measurement of VOCs,” *J. Environ. Monit.*, vol. 10, no. 12, pp. 1454–1459, 2008, doi: 10.1039/b810557j.
- [156] A. Schütze, T. Baur, M. Leidinger, W. Reimringer, R. Jung, T. Conrad, and T. Sauerwald, “Highly Sensitive and Selective VOC Sensor Systems Based on Semiconductor Gas Sensors: How to?,” *Environments*, vol. 4, no. 1, p. 20, Mar. 2017, doi: 10.3390/environments4010020.
- [157] M. F. Santangelo, I. Shtepliuk, D. Filippini, D. Puglisi, M. Vagin, R. Yakimova, and J. Eriksson, “Epitaxial graphene sensors combined with 3D-printed microfluidic chip for heavy metals detection,” *Sensors (Switzerland)*, vol. 19, no. 10, pp. 1–13, 2019, doi: 10.3390/s19102393.
- [158] M. F. Santangelo, I. Shtepliuk, D. Filippini, I. G. Ivanov, R. Yakimova, and J. Eriksson, “Real-time sensing of lead with epitaxial graphene-integrated microfluidic devices,” *Sensors Actuators, B Chem.*, vol. 288, no. February, pp. 425–431, 2019, doi: 10.1016/j.snb.2019.03.021.
- [159] World Health Organisation, “Lead in Drinking-water,” Geneva, 2011. [Online]. Available: [https://www.who.int/water\\_sanitation\\_health/dwq/chemicals/lead.pdf](https://www.who.int/water_sanitation_health/dwq/chemicals/lead.pdf).
- [160] A. Zilli, “Design and test of a graphene-based sensor towards detection of cancer biomarkers,” Linköping University, 2020.
- [161] I. Cederquist, “Bioinspired smell sensor to trace pheromone released by the European spruce bark beetle,” Linköping University, 2020.

## References

- [162] R. M. McCormick and B. L. Karger, "Guidelines For Data Acquisition And Data Quality Evaluation In Environmental Chemistry," *Anal. Chem.*, vol. 52, no. 14, pp. 2242–2249, 1980, doi: 10.1021/ac50064a004.

# Abbreviations

AFM	Atomic Force Microscopy
AQM	Air Quality Monitoring
BSSE	Basis Set Superposition Error
BZ	Brillouin Zone
CNT	Carbonnanotube
CCD	Charge-Coupled Device
CDA	Canonical Discriminant Analysis
CVD	Chemical Vapor Deposition
DEG	Decorated Epitaxial Graphene
DFT	Density Functional Theory
DOS	Density Of States
EG	Epitaxial Graphene
FET	Field Effect Transistor
FWHM	Full Width at Half Maximum
GMA	Gas Mixing Apparatus
IEG	Intercalated Epitaxial Graphene
LANL2DZ	Los Alamos National Laboratory 2 Double-Zeta
LDA	Linear Discriminant Analysis
LED	Light Emitting Diode
LOD	Limit Of Detection
MFC	Mass Flow Controller
MOS	Metal Oxide Semiconductor
NL	Nanolayer
NP	Nanoparticle
PBS	Phosphate-Buffered Saline
PCA	Principal Component Analysis
PEG	Pristine Epitaxial Graphene
PFA	Perfluoroalkoxy Alkane
PID	Photo-Ionization Detector
PLD	Pulsed Laser Deposition
PVD	Physical Vapor Deposition
QHE	Quantum Hall Effect
REL	chronic Reference Exposure Level
RH	Relative Humidity
SNR	Signal-to-Noise-Ratio

## Abbreviations

TVOC	Total Volatile Organic Compounds
UV	Ultraviolet
VOC	Volatile Organic Compound
WHO	World Health Organization

PAPER I





# Performance tuning of gas sensors based on epitaxial graphene on silicon carbide

Marius Rodner <sup>a,\*</sup>, Jasna Bahonjic <sup>a</sup>, Marcus Mathisen <sup>a</sup>, Rickard Gunnarsson <sup>b</sup>, Sebastian Ekeroth <sup>b</sup>, Ulf Helmersson <sup>b</sup>, Ivan G. Ivanov <sup>c</sup>, Rositsa Yakimova <sup>c</sup>, Jens Eriksson <sup>a</sup>

<sup>a</sup> Applied Sensor Science Unit, IFM, Linköping University, Sweden

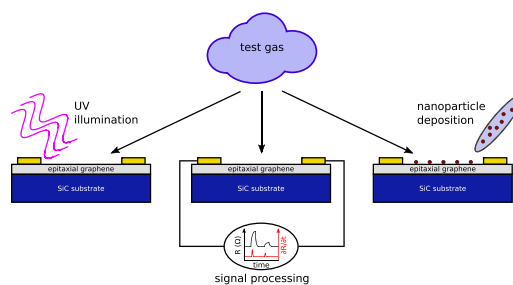
<sup>b</sup> Plasma & Coatings Physics Division, IFM, Linköping University, Sweden

<sup>c</sup> Semiconductor Materials Division, IFM, Linköping University, Sweden

## HIGHLIGHTS

- Hollow cathode pulsed plasma sputtering enables deposition of TiO<sub>2</sub> and Fe<sub>3</sub>O<sub>4</sub> nanoparticles on epitaxial graphene.
- Nanoparticle decoration of epitaxial graphene yields detection of 5 ppb benzene with a signal to noise ratio of 35 dB.
- Integration of UV LED into the sensor package expands the dynamic range for oxygen detection.
- Use of time derivative signal allows reduction of response time by more than an order of magnitude.

## GRAPHICAL ABSTRACT



## ARTICLE INFO

### Article history:

Received 30 October 2017

Received in revised form 26 April 2018

Accepted 28 April 2018

Available online 04 May 2018

### Keywords:

Epitaxial graphene

Metal oxide nanoparticles

Gas sensor

UV light

Derivative sensor signal

Benzene

## ABSTRACT

In this study, we investigated means of performance enhancement in sensors based on epitaxial graphene on silicon carbide (SiC). Epitaxially grown graphene on SiC substrates were successfully decorated with metal oxide nanoparticles such as TiO<sub>2</sub> and Fe<sub>3</sub>O<sub>4</sub> using hollow cathode pulsed plasma sputtering. Atomic Force Microscopy and Raman data verified that no damage was added to the graphene surface. It could be shown that it was easily possible to detect benzene, which is one of the most dangerous volatile organic compounds, with the Fe<sub>3</sub>O<sub>4</sub> decorated graphene sensor down to an ultra-low concentration of 5 ppb with a signal to noise ratio of 35 dB. Moreover, upon illumination with a UV light LED (265 nm) of the TiO<sub>2</sub> decorated graphene sensor, the sensitivity towards a change of oxygen could be enhanced such that a clear sensor response could be seen which is a significant improvement over dark conditions, where almost no response occurred. As the last enhancement, the time derivative sensor signal was introduced for the sensor data evaluation, testing the response towards a change of oxygen. This sensor signal evaluation approach can be used to decrease the response time of the sensor by at least one order of magnitude.

© 2017 Elsevier Ltd. All rights reserved.

## 1. Introduction

Nowadays, many people in advanced societies spend up to 85% of their time indoors under prolonged exposure to indoor air that is often controlled in terms of temperature, humidity, and the oxygen/carbon dioxide ratio, but not in terms of toxic gases. Volatile organic

\* Corresponding author.

E-mail address: [marius.rodner@liu.se](mailto:marius.rodner@liu.se) (M. Rodner).

compounds (VOCs), defined by the World Health Organization as all organic compounds having their boiling points between 50–100 °C and 240–260 °C, are in the top 5 of global air pollutants [1]. Although some of them are hazardous to humans even at very low concentrations, they are widely used in industry and everyday products such as solvents. For example, the safety level for formaldehyde is 81 ppb, for naphthalene 1.9 ppb and no exposure at all for benzene [2]. Moreover, indoor air pollution is in the top 5 of environmental risks to human health with 4.3 million deaths/year including 570,000 children under the age of 5. This number is estimated to rise up to 6 million deaths/year in 2050 [3]. There is clearly a demand for gas sensors where ultra-high sensitivity is necessary. Until now, there are not sensors available for all the relevant gases although the market is estimated to be \$1.4 billion by 2021 [4].

Since the isolation and first characterization of graphene in 2004, it has become the best investigated two-dimensional (2D) material with many outstanding properties like perfect thermal conductivity, ballistic electron transport at room temperature, low mass and an ultimate surface to volume ratio [5]. It can therefore be of use in very different fields of applications, one of which is as very sensitive chemical gas sensors [6]. Due to the low density of states near the Dirac point, a small change in the number of charge carriers results in a large change in the electronic state which then can easily be measured as a change in resistance of the sensor surface [7].

Epitaxial growth of graphene on silicon carbide (SiC) [8] is not the most used but a highly suitable production process when it comes to electrical devices [9]. Si atoms sublime in argon ambient at 2000 °C and the carbon atoms self-assemble with the bulk SiC to form a monolayer of graphene with a carbon buffer layer that is formed in between graphene and the SiC interface and is still partially covalently bonded to the Si atoms which makes it insulating. High temperature growth leads to high quality where the thickness can be controlled by the temperature, achieving monolayer graphene with a thickness uniformity of about 98% (2% bilayer). Since it is grown on a semiconducting or semi insulating substrate, there is no graphene transfer needed after the growth and it can be used directly to fabricate electronic devices without short circuit effects.

Besides the sensitivity of a gas sensor, also the selectivity is of importance. Since graphene is quite sensitive to a large number of gases, there is a lack of selectivity that has to be overcome. Enhancing the sensing properties of gas sensors can be done with several different approaches. It was shown that metal- and metal oxide nanoparticles can be used effectively to enhance the selectivity of graphene, and also to generate sensitivity towards gases to which as-grown graphene does not respond [10,11]. The addition of nanoparticles onto graphene results in specific sensor responses to different gases. The most common materials used are SnO<sub>2</sub> [12,13], ZnO [14,15] and TiO<sub>2</sub> [11,16]. Hollow cathode sputtering where the nanoparticles are grown in the gas phase is one of the most suitable techniques for scalable deposition of nanoparticles in a very ordered way on top of a surface without introducing much damage to it [17]. Another approach towards selectivity tuning is to use UV light exposure during the measurement to decrease time constants and also increase sensitivity towards certain gases by tuning the energy level [18]. In a last step, smart data processing can be used to further increase selectivity and decrease time constants if applied correctly [19]. In the following, we will introduce all of these techniques and show that they can be used to enhance the performance of graphene gas sensors.

## 2. Methods

### 2.1. Graphene growth

As a sensor basis, epitaxial graphene with a monolayer ratio of about 98% (2% bilayer), grown on SiC was used. Epitaxial graphene (EG) was prepared by sublimation of SiC and subsequent graphene formation

on semi-insulating, Si-terminated, 4H-SiC (0001) on-axis substrates at 2000 °C in argon and at a pressure of 1 bar [20].

### 2.2. Nanoparticle deposition

TiO<sub>2</sub> and Fe<sub>3</sub>O<sub>4</sub> nanoparticles were deposited on top of the graphene layer using a hollow cathode pulsed plasma sputtering technique [21]. The nanoparticles nucleate and grow in the plasma ejected from the hollow cathode. The substrates were placed outside the dense plasma region, preventing energetic species from reaching them. The discharge parameters for the Fe<sub>3</sub>O<sub>4</sub> particles were: pulse frequency 1200 Hz, pulse width 80 μs and an average power of 90 W. A substrate bias was used to attract the particles to the substrate surface. For the Fe<sub>3</sub>O<sub>4</sub> particles this bias was +3 V and the substrates were exposed to nanoparticle deposition for 15 s. For the TiO<sub>2</sub> nanoparticles the deposition time was 30 s; other process parameters are given in reference [17].

### 2.3. Characterization techniques

Before and after the deposition of nanoparticles, a series of characterization measurements were conducted to see if any damage of the graphene surface occurred during the deposition. Atomic Force Microscopy (AFM) (Quadrex Dimension 3100 with a Nanoscope IVa controller) with a Si tip (PPP-NCHR-50 from Nanosensors) and a tip radius of curvature <7 nm was used in tapping mode to obtain topography images of the sensing layers. A micro Raman setup was used to perform Raman spectroscopy and reflectance measurements. A CCD camera coupled to a monochromator (HR460) was used along with a 100× magnification objective which were excited at 532 nm using a solid-state laser with a power of 17 mW focused to a spot with diameter ~0.9 μm on the sample, and a system spectral resolution of approximately 5 cm<sup>-1</sup>. The Raman spectra of Si-face graphene were obtained by subtracting a reference Raman spectrum of 4H-SiC (0001).

### 2.4. Sensor device fabrication

Sensor devices have been fabricated on SiC substrates by depositing electrodes on top of the graphene surface through thermal evaporation of titanium (2 nm) and gold (200 nm) sequentially. The electrodes are 1 mm wide with a 1 mm gap in between. To enable a controlled temperature loop, each sensor chip is glued using Aremco Ceramabond 571 on top of a ceramic heater substrate (Heraeus GmbH, Germany) with an additional Pt-100 temperature sensor (Heraeus GmbH, Germany). This device was mounted on top of a TO8-socket and connected to its pins using gold-wire bonding and silver glue (Epotek E3081). This setup limits the temperature that can be used within stable conditions to 300 °C. The final sensor is inserted into a flow cell which is attached to a gas mixing system. A brief description of this system can be found here [22]. A dry background mixture of N<sub>2</sub> and O<sub>2</sub> with a ratio of 80:20 ml/min and a constant flow rate of 100 ml/min was used both as a carrier gas and purging gas. The nitrogen concentration was then adjusted when introducing a test gas to the gas flow. To test the influence of UV light, a UV LED (Sensor Electronic Technology Inc, S-T39B-F1-265-01-1-050) with a wavelength of 265 nm and an optical output power of 0.8 mW was used for some measurements.

## 3. Results and discussion

### 3.1. Morphological and structural characterization

#### 3.1.1. Atomic force microscopy

To see that the surface decoration with TiO<sub>2</sub> and Fe<sub>3</sub>O<sub>4</sub> nanoparticles was successfully performed, AFM measurements were conducted before and after the deposition. Fig. 1(a) shows the distinct topography of an as-grown graphene layer with almost no roughness, but the characteristic steps from the SiC substrate after step-bunching upon the high

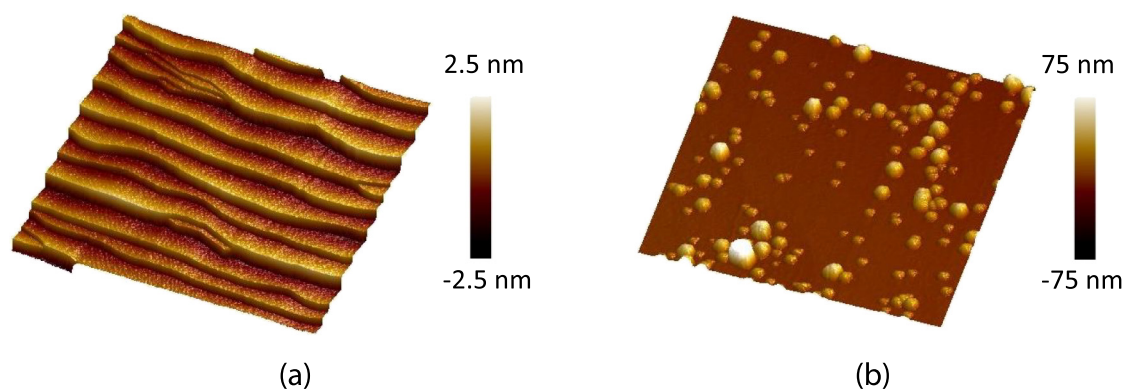


Fig. 1. AFM scans over an area of  $5 \times 5 \mu\text{m}^2$  of (a) as-grown graphene and an area of  $2 \times 2 \mu\text{m}^2$  (b) with  $\text{Fe}_3\text{O}_4$  nanoparticles decorated on top of the graphene surface.

temperature graphene growth. The topography after the additional deposition of iron oxide nanoparticles is shown in Fig. 1(b), showing monodispersed, spherical particles with diameters mostly in the range of 40–80 nm, with a few larger aggregates.

### 3.1.2. Raman spectroscopy

Raman spectroscopy measurements were also conducted before and after the deposition to ascertain the quality of the graphene and to study potential damage introduced through the nanoparticle deposition. The comparison between the as-grown graphene and graphene decorated with  $\text{Fe}_3\text{O}_4$  nanoparticles is shown in Fig. 2. The intensity scale is in arbitrary units and the signals were fitted to have the same maximum peak height for the G-peak at around  $1610 \text{ cm}^{-1}$ . The black line corresponds to the Raman spectrum for an as-grown graphene reference which shows the typical G and 2D peaks around  $1610 \text{ cm}^{-1}$  and  $2737 \text{ cm}^{-1}$ , respectively [23]. The features starting in the range of  $1280 \text{ cm}^{-1}$  and extending into the G-peak are all related to the interfacial buffer layer between the graphene and the SiC substrate [23], and while they overlap with the position of the D peak they are not related to defects. It can be clearly seen that the spectra almost completely overlap, indicating that no damage was introduced into the graphene surface during the nanoparticle deposition. If damage is introduced to the graphene surface, the broad D peak around  $1350 \text{ cm}^{-1}$  would rise, indicating a rise of level of disorder and impurities. Furthermore, the 2D

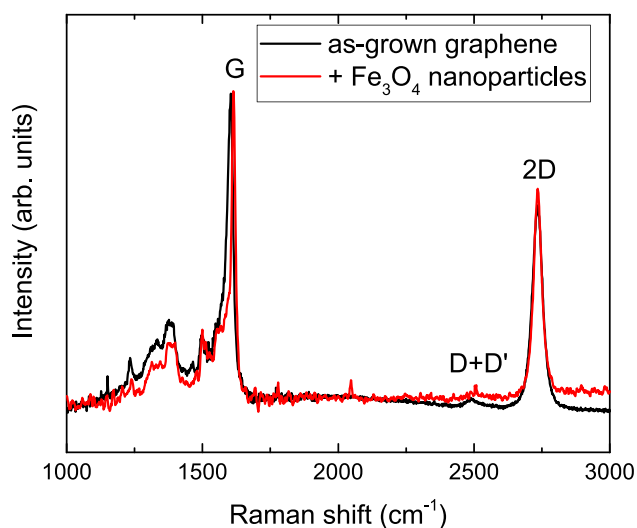


Fig. 2. Raman spectra of the graphene surface before and after the deposition of  $\text{Fe}_3\text{O}_4$  nanoparticles on top.

peak FWHM value of around  $35 \text{ cm}^{-1}$  is an additional indicator of the high level of monolayer graphene [24].

## 3.2. Gas measurements

### 3.2.1. Surface decoration

After the verification that the graphene sensors were successfully decorated with nanoparticles and that the graphene structure is maintained, gas measurements were performed. It was already shown in earlier work that  $\text{TiO}_2$  nanoparticle decorated graphene sensors can be used for formaldehyde detection [16]. Here, the response of  $\text{Fe}_3\text{O}_4$  nanoparticle decorated graphene is used for the detection of the even more toxic benzene. The sensor was exposed for 40 min towards 100, 50, 10 and 5 ppb benzene at  $150 \text{ }^\circ\text{C}$  in dry air, respectively. Each exposure was conducted twice and the final resistance signal was processed to show the data without drift. The sensor response is shown in Fig. 3. The response is defined as  $\text{Response} = \frac{R - R_0}{R_0}$ , where  $R$  is the saturated resistance signal and  $R_0$  corresponds to the baseline resistance before the exposure. It can be clearly seen that the sensor response is distinct over the whole range and even an exposure towards only 5 ppb benzene leads to a significant change of  $7 \Omega$  or 0.3%. Although this value is very small, it is no problem to detect it with the used setup, because the sensor has a very high signal to noise ratio of 35 dB towards 5 ppb benzene, calculated based on a noise level of three times the standard deviation of the baseline signal. Since benzene has no safety level yet, due to difficulties in determining its toxicity at trace concentrations, the aim has to be to measure concentrations as low as possible. Indeed benzene has been shown to be carcinogenic at any concentration [25]. With a detection of 5 ppb of benzene, we reach the range of safety level for other VOCs like formaldehyde. Moreover, it can be clearly seen that the detection limit is not yet reached and even concentrations in the sub-ppb level should be possible to detect with this sensor (5 ppb is the lowest reliable concentration permitted by the experimental setup), making it even more promising for benzene monitoring.

### 3.2.2. UV-light illumination

UV light can be used to additionally change surface properties and enhance the sensing performance [18]. Especially for graphene, it was shown that UV light illumination can be attributed to cleaning of the surface, hence freeing active sites for target gas adsorption [26]. This is demonstrated on a  $\text{TiO}_2$  nanoparticle decorated graphene sensor detecting different levels of oxygen. Fig. 4 shows the difference of the same sensor at  $100 \text{ }^\circ\text{C}$  and exposed to a varying oxygen percentage between 15 and 2% (from a baseline of 20%), without (a) and with (b) UV light illumination throughout the whole measurement. Not only does the UV light introduce a change in the baseline resistance of about  $-270 \Omega$ , but it can also be clearly seen that there is almost no distinct

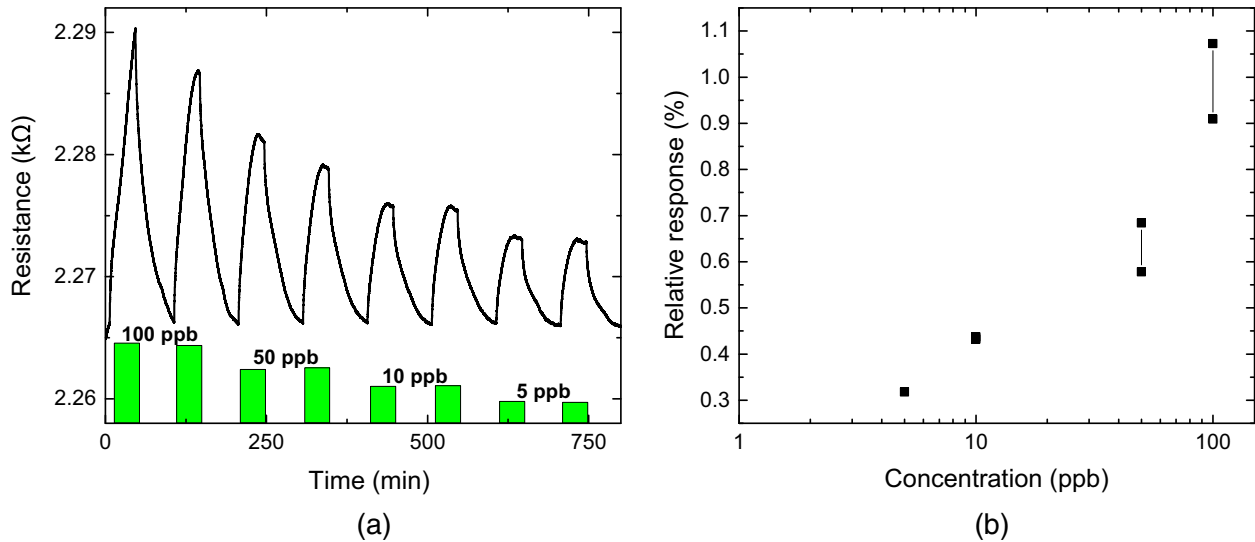


**Fig. 3.** Sensor response (a) of  $Fe_3O_4$  decorated graphene sensor at  $150\text{ }^\circ\text{C}$  towards different benzene concentrations of 100, 50, 10 and 5 ppb. (b) Shows the relative response versus benzene concentration for the exposures shown in (a).

change of resistance (response) without UV light, whereas the measurement with UV illumination shows the typical shape of a gas sensor response. Moreover, the desorption process is enhanced under the illumination, decreasing the time needed for the sensor to get back to its baseline after the gas exposure, making it faster and more effective. Indeed the low response without UV is likely due to an oxygen saturated surface in the background of 20%  $O_2$ ; UV illumination promotes oxygen desorption, leading to an increased dynamic range for oxygen detection.

### 3.2.3. Signal processing

As a final step, smart data processing is evaluated towards decreasing the time constants needed for a good sensor response. It was already shown above that the introduction of UV light enhances the sensor, but still, time constants ( $\tau_{90}$ ) of around 1600 s for adsorption are needed before the sensor signal saturates (see Fig. 5(a) blue line). In this measurement, oxygen was varied between 16 and 1% (from a baseline of 20%) with a varying exposure time of 5 and 10 min while the sensor

was used at  $200\text{ }^\circ\text{C}$  and UV light was applied. Instead of waiting until the sensor response reaches a saturated level, we introduce the use of the time derivative signal. This signal is equal to the slope of the change in resistance during the measurement and as one can clearly see on the red line with the right y-axis in Fig. 5(a), also the derivative signal exhibits distinct peaks for the gas exposures with not much change after this peak hits its maximum. After smoothing the data with a moving average filter, the time constant for the derivative signal peak can be calculated. The improvement in response time resulting from having to expose the sensor just the time needed to reach the maximum of the derivative signal is in this case up to a factor of 25. For example the sensor needs 1540 s to reach  $\tau_{90}$  (90% of the saturated response), whereas it only needs 60 s to reach  $\tau_{90}$  of the derivative signal, for a change to 10% oxygen. Moreover, the peak height of the derivative signal also corresponds to the concentration and could consequently be used as a sensor response. However, the desorption peak heights do not correspond that clearly to the concentration. Because of the smaller time constants,

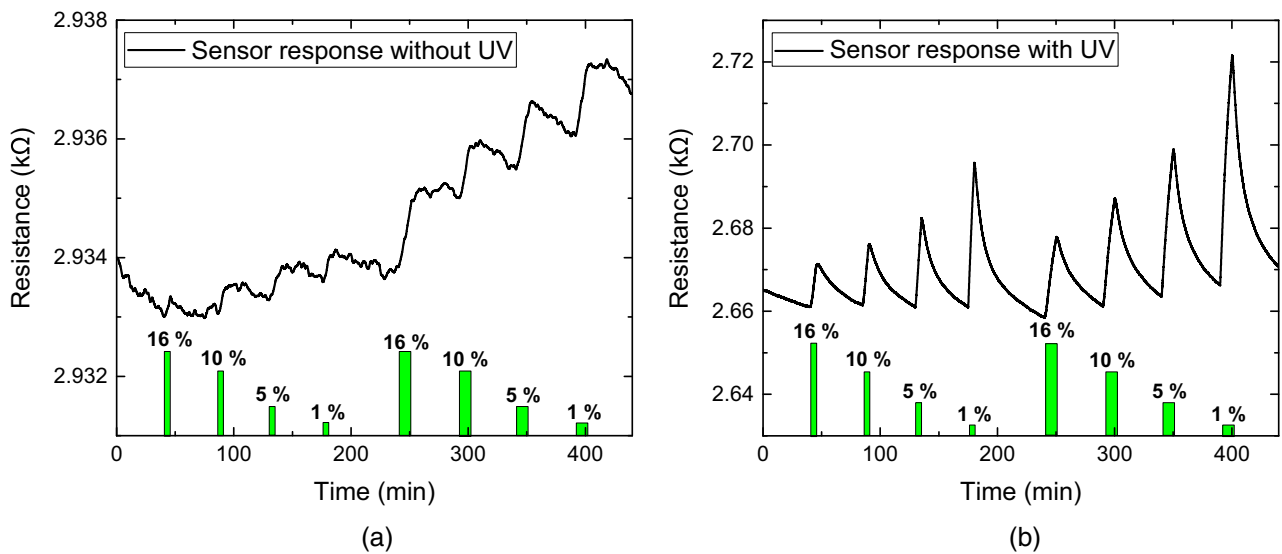


**Fig. 4.** Sensor response of  $TiO_2$  nanoparticle decorated graphene sensor at  $100\text{ }^\circ\text{C}$  towards a change of oxygen from a background of 20% to between 16 and 1% (a) without and (b) with UV light illumination.

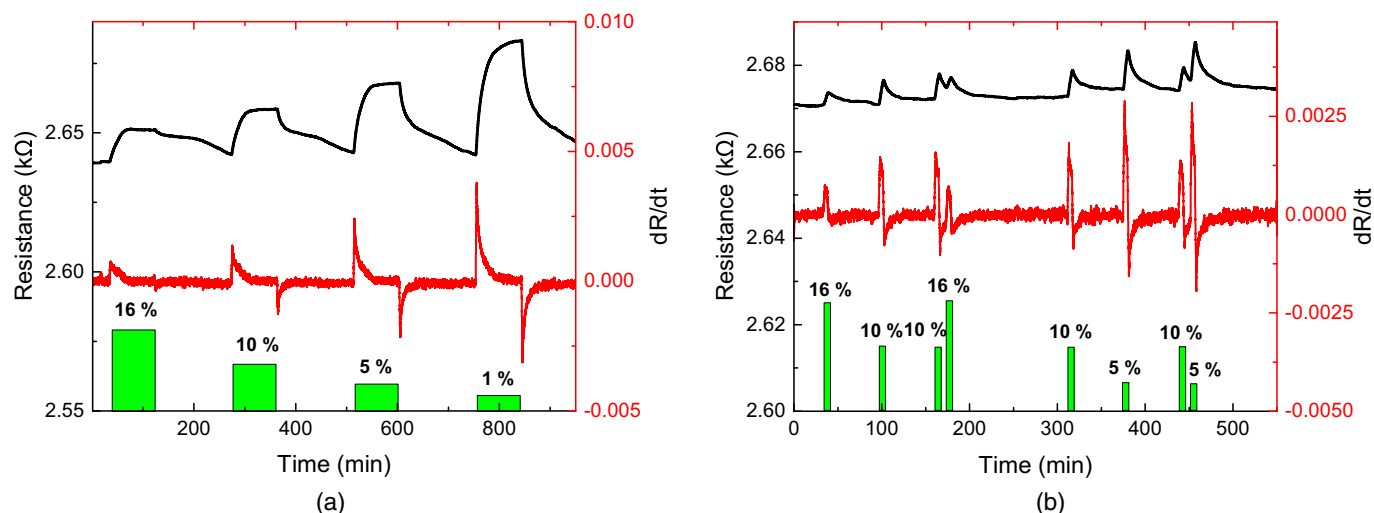


**Fig. 5.** (a) Sensor responses (black upper line with left y-axis) and time derivative of the responses (red lower line with right y-axis) of TiO<sub>2</sub> nanoparticle decorated graphene sensor at 200 °C towards a change of oxygen between 16 and 1% (from a baseline of 20%) with UV light illumination. (b) Response of the raw sensor signal and the time derivative signal upon incomplete sensor signal recovery between changes in gas concentration.

the actual sensor response does not have to be saturated when using the slope instead of the absolute value of resistance.

Fig. 5(b) shows what happens when the actual sensor signal is not fully recovered before the next concentration is introduced. Not only the derivative response is very stable for the different concentrations, the response magnitude is also stable if the raw sensor signal is not fully recovered, but the exposure time exceeds the time needed for the derivative signal to reach its maximum.

This behavior was also found for other sensing layers and other test gases, leading to a huge improvement when it comes to time constants. This can be especially useful for applications where short sampling times are needed, for example air quality monitoring.

#### 3.2.4. Sensor design implications

The sensor design described in this study is completely scalable: the use of epitaxial graphene on SiC allows wafer scale production of devices that can be processed directly on the as-grown material as the graphene is grown on a semi-insulating substrate. The sputter-based technique used for nanoparticle deposition can be done on several wafers in one run, and the UV-LED is an off the shelf product which can be easily integrated into a sensor layout.

## 4. Conclusion

The successful decoration of epitaxial graphene sensors with metal oxide nanoparticles (TiO<sub>2</sub> and Fe<sub>3</sub>O<sub>4</sub>) using hollow cathode sputtering without damaging the graphene surface was shown using AFM and Raman. With the iron oxide nanoparticle decorated graphene sensor, it was easily possible to detect benzene down to 5 ppb making it a promising sensor setup for ultra-high sensitivity gas sensors for VOC detection. It was also shown that with illumination with UV light of the titanium oxide nanoparticle decorated graphene sensor during the gas exposure, sensitivity towards a change of oxygen could be created where almost none could be seen without the UV light. As a final improvement, the time derivative signal was introduced to show that time constants can be decreased by at least one order of magnitude and that it might be used as a sensor response because it exhibits distinct changes corresponding to the applied gas concentration even if the actual sensor response is not saturated or if a new exposure takes place before the sensor had time to fully relax. All these three means of sensor improvement show very promising results for future sensor

setups and will be investigated further to optimize sensitivity, selectivity and time constants of epitaxial graphene based gas sensors.

#### Data availability

The raw/processed data required to reproduce these findings cannot be shared at this time due to technical or time limitations. The authors will happily share data with anyone interested on request.

#### Acknowledgements

The authors would like to thank Anita Lloyd Spetz for discussion and support. Moreover, we thank the Swedish Foundation for Strategic research (SSF) for financial support through the grant GMT14-0077. We acknowledge support from the Swedish Government Strategic Research Area in Materials Science on Functional Materials at Linköping University (Faculty Grant SFO-Mat-LiU # 2009-00971). This work has been supported by The Centre in Nano science and technology (CeNano) through the project “Graphene-nanoparticle hybrid gas sensor”.

#### References

- [1] World Health Organisation, Indoor Air Quality: Organic Pollutant, Copenhagen, 1989.
- [2] Council of the European Union, Off. J. Eur. Communities L152 (2008) 1–43.
- [3] World Health Organisation, Inheriting a Sustainable World? Atlas on Children's Health and the Environment, Geneva, 2017 (ISBN 978 92 415 1177 3).
- [4] BCC Research, Portable Gas Detection Systems: Global Markets, 2016.
- [5] A.C. Ferrari, et al., Science and technology roadmap for graphene, related two-dimensional crystals, and hybrid systems, *Nano* 7 (2015) 4598.
- [6] S.S. Varghesea, S. Lonkara, K.K. Singhc, S. Swaminathan, A. Abdalad, Recent advances in graphene based gas sensors, *Sensors Actuators B* 218 (2015) 160–183.
- [7] R. Pearce, J. Eriksson, T. Iakimov, L. Hultman, A. Lloyd Spetz, R. Yakimova, On the differing sensitivity to chemical gating of single and double layer epitaxial graphene explored using scanning kelvin probe microscopy, *ACS Nano* 7 (5) (2013) 4647–4656.
- [8] C. Virojanadara, M. Syväjärvi, R. Yakimova, L.L. Johansson, *Phys. Rev. B* 78 (2008), 245403.
- [9] A. Tzalenchuk, S. Lara-Avila, A. Kalaboukhov, S. Paolillo, M. Syväjärvi, R. Yakimova, O. Kazakova, T.J.B.M. Janssen, V. Fal'ko, S. Kubatin, Towards a quantum resistance standard based on epitaxial graphene, *Nat. Nanotechnol.* 5 (2010) 186–189.
- [10] Jens Eriksson, Donatella Puglisi, Yu Hsuan Kang, Rositza Yakimova, Anita Lloyd Spetz, Adjusting the electronic properties and gas reactivity of epitaxial graphene by thin surface metallizations, *Physica B* 439 (2014) 105–108.
- [11] J. Eriksson, D. Puglisi, C. Strandqvist, R. Gunnarsson, S. Ekeröth, I.G. Ivanov, U. Helmersson, K. Uvdal, R. Yakimova, A. Lloyd Spetz, Modified epitaxial graphene on SiC for extremely sensitive and selective gas sensors, *Mater. Sci. Forum* 858 (2016) 1145–1148.

- [12] F.-L. Meng, H.-H. Li, L.-T. Kong, J.-Y. Liu, Z. Jin, W. Li, Y. Jia, J.-H. Liu, X.-J. Huang, Parts per billion-level detection of benzene using SnO<sub>2</sub>/graphene nanocomposite composed of sub-6 nm SnO<sub>2</sub> nanoparticles, *Anal. Chim. Acta* 736 (2012) 100–107.
- [13] S. Mao, S.M. Cui, G.H. Lu, K.H. Yu, Z.H. Wen, J.H. Chen, Tuning gas-sensing properties of reduced graphene oxide using tin oxide nanocrystals, *J. Mater. Chem.* 22 (2012) 11009–11013.
- [14] S. Liu, B. Yu, H. Zhang, T. Fei, T. Zhang, Enhancing NO<sub>2</sub> gas sensing performances at room temperature based on reduced graphene oxide–ZnO nanoparticles hybrids, *Sens. Actuators B Chem.* 202 (2014) 272–278.
- [15] G. Singh, A. Choudhary, D. Haranath, A.G. Joshi, N. Singh, S. Singh, R. Pasricha, ZnO decorated luminescent graphene as a potential gas sensor at room temperature, *Carbon* 50 (2012) 385–394.
- [16] A. Esfandiari, S. Ghasemi, A. Irajizad, O. Akhavan, M.R. Gholami, The decoration of TiO<sub>2</sub>/reduced graphene oxide by Pd and Pt nanoparticles for hydrogen gas sensing, *Int. J. Hydrog. Energy* 37 (2012) 15423–15432.
- [17] R. Gunnarsson, U. Helmersson, I. Pilch, Synthesis of titanium-oxide nanoparticles with size and stoichiometry control, *J. Nanopart. Res.* 17 (9) (2015) 1–11.
- [18] M. Kodu, A. Berholts, T. Kahro, T. Avarmaa, A. Kasikov, A. Niilisk, H. Alles, R. Jaaniso, Highly sensitive NO<sub>2</sub> sensors by pulsed laser deposition on graphene, *Appl. Phys. Lett.* 109 (2016), 113108.
- [19] A. Schütze, T. Baur, M. Leidinger, W. Reimringer, R. Jung, T. Conrad, T. Sauerwald, Highly sensitive and selective VOC sensor systems based on semiconductor gas sensors: how to? *Environments* 4 (2017) 20.
- [20] R. Yakimova, C. Virojanadara, D. Gogova, M. Syväjärvi, D. Siche, K. Larsson, L.I. Johansson, Analysis of the formation conditions for large area epitaxial graphene on SiC substrates, *Mater. Sci. Forum* 565–568 (2010) 645.
- [21] I. Pilch, D. Söderström, M.I. Hasan, U. Helmersson, N. Brenning, Fast growth of nanoparticles in a hollow cathode plasma through orbit motion limited ion collection, *Appl. Phys. Lett.* 103 (19) (2013), 193108.
- [22] A. Lloyd Spetz, M. Andersson, Technology and Application Opportunities for SiC-FET Gas Sensors, *Solid State Gas Sensors - Industrial Application*, 281, 2012.
- [23] D.S. Lee, C. Riedl, B. Krauss, K. von Klitzing, U. Starke, J.H. Smet, Raman spectra of epitaxial graphene on SiC and of epitaxial graphene transferred to SiO<sub>2</sub>, *Nano Lett.* 8 (12) (2008) 4320–4325.
- [24] A.C. Ferrari, Raman spectroscopy of graphene and graphite: disorder, electron-phonon coupling, doping and nonadiabatic effects, *Solid State Commun.* 143 (2007) 47–57.
- [25] WHO Guidelines for Indoor Air Quality: Selected Pollutants 2010 (ISBN 978 92 890 0213 4).
- [26] A. Berholts, T. Kahro, A. Floren, H. Alles, R. Jaaniso, Photo-activated oxygen sensitivity of graphene at room temperature, *Appl. Phys. Lett.* 105 (16) (2014), 163111.

PAPER **II**



Article

# Graphene Decorated with Iron Oxide Nanoparticles for Highly Sensitive Interaction with Volatile Organic Compounds <sup>†</sup>

Marius Rodner <sup>1,\*</sup> , Donatella Puglisi <sup>1</sup> , Sebastian Ekeroth <sup>2</sup> , Ulf Helmersson <sup>2</sup>,  
Ivan Shteplyuk <sup>3</sup> , Rositsa Yakimova <sup>3</sup>, Andreas Skallberg <sup>4</sup>, Kajsa Uvdal <sup>4</sup>, Andreas Schütze <sup>5</sup>   
and Jens Eriksson <sup>1</sup>

<sup>1</sup> Applied Sensor Science Unit, IFM, Linköping University, 58183 Linköping, Sweden; donatella.puglisi@liu.se (D.P.); jens.eriksson@liu.se (J.E.)

<sup>2</sup> Plasma & Coatings Physics Division, IFM, Linköping University, 58183 Linköping, Sweden; sebastian.ekeroth@liu.se (S.E.); ulf.helmersson@liu.se (U.H.)

<sup>3</sup> Semiconductor Materials Division, IFM, Linköping University, 58183 Linköping, Sweden; ivan.shteplyuk@liu.se (I.S.); rositsa.yakimova@liu.se (R.Y.)

<sup>4</sup> Division of Molecular Surface Physics & Nanoscience, IFM, Linköping University, 58183 Linköping, Sweden; andreas.skallberg@liu.se (A.S.); kajsa.uvdal@liu.se (K.U.)

<sup>5</sup> Lab for Measurement Technology, Department of Systems Engineering, Saarland University, 66041 Saarbrücken, Germany; schuetze@imt.uni-saarland.de

\* Correspondence: marius.rodner@liu.se; Tel.: +46-700-896785

<sup>†</sup> This paper is an extended version of the conference paper: Iron Oxide Nanoparticle Decorated Graphene for Ultra-Sensitive Detection of Volatile Organic Compounds. In Proceedings of the EUROSENSORS 2018, Graz, Austria, 9–12 September 2018.

Received: 29 January 2019; Accepted: 19 February 2019; Published: 22 February 2019



**Abstract:** Gases, such as nitrogen dioxide, formaldehyde and benzene, are toxic even at very low concentrations. However, so far there are no low-cost sensors available with sufficiently low detection limits and desired response times, which are able to detect them in the ranges relevant for air quality control. In this work, we address both, detection of small gas amounts and fast response times, using epitaxially grown graphene decorated with iron oxide nanoparticles. This hybrid surface is used as a sensing layer to detect formaldehyde and benzene at concentrations of relevance (low parts per billion). The performance enhancement was additionally validated using density functional theory calculations to see the effect of decoration on binding energies between the gas molecules and the sensor surface. Moreover, the time constants can be drastically reduced using a derivative sensor signal readout, allowing the sensor to work at detection limits and sampling rates desired for air quality monitoring applications.

**Keywords:** epitaxial graphene; metal oxide nanoparticle; gas sensor; volatile organic compounds; benzene; formaldehyde; derivative sensor signal; air quality sensor

## 1. Introduction

Several toxic air pollutants in more than 80% of the urban areas where air pollution is monitored exceed the World Health Organization's (WHO) recommended safe exposure levels. Poor air quality has been associated with several negative health aspects ranging from less severe conditions, such as skin and eye irritation, to more acute respiratory problems, cancer, or death. Air pollution has been estimated to cause 8 million annual deaths and to financially burden the European region by about 1.6 trillion US dollars per year [1,2].

Air quality (AQ) monitoring and control using extremely sensitive sensors are crucial from the viewpoint of preventing further deaths and diseases correlated with toxic air substances. However, commercial sensors/instruments available today are either large, expensive, and complex or small but limited by poor selectivity, sensitivity, and a slow sampling rate [3]. In addition, there are no commercially available sensors with sufficiently low detection limits to monitor carcinogenic volatile organic compounds (VOCs), such as formaldehyde ( $\text{CH}_2\text{O}$ ) and benzene ( $\text{C}_6\text{H}_6$ ), at levels of relevance to human health. Benzene is a genotoxic aromatic compound, especially associated with leukemia. There are no safe exposure limits for  $\text{C}_6\text{H}_6$  according to the last published WHO recommendations [4], however the European Air Quality Directive guidelines [5] recommend an exposure limit of 1.6 parts per billion (ppb), and in France, which has very strict guidelines, the limit is 0.6 ppb [6].

In the future, AQ assessment should ideally be based on real-time monitoring of air pollutants with high spatial resolution [7], allowing pollution mapping and forecasting. This can only be satisfied by utilizing low-cost monitoring devices of small size. Szulczynski et al. [3] recently published a review of currently commercially available sensors for VOC detection in outdoor and indoor air, in which they concluded that current sensor technologies suffer from too high limit of detection or poor selectivity.

In a report by Spinelle et al. from 2017, commercially available portable low-cost sensors for VOCs were reviewed, and it was found that few sensors can detect  $\text{C}_6\text{H}_6$  at the concentrations of relevance for AQ monitoring [8], with most sensors showing detection limits that are at least one order of magnitude above the guideline levels. Some of these small sensors can reach a low  $\text{C}_6\text{H}_6$  detection limit down to 0.5 ppb. Unfortunately, none of the sensors are selective to a particular VOC, making it impossible to distinguish, e.g., the  $\text{C}_6\text{H}_6$  concentration. Some of the reviewed sensors also include a selective absorbing cartridge for benzene. Unfortunately, the best limit of detection for commercially available sensors selective to  $\text{C}_6\text{H}_6$  was found to be 10 ppb for the Ion Science Tiger Select (Ion Science, Great Britain).

Among state-of-the-art research studies on portable AQ sensors [9], there are reports of prototypes including gas sensitive field effect transistors based on silicon carbide (SiC-FETs) that allow detection of 1–3 ppb of  $\text{C}_6\text{H}_6$  [10]. Both SiC-FETs [11] and metal-oxide based sensors [12] operated in Temperature Cycled Operation can yield selectivity to specified VOCs. A drawback of this approach is the required sampling time, which increases the response time. An approach to improve the detection limit even further is the use of pre-concentrators [13], in which the gas concentration is temporarily increased by adsorbing gas over a long time and then releasing it. A similar approach is used by Trzcinski et al., where a miniaturized photoionization detector is coupled to a specifically designed pre-concentrator with selective desorption of benzene [14]. However, also those approaches have a prolonged response time as a drawback.

A low cost, portable sensor capable of detecting benzene at 1 ppb or lower concentrations would thus constitute a breakthrough in the field of air quality monitoring.

Using the unique properties of graphene as a transducer allows fabrication of sensor devices that can be used for gas detection where low concentrations can be detected, including air quality control for human health. Besides a high sensitivity, also interaction with specific target analytes and a good selectivity must be addressed to get a useful sensor device. It has already been shown that decoration of the graphene surface with metal/oxide nanoparticles can lead to a higher sensitivity and selectivity towards certain gases, e.g., nitrogen dioxide ( $\text{NO}_2$ ),  $\text{C}_6\text{H}_6$  and  $\text{CH}_2\text{O}$  [15,16]. Using a “soft” decoration approach, the surface chemistry of the sensing layer could be modified without changing the transducer’s electronic properties. In addition, zinc oxide (ZnO) fibers [17] and iron oxide ( $\text{Fe}_3\text{O}_4$ ) decorated multiwall carbon nanotubes [18] in combination with ultraviolet (UV) irradiation have shown sensitivity towards  $\text{C}_6\text{H}_6$ . However, poor reproducibility and insufficient detection limits make the state-of-the-art sensors ill-suited for human safety applications. So far, these sensors were able to detect the mentioned gases down to tens of ppb, but not reliably lower. In this paper, which is an extension of a conference contribution [19], we demonstrate how it is possible to detect even single

ppb concentrations, and we further introduce a data evaluation approach allowing fast response times to meet the criteria for AQ monitoring.

## 2. Materials and Methods

### 2.1. Sensing Layer Preparation

The graphene was grown epitaxially on silicon carbide (SiC) through a sublimation process where an on-axis, semi-insulating (0001) 4H-SiC substrate (7 mm × 7 mm) is used for the formation of graphene in argon (Ar) at a temperature of 2000 °C and a pressure of 1 bar [20]. The method allows a highly homogenous growth of monolayer graphene and requires no further transfer to another insulator. Hollow cathode pulsed plasma sputtering [21] was used to functionalize the graphene surface with iron oxide nanoparticles (NP).

### 2.2. Characterization Techniques

Before and after the deposition of nanoparticles, a series of characterization measurements was conducted to determine the graphene uniformity and quality, and to see if any damage of the graphene occurred during the deposition. Atomic Force Microscopy (AFM) (Quadrex Dimension 3100 with a Nanoscope IVa controller) was used in tapping mode to obtain topography images of the sensing layers. The measurements were performed using silicon (Si) tips (PPP-NCHR-50 from Nanosensors) with a tip radius of curvature below 7 nm. X-ray photoelectron spectroscopy (XPS) studies using a Microlab 310-F spectrometer were performed to investigate possible alterations made to the sample after deposition of NPs and to establish if Fe<sub>3</sub>O<sub>4</sub> was present on the surface.

### 2.3. Sensor Device Fabrication

As a first step, titanium on gold (Ti/Au, 2/200 nm) contact pads were thermally evaporated onto the epitaxially grown graphene on SiC (EG/SiC) before functionalization. The contacts have a size of 1 mm × 1 mm with a distance of 1 mm between them. The sensor chip and a Pt-100 resistance thermometer were glued (Aremco Ceramabond 571) onto a ceramic heater (Heraeus GmbH) to enable a controlled temperature loop, and welded to a 16 pin TO8 header to establish the electrical contacts. This device was mounted on top of a TO8-socket and connected to its pins using gold-wire bonding and silver glue (Epotek E3081). The final sensor was placed in a flow chamber connected to a gas mixing setup. A Keithley 2601B SourceMeter was used in a two-wire mode to measure the resistance between the contacts during gas exposure. The total gas flow was kept constant at 100 mL/min, and a dry mixture of 80% N<sub>2</sub> and 20% O<sub>2</sub> was used as a purging and carrier gas. A more detailed description of the measurement system can be found in a previous work [22].

### 2.4. Theoretical Approach

The adsorption of gas molecules (C<sub>6</sub>H<sub>6</sub> and CH<sub>2</sub>O) on pristine EG (PEG) and Fe<sub>3</sub>O<sub>4</sub>-decorated epitaxial graphene (DEG) on Si-face 4H-SiC was investigated based on hybrid gas-phase density functional theory (DFT) calculations performed by using Gaussian 16 Rev. B.01 program package [23]. As a model of PEG, 4 × 5 first graphene layer located above 4 × 5 buffer layer, which is covalently bonded to 4 × 4 Si-face surface of hexagonal SiC, has been chosen. DEG was simulated by full geometrical optimization of Fe<sub>3</sub>O<sub>4</sub> located on PEG. All dangling bonds are passivated by the hydrogen atoms. The calculations were carried out using M06-2X level of theory with consideration of split basis set [24]. It is important to note that the dispersion-corrected DFT functional M06-2X includes implicitly modified parameters associated with the Hartree-Fock exchange interaction, thereby allowing prediction of the weak van der Waals interaction [25]. A 6-31G basis set was used for carbon (C), silicon (Si), oxygen (O) and hydrogen (H) atoms, while a LANL2DZ (Los Alamos National Laboratory 2 Double-Zeta) basis set was utilized for Fe species [26]. All atoms

were enabled to be fully relaxed during geometrical optimization. All calculations were carried out without symmetry restrictions.

The adsorption energy of gas molecules ( $E_{\text{ads}}$ ) was calculated by using the following Equation:

$$E_{\text{ads}} = \left( E_{\text{tot}}^{\text{PEG/DEG}} + E_{\text{tot}}^{\text{gas}} \right) - E_{\text{tot}}^{\text{gas@PEG/DEG}} \quad (1)$$

where  $E_{\text{tot}}^{\text{PEG/DEG}}$  and  $E_{\text{tot}}^{\text{gas}}$  are the total energies of isolated templates and gas molecules ( $\text{C}_6\text{H}_6$  or  $\text{CH}_2\text{O}$ ), respectively, whereas  $E_{\text{tot}}^{\text{gas@PEG/DEG}}$  is the total energy of the PEG or DEG after complexation with gas molecules. Counterpoise correction for basis set superposition error (BSSE) [27] was applied for accurate prediction of the adsorption energy.

### 3. Results and Discussions

#### 3.1. Morphological and Structural Characterization

Figure 1 shows AFM graphs of the graphene sensor surface before (a) and after (b) decoration with  $\text{Fe}_3\text{O}_4$  NPs. Neglecting the characteristic steps corresponding to the SiC step bunching (typically 0.5–1.5 nm in height), the as-grown graphene surface in Figure 1a shows almost no roughness ( $R_q \approx 0.25$  nm on the terraces). The particle coverage is about 60%, and single particles have an average diameter of about 80 nm. The histogram in Figure 1c shows the width distribution for single particles and particle clusters. The main peaks arise for particles between 70 and 90 nm, but also much larger agglomerates up to 290 nm can be seen. Raman spectroscopy confirms structural integrity of the graphene surface also after the decoration [16].

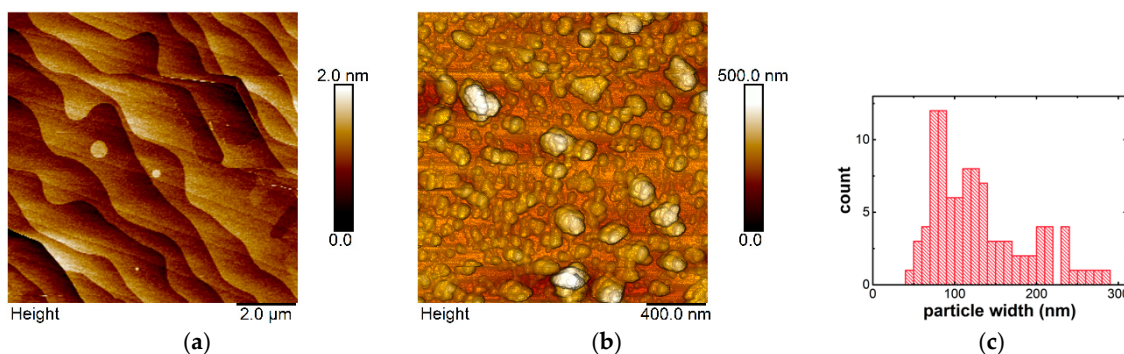


**Figure 1.** Atomic Force Microscopy (AFM) image of the graphene sensor surface before (a) and after (b) decoration with  $\text{Fe}_3\text{O}_4$  NPs, and (c) the particle width distribution.

The effect of deposition of  $\text{Fe}_3\text{O}_4$  NPs onto graphene was investigated by means of XPS. The elemental compositions of as-grown EG/SiC prior to and after deposition of  $\text{Fe}_3\text{O}_4$  NPs ( $\text{Fe}_3\text{O}_4/\text{EG}/\text{SiC}$ ) were obtained to demonstrate the presence of  $\text{Fe}_3\text{O}_4$  NPs on the latter sample. The XPS survey spectra for EG/SiC sample and  $\text{Fe}_3\text{O}_4/\text{EG}/\text{SiC}$  sample are shown in Figure 2a. The XPS survey spectrum for  $\text{Fe}_3\text{O}_4/\text{EG}/\text{SiC}$  showed the presence of iron and gold (Au) with XPS peaks  $\text{Fe}2p$ ,  $\text{Au}4d$ , and  $\text{Au}4f$  found at binding energy position about 711 eV, 340 eV and 84 eV [28]. The gold peaks in the XPS spectra come from the Ti/Au contacts (see Section 2.3). Both samples also showed the presence of oxygen, carbon, and silicon, see Figure 2 with XPS peaks  $\text{O}1s$ ,  $\text{C}1s$ ,  $\text{Si}2s$  and  $\text{Si}2p$  at binding energy positions about 532 eV, 285 eV, 151 eV and 100 eV respectively. XPS  $\text{O}1s$ ,  $\text{Fe}2p$ , and  $\text{C}1s$  core level spectra for EG/SiC and  $\text{Fe}_3\text{O}_4/\text{EG}/\text{SiC}$  are shown in Figure 2b–d. Quantification of oxygen and carbon content for EG/SiC and  $\text{Fe}_3\text{O}_4/\text{EG}/\text{SiC}$ , based on the XPS  $\text{O}1s$  and  $\text{C}1s$  core level spectra has been performed. An increase of O, estimated to be a fivefold increase, and a decrease of C, reduced to about half for  $\text{Fe}_3\text{O}_4/\text{EG}/\text{SiC}$ , were observed. The strong increase in oxygen signal is shown for  $\text{Fe}_3\text{O}_4/\text{EG}/\text{SiC}$  sample, with an additional peak at binding energy position 530.0 eV, in good agreement with the presence of the chemical structure Fe–O in  $\text{Fe}_3\text{O}_4$  NPs. XPS  $\text{Fe}2p$  core level

spectra before and after deposition of  $\text{Fe}_3\text{O}_4$  NPs are shown in Figure 2c. As expected, no iron could be detected for EG/SiC. After deposition, two strong peaks at binding energy position 710.9 eV and 724.4 eV were observed for  $\text{Fe}_3\text{O}_4$ /EG/SiC. The corresponding XPS C1s core level spectra for EG/SiC and  $\text{Fe}_3\text{O}_4$ /EG/SiC are presented in Figure 2d.

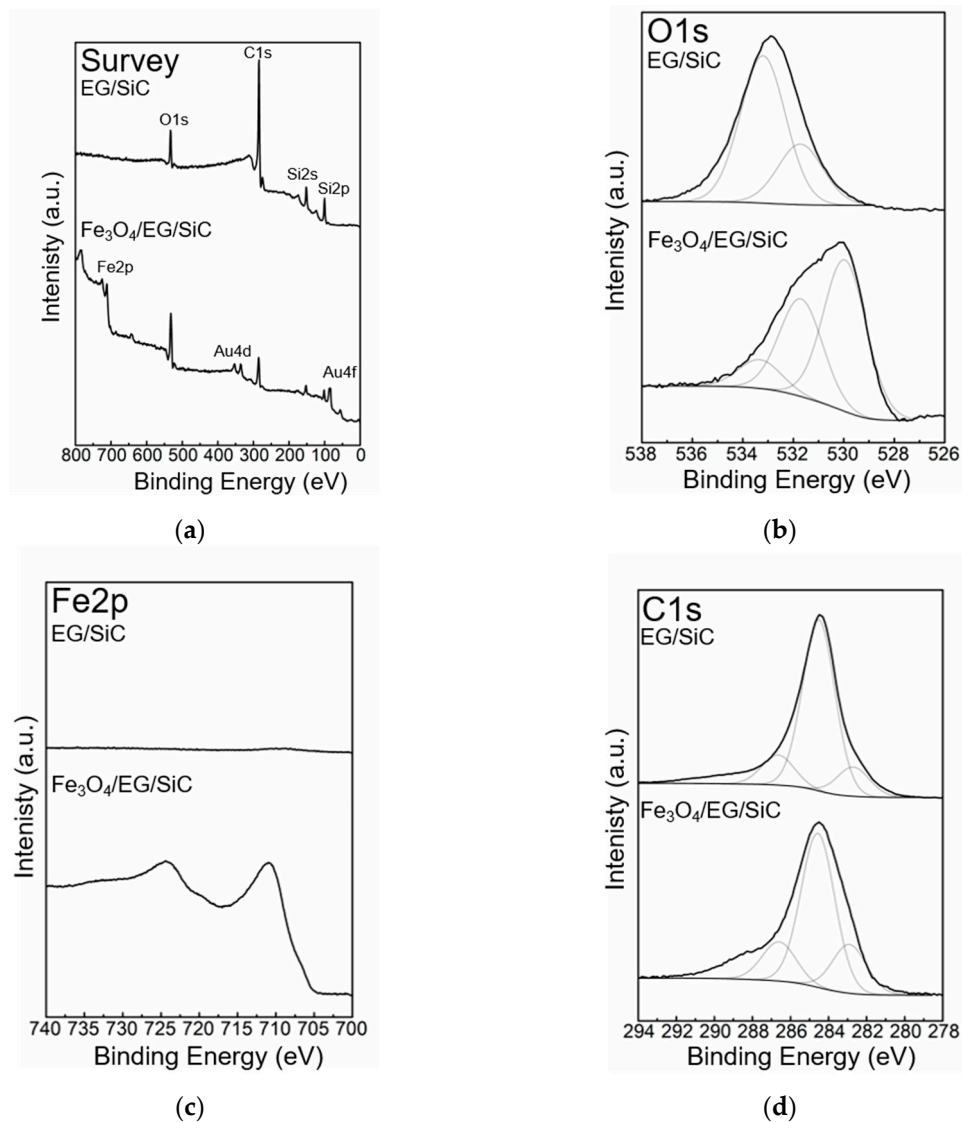


**Figure 2.** X-ray photoelectron spectroscopy (XPS) survey spectra (a), O1s (b), Fe2p (c) and C1s (d) XPS core level spectra for as-grown EG/SiC and  $\text{Fe}_3\text{O}_4$  NP deposited on graphene ( $\text{Fe}_3\text{O}_4$ /EG/SiC).

### 3.2. Gas Measurements

After the successful decoration of the graphene surface with  $\text{Fe}_3\text{O}_4$  NPs, gas measurements were performed. Figure 3a shows how the resistance of the sensor changes with the exposure towards  $\text{CH}_2\text{O}$ . The sensor was exposed to  $\text{CH}_2\text{O}$  and  $\text{C}_6\text{H}_6$  in a dry background of synthetic air using concentrations ranging from 5 parts per million (ppm) to 1 ppb, and a pulse duration of 30 min. Tests to identify a good operating temperature have been conducted and 150 °C, which is a good compromise between stability and high response, was chosen for all measurements shown here. Similar measurements with pure graphene did not show any response to both test gases. In an earlier work of ours [16], it has already been shown that  $\text{Fe}_3\text{O}_4$  nanoparticle-decorated graphene sensors can be used for formaldehyde and benzene detection, but not over such a large range and down to a single ppb. The same measurement was repeated twice in the same environment and was repeated once more approximately one year later

with the same sensor. The measured responses show some small deviations between the measurements without a clear trend of decreasing response over time. The sensor response shown here is from the first measurement. The response is defined as  $\frac{R-R_0}{R_0}$ , where  $R$  is the saturated resistance signal and  $R_0$  corresponds to the baseline resistance before the gas exposure. The raw sensor signal in Figure 3a shows that the sensor does relax completely, but a slow drift hinders the baseline resistance to stay stable over time. DFT calculations support the choice of operating temperature, as they show that it is possible to overcome the desorption barrier of  $C_6H_6$  at the sensor surface at  $150\text{ }^\circ\text{C}$  (see Figure S1). The relative response for different concentrations of the two target gases is shown in Figure 3b. A distinct response for both gases over the whole range can clearly be observed. Both formaldehyde and benzene can be quantitatively measured down to a single ppb. The relative responses towards 1 ppb  $CH_2O$  and  $C_6H_6$  are about 0.04% and 0.02%, respectively. It is worth to be noticed that the WHO recommended safety limit for  $CH_2O$  (81 ppb over 30 min of exposure) is easily reached with a relative response above 0.1%.

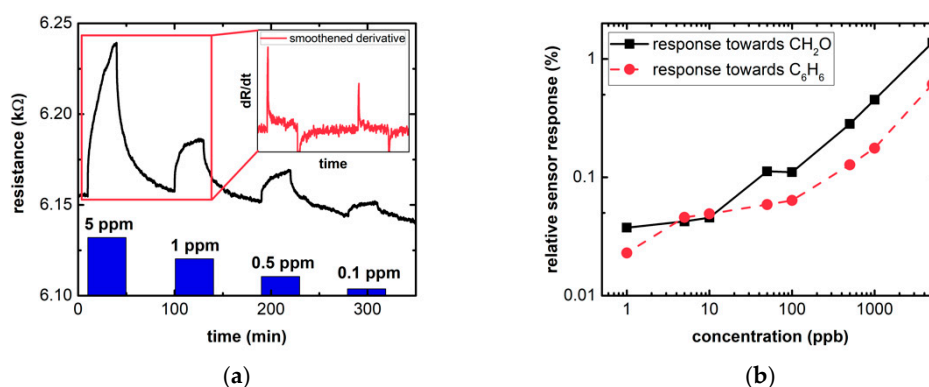


**Figure 3.** (a) Sensor behavior exemplarily shown for the first four exposures (5 ppm–0.1 ppm, 30 min exposure and relaxation) towards formaldehyde at  $150\text{ }^\circ\text{C}$  in dry air with the smoothed derivative signal as inset and (b) relative sensor response towards different concentrations of formaldehyde and benzene.

Besides a very good sensitivity, also time constants of these measurements need to be addressed. For an application in indoor air monitoring, the time constants for the sensor should be in the range of half a minute to several minutes, depending on the application. However, as shown in Figure 3a, even an exposure towards the gas over 30 min does not lead to a saturated sensor response. Using the time it takes for the first order time derivative of the sensor signal to reach its maximum for each exposure instead, the time constant can be decreased significantly. This is exemplarily shown for the first two exposures in the inset in Figure 3a, comparing the raw sensor signal with  $dR/dt$  (after smoothing the data with a 500-point moving average filter), where the time derivative signal reaches its maximum value after about 50 s. It is evident from the insert that  $dR/dt$  exhibits distinct peaks in response to  $CH_2O$  and the peak values are concentration dependent. Because of the smaller time constants needed to reach maximum  $dR/dt$ , the actual sensor signal does not have to be saturated when using the rate of change instead of the absolute value of resistance. It is therefore possible to significantly improve the speed of the sensor by utilizing  $dR/dt$  as a sensor parameter.

### 3.3. DFT Calculations

An efficiency of the decoration approach towards gas sensing can be directly demonstrated and validated by the DFT results. For this aim, a comparative analysis of the adsorption of benzene and formaldehyde onto non-decorated and  $Fe_3O_4$ -decorated epitaxial graphene was performed. Energetically favored adsorption configurations of considered gas molecules on PEG and DEG are illustrated in Figure 4. The adsorption energy for  $C_6H_6$  on DEG,  $E_{ads} = 1.795\text{ eV}$ , is significantly higher than on PEG with a value of  $E_{ads} = 0.284\text{ eV}$ . In the absence of the  $Fe_3O_4$  nanoparticle,  $C_6H_6$  molecule

adsorbs in the flat geometry, which is parallel to the surface. In this case, the center of  $C_6H_6$  ring lays on top of a carbon atom belonging to graphene. On the other hand, a functionalization of graphene with  $Fe_3O_4$  causes the formation of a strong chemical bond between  $C_6H_6$  ring and one of the Fe atoms, facilitating the  $C_6H_6$  adsorption in the tilted geometry regarding the graphene surface. Like the situation for  $C_6H_6$ , we found that  $CH_2O$  molecule prefers to accommodate in a parallel geometry to graphene surface with weak adsorption energy of 0.149 eV, while the energetically preferred adsorption mode for  $CH_2O$  on DEG is related to the formation of strong Fe-O covalent bond with a bond length of the 1.98 Å. The calculated adsorption energy of 1.870 eV is much higher than the value predicted for adsorption on pristine graphene sample, implying the strong chemisorption case. To summarize, one can conclude that weak physisorption of gas molecules on non-decorated graphene is immediately changed to strong chemisorption when iron oxide NPs are involved in adsorption phenomena. From an experimental point of view, the observed chemical similarity between adsorption configurations of benzene and formaldehyde enables us to anticipate comparable responses of  $Fe_3O_4$ -decorated epitaxial graphene to exposure of both gases, with slightly higher sensitivity towards formaldehyde.

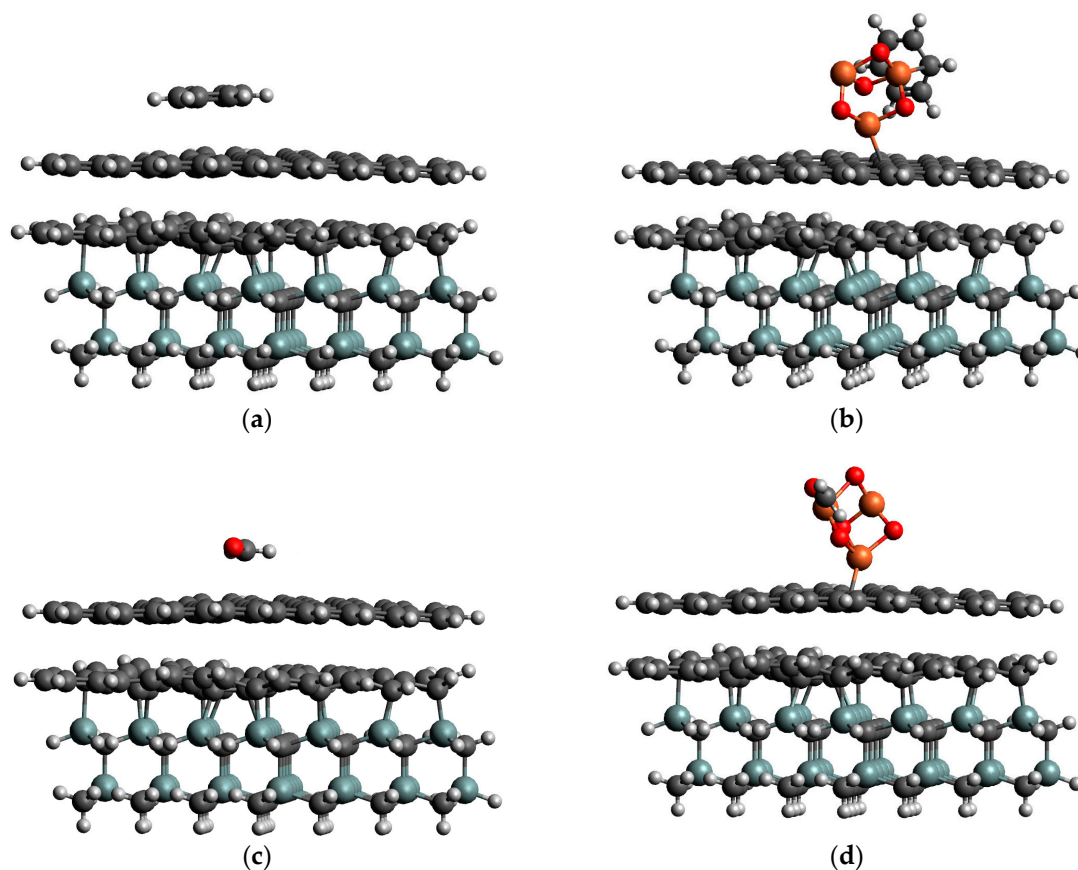


**Figure 4.** Optimized adsorption configurations of benzene on (a) PEG and (b) DEG. Preferred adsorption geometries of formaldehyde on PEG and DEG are presented as (c) and (d).

#### 4. Conclusions

Benzene and Formaldehyde sensing properties were investigated using epitaxially grown graphene on silicon carbide decorated with  $Fe_3O_4$  NPs. We could verify the decoration and the integrity of the graphene surface using AFM and XPS. With this sensor platform, concentrations down to a single ppb of toxic VOCs could be quantitatively measured, which makes it very promising for air quality monitoring. DFT calculations show that the gas molecules are more likely to bind to the decorated sensor surface. Moreover, by evaluating the first-order time derivative of the sensor signal,

it was possible to significantly enhance the speed of the sensor, yielding response times of less than one minute, in turn allowing sampling rates desired in air quality monitoring.

**Supplementary Materials:** The following are available online at <http://www.mdpi.com/1424-8220/19/4/918/s1>, Figure S1: Reaction energy profile corresponding to benzene desorption. IS, TS and FS represent the initial state, transition state and final state, respectively.

**Author Contributions:** Conceptualization, M.R., D.P. and J.E.; methodology, M.R., A.S. (Andreas Skallberg), S.E. and I.S.; software, I.S.; validation, M.R. and I.S.; formal analysis, M.R., A.S. (Andreas Skallberg) and I.S.; investigation, M.R., A.S. (Andreas Skallberg) and I.S.; resources, A.S. (Andreas Schütze); data curation, M.R., A.S. (Andreas Skallberg) and I.S.; writing—original draft preparation, M.R., A.S. (Andreas Skallberg) and I.S.; writing—review and editing, M.R., D.P., S.E., U.H., I.S., R.Y., A.S. (Andreas Skallberg), K.U., A.S. (Andreas Schütze) and J.E.; visualization, M.R., A.S. (Andreas Skallberg) and I.S.; supervision, J.E.; project administration, J.E.; funding acquisition, J.E.

**Funding:** This research was funded by the Swedish Foundation for Strategic research (SSF) for financial support through the grants GMT14-0077 and RMA15-024, and Knut and Alice Wallenberg Foundation through grant KAW14.0276. This work has been supported by The Centre in Nano science and technology (CeNano) through the project “Graphene-nanoparticle hybrid gas sensor” and the Swedish Government Strategic Research Area in Materials Science on Functional Materials at Linköping University (Faculty Grant SFO-Mat-LiU #2009-00971), the Knut and Alice Wallenberg Foundation through Grant No. 2012.0083. I.S. acknowledges the support from Ångpanneföreningens Forskningsstiftelse (Grant 16-541). The research part in Germany was financed by a Hans Werthén Foundation grant.

**Acknowledgments:** The authors would like to thank Anita Lloyd Spetz and Manuel Bastuck for valuable discussion and support. DFT calculations were performed using the supercomputer resources of the Swedish National Infrastructure for Computing (SNIC), National Supercomputing Center (NSC).

**Conflicts of Interest:** The authors declare no conflict of interest.

## References

1. WHO Social Media Toolkit for Air Pollution and Child Health: Prescribing Clean Air Launch. Available online: [https://www.who.int/ceh/publications/Social\\_Media\\_Toolkit\\_AirPollution\\_Children\\_Health\\_Report\\_Launch.pdf](https://www.who.int/ceh/publications/Social_Media_Toolkit_AirPollution_Children_Health_Report_Launch.pdf) (accessed on 21 February 2019).
2. Economic Cost of the Health Impact of Air Pollution in Europe: Clean Air, Health and Wealth. Available online: [http://www.euro.who.int/\\_\\_data/assets/pdf\\_file/0004/276772/Economic-cost-health-impact-air-pollution-en.pdf](http://www.euro.who.int/__data/assets/pdf_file/0004/276772/Economic-cost-health-impact-air-pollution-en.pdf) (accessed on 21 February 2019).
3. Szulczyński, B.; Gębicki, J. Currently Commercially Available Chemical Sensors Employed for Detection of Volatile Organic Compounds in Outdoor and Indoor Air. *Environments* **2017**, *4*, 21. [CrossRef]
4. World Health Organization. Guidelines for Indoor Air Quality: Selected Pollutants. Available online: [http://www.euro.who.int/\\_\\_data/assets/pdf\\_file/0009/128169/e94535.pdf](http://www.euro.who.int/__data/assets/pdf_file/0009/128169/e94535.pdf) (accessed on 21 February 2019).
5. Directive 2008/50/EC of the European Parliament and of the Council of 21 May 2008 on Ambient Air Quality and Cleaner Air for Europe. Available online: <http://eur-lex.europa.eu/LexUriServ/LexUriServ.do?uri=OJ:L:2008:152:0001:0044:EN:PDF> (accessed on 21 February 2019).
6. Décret no 2011-1727 du 2 Décembre 2011 Relatif aux Valeurs-Guides pour L’air Intérieur pour le Formaldéhyde et le Benzène. Available online: <https://www.legifrance.gouv.fr/eli/decret/2011/12/2/2011-1727/jo/texte> (accessed on 21 February 2019).
7. Batterman, S.; Chambliss, S.; Isakov, V. Spatial resolution requirements for traffic-related air pollutant exposure evaluations. *Atmos. Environ.* **2014**, *94*, 518–528. [CrossRef] [PubMed]
8. Spinelle, L.; Gerboles, M.; Kok, G.; Persijn, S.; Sauerwald, T. Review of portable and low-cost sensors for the ambient air monitoring of benzene and other volatile organic compounds. *Sensors* **2017**, *17*, 1520. [CrossRef] [PubMed]
9. Schütze, A.; Baur, T.; Leidinger, M.; Reimringer, W.; Jung, R.; Conrad, T.; Sauerwald, T. Highly Sensitive and Selective VOC Sensor Systems Based on Semiconductor Gas Sensors: How to? *Environments* **2017**, *4*, 20. [CrossRef]
10. Puglisi, D.; Eriksson, J.; Bur, C.; Schuetze, A.; Lloyd Spetz, A.; Andersson, M. Catalytic metal-gate field effect transistors based on SiC for indoor air quality control. *J. Sens. Sens. Syst.* **2015**, *4*, 1–8. [CrossRef]

11. Bur, C.; Bastuck, M.; Puglisi, D.; Schütze, A.; Lloyd Spetz, A.; Andersson, M. Discrimination and quantification of volatile organic compounds in the ppb-range with gas sensitive SiC-FETs using multivariate statistics. *Sens. Actuators B Chem.* **2015**, *214*, 225–233. [CrossRef]
12. Leidinger, M.; Sauerwald, T.; Reimringer, W.; Ventura, G.; Schütze, A. Selective detection of hazardous VOCs for indoor air quality applications using a virtual gas sensor array. *J. Sens. Sens. Syst.* **2014**, *3*, 253–263. [CrossRef]
13. Leidinger, M.; Rieger, M.; Sauerwald, T.; Alépée, C.; Schütze, A. Integrated pre-concentrator gas sensor microsystem for ppb level benzene detection. *Sens. Actuators B Chem.* **2016**, *236*, 988–996. [CrossRef]
14. Trzciński, J.W.; Pinalli, R.; Riboni, N.; Pedrini, A.; Bianchi, F.; Zampolli, S.; Elmi, I.; Massera, C.; Ugozzoli, F.; Dalcanale, E. In Search of the Ultimate Benzene Sensor: The EtQxBox Solution. *ACS Sens.* **2017**, *2*, 590–598. [CrossRef]
15. Eriksson, J.; Puglisi, D.; Strandqvist, C.; Gunnarsson, R.; Ekeröth, S.; Ivanov, I.G.; Helmersson, U.; Uvdal, K.; Yakimova, R.; Lloyd Spetz, A. Modified Epitaxial Graphene on SiC for Extremely Sensitive and Selective Gas Sensors. *Mater. Sci. Forum* **2016**, *858*, 1145–1148. [CrossRef]
16. Rodner, M.; Bahonjic, J.; Mathisen, M.; Gunnarsson, R.; Ekeröth, S.; Helmersson, U.; Ivanov, I.G.; Yakimova, R.; Eriksson, J. Performance tuning of gas sensors based on epitaxial graphene on silicon carbide. *Mater. Des.* **2018**, *153*, 153–158. [CrossRef]
17. Gong, J.; Li, Y.; Chai, X.; Hu, Z.; Deng, Y. UV-light-activated ZnO fibers for organic gas sensing at room temperature. *J. Phys. Chem. C* **2010**, *114*, 1293–1298. [CrossRef]
18. Clément, P.; Hafaiedh, I.; Parra, E.J.; Thamri, A.; Guillot, J.; Abdelghani, A.; Llobet, E. Iron oxide and oxygen plasma functionalized multi-walled carbon nanotubes for the discrimination of volatile organic compounds. *Carbon N. Y.* **2014**, *78*, 510–520. [CrossRef]
19. Rodner, M.; Puglisi, D.; Ekeröth, S.; Helmersson, U.; Ivanov, I.G.; Yakimova, R.; Uvdal, K.; Schütze, A.; Eriksson, J. Iron Oxide Nanoparticle Decorated Graphene for Ultra-Sensitive Detection of Volatile Organic Compounds. *Proceedings* **2018**, *2*, 985. [CrossRef]
20. Yakimova, R.; Virojanadara, C.; Gogova, D.; Syväjärvi, M.; Siche, D.; Larsson, K.; Johansson, L. Analysis of the Formation Conditions for Large Area Epitaxial Graphene on SiC Substrates. *Mater. Sci. Forum* **2010**, *645–648*, 565–568. [CrossRef]
21. Pilch, I.; Söderström, D.; Hasan, M.I.; Helmersson, U.; Brenning, N. Fast growth of nanoparticles in a hollow cathode plasma through orbit motion limited ion collection. *Appl. Phys. Lett.* **2013**, *103*, 193108. [CrossRef]
22. Lloyd Spetz, A.; Andersson, M. Technology and Application Opportunities for SiC-FET Gas Sensors. In *Solid State Gas Sensors—Industrial Application*; Fleischer, M., Lehmann, M., Eds.; Springer: Berlin/Heidelberg, Germany, 2012; pp. 189–214. ISBN 978-3-642-28092-4.
23. Available online: <http://gaussian.com/citation/> (accessed on 22 February 2019).
24. Zhao, Y.; Truhlar, D.G. A new local density functional for main-group thermochemistry, transition metal bonding, thermochemical kinetics, and noncovalent interactions. *J. Chem. Phys.* **2006**, *125*, 194101. [CrossRef]
25. Zhao, Y.; Truhlar, D.G. The M06 suite of density functionals for main group thermochemistry, thermochemical kinetics, noncovalent interactions, excited states, and transition elements: Two new functionals and systematic testing of four M06-class functionals and 12 other function. *Theor. Chem. Acc.* **2008**, *120*, 215–241. [CrossRef]
26. Hay, P.J.; Wadt, W.R. Ab initio effective core potentials for molecular calculations. Potentials for K to Au including the outermost core orbitals. *J. Chem. Phys.* **1985**, *82*, 299–310. [CrossRef]
27. Boys, S.F.; Bernardi, F. The calculation of small molecular interactions by the differences of separate total energies. Some procedures with reduced errors. *Mol. Phys.* **1970**, *19*, 553–566. [CrossRef]
28. Wang, G.; Zhang, X.; Skallberg, A.; Liu, Y.; Hu, Z.; Mei, X.; Uvdal, K. One-step synthesis of water-dispersible ultra-small Fe<sub>3</sub>O<sub>4</sub> nanoparticles as contrast agents for T<sub>1</sub> and T<sub>2</sub> magnetic resonance imaging. *Nanoscale* **2014**, *6*, 2953–2963. [CrossRef] [PubMed]





PAPER III





# First-order time-derivative readout of epitaxial graphene-based gas sensors for fast analyte determination

Marius Rodner, Jens Eriksson\*

Applied Sensor Science Unit Department of Physics Chemistry and Biology, Linköping University, Linköping, Sweden



## ARTICLE INFO

### Keywords:

Epitaxial graphene on SiC  
Chemical gas sensor  
First-order time-derivative signal  
Fast sensor readout  
Air quality monitoring

## ABSTRACT

For many applications, gas sensors need to be very sensitive, selective and exhibit a good stability. Moreover, they should also be cheap and small, and allow a fast response time. Usually, sensors are optimized for specific applications with a compromise between the mentioned criteria. Here, we show a method that allows very sensitive, but rather slow, graphene metal oxide hybrid sensors to be used in a much faster and more effective way with a focus on targeting trace level concentrations of some common toxic air pollutants. By exploiting the first-order time-derivative of the measured resistance signal after a concentration step, the response peak is achieved much faster, while also being more robust against sensor exposure and relaxation times, and concomitantly maintaining the very high sensitivities inherent to graphene. We propose to use this method to generate an additional signal to allow using sensors that are normally rather slow in applications where steep concentration changes need to be detected with much faster time constants.

## 1. Introduction

Two dimensional materials such as graphene gain an increasing interest in the field of gas sensors where very low detection limits are needed. One of those fields is the application in air quality monitoring (AQM), where gases like toxic volatile organic compounds (VOCs) must be detected in the lower or even sub-parts-per-billion (ppb) range. Some VOCs are very toxic even at very low concentrations and therefore usually have safety levels in the low ppb range. Formaldehyde for example has a safety level of 80 ppb whereas benzene is carcinogenic at any concentration [1]. Metal oxide films such as  $\text{TiO}_2$ ,  $\text{WO}_3$  or  $\text{SnO}_2$  as gas sensing layers are commonly used in air quality sensors [2]. Although exhibiting a good sensitivity at elevated temperatures, trace concentrations of single ppb are so far not easily detectable and no commercial low-cost sensor system is available yet [3]. In an earlier study, we have already shown that sufficient sensitivity can be reached towards low ppb concentrations of benzene by combining the surface chemistry of metal oxide nanoparticles with the sensitivity of epitaxial graphene on silicon carbide (SiC) in a hybrid sensing-layer-transducer structure [4].

Besides high sensitivity and low detection limit, also other performance requirements related to stability, selectivity and time constants need to be met to make an overall useful gas sensor. For indoor air quality monitoring, the sampling rate should be within a range of a few minutes to allow real-time monitoring [5]. To achieve a faster sensor response, usually elevated temperatures are used or the sensor is additionally irradiated with a light source [6,7]. Another method is the use

of the sensor signal's first-order time-derivative, which was already shown to work for various kinds of chemical gas sensors like field-effect transistors, as well as thick and thin films of metals and metal oxides for abrupt changes in gas concentration [8–10]. In an earlier study, we demonstrated that this approach might be used also for two-dimensional materials, but it was not fully studied and developed [4]. Here, we focus on sensor response evaluation based on the first-order time-derivative of the sensor signal and how stable it is towards changing exposure and relaxation times compared to the standard sensor response.

## 2. Experimental

The used materials were epi-graphene on SiC [11] functionalized with monodispersed  $\text{Fe}_3\text{O}_4$  nanoparticles (NP) or a nanolayer (NL; nominally 0.5 – 1 nm) of  $\text{Fe}_3\text{O}_4$ . They are referred to as NP and NL DEG (decorated epitaxial graphene). The sensor resistance between two contacts on the surface is used as the sensor signal. More information about the growth parameters and sensor fabrication can be found in our previous works [12,13]. Different gases like nitrogen dioxide and ammonia were used to demonstrate the method in general, but benzene and formaldehyde, i.e. gases of relevance for AQM are investigated as well and discussed in the context of previous results and the state-of-the-art. Moreover, the different sensors were also operated at different temperatures when exposed to the various gases in order to always be able to explain the occurring phenomena at conditions with a good compromise between speed and magnitude of sensor response.

\* Corresponding author.

E-mail address: [jens.eriksson@liu.se](mailto:jens.eriksson@liu.se) (J. Eriksson).

<https://doi.org/10.1016/j.snr.2020.100012>

Received 28 February 2020; Revised 27 May 2020; Accepted 27 May 2020

Available online 4 June 2020

2666-0539/© 2020 The Author(s). Published by Elsevier B.V. This is an open access article under the CC BY license. (<http://creativecommons.org/licenses/by/4.0/>)

The gas measurements were performed using a gas mixing system where the sensor is inserted in a flow cell [14]. The background mixture of nitrogen and oxygen was kept at a ratio of 80:20 ml/min and at 0% relative humidity (RH) if not mentioned otherwise. The flow during both test gas and background exposure was constantly at 100 ml/min. When introducing a test gas (in N<sub>2</sub> background) to the flow, the nitrogen concentration was adjusted accordingly to maintain a constant 80:20 ratio. The measurement data is recorded using a Keithley Sourcemeter 2600 and the first-order time-derivative signal is further smoothed in post-processing using an adjacent average filter. The sensor response is defined as

$$r = (R - R_0) / R_0 * 100\%, \quad (1)$$

where R is the saturated/absolute highest resistance signal and R<sub>0</sub> corresponds to the baseline resistance before gas exposure. The derivative response is defined as

$$r_{dt} = R_{dt} - R_{dt,0}, \quad (2)$$

where R<sub>dt</sub> is the absolute highest derivative signal and R<sub>dt,0</sub> corresponds to the baseline before gas exposure.

### 3. Results and discussion

#### 3.1. Introduction of the first-order time-derivative signal

Fig. 1 shows a standard gas exposure response shape of graphene with p-type conductivity towards an oxidizing gas (upper black line). In this case, the sensor was exposed to NO<sub>2</sub> concentrations of 400, 300, 200 and 100 ppb at 150 °C for 15 min with a relaxation time of 60 minutes. It can be clearly seen that the sensor signal neither reaches a saturated response, nor does it fully relax back to its initial baseline. With a very high signal to noise ratio (calculated using three times the standard deviation of the baseline) of 133 dB and a relative response of about -3.3% for 100 ppb after the 15 minutes exposure, this material seems to be a promising sensing transducer. Unfortunately, as the sensor response is not saturated at the end of the gas exposure, it is not straightforward to compare its performance with other sensors from the literature. Moreover, common time constants like τ<sub>90</sub> or τ<sub>63</sub>, defined as the time when 90 or 63% of the total change during one gas exposure compared to the baseline signal is achieved, cannot always easily be extracted using an exponential fit of the sensor response. To circumvent the slow response characteristics, we investigated the use of the first-order time-derivative of the sensor resistance as an additional sensor signal to the sensor resistance. This is shown as the red (lower) curve in Fig. 1.

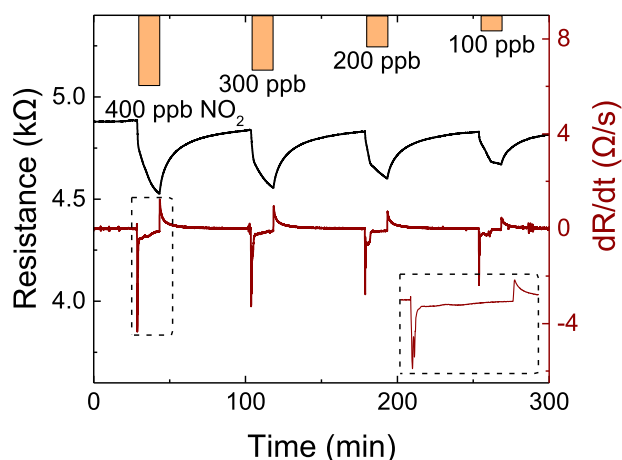


Fig. 1. Resistance over time (black, upper) of Fe<sub>3</sub>O<sub>4</sub> NP DEG with its corresponding time-derivative (red, lower) for NO<sub>2</sub> exposures at 150 °C at 0%RH. The inset in the lower right corner shows the enlarged time-derivative response of the first gas exposure.

The time-derivative signal is more stable against short exposure times and relaxes much faster, while exhibiting a very stable baseline. Moreover, the peaks arise much faster and are also concentration dependent, making it very promising as an additional sensor signal. This behavior is in good agreement with the findings of Wu et al. who concluded that the rate of change in resistance is directly proportional to the applied gas concentration as well as the rate of gas ad- and desorption [9]. The desorption response is normally not utilized as a standard indicator as it occurs after the adsorption, but it might be useful as a feature in multivariate statistics for selectivity enhancement [10,15].

If the resistance does not have a very smooth baseline, the first-order time-derivative signal can exhibit too much noise to analyze it easily. Therefore, a smoothing filter, e.g. adjacent average smoothing can be used. However, τ<sub>dt</sub>, defined as the time from the start of a gas exposure until r<sub>dt</sub> reaches its maximum, can be strongly altered if the filter is not used properly (compare Fig. S1). An adjacent average filter with 10 point smoothing was used for all measurements.

#### 3.2. Influence of exposure times

The first-order time-derivative of the resistance is the slope of the signal change and thus the peak value should be independent of the gas exposure time (if the exposure time is long enough for r<sub>dt</sub> to reach its peak), whereas the change in resistance should increase with increasing gas exposure time until the gas-adsorption reaches equilibrium. This phenomenon can be seen in Fig. 2(a), where the sensor response is shown towards 50 ppb of NO<sub>2</sub> with exposure times of 5, 10, 15 and 20 minutes, with 60 min of relaxation in between exposures. The magnitude of change in resistance clearly increases with longer exposure times from -1.2% for 5 min to -2.8% for 20 min. Gas sensors often need significant time to reach the maximum response and usually even longer time to relax back to its baseline value. If the steady state maximum is not reached, time constants cannot always be calculated and if the sensor is not fully relaxed, the response magnitude can vary, potentially leading to a misclassification of the exposed gas concentration. The time needed to reach r<sub>dt</sub>, on the other hand, is much shorter and can therefore be applied for determination of analyte concentration even if the raw sensor signal did not reach steady state. Here, r<sub>dt</sub> towards 50 ppb NO<sub>2</sub> is approximately 2.5 Ω/s, with a slight increase after the third exposure, regardless of the exposure time. This invariance with exposure time comes from r<sub>dt</sub> being determined by the initial adsorption/desorption phase during which the change in resistance is the highest, after which further adsorption/desorption proceeds at a slower pace.

Another problem arises when the sensor signal is not fully relaxed before the next gas exposure starts, leading to an induced drift and therefore possible misclassifications of the measured gas concentration. Fig. 2 (b) shows the sensor response towards 50 and 200 ppb of NO<sub>2</sub>, which were applied in sequences of decreasing relaxation time. Each exposure lasted for 15 min, but the relaxation time in between exposures was altered from 60 down to 30 and 15 minutes, respectively. The relative response as well as the response of the first-order time-derivative signal are summarized in Table 1. As the baseline does not fully recover even at 60 minutes relaxation time, the classification of the two different gas concentrations becomes more difficult with shorter relaxation times. Using the standard sensor signal (upper black line), the sensor is able to distinguish between 50 and 200 ppb of NO<sub>2</sub> for all relaxation times. However, the ratio between the responses at 200 ppb and the responses at 50 ppb continuously decreases with a decrease in relaxation time as the response towards 50 ppb stays approximately the same (-2.6%), but the response for 200 ppb decreases with a decrease in relaxation time from -5.5 to -4.7% for 60 and 15 min relaxation time, respectively. This is a clear sign that the sensor surface is not fully recovered, and not enough adsorption sites are available for a reaction with NO<sub>2</sub> molecules at the second exposure. When using the time-derivative signal instead, this decreasing trend for the response for 200 ppb is not observed. The differentiation between both concentrations is possible at all tested

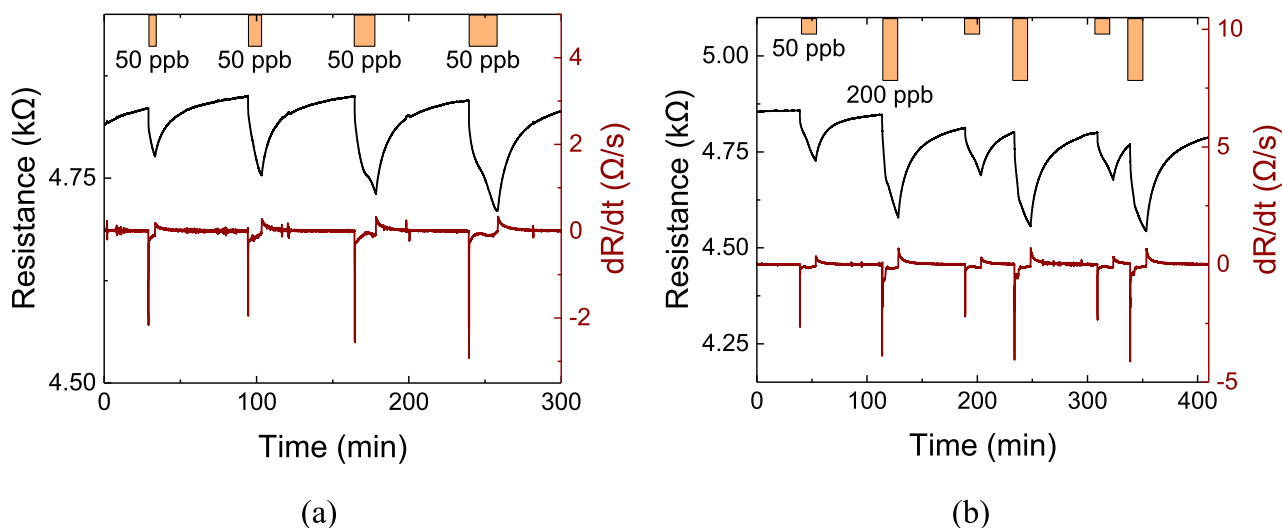


Fig. 2. Resistance over time (black, upper) of  $\text{Fe}_3\text{O}_4$  NP DEG with its corresponding time-derivative (red, lower) for  $\text{NO}_2$  exposures at  $150^\circ\text{C}$  at  $0\%RH$  with (a) different exposure times and (b) different relaxation times.

relaxation times and the ratio between the responses at 200 and 50 ppb stays approximately constant. This is because the baseline of the derivative signal relaxes much faster after the initial adsorption/desorption phase, while the change in the raw sensor signal occurs very slowly. Moreover, the variation, calculated as the single standard deviation based on the baseline noise, of the responses towards a single concentration changes drastically for the relative sensor response. While the variation in relative response for exposures towards 50 ppb is only about  $\pm 0.08\%$ , it is with  $\pm 0.38\%$  almost 5 times higher for 200 ppb. For the time-derivative response, the variations are  $\pm 0.20$  and  $\pm 0.13$   $\Omega/\text{s}$  for 50 and 200 ppb, respectively, which shows a slightly more fluctuating response in general, but without a large difference between both concentrations.

### 3.3. Influence of environmental factors

It is known that not only the sensor response heavily depends on the sensor temperature but also the speed of response changes [16]. Hence the operation temperature is often optimized to decrease time constants

and operate the sensor at a point of highest response towards a specific gas. Considering this, also the first order time derivative of the sensor signal is expected to change with temperature. Fig. 3(a) shows the derivative response over sensor temperature towards exposures of 1 ppm formaldehyde (blue) and benzene (orange), respectively. As expected, the derivative response is not constant over temperature but exhibits a trend towards increasing sensitivity with increasing temperature in the tested range. This correlation between response magnitude and temperature is similar to the one observed for the raw sensor response. Moreover, the time constant of the raw signal response,  $\tau$ , strongly depends on the operating temperature and increases from approximately 300 s at  $170^\circ\text{C}$  to 400 and 450 s at  $100^\circ\text{C}$  for  $\text{CH}_2\text{O}$  and  $\text{C}_6\text{H}_6$ . The time needed for the derivative signal to reach its maximum, in contrast, is not significantly dependent on the temperature and stays at around 50 s for both gases. This is unexpected, but could be due the relatively small tested temperature range, thus only small changes might occur.

Similar to an increase in operating temperature, the sensor response can be increased with the irradiation of UV light during the gas exposure. However, this does not work for all material/gas combinations.

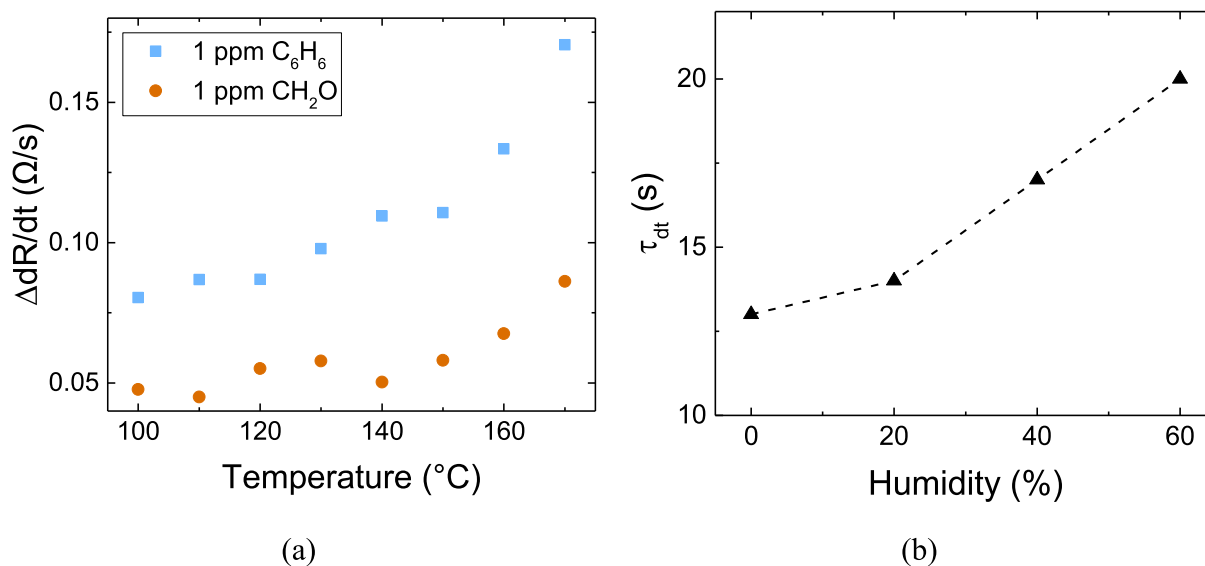


Fig. 3. (a) First-order time-derivative response of  $\text{Fe}_3\text{O}_4$  NP DEG towards  $\text{CH}_2\text{O}$  (blue) and  $\text{C}_6\text{H}_6$  (orange) at different operating temperatures at  $0\%RH$  and (b)  $\tau_{dt}$  of the first-order time-derivative responses of  $\text{Fe}_3\text{O}_4$  NL DEG for 25 ppm  $\text{NH}_3$  exposures at  $75^\circ\text{C}$  at different RH.

**Table 1**

Comparison of the regular relative sensor response and the time-derivative response of Fe<sub>3</sub>O<sub>4</sub> NP DEG for NO<sub>2</sub> exposures at 150 °C at 0%RH (compare Fig. 2(b)).

NO <sub>2</sub> concentration	Relaxation time	Relative response	Derivative response
ppb	min	%	Ω/s
50	60	-2.7	-2.6
200		-5.5	-3.9
50	30	-2.6	-2.2
200		-5.1	-4.1
50	15	-2.6	-2.3
200		-4.7	-4.2

Comparably to the exposure shown in Fig. 1, the sensor was tested again while under the permanent influence of UV irradiation (355 nm). With UV irradiation, the response towards NO<sub>2</sub> increases with about 28% compared to without irradiation. The derivative response  $r_{dt}$  increases even more with about 100%. However,  $\tau_{63}$  and  $\tau_{dt}$  stay approximately the same for both cases.

The response of the Fe<sub>3</sub>O<sub>4</sub> nanolayer decorated sample towards 25 ppm NH<sub>3</sub> with varying relative humidity (RH) at 75 °C operating temperature was analyzed towards changes in the first-order time-derivative response. The changes in response for different RH is again similar to what was observed for the standard response, e.g. a decrease in response for an increase in RH. More interesting is the time needed to reach  $r_{dt}$ . As shown in Fig. 3(b), the time to peak increases if humidity is introduced.  $\tau_{dt}$  increased from 13 s at 0%RH up to 20 s at 60%RH, respectively. This could be due to water molecules occupying possible reaction sites, or a competition between H<sub>2</sub>O and NH<sub>3</sub> over available sites, and/or reactions between the two molecules to form ammonium and hydroxyl groups on the sensor surface, thus increasing the reaction time [17]. The sensors were operated in total over a period of almost two years and the measured responses towards several gases show some small deviations between the measurements but without a clear trend of decreasing response over time.

### 3.4. Time constants

As described above, the responses of the first-order time-derivative signal reach their peaks already after a short period of time. The time constant  $\tau_{dt}$  for Fe<sub>3</sub>O<sub>4</sub> nanoparticle decorated graphene towards NO<sub>2</sub> exposure lies around 10 s (compare Fig. 1) which is 25 times faster compared to the extrapolated time constant of the standard resistance response. Other measurements suggest a decrease of time constants from approximately 300 s down to 50 s for measurements with the same sensor towards C<sub>6</sub>H<sub>6</sub> and CH<sub>2</sub>O [12]. For the nanolayer decorated sample,  $\tau_{dt}$  was found to be approximately 10 s for exposures towards 200 ppb C<sub>6</sub>H<sub>6</sub> and CH<sub>2</sub>O and 15 s for 25 ppm NH<sub>3</sub>. For a TiO<sub>2</sub> nanoparticles decorated graphene sensor, the time constants towards changing oxygen concentrations could be decreased from 1500s down to 60 s using this approach [4]. This is an improvement with a factor of 25 compared to the standard resistance signal. Therefore, we conclude that the time needed to reach  $r_{dt, MAX}$  depends on the combination of sensor material and test gas, but should be applicable to all resistive type gas sensors.

### 3.5. Applications and limitations

It should be noted that in the practical applications of gas sensors, the change in the gas concentration in the studied environment usually does not occur by leaps and bounds, but rather slow-changing processes. Therefore, the applied method might not be useful for processes where the concentration change to be measured occurs slowly over time. However, an option could be a sensor setup, where an abrupt change in concentration is actively induced through changing between a reference

and test gas flow. In stand-alone systems, this would require extra costs and space, as a defined reference flow would need to be established, for example through a reference gas reservoir and a pump. Nevertheless, there are also examples where this approach might be used even if an abrupt switch needs to be implanted either passively (leak test or battery system fault detection [18]) or actively (valve switch between two existing gas streams). Another option could be the use of pre-concentrators [19], where the test gas is collected first and only released under defined conditions, e.g. degassing through heating. Possible application fields, where the test gas is not put over the sensor in a constant flow, but abrupt changes are monitored, are for example in breath-analysis [20] or measuring the gaseous by-product of biological processes. Moreover, this method could still be used as an additional signal to create more transient data for multivariate statistical analysis, which could be used for selectivity enhancement [10,15].

## 4. Conclusion

In conclusion, the first-order time-derivative can be used as an additional sensor signal for gas sensors with low intrinsic noise such as graphene metal oxide hybrids, with maintained high sensitivity for applications, where abrupt concentrations changes need to be monitored. Using this approach, a more stable time-derivative signal baseline compared to the resistance baseline can be achieved, and an independency of exposure and relaxation times can be gained to some extent. The best improvement though is the highly decreased time constants, which, in combination with the maintained high sensitivity of epitaxial graphene on SiC, makes the sensors applicable in areas where both low detection limits and relatively fast gas sensor readout are required, e.g. air quality monitoring. Moreover, the approach can save a lot of lab testing time, hence saving time and money during research activities.

## Declaration of Competing Interest

None.

## Acknowledgments

The authors would like to acknowledge the Swedish Foundation for Strategic Research (SSF) for financial support through the grants GMT14-0077 and RMA15-024. This work has been supported by The Centre in Nano science and technology (CeNano) through the project "Graphene-nanoparticle hybrid gas sensor". Moreover, we would like to thank Professor Rositsa Yakimova from the Semiconductor Materials Division at Linköping University, Sweden for the provision of pristine epitaxial graphene, Dr. Sebastian Ekeröth and Professor Ulf Helmersson from the Plasma & Coatings Physics Division at Linköping University, Sweden for the decoration with nanoparticles, and Dr. Margus Kodu and Professor Raivo Jaanisoo from the Institute of Physics at University of Tartu, Estonia for the decoration with nanolayers.

## Supplementary materials

Supplementary material associated with this article can be found in the online version at doi:10.1016/j.sn.2020.100012.

## Appendices

See the supplementary material for further details about the used adjacent average smoothing filter.

## References

- [1] World Health Organisation, Guidelines for Indoor Air Quality: selected Pollutants, WHO Guidel. 9 (2010) 454.

- [2] A. Mirzaei, S.G. Leonardi, G. Neri, Detection of hazardous volatile organic compounds (VOCs) by metal oxide nanostructures-based gas sensors: a review, *Ceram. Int.* 42 (2016) 15119–15141, doi: 10.1016/j.ceramint.2016.06.145.
- [3] B. Szulczyński, J. Gębicki, Currently commercially available chemical sensors employed for detection of volatile organic compounds in outdoor and indoor air, *Environments* 4 (2017) 21, doi: 10.3390/environments4010021.
- [4] M. Rodner, J. Bahonjic, M. Mathisen, R. Gunnarsson, S. Ekeröth, U. Helmersson, I.G. Ivanov, R. Yakimova, J. Eriksson, Performance tuning of gas sensors based on epitaxial graphene on silicon carbide, *Mater. Des.* 153 (2018) 153–158, doi: 10.1016/j.matdes.2018.04.087.
- [5] B. Timmer, W. Olthuis, A. Van Den Berg, Ammonia sensors and their applications - A review, *Sensors Actuators B Chem.* 107 (2005) 666–677, doi: 10.1016/j.snb.2004.11.054.
- [6] N. Barsan, D. Koziej, U. Weimar, Metal oxide-based gas sensor research: how to? *Sensors Actuators B Chem* 121 (2007) 18–35, doi: 10.1016/j.snb.2006.09.047.
- [7] E. Espid, F. Taghipour, UV-LED Photo-activated Chemical Gas Sensors: a Review, *Crit. Rev. Solid State Mater. Sci.* 42 (2017) 416–432, doi: 10.1080/10408436.2016.1226161.
- [8] R. Muller, E. Lange, Multidimensional sensor for gas analysis, *Sens. Actuators* 9 (1986) 39–48.
- [9] C.H. Wu, G.J. Jiang, C.C. Chiu, P. Chong, C.C. Jeng, R.J. Wu, J.H. Chen, Fast gas concentration sensing by analyzing the rate of resistance change, *Sens. Actuators B Chem.* 209 (2015) 906–910, doi: 10.1016/j.snb.2014.12.066.
- [10] T. Eklöv, P. Martensson, I. Lundström, Enhanced selectivity of MOSFET gas sensors by systematical analysis of transient parameters, *Anal. Chim. Acta.* 353 (1997) 291–300, doi: 10.1016/S0003-2670(97)87788-4.
- [11] G.R. Yazdi, T. Iakimov, R. Yakimova, Epitaxial graphene on SiC: a review of growth and characterization, *Crystals* 6 (2016), doi: 10.3390/cryst6050053.
- [12] M. Rodner, D. Puglisi, S. Ekeröth, U. Helmersson, I. Shteplyuk, R. Yakimova, A. Skallberg, K. Uvdal, A. Schütze, J. Eriksson, Graphene decorated with iron oxide nanoparticles for highly sensitive interaction with volatile organic compounds, *Sensors (Switzerland)* 19 (2019), doi: 10.3390/s19040918.
- [13] M. Kodu, A. Berholts, T. Kahro, J. Eriksson, R. Yakimova, T. Avarmaa, I. Renge, H. Alles, R. Jaaniso, Graphene-based ammonia sensors functionalised with sub-monolayer  $V_2O_5$ : a comparative study of chemical vapour deposited and epitaxial graphene, *Sensors* 19 (2019) 1–17, doi: 10.3390/s19040951.
- [14] A. Lloyd Spetz, M. Andersson, Technology and Application Opportunities for SiC-FET Gas Sensors, in: M. Fleischer, M. Lehmann (Eds.), *Solid State Gas Sensors - Ind. Appl.*, Springer, Berlin, 2011, pp. 189–214, doi: 10.1007/5346\_2011\_5.
- [15] S. Marco, A. Gutierrez-Galvez, Signal and data processing for machine olfaction and chemical sensing: a review, *IEEE Sens. J.* 12 (2012) 3189–3214, doi: 10.1109/JSEN.2012.2192920.
- [16] C. Schultealbert, T. Baur, A. Schütze, S. Böttcher, T. Sauerwald, A novel approach towards calibrated measurement of trace gases using metal oxide semiconductor sensors, *Sens. Actuators B Chem* 239 (2017) 390–396, doi: 10.1016/j.snb.2016.08.002.
- [17] N. Barsan, U. Weimar, Conduction model of metal oxide gas sensors, *J. Electroceramics.* 7 (2001) 143–167, doi: 10.1023/A:1014405811371.
- [18] M. Wenger, R. Waller, V.R.H. Lorentz, M. Marz, M. Herold, Investigation of gas sensing in large lithium-ion battery systems for early fault detection and safety improvement, in: *Proceedings of the Conference of the IEEE Industrial Electronics Society*, 2014, pp. 5654–5659, doi: 10.1109/IECON.2014.7049366.
- [19] M. Leidinger, M. Rieger, T. Sauerwald, C. Alépée, A. Schütze, Integrated pre-concentrator gas sensor microsystem for ppb level benzene detection, *Sens. Actuators B Chem.* 236 (2016) 988–996, doi: 10.1016/j.snb.2016.04.064.
- [20] N.A. Rakow, K.S. Suslick, A colorimetric sensor array for odour visualization, *Nature* 406 (2000) 710–713, doi: 10.1038/35021028.



PAPER IV



Article

# Metal Oxide Nanolayer-Decorated Epitaxial Graphene: A Gas Sensor Study

Marius Rodner <sup>1</sup>, Adam Icardi <sup>1</sup>, Margus Kodu <sup>2</sup>, Raivo Jaaniso <sup>2</sup>, Andreas Schütze <sup>3</sup> and Jens Eriksson <sup>1,\*</sup>

<sup>1</sup> Applied Sensor Science Unit, IFM, Linköping University, 58183 Linköping, Sweden; marius.rodner@liu.se (M.R.); adaic903@student.liu.se (A.I.)

<sup>2</sup> Institute of Physics, University of Tartu, 50411 Tartu, Estonia; margus.kodu@ut.ee (M.K.); raivo.jaaniso@ut.ee (R.J.)

<sup>3</sup> Department of Systems Engineering, Lab for Measurement Technology, Saarland University, 66123 Saarbrücken, Germany; schuetze@imt.uni-saarland.de

\* Correspondence: jens.eriksson@liu.se; Tel.: +46-(0)-13-286-613

Received: 8 October 2020; Accepted: 28 October 2020; Published: 30 October 2020



**Abstract:** In this manuscript, we explore the sensor properties of epitaxially grown graphene on silicon carbide decorated with nanolayers of CuO, Fe<sub>3</sub>O<sub>4</sub>, V<sub>2</sub>O<sub>5</sub>, or ZrO<sub>2</sub>. The sensor devices were investigated in regard to their response towards NH<sub>3</sub> as a typical reducing gas and CO, C<sub>6</sub>H<sub>6</sub>, CH<sub>2</sub>O, and NO<sub>2</sub> as gases of interest for air quality monitoring. Moreover, the impact of operating temperature, relative humidity, and additional UV irradiation as changes in the sensing environment have been explored towards their impact on sensing properties. Finally, a cross-laboratory study is presented, supporting stable sensor responses, and the final data is merged into a simplified sensor array. This study shows that sensors can be tailored not only by using different materials but also by applying different working conditions, according to the requirements of certain applications. Lastly, a combination of several different sensors into a sensor array leads to a well-performing sensor system that, with further development, could be suitable for several applications where there is no solution on the market today.

**Keywords:** metal oxide; epitaxial graphene on SiC; chemical gas sensor; nanolayer; inter-lab comparison

## 1. Introduction

It is estimated that people in North America and Europe spend 90% of their time indoors, where the air quality is usually worse than in outdoor air. Poor indoor air quality is responsible for about 4 million premature deaths and costs about USD5 trillion in welfare costs per year [1,2]. One of the main challenges is to have a sensor solution that is accurate and reliable enough, while also being affordable [3]. Another big challenge is the miniaturization of such gas sensors, with reliable selectivity, stability, and sensitivity [4]. Moreover, IDTechEx expects that the total market for environmental sensors will be over USD3.8 billion by 2030 [5].

Two-dimensional materials such as graphene have been shown to exhibit outstanding sensitivity if used as gas sensors [6]. However, to achieve sensitivity and selectivity to desired target analytes, the surface normally needs to be functionalized. Often, metals or metal oxides are used for the functionalization, as there is a wide range of well-studied materials, which are not only well known in the scientific community but also dominate in commercial sensor applications [7]. A well-designed sensor focuses on a specific application, and the optimal material/gas combination already leads to very good sensor performance. To further increase the sensitivity, the surface-to-volume ratio of the sensing layers can be increased, as a larger detection area per unit volume results in more

material/gas interaction due to a higher adsorption of gas molecules per volume. Especially when thinking about a miniaturization of the whole sensor device, nanostructured materials are often used with highly sensitive materials to combine their advantages. For example, the combination of sensitive and more selective nanostructured metal oxides with very sensitive and low noise graphene leads to promising sensor hybrids. There, the gas reaction mainly takes place on the metal oxide nanostructure, and the graphene is used as a highly sensitive transducer [8,9]. In this work, we show that decorating an epitaxially grown graphene surface with continuous metal oxide nanolayers (NLs) can lead to increased sensitivity and selectivity towards different desired target gases. The choice of material is based on previous observations. For example, we have shown that using Fe<sub>3</sub>O<sub>4</sub> or TiO<sub>2</sub> nanoparticles to decorate epitaxial graphene has very promising results regarding sensitivity [10,11]. However, controlled coverage of the whole surface with an NL is much easier compared to controlling the distribution of nanoparticles. Moreover, epitaxially grown graphene was found to outperform commercially available CVD graphene when used as a transducer in a gas sensor and decorated with V<sub>2</sub>O<sub>5</sub> [12]. ZrO<sub>2</sub> is used in many catalytic applications, such as the lambda sensor, and CuO was also found to be a very promising material for gas sensors [13,14]. Furthermore, the influence of several environmental properties on sensor performance is evaluated. The aim of this study is to provide an overview of how different material combinations affect sensor performance for a selection of typical toxic AQ pollutants.

## 2. Materials and Methods

The graphene surface was epitaxially grown on silicon carbide (SiC) through a silicon sublimation process [15]. As a semi-insulating 4H-SiC (0001) substrate is used, no further transfer of the grown graphene lattice is needed. Gold on titanium (Ti/Au, 2/200 nm) contact pads are sputtered onto the surface, and the resistance between the contacts is measured as a sensor response in the final device. More detailed information about the growth parameters, sensor fabrication, and the gas mixing system can be found in our previous works [10,12]. Gas measurements were performed with different gas mixing systems at Linköping University (LiU) [16] and Saarland University (UdS) [17,18]. Both laboratories use gas bottles with a purity of 6.0, and the gas mixing systems are calibrated on flow rather than concentration by using calibrated mass flow controllers (MFCs). To test the influence of UV irradiation on sensor response, two different UV LEDs, with wavelengths of 265 nm (Sensor Electronic Technology Inc, Colombia, GA, USA, S-T39B-F1-265-01-1-050) and 355 nm (Roithner Lasertechnik GmbH, Vienna, Austria, XSL-355-3E-R6), were used separately to illuminate the sensor layers.

The pulsed laser deposition (PLD) process used in this work is described in [12]. Copper oxide (CuO), iron (Fe) foil, vanadium pentoxide (V<sub>2</sub>O<sub>5</sub>), and zirconium dioxide (ZrO<sub>2</sub>) have been used as target materials. A krypton fluoride (KrF) excimer laser COMPexPro 205 (Coherent GmbH, Germany) at a wavelength of 248 nm and laser fluences between 3–7 J/cm<sup>2</sup> have been used for ablation. The number of laser pulses was adjusted to achieve a layer thickness of around 0.5–1 nm. The sensor substrates were kept at room temperature during deposition.

In this manuscript, pristine epitaxial graphene on SiC will be referred to as PEG and decorated epitaxial graphene as DEG.

As mentioned before, the sensor resistance is measured over time, and the response is defined as

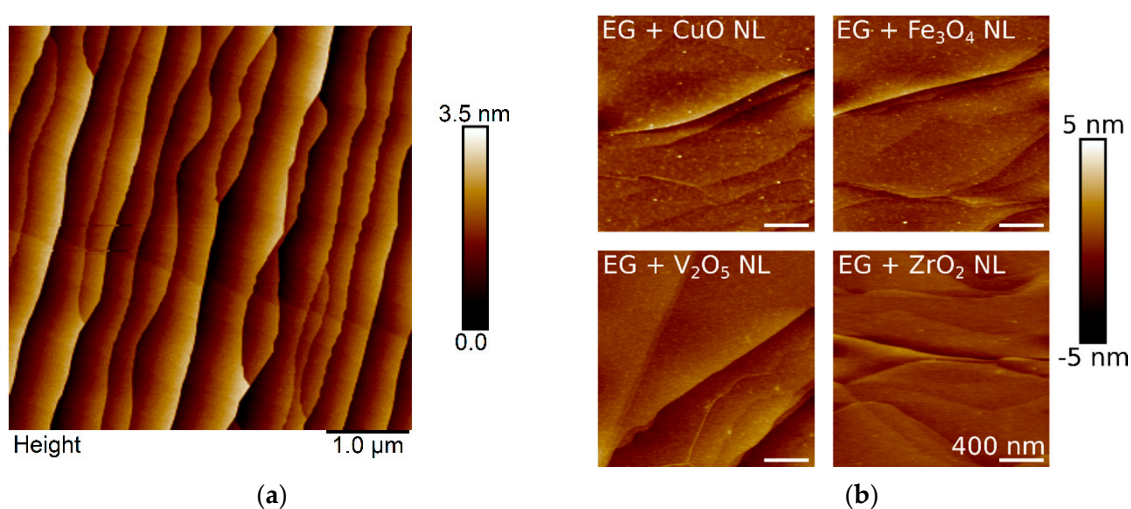
$$Response = \frac{R_{gas} - R_0}{R_0} * 100\% \quad (1)$$

where  $R_{gas}$  is the saturated/absolute highest resistance signal during the gas exposure, and  $R_0$  corresponds to the baseline resistance before gas exposure.

### 3. Results

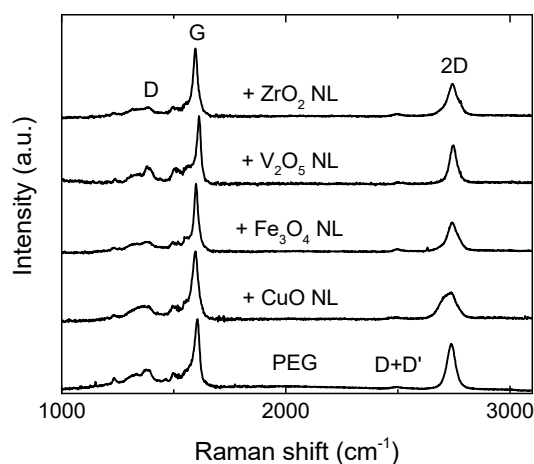
#### 3.1. Morphological and Structural Characterization

Figure 1a shows Atomic Force Microscopy (AFM) images obtained before the decoration of the graphene surface with the different metal oxide NLs, and Figure 1b shows a summary for all four surfaces after the decoration. The observed morphologies of the NL-decorated sensor surfaces are not very different compared to each other and still show a similar surface roughness compared to the pristine epitaxially grown graphene sample on SiC. The dominating features belong to the step-bunching edges formed at the SiC surface during high-temperature graphene growth. This is expected, as tapping mode AFM in ambient conditions does not allow the resolution of atomic structure, and the different layers form continuous films of a few atomic layers in thickness (0.5–1 nm) on top of a very flat substrate.



**Figure 1.** AFM images of pristine epitaxial graphene (PEG) (a) before and (b) after the decoration with nanolayers (NLs).

To ensure that the integrity of the graphene lattice is still given after the surface decoration, Raman spectroscopy measurements have been performed (see Figure 2). For a better comparison, all spectra are normalized to the G peak. All spectra exhibit the typical G and 2D peaks around 1610 and 2737  $\text{cm}^{-1}$ , respectively [19]. The peak observed around 1350  $\text{cm}^{-1}$  could be misinterpreted as the D peak, which is related to defects of the graphene lattice. Instead, these features, arising above 1280  $\text{cm}^{-1}$  and extending into the G peak, are related to the interfacial buffer layer between the graphene and the SiC substrate [19]. The small full width at half maximum (FWHM) value of the 2D peak of the pristine graphene reference is an indication of a uniform monolayer of graphene [20]. After the surface decoration, the Raman spectrum stays approximately the same as the reference, indicating no induced structural damage. While the position of the 2D peak occurs at the same Raman shift for all samples, the G peak varies a bit for the different samples. It occurs at  $1605 \pm 10 \text{ cm}^{-1}$ . This could be due to different levels of doping in the graphene due to the charge transfer between the graphene and the various metal oxide decoration materials or simply due to different levels of strain in the graphene lattices [21]. It can also be seen that the 2D peaks broaden a bit after the surface decoration, and the ratios between G and 2D peaks slightly decrease. This could be related to some inclusions of bi- or multilayer graphene in the measured spot.



**Figure 2.** Raman spectra for PEG and after NL decoration.

### 3.2. Gas Measurements

Ammonia ( $\text{NH}_3$ ) gas was used to generally study the response of the different hybrid sensors towards influences of operating temperature, relative humidity, and irradiation with UV light during the gas measurements. In addition, the sensor response to benzene ( $\text{C}_6\text{H}_6$ ), formaldehyde ( $\text{CH}_2\text{O}$ ), nitrogen dioxide ( $\text{NO}_2$ ), and carbon monoxide ( $\text{CO}$ ), i.e., gases of interest for, e.g., air quality monitoring, is discussed. The results were obtained over a period of about two years with the same sensors, showing that the sensors work without significant degradation during this time span if the operating temperature is kept at  $150\text{ }^\circ\text{C}$  or lower.

#### 3.2.1. Influence of Operating Temperature

It is well known that the operating temperature of a sensing layer has a huge impact on the sensor response, especially when using metal oxides or catalytic metals [22]. The sensor response was tested at several rather low temperatures, as the current sensor packaging limits the operating temperature to  $200\text{ }^\circ\text{C}$ . Therefore, no temperature above  $150\text{ }^\circ\text{C}$  was used.

All sensors have been tested at  $125$ ,  $100$ ,  $75$ , and  $50\text{ }^\circ\text{C}$  at  $50\%$  relative humidity (RH) and exposed to  $25$  and  $100\text{ ppm NH}_3$ . Each exposure lasted for  $30\text{ min}$ , with a relaxation phase of  $90\text{ min}$  in between exposures, where the system was purged with synthetic air as background gas ( $80/20\text{-N}_2/\text{O}_2$ ), also at  $50\%$  RH. The resistance over time is exemplarily shown for the  $\text{Fe}_3\text{O}_4$  NL DEG sensor in Figure 3a, and the results for all sensors towards  $25\text{ ppm}$  are shown in Figure 3b. The sharp peaks in resistance when changing temperatures are due to an overshoot in the temperature control mechanism. The highest observed absolute responses for each sample are highlighted in bold. It can be clearly seen that an increase in operating temperature does not always mean an increase in sensor response. Only  $\text{ZrO}_2$  has its highest response at  $125\text{ }^\circ\text{C}$ , while all other sensors exhibit their highest response at  $50\text{ }^\circ\text{C}$ . However, this rather untypical behavior with increasing temperature could be due to a reaction with OH groups or be products of reactions from OH groups and  $\text{NH}_3$  instead, leading to a higher overall response at the lower temperature, which is not necessarily related only to the  $\text{NH}_3$  exposure itself. This phenomenon was shown to occur for metal oxide gas sensors when operating them at relatively low temperatures in a humid environment [23,24]. While a higher sensor response is normally desired, the conditions at which this occurs may impose other disadvantages like higher time constants or a less stable sensor baseline. A perfect example of this behavior can be clearly seen in Figure 3a, as only exposures at  $125\text{ }^\circ\text{C}$  come close to a steady-state sensor response during the  $30\text{ min}$  gas exposure.  $\tau_{63}$  is extrapolated for all four operating temperatures using an exponential fit. It continuously increases, from approximately  $150\text{ s}$  at  $125\text{ }^\circ\text{C}$  up to  $550\text{ s}$  at  $50\text{ }^\circ\text{C}$  on average. Furthermore, the sensors are not always able to relax back to the baseline after  $90\text{ min}$  when operated at lower temperatures. As a compromise between the level of response, response shape, and relaxation,

all further measurements with ammonia were conducted at 75 °C except for ZrO<sub>2</sub>, which was operated at 125 °C. The overall highest response was observed for ZrO<sub>2</sub> with a change of −21.2% for 25 ppm NH<sub>3</sub> at 125 °C. Moreover, ZrO<sub>2</sub> and Fe<sub>3</sub>O<sub>4</sub> NL DEG sensors exhibit n-type behavior, i.e., resistance is reduced during exposure to reducing gases, while V<sub>2</sub>O<sub>5</sub> exhibits p-type behavior. Presumably, this difference is due to different charge transfers between the metal oxide layer and the graphene, which will depend on the work function difference between the materials. CuO, on the other hand, shows a positive response at 125 °C and then switches to a negative response at lower temperatures. This change can also be induced at 125 °C when using a higher concentration (100 ppm) instead. The reason for this change in response direction is likely due to increasing gas adsorption, resulting in sufficient electrons being donated to the graphene for the Fermi level to move from below the Dirac point (p-type conductivity) to above the Dirac point (n-type conductivity). The change with temperature could also partly explain why the absolute response increases with lower temperatures as temperature and NH<sub>3</sub> concentration work against each other in terms of charge carrier generation.

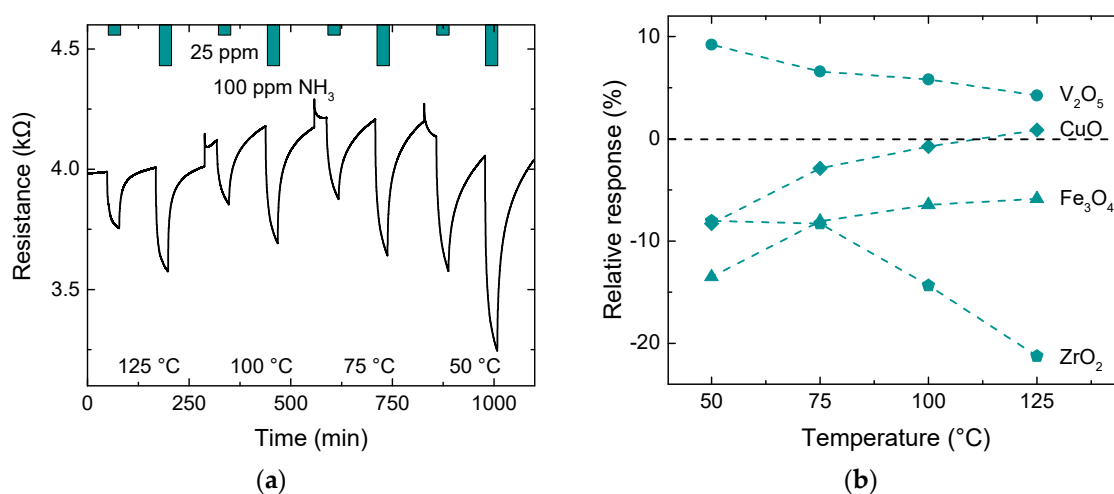


**Figure 3.** (a) Resistance over time of Fe<sub>3</sub>O<sub>4</sub> NL decorated epitaxial graphene (DEG) vs. 25 and 100 ppm NH<sub>3</sub> at different operating temperatures at 50% relative humidity (RH) and (b) relative responses of NL DEG samples for 25 ppm NH<sub>3</sub> exposures at different operating temperatures at 50% RH.

Other gases like benzene or formaldehyde, both volatile organic compounds (VOC), on the other hand, normally require a higher temperature to interact with the sensor surface. In a dry ambient, the four sensors were exposed to 200 ppb of C<sub>6</sub>H<sub>6</sub> and CH<sub>2</sub>O at 50, 100, and 150 °C. Only CuO DEG was able to detect gas pulses down to 50 °C. While the ZrO<sub>2</sub> DEG sensors showed a response only at 150 °C, Fe<sub>3</sub>O<sub>4</sub> and V<sub>2</sub>O<sub>5</sub> DEG sensors also exhibited a response at 100 °C.

### 3.2.2. Influence of Relative Humidity

Besides the operating temperature, relative humidity in the ambient can be another critical parameter for sensor response. It was shown that many metal oxides exhibit a cross-sensitivity towards RH, and a higher level of RH in the ambient usually results in a lower gas sensitivity, as the target gas molecules compete with water molecules for available adsorption sites.

Figure 4 summarizes the response magnitudes for all four NL DEG sensors towards 30 min exposures of 25 ppm NH<sub>3</sub> at different levels of RH. The sensors were tested at approximately 0%, 20%, 40%, and 60% RH, and the operating temperature was kept at 125 °C (ZrO<sub>2</sub>) and 75 °C (all other NLs), respectively. Comparing the response at 0% to 20% RH, all sensors exhibit a decrease in response except V<sub>2</sub>O<sub>5</sub>, which not only increases for the first 20% RH but progressively increases from 8.8% at 0% RH to 13.8% at 60% RH. On the contrary, the response of the Fe<sub>3</sub>O<sub>4</sub> NL DEG sensor decreases progressively with an increase in humidity, from initially −8.4% at 0% RH down to −4.3% at 60% RH. CuO, on the other hand, starts with a decrease in response for the first 20% RH but then stays almost constant for

40% and 60% RH. After the first drop in response at 20% RH compared to 0% RH, the ZrO<sub>2</sub> NL DEG sensor increases its response for 40% and 60% RH again, eventually exceeding the response observed at 0% RH. This increase in response with an increase of relative humidity in the environment could be due to an additional sensor reaction with OH groups or with products resulting from reactions of OH groups with NH<sub>3</sub>, which can occur for metal oxide gas sensors when operated in a humid environment at relatively low temperatures [23,24]. An analysis of the change in baseline resistance due to the change in relative humidity can be found in the supplementary material (compare Table S1).

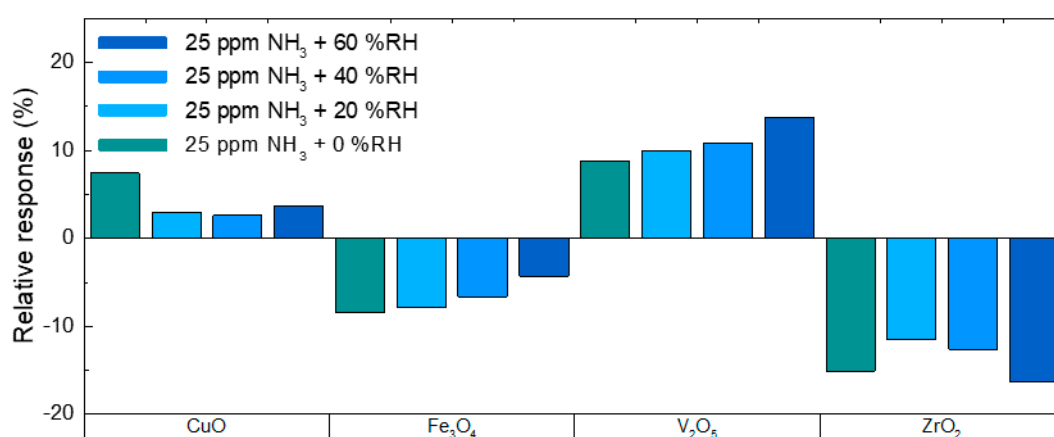


**Figure 4.** Relative responses of NL DEG samples for 25 ppm NH<sub>3</sub> exposures at 75 °C (except ZrO<sub>2</sub> at 125 °C) at different levels of RH.

Table 1 summarizes several measurements of all sensors towards all measured gases when exposed in a dry (0% RH; <5 ppm H<sub>2</sub>O for gas from gas bottles (6.0) and <63.2 ppm for gas from a 0-air generator; see Section 3.3) or a humid (25% or 50% RH) environment. The measurements were performed in different laboratories, and the differences are discussed in Section 3.3. In this section, we show only one value per gas. All measurements were performed at 150 °C operating temperature, and the response was measured after 30 min of exposure. It can be clearly seen that the introduction of relative humidity can have a severe effect on the measured sensor response, e.g., no sensor was able to detect CO, C<sub>6</sub>H<sub>6</sub>, or CH<sub>2</sub>O in the presence of humidity. Similar to the observations for NH<sub>3</sub>, relative humidity enhances or hinders the response towards NO<sub>2</sub>. It greatly increases the response for V<sub>2</sub>O<sub>5</sub> by almost 50% but only marginally increases it for ZrO<sub>2</sub> by about 8% of the original response. The high response of the Fe<sub>3</sub>O<sub>4</sub> NL DEG sensor decreases by about one-third. The response for CuO does not only decrease strongly, but it also changes direction from an increase in resistance towards NO<sub>2</sub> exposure to a decrease in resistance if relative humidity is added. This is similar to what was observed for this sensor when exposed to NH<sub>3</sub> + 50% RH at a temperature below 125 °C.

**Table 1.** Summary of relative responses towards CO, C<sub>6</sub>H<sub>6</sub>, CH<sub>2</sub>O, and NO<sub>2</sub> in dry and humid conditions.

	Relative Response (%)							
	CO 500 ppb 0% RH	CO 500 ppb 50% RH	C <sub>6</sub> H <sub>6</sub> 200 ppb 0% RH	C <sub>6</sub> H <sub>6</sub> 200 ppb 25% RH	CH <sub>2</sub> O 200 ppb 0% RH	CH <sub>2</sub> O 200 ppb 25% RH	NO <sub>2</sub> 200 ppb 0% RH	NO <sub>2</sub> 200 ppb 25% RH
CuO	0.12	/	2.81	/	1.54	/	5.28	-0.89
Fe <sub>3</sub> O <sub>4</sub>	0.09	/	0.40	/	0.33	/	39.69	26.68
V <sub>2</sub> O <sub>5</sub>	0.14	/	0.17	/	0.25	/	-5.84	-8.65
ZrO <sub>2</sub>	/	/	0.02	/	/	/	-14.60	-15.75

### 3.2.3. Influence of UV Irradiation

The sensitivity of a chemical gas sensor was shown to be enhanced through UV irradiation for many different material/gas combinations, and, normally, the irradiation also decreases time constants,

hence speeding up the sensor response [25]. Moreover, it was shown that UV irradiation can be used to clean graphene surfaces, thus freeing active sites for a target gas interaction [26]. Through the irradiation with light, photons can react with the target gas or the sensing material, which depends on the possibility of adsorbing photons at the given photon energy. Therefore, certain wavelengths work best for a given material/gas combination, and longer wavelengths will not have an effect at all.

Figure 5 summarizes the responses towards a 30 min exposure of 25 ppm  $\text{NH}_3$  at 50% RH without and with the influence of UV irradiation. The sensors were operated at 75 °C except for  $\text{ZrO}_2$ , which was operated at 125 °C. A clear trend can be observed as the relative sensor response is highest with 355 nm UV irradiation and decreases with no irradiation for all sensors except  $\text{ZrO}_2$ . For  $\text{ZrO}_2$ , on the other hand, a small decrease is observed with UV irradiation (−19.3%) compared to −21.3% without irradiation. When changing the UV irradiation from 355 to 265 nm, the sensor response decreases slightly. Both wavelengths have a strong impact on the time constants, which are lower with additional UV light compared to no irradiation. With UV irradiation, the time constants range between 350–500 s, whereas without irradiation, they go up to 550–1000 s. In contrast to the small effect on the response when adding UV irradiation, the  $\text{ZrO}_2$  DEG sensor shows the highest enhancement in time constant from 1000 s down to 450 s.

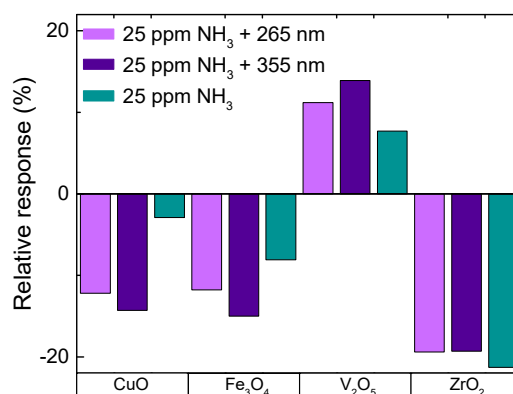


**Figure 5.** Relative responses of NL DEG sensors vs. 25 ppm of  $\text{NH}_3$  at 50% RH, without and with UV irradiation, based on [27].

The complete sensing mechanism of DEG is not fully understood yet, and the introduction of one more variable like UV irradiation results in additional complexity. It is known that if the bandgap is below the photon energy (e.g., 3.49 eV for 355 nm), there will be charge excitation, changing the charge density in the surface modification and graphene as well [25]. This effect should be more distinct for thicker surface layers. This is in agreement with the observation that only  $\text{ZrO}_2$ , with its comparably large bandgap (>5 eV), shows no significant difference in response magnitude under UV irradiation, while all other sensors did exhibit a significant difference ( $\text{CuO} \approx 1.4$  eV,  $\text{Fe}_3\text{O}_4 \approx 3$  eV, and  $\text{V}_2\text{O}_5 \approx 2.4$  eV).

### 3.3. Interlab Studies

To verify that measurements performed are valid regardless of the lab-setting, some measurements were first performed in the gas sensing lab at Linköping University (LiU) and then repeated in another lab at Saarland University (UdS). All measurements were performed at 150 °C operating temperature, but the tested gas concentrations and levels of relative humidity were not always the same due to some restrictions of the respective systems. For example, the level of humidity and the gas concentrations changed between 25% RH and 200 ppb for LiU and 50% RH and 500 ppb for UdS, respectively. This means that a higher sensor response is expected for measurements performed at UdS as a higher concentration was used. Nevertheless, we tried to keep everything as close as possible to support the comparison. Measurements that did not show a response at both labs are not included (e.g.,  $\text{CH}_2\text{O}$  with humidity; compare Section 3.2.2). An overview of the comparison is given in Table 2. If exposed to  $\text{C}_6\text{H}_6$  and  $\text{CH}_2\text{O}$ , the response measured at UdS is lower for all sensors except for  $\text{V}_2\text{O}_5$ . Especially for

the CuO DEG sensor, the response varies a lot. The reported response for ZrO<sub>2</sub> towards C<sub>6</sub>H<sub>6</sub> was only observed at LiU, but the response (0.02%) was very small. Therefore, the measurements conducted with VOCs do not result in a clear outcome for the interlab studies. On the other hand, measurements with exposures towards NO<sub>2</sub> show the same trend for three of the four sensors: the response increases with an increase in concentration and decreases with the introduction of relative humidity, indicating that the sensors show very similar performance at both laboratories. The only exception is the exposure of the CuO NL towards 200 ppb at 25% RH at LiU, where the response direction changed compared to the exposure at 0% RH or towards 500 ppb at 50% RH at UdS, which could be explained by the competing effects of NO<sub>2</sub> and RH on the sensor surface.

**Table 2.** Summary of responses of all sensors towards C<sub>6</sub>H<sub>6</sub>, CH<sub>2</sub>O, and NO<sub>2</sub> at 150 °C under dry and humid conditions.

	Relative Response (%)							
	C <sub>6</sub> H <sub>6</sub> 200 ppb 0% RH LiU	C <sub>6</sub> H <sub>6</sub> 500 ppb 0% RH UdS	CH <sub>2</sub> O 200 ppb 0% RH LiU	CH <sub>2</sub> O 500 ppb 0% RH UdS	NO <sub>2</sub> 200 ppb 0% RH LiU	NO <sub>2</sub> 500 ppb 0% RH UdS	NO <sub>2</sub> 200 ppb 25% RH LiU	NO <sub>2</sub> 500 ppb 50% RH UdS
CuO	2.81	0.45	1.54	0.92	5.28	14.60	−0.89	5.87
Fe <sub>3</sub> O <sub>4</sub>	0.40	0.20	0.33	0.19	39.69	65.82	26.68	60.63
V <sub>2</sub> O <sub>5</sub>	0.17	0.27	0.25	0.38	−5.84	−8.93	−8.65	−11.87
ZrO <sub>2</sub>	0.02	/	/	/	−14.60	−17.10	−15.75	−16.94

The single standard deviation of the baseline resistance was used as an indicator of noise. Since a similar electronic setup was used in both labs, there is no distinct trend in the noise level between the labs. The standard deviation stayed below 0.1 Ω for all sensors, leading to a worst-case relative noise level of approximately 0.007%. This highly depends on the baseline resistance of the different sensors, which varied between 1.5 to 3.2 kΩ. With the ZrO<sub>2</sub> DEG sensor, the relative baseline noise was even 10 times lower.

Additional deviations could come from the uncertainties in concentration from the gas bottles, as each bottle, even with a purity of 6.0, has an approximate error range in concentration of up to ±10%. This alone can have a major impact on the observed sensor response. Another problem could come from the administered flows from the MFCs, although this is rather unlikely as only calibrated MFCs are used and frequently reassessed. Moreover, the background gas (purity of 6.0) used for mixing of test gases still contains approximately 1 ppm of contaminants, or the system could be contaminated by prior gas tests [28]. This can especially influence the comparison between both labs as the background gas at LiU is mixed from gas bottles (N<sub>2</sub> and O<sub>2</sub>), while the background gas at UdS comes from a 0-air generator. Since only relative responses and not absolute values are compared, the comparison is still valid. A variation due to the very small difference in background humidity is not expected (compare Section 3.2.2).

Nevertheless, we think that interlab studies should be conducted to verify sensor performances, at least qualitatively, and to raise awareness that published results may only be accurate for the specific setup used for the investigation, which itself can have an influence on sensor response. In-depth studies, comparing their gas measurements with certified labs, have shown that even there, unexpected deviations can occur, which opens the possibility for more insight into sensor behavior [29,30]. Unfortunately, round-robin testing, which is the standard in analytical chemistry to ensure that experimental procedures are correct, is still not applied in the field of chemical sensor research [31,32].

### 3.4. Data Analysis/Multisensor Array

As we have seen in the earlier sections, the different NL DEG sensors respond differently to different gases and environmental influences. This is summarized in Table 3. If the gas has the addition “+RH”, either 25% or 50% RH was used, which did not matter for the direction of response in this

case. The addition “+UV” means that the measurement was performed with 355 nm UV LED and at 50% RH.

**Table 3.** Summary of response directions (+ for positive, – for negative, and/or for no response) of all sensors towards CO, C<sub>6</sub>H<sub>6</sub>, CH<sub>2</sub>O, NH<sub>3</sub>, and NO<sub>2</sub> under dry and humid conditions.

	CO	CO + RH	C <sub>6</sub> H <sub>6</sub>	C <sub>6</sub> H <sub>6</sub> + RH	CH <sub>2</sub> O	Qualitative Response					
						CH <sub>2</sub> O + RH	NH <sub>3</sub>	NH <sub>3</sub> + RH	NH <sub>3</sub> + UV	NO <sub>2</sub>	NO <sub>2</sub> + RH
CuO	+	/	+	/	+	/	+	+	–	+	–
Fe <sub>3</sub> O <sub>4</sub>	+	/	+	/	+	/	–	–	–	+	+
V <sub>2</sub> O <sub>5</sub>	+	/	+	/	+	/	+	+	+	–	–
ZrO <sub>2</sub>	/	/	+	/	/	/	–	–	–	–	–

However, one sensor alone would not be able to distinguish between different gases very effectively. Therefore, using a sensor array with all or some of the used sensors could lead to a better classification of exposed gases [33]. A simple LDA (linear discriminant analysis) [34] was used to differentiate between three gases (C<sub>6</sub>H<sub>6</sub>, CH<sub>2</sub>O, and NO<sub>2</sub>) applied to all sensors during several single gas exposures at 0% RH. Each gas was applied three times, with a concentration of 200 ppb and a sensor operating temperature of 150 °C. The gas cycle was repeated twice, resulting in six exposures per gas in total. DAV<sup>3</sup>E, a MATLAB toolbox [35], was used to calculate an LDA scatter plot based on each measurement point during the exposure of each sensor. Each measurement point is used as this is exactly what would happen if the sensors are used in a real setup, where the resistance over time is measured and gas exposures need to be determined. For better clarity, however, only every 50th point is plotted. The first five seconds of each exposure are neglected due to time constants of the gas mixing system. The result of this LDA is shown in Figure 6. As expected, it is rather easy to discriminate between NO<sub>2</sub> and the two VOCs, as the response towards NO<sub>2</sub> is much higher in comparison. It is harder, but still not impossible, to discriminate between benzene and formaldehyde. This example is very much oversimplified as, for example, similar concentrations of different gases might give very different magnitudes of response (e.g., NO<sub>2</sub> vs. VOCs). Another problem is the high time constants of the sensor, and, therefore, each measurement point was used and not the slope of the change of the signal during exposure. One way to overcome this issue would be the application of cycled methods like temperature cycled operation (TCO) to create steep changes and more transient data for evaluation [33,36,37]. A more extensive data set with different gases, concentration levels, and combined gas exposures would be needed to make a proper statement about the applicability of these exact four sensors to real-world applications, which, in turn, would be highly application-dependent.

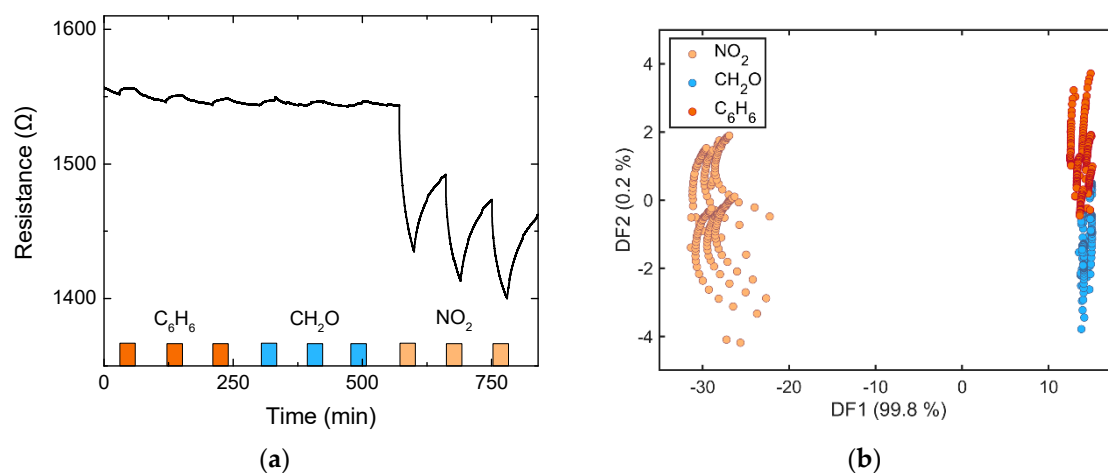


**Figure 6.** (a) Resistance over time of V<sub>2</sub>O<sub>5</sub> NL DEG towards 200 ppb of C<sub>6</sub>H<sub>6</sub>, CH<sub>2</sub>O, and NO<sub>2</sub> at 0% RH and 150 °C and (b) linear discriminant analysis (LDA) based on gas exposures of all four sensors.

#### 4. Conclusions

In conclusion, we have shown that nanolayer-decorated epitaxial graphene sensors perform differently depending on the decoration material used and the measurement conditions. Increased operating temperature and level of relative humidity were found to either increase or decrease the sensor response towards  $\text{NH}_3$ , depending on the material. Moreover, illumination with UV light, in general, results in increased sensor response and decreased time constants, although some decoration materials are not significantly affected by UV. Investigating gases of interest for AQM, the influence of relative humidity is large as it inhibits the response towards  $\text{C}_6\text{H}_6$ ,  $\text{CH}_2\text{O}$ , and  $\text{CO}$  completely, at least at the low concentrations tested here. Comparing the sensors in an interlab study, the responses vary strongly for the measured VOCs but stay very comparable for  $\text{NO}_2$ . This could indicate significant variations in either the concentrations of the source gases or, more likely, the concentrations of impurities in the source gas bottles, which, in turn, is an important aspect to consider for sensor calibration. Combining all four sensors into a sensor array, it was possible to distinguish between  $\text{C}_6\text{H}_6$ ,  $\text{CH}_2\text{O}$ , and  $\text{NO}_2$  in a dry ambient using an LDA.

**Supplementary Materials:** The following are available online at <http://www.mdpi.com/2079-4991/10/11/2168/s1>, Table S1: Summary of changes of baseline resistance with varying relative humidity.

**Author Contributions:** Conceptualization, M.R. and J.E.; methodology, M.R. and M.K.; software, M.R.; validation, M.R.; formal analysis, M.R.; investigation, M.R., A.I. and M.K.; resources, R.J. and A.S.; data curation, M.R.; writing—original draft preparation, M.R.; writing—review and editing, M.R., A.I., M.K., R.J., A.S. and J.E.; visualization, M.R.; supervision, J.E.; project administration, J.E.; funding acquisition, J.E. and R.J. All authors have read and agreed to the published version of the manuscript.

**Funding:** This research was funded by the Swedish Foundation for Strategic Research (SSF) through the grants GMT14-0077 and RMA15-024, as well as by the Estonian Ministry of Education and Research (institutional grant IUT34-27) and HORIZON 2020 Project No. 881603.

**Acknowledgments:** The authors would like to thank Professor Rositsa Yakimova and Ivan G. Ivanov from the Semiconductor Materials Division at Linköping University, Sweden, for the provision of pristine epitaxial graphene and the collection of Raman spectra, respectively, and Tobias Baur from the Lab for Measurement Technology at Saarland University, Germany, for helpful discussions regarding the usage of  $\text{DAV}^3\text{E}$ .

**Conflicts of Interest:** The authors declare no conflict of interest. The funders had no role in the design of the study; in the collection, analyses, or interpretation of data; in the writing of the manuscript, or in the decision to publish the results.

#### References

1. World Health Organisation. *WHO Social Media Toolkit for Air Pollution and Child Health: Prescribing Clean Air Launch*; WHO: Geneva, Switzerland, 2018.
2. The World Bank. *The Cost of Air Pollution: Strengthening the Economic Case for Action*; World Bank: Washington, DC, USA, 2016.
3. Szulczyński, B.; Gębicki, J. Currently commercially available chemical sensors employed for detection of volatile organic compounds in outdoor and indoor air. *Environments* **2017**, *4*, 21. [CrossRef]
4. Spinelle, L.; Gerboles, M.; Kok, G.; Persijn, S.; Sauerwald, T. Review of portable and low-cost sensors for the ambient air monitoring of benzene and other volatile organic compounds. *Sensors* **2017**, *17*, 1520. [CrossRef] [PubMed]
5. Jiang, L. *Environmental Gas Sensors 2020–2030: Technologies, Manufacturers, Forecasts*; IDTechEx: Boston, MA, USA, 2020.
6. Anichini, C.; Czepa, W.; Pakulski, D.; Aliprandi, A.; Ciesielski, A.; Samorì, P. Chemical sensing with 2D materials. *Chem. Soc. Rev.* **2018**, *47*, 4860–4908. [CrossRef] [PubMed]
7. Malik, R.; Tomer, V.K.; Mishra, Y.K.; Lin, L. Functional gas sensing nanomaterials: A panoramic view. *Appl. Phys. Rev.* **2020**, *7*. [CrossRef]
8. Meng, F.L.; Guo, Z.; Huang, X.J. Graphene-based hybrids for chemiresistive gas sensors. *TrAC—Trends Anal. Chem.* **2015**, *68*, 37–47. [CrossRef]
9. Gupta Chatterjee, S.; Chatterjee, S.; Ray, A.K.; Chakraborty, A.K. Graphene-metal oxide nanohybrids for toxic gas sensor: A review. *Sens. Actuators B Chem.* **2015**, *221*, 1170–1181. [CrossRef]

10. Rodner, M.; Puglisi, D.; Ekeroth, S.; Helmersson, U.; Shtepliuk, I.; Yakimova, R.; Skallberg, A.; Uvdal, K.; Schütze, A.; Eriksson, J. Graphene decorated with iron oxide nanoparticles for highly sensitive interaction with volatile organic compounds. *Sensors* **2019**, *19*, 918. [CrossRef]
11. Rodner, M.; Bahunjic, J.; Mathisen, M.; Gunnarsson, R.; Ekeroth, S.; Helmersson, U.; Ivanov, I.G.; Yakimova, R.; Eriksson, J. Performance tuning of gas sensors based on epitaxial graphene on silicon carbide. *Mater. Des.* **2018**, *153*, 153–158. [CrossRef]
12. Kodu, M.; Berholts, A.; Kahro, T.; Eriksson, J.; Yakimova, R.; Avarmaa, T.; Renge, I.; Alles, H.; Jaaniso, R. Graphene-based ammonia sensors functionalised with sub-monolayer V<sub>2</sub>O<sub>5</sub>: A comparative study of chemical vapour deposited and epitaxial graphene. *Sensors* **2019**, *19*, 951. [CrossRef]
13. Eschnauer, H.R. Pollution reduction in motor car exhaust gases by regulation of the fuel mixture with the lambda-sensor. In *Anthropogenic Platinum-Group Element Emissions: Their Impact on Man and Environment*; Zereini, F., Alt, F., Eds.; Springer: Berlin/Heidelberg, Germany, 2000; pp. 285–291. ISBN 978-3-642-59678-0.
14. Samarasekera, P.; Kumara, N.T.R.N.; Yapa, N.U.S. Sputtered copper oxide (CuO) thin films for gas sensor devices. *J. Phys. Condens. Matter* **2006**, *18*, 2417–2420. [CrossRef]
15. Yakimova, R.; Virojanadara, C.; Gogova, D.; Syväjärvi, M.; Siche, D.; Larsson, K.; Johansson, L.I. Analysis of the formation conditions for large area epitaxial graphene on SiC substrates. *Mater. Sci. Forum* **2010**, *645–648*, 565–568. [CrossRef]
16. Lloyd Spetz, A.; Andersson, M. Technology and application opportunities for SiC-FET gas sensors. In *Solid State Gas Sensors—Industrial Application*; Fleischer, M., Lehmann, M., Eds.; Springer: Berlin/Heidelberg, Germany, 2011; pp. 189–214. ISBN 978-3-642-28092-4.
17. Helwig, N.; Schüler, M.; Bur, C.; Schütze, A.; Sauerwald, T. Gas mixing apparatus for automated gas sensor characterization. *Meas. Sci. Technol.* **2014**, *25*, 055903. [CrossRef]
18. Leidinger, M.; Schultealbert, C.; Neu, J.; Schütze, A.; Sauerwald, T. Characterization and calibration of gas sensor systems at ppb level—A versatile test gas generation system. *Meas. Sci. Technol.* **2018**, *29*. [CrossRef]
19. Lee, D.S.; Riedl, C.; Krauss, B.; Von Klitzing, K.; Starke, U.; Smet, J.H. Raman spectra of epitaxial graphene on SiC and of epitaxial graphene transferred to SiO<sub>2</sub>. *Nano Lett.* **2008**, *8*, 4320–4325. [CrossRef]
20. Ferrari, A.C. Raman spectroscopy of graphene and graphite: Disorder, electron-phonon coupling, doping and nonadiabatic effects. *Solid State Commun.* **2007**, *143*, 47–57. [CrossRef]
21. Bouhafs, C.; Zakharov, A.A.; Ivanov, I.G.; Giannazzo, F.; Eriksson, J.; Stanishev, V.; Kühne, P.; Iakimov, T.; Hofmann, T.; Schubert, M.; et al. Multi-scale investigation of interface properties, stacking order and decoupling of few layer graphene on C-face 4H-SiC. *Carbon. N. Y.* **2017**, *116*, 722–732. [CrossRef]
22. Barsan, N.; Koziej, D.; Weimar, U. Metal oxide-based gas sensor research: How to? *Sens. Actuators B Chem.* **2007**, *121*, 18–35. [CrossRef]
23. Barsan, N.; Weimar, U. Conduction model of metal oxide gas sensors. *J. Electron.* **2001**, *7*, 143–167. [CrossRef]
24. Dickey, E.C.; Varghese, O.K.; Ong, K.G.; Gong, D.; Paulose, M.; Grimes, C. A room temperature ammonia and humidity sensing using highly ordered Nanoporous alumina films. *Sensors* **2002**, *2*, 91–110. [CrossRef]
25. Espid, E.; Taghipour, F. UV-LED photo-activated chemical gas sensors: A review. *Crit. Rev. Solid State Mater. Sci.* **2017**, *42*, 416–432. [CrossRef]
26. Berholts, A.; Kahro, T.; Floren, A.; Alles, H.; Jaaniso, R. Photo-activated oxygen sensitivity of graphene at room temperature. *Appl. Phys. Lett.* **2014**, *105*. [CrossRef]
27. Rodner, M.; Icardi, A.; Kodu, M.; Jaaniso, R.; Eriksson, J. Metal oxide nanolayer decorated epitaxial Graphene gas sensors for Air quality Monitoring. In Proceedings of the SMSI 2020 Conference—Sensor and Measurement Science International, Nuremberg, Germany, 22–25 June 2020; pp. 129–130.
28. Schütze, A.; Baur, T.; Leidinger, M.; Reimringer, W.; Jung, R.; Conrad, T.; Sauerwald, T. Highly sensitive and selective voc sensor systems based on semiconductor gas sensors: How to? *Environments* **2017**, *4*, 20. [CrossRef]
29. Bastuck, M.; Baur, T.; Richter, M.; Mull, B.; Schütze, A.; Sauerwald, T. Comparison of ppb-level gas measurements with a metal-oxide semiconductor gas sensor in two independent laboratories. *Sens. Actuators B Chem.* **2018**, *273*, 1037–1046. [CrossRef]
30. Sauerwald, T.; Baur, T.; Leidinger, M.; Reimringer, W.; Spinelle, L.; Gerboles, M.; Kok, G.; Schütze, A. Highly sensitive benzene detection with metal oxide semiconductor gas sensors—An inter-laboratory comparison. *J. Sens. Sens. Syst.* **2018**, *7*, 235–243. [CrossRef]

31. Buttner, W.; Burgess, R.; Rivkin, C.; Post, M.; Boon-Brett, L.; Black, G.; Harskamp, F.; Moretto, P. Round robin Testing of commercial hydrogen sensor performance—Observations and results: Preprint. In Proceedings of the National Hydrogen Association Conference and Expo, Long Beach, CA, USA, 3–6 May 2010.
32. Moritz, A.; Breuer, D. Production of test gases in the ppb range for round-robin tests and quality assurance measures during the measurement of VOCs. *J. Environ. Monit.* **2008**, *10*, 1454–1459. [CrossRef] [PubMed]
33. Reimann, P.; Schütze, A. Sensor arrays, Virtual multisensors, data fusion, and Gas sensor data evaluation. In *Springer Series on Chemical Sensors and Biosensors*; Springer: Berlin/Heidelberg, Germany, 2014; Volume 15, pp. 67–107. ISBN 978-3-642-54518-4.
34. Duda, R.; Hart, P.; Stork, D. *Pattern Classification*; John Wiley & Sons: Hoboken, NY, USA, 2001.
35. Bastuck, M.; Baur, T.; Schütze, A. DAV<sup>3</sup>E—A MATLAB toolbox for multivariate sensor data evaluation. *Sensors* **2018**, 489–506.
36. Bur, C.; Bastuck, M.; Puglisi, D.; Schütze, A.; Lloyd Spetz, A.; Andersson, M. Discrimination and quantification of volatile organic compounds in the ppb-range with gas sensitive SiC-FETs using multivariate statistics. *Sens. Actuators B Chem.* **2015**, *214*, 25–233. [CrossRef]
37. Bastuck, M. *Improving the Performance of Gas Sensor Systems with Advanced Data Evaluation, Operation, and Calibration Methods*; Linköping University: Linköping, Sweden, 2019.

**Publisher's Note:** MDPI stays neutral with regard to jurisdictional claims in published maps and institutional affiliations.



© 2020 by the authors. Licensee MDPI, Basel, Switzerland. This article is an open access article distributed under the terms and conditions of the Creative Commons Attribution (CC BY) license (<http://creativecommons.org/licenses/by/4.0/>).